# CUTTING EDGE METHODOLOGIES IN EXPERIMENTAL CARDIOVASCULAR RESEARCH

EDITED BY: Gabriela Kania, Przemyslaw Blyszczuk and Kenneth Boheler
PUBLISHED IN: Frontiers in Cardiovascular Medicine

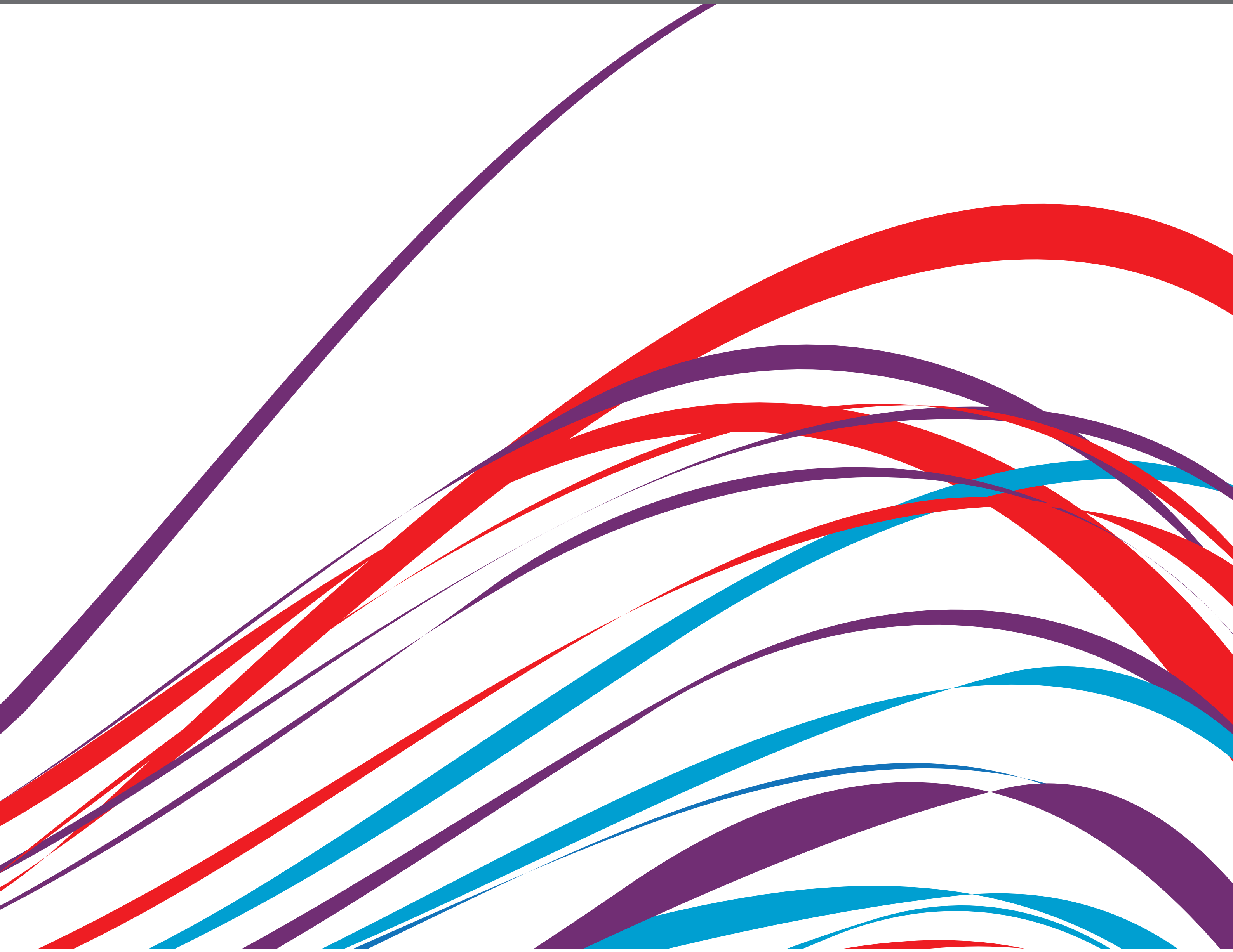

frontiers Research Topics

ISSN 1664-8714
ISBN 978-2-88966-444-3
DOI 10.3389/978-2-88966-444-3

## About Frontiers

Frontiers is more than just an open-access publisher of scholarly articles: it is a pioneering approach to the world of academia, radically improving the way scholarly research is managed. The grand vision of Frontiers is a world where all people have an equal opportunity to seek, share and generate knowledge. Frontiers provides immediate and permanent online open access to all its publications, but this alone is not enough to realize our grand goals.

## Frontiers Journal Series

The Frontiers Journal Series is a multi-tier and interdisciplinary set of open-access, online journals, promising a paradigm shift from the current review, selection and dissemination processes in academic publishing. All Frontiers journals are driven by researchers for researchers; therefore, they constitute a service to the scholarly community. At the same time, the Frontiers Journal Series operates on a revolutionary invention, the tiered publishing system, initially addressing specific communities of scholars, and gradually climbing up to broader public understanding, thus serving the interests of the lay society, too.

## Dedication to Quality

Each Frontiers article is a landmark of the highest quality, thanks to genuinely collaborative interactions between authors and review editors, who include some of the world's best academicians. Research must be certified by peers before entering a stream of knowledge that may eventually reach the public - and shape society; therefore, Frontiers only applies the most rigorous and unbiased reviews.
Frontiers revolutionizes research publishing by freely delivering the most outstanding research, evaluated with no bias from both the academic and social point of view. By applying the most advanced information technologies, Frontiers is catapulting scholarly publishing into a new generation.

## What are Frontiers Research Topics?

Frontiers Research Topics are very popular trademarks of the Frontiers Journals Series: they are collections of at least ten articles, all centered on a particular subject. With their unique mix of varied contributions from Original Research to Review Articles, Frontiers Research Topics unify the most influential researchers, the latest key findings and historical advances in a hot research area! Find out more on how to host your own Frontiers Research Topic or contribute to one as an author by contacting the Frontiers Editorial Office: frontiersin.org/about/contact

# CUTTING EDGE METHODOLOGIES IN EXPERIMENTAL CARDIOVASCULAR RESEARCH

Topic Editors:
**Gabriela Kania,** University Hospital Zürich, Switzerland
**Przemyslaw Blyszczuk,** Jagiellonian University Medical College, Poland
**Kenneth Boheler,** Johns Hopkins University, United States

**Citation:** Kania, G., Blyszczuk, P., Boheler, K., eds. (2021). Cutting Edge Methodologies in Experimental Cardiovascular Research. Lausanne: Frontiers Media SA. doi: 10.3389/978-2-88966-444-3

# Table of Contents

frontiers
in Cardiovascular Medicine

EDITORIAL
published: 14 December 2020
doi: 10.3389/fcvm.2020.621900

# Editorial: Cutting Edge Methodologies in Experimental Cardiovascular Research

*Przemysław Błyszczuk* [1,2]*, *Kenneth R. Boheler* [3]* *and Gabriela Kania* [1]*

[1] *Department of Rheumatology, Center of Experimental Rheumatology, University Hospital Zurich, Zurich, Switzerland,* [2] *Department of Clinical Immunology, Jagiellonian University Medical College, Krakow, Poland,* [3] *Department of Biomedical Engineering, Johns Hopkins School of Medicine, Baltimore, MD, United States*

**Keywords: cardiovacsular disease(s), methodolody, heart, cutting edge, therapy**

OPEN ACCESS

**Edited by:**
*Paolo Madeddu,*
*University of Bristol, United Kingdom*

**Reviewed by:**
*Martino Deidda,*
*University of Cagliari, Italy*
*Federico Quaini,*
*University of Parma, Italy*
*Isotta Chimenti,*
*Sapienza University of Rome, Italy*
*Alessandra Magenta,*
*Consiglio Nazionale delle Ricerche (CNR), Italy*

***Correspondence:**
*Przemysław Błyszczuk*
*przemyslaw.blyszczuk@uzh.ch*
*Kenneth R. Boheler*
*kbohele1@jhmi.edu*
*Gabriela Kania*
*gabriela.kania@uzh.ch*

**Specialty section:**
*This article was submitted to Cardiovascular Biologics and Regenerative Medicine, a section of the journal Frontiers in Cardiovascular Medicine*

**Received:** *27 October 2020*
**Accepted:** *20 November 2020*
**Published:** *14 December 2020*

**Citation:**
*Błyszczuk P, Boheler KR and Kania G (2020) Editorial: Cutting Edge Methodologies in Experimental Cardiovascular Research. Front. Cardiovasc. Med. 7:621900. doi: 10.3389/fcvm.2020.621900*

**Editorial on the Research Topic**

**Cutting Edge Methodologies in Experimental Cardiovascular Research**

Cardiovascular disease is a leading cause of death and a serious economic burden to patients and society. An estimated 18 million people die of cardiovascular disease (including coronary heart disease, stroke, and non-ischemic heart failure) annually (1), and despite improvements in the treatment of cardiovascular disease, hospitalizations, morbidity, and mortality continue to increase. Over the past decade, clinical data has also shown that certain modern medications may be harmful when applied to heart failure patients (2). This is an emerging challenge and has driven the development of novel drugs and new therapeutic strategies for the prevention and management of this devastating disease that are both cardiac-oriented and disease-specific. Continued advancements in preclinical models may provide evidence for innovative and effective treatment strategies, while experimental research requires the use of up-to-date and standardized methodologies.

This Research Topic on *Cutting Edge Methodologies in Experimental Cardiovascular Research* presents a collection of nine experimental and review articles covering a broad area of experimental cardiovascular research ranging from studies on the preclinical cell (Burja et al.; Stellato et al.; Woulfe et al.; Zuppinger) and animal models (Bacmeister et al.; Błyszczuk; Daskalopoulos et al.; Oppi et al.) to mathematical modeling (Faes et al.). Two articles represent typical methodological studies demonstrating novel or improved protocols. In the first, Woulfe et al. present a method for the isolation of myofibrils (a basic unit of a muscle) from rat primary cardiomyocytes. Experiments with these isolated myofibrils provide insight into muscle mechanics in the absence of non-motor proteins. This advancement enables the study of specific aspects of the function of the cardiomyocyte contractile apparatus that are not possible when using intact cells. Myofibrils are traditionally obtained from a small section of cardiac muscle and their isolation from cultured cardiomyocytes opens new opportunities for the *in vitro* manipulation of cultured cells prior to the isolation of myofibrils. In the second methodological study, Stellato et al. present a new approach to identifying and isolating murine cardiac fibroblasts using simple two-color flow cytometry. They showed that the defined combination of cell surface antigens (lineage markers Ter119, CD45, and CD31 vs. gp38) allowed the identification of collagen-producing fibroblasts in freshly isolated hearts of wild-type, non-transgenic mice (Stellato et al.). This method is breaking new ground for employing flow cytometry-based approaches to study cardiac fibroblasts in mouse models without the need for specific reporter mouse strain. In an experimental study, Burja et al. used an *in vitro* model of atherosclerosis to show the anti-inflammatory effects of olive leaf extracts in human coronary artery endothelial cells activated by serum amyloid A. The proof-of-concept provided by this early preclinical study demonstrates how promising candidates (here olive oil) may be employed for future therapeutic use. The next step in this bench-to-bedside approach is to validate any beneficial effects of these potential therapeutic agents in a living organism.

Currently, experimental animal models of human disease represent the most advanced platform for preclinical research. A review paper by Oppi et al. describes commonly used mouse models of atherosclerosis. Because atherosclerosis can be induced in several atherosclerosis-prone genetic mouse strains by different mechanisms, the paper provides a road map for researchers to choose the most appropriate model for a specific scientific question (Oppi et al.). In another review article on animal models, Błyszczuk focused on myocarditis and its consequence of dilated cardiomyopathy. This review presents the pathogenesis of myocarditis with possible clinical scenarios for the patients as well as the most commonly used experimental mouse models (Błyszczuk). This Research Topic also contains two experimental studies on animal models. In the first, Bacmeister et al. identified key methodological factors in the murine pressure-volume analysis under β-adrenergic stimulation. The authors emphasized the importance of establishing measurement protocols for both accuracy and the reproducibility of experimental data. In the second, Daskalopoulos et al. describe problems of data irreproducibility in animal models. As an example, the authors presented experimental results following treatment with a homologous peptide fragment of Wnt3a/5a UM206 in a mouse model of myocardial infarction. The authors go on to describe the inherent weaknesses associated with a single animal study due to the high number of uncontrollable variables (Daskalopoulos et al.). In laboratory practice, large scale, multicenter animal studies are often not possible for ethical and economic reasons. These data underscore the difficulty of assessing animal studies where the complexity of living organisms and the variability of housing conditions can affect outcomes.

An alternative to animal studies is offered by *in vitro* and *in silico* models. Zuppinger presents an overview of cardiovascular 3D cell culture technologies and discusses the advantages and drawbacks of various cardiac organoid cultures. The generation of human-induced pluripotent stem cell (iPSC)-derived cardiomyocytes have been proposed as models of human cardiac tissue, while advanced cell culture models coupled with human genetics are highly desirable in both experimental research and in regenerative medicine. However, these models have a number of limitations and must be considered premature as a replacement for animal studies. Although certain aspects of cardiovascular physiology and pathophysiology can be reliably mirrored by such *in vitro* models, it seems that the complete rejection of animal-based research is currently not possible. Mathematical modeling represents another option in cardiovascular research. Through the use of clinical data, Faes et al. built a mathematical model of coronary circulation to address the effects of the fractional flow reserve on the degree of coronary arterial stenosis. The successful implementation of a mathematical model to diagnostic procedures could reduce costs, save time, and minimize risk along with the social and economical burden for the patient.

Novel technologies and continued improvements to established protocols need to be shared across the scientific community to enhance experimental research and ensure that it is time- and cost- effective. The rapid development of machine learning, deep learning, and artificial intelligence may broaden the application of *in silico* approaches to address more complex scientific questions in the future. On a global scale, such advances would contribute to the faster translation of bench findings into clinical applications. This collection of Research Topic articles offers important insights into recent methodological advances in cardiovascular research that will help in the development of innovative treatment strategies.

## AUTHOR CONTRIBUTIONS

PB, KB, and GK wrote manuscript. All authors contributed to the article and approved the submitted version.

## REFERENCES

1. GBD 2017 Causes of Death Collaborators. Global, regional, and national age-sex-specific mortality for 282 causes of death in 195 countries and territories, 1980-2017: a systematic analysis for the Global Burden of Disease Study 2017. *Lancet*. (2018) 392:1736–88. doi: 10.1016/S0140-6736(18)32203-7
2. Rolski F, Blyszczuk P. Complexity of TNF-alpha signaling in heart disease. *J Clin Med*. (2020) 9:3267. doi: 10.3390/jcm9103267

**Conflict of Interest:** The authors declare that the research was conducted in the absence of any commercial or financial relationships that could be construed as a potential conflict of interest.

frontiers
in Cardiovascular Medicine

ORIGINAL RESEARCH
published: 19 February 2019
doi: 10.3389/fcvm.2019.00012

# A Novel Method of Isolating Myofibrils From Primary Cardiomyocyte Culture Suitable for Myofibril Mechanical Study

**Kathleen C. Woulfe [1]*, Claudia Ferrara [2], Jose Manuel Pioner [2], Jennifer H. Mahaffey [1], Raffaele Coppini [2], Beatrice Scellini [2], Cecilia Ferrantini [2], Nicoletta Piroddi [2], Chiari Tesi [2], Corrado Poggesi [2] and Mark Jeong [1]**

[1] Division of Cardiology, Department of Medicine, University of Colorado, Denver, CO, United States, [2] Division of Physiology, Department of Experimental and Clinical Medicine, University of Florence, Florence, Italy

OPEN ACCESS

**Edited by:**
Przemyslaw Blyszczuk,
University of Zurich, Switzerland

**Reviewed by:**
Akiyoshi Uezumi,
Tokyo Metropolitan Institute of Gerontology, Japan
Bertrand C.W. Tanner,
Washington State University, United States

***Correspondence:**
Kathleen C. Woulfe
Kathleen.woulfe@ucdenver.edu

**Specialty section:**
This article was submitted to Cardiovascular Biologics and Regenerative Medicine, a section of the journal Frontiers in Cardiovascular Medicine

**Received:** 30 November 2018
**Accepted:** 01 February 2019
**Published:** 19 February 2019

**Citation:**
Woulfe KC, Ferrara C, Pioner JM, Mahaffey JH, Coppini R, Scellini B, Ferrantini C, Piroddi N, Tesi C, Poggesi C and Jeong M (2019) A Novel Method of Isolating Myofibrils From Primary Cardiomyocyte Culture Suitable for Myofibril Mechanical Study. Front. Cardiovasc. Med. 6:12. doi: 10.3389/fcvm.2019.00012

Myofibril based mechanical studies allow evaluation of sarcomeric protein function. We describe a novel method of obtaining myofibrils from primary cardiomyocyte culture. Adult rat ventricular myocytes (ARVMs) were obtained by enzymatic digestion and maintained in serum free condition. ARVMs were homogenized in relaxing solution (pCa 9.0) with 20% sucrose, and myofibril suspension was made. Myofibrils were $Ca^{2+}$-activated and relaxed at 15°C. Results from ARVM myofibrils were compared to myofibrils obtained from ventricular tissue skinned with Triton X-100. At maximal $Ca^{2+}$-activation (pCa 4.5) myofibril mechanical parameters from ARVMs were $6.8 \pm 0.9$ mN/mm$^2$ (resting tension), $146.8 \pm 13.8$ mN/mm$^2$ (maximal active tension, $P_0$), $5.4 \pm 0.22$ s$^{-1}$ (rate of force activation), $53.4 \pm 4.4$ ms (linear relaxation duration), $0.69 \pm 0.36$ s$^{-1}$ (linear relaxation rate), and $10.8 \pm 1.3$ s$^{-1}$ (exponential relaxation rate). Force-pCa curves were constructed from Triton skinned tissue, ARVM culture day 1, and ARVM culture day 3 myofibrils, and $pCa_{50}$ were $5.79 \pm 0.01$, $5.69 \pm 0.01$, and $5.71 \pm 0.01$, respectively. Mechanical parameters from myofibrils isolated from ARVMs treated with phenylephrine were compared to myofibrils isolated from time-matched non-treated ARVMs. Phenylephrine treatment did not change the kinetics of activation or relaxation but decreased the $pCa_{50}$ to $5.56 \pm 0.03$ (vehicle treated control: $5.67 \pm 0.03$). For determination of protein expression and post-translational modifications, myofibril slurry was re-suspended and resolved for immunoblotting and protein staining. Troponin I phosphorylation was significantly increased at serine 23/24 in phenylephrine treated group. Myofibrils obtained from ARVMs are a viable method to study myofibril mechanics. Phenylephrine treatment led to significant decrease in $Ca^{2+}$-sensitivity that is due to increased phosphorylation of TnI at serine 23/24. This culture based approach to obtaining myofibrils will allow pharmacological and genetic manipulation of the cardiomyocytes to correlate biochemical and biophysical properties.

**Keywords: myofibril, cell culture, mechanics, sarcomere, signaling**

# INTRODUCTION

Since its development, myofibril mechanical assessment has led to advances in understanding of muscle function (1–4). Myofibril-based mechanical assays, compared to studies using larger preparations, offer several advantages. First, as the smallest ensemble of muscle motor proteins, myofibril mechanical experiments provide an evaluation of muscle mechanics without influence by non-motor protein systems such as those involved in calcium handling, energy metabolism, and the extracellular matrix. Second, the level of detail which myofibril mechanical experiments provide, such as resolution of the two phases of cardiac muscle fiber relaxation, is not possible with skinned cardiac fiber or intact cardiomyocyte preparations.

Traditionally, myofibrils are obtained from a small section of muscle that is either glycerinated or skinned in Triton X-100 and homogenized (5, 6). A major limitation of this approach is that these myofibrils are "as-is" with limited potential for biochemical manipulations. In this regard, specifically targeting a particular signaling pathway can only be achieved by generating transgenic animals, which is time-intensive and costly. The major strength of cardiomyocyte culture-based experiments is the ability to utilize readily available reagents and tools to address the myofilament mechanical consequences of altering a particular cellular function. Furthermore, with rapid advancement in stem cell-derived cellular systems, an *in vitro* method of obtaining myofibrils will provide a powerful experimental platform to better understand the pathobiology of diseases involving striated muscle. In this paper, we report a novel method of obtaining myofibrils from primary adult rat ventricular myocyte (ARVM) culture. We show that myofibrils obtained from primary ARVMs are equivalent to the traditional method and show applicability of this method to dissect the functional consequences of manipulating a specific signaling cascade.

# METHODS

## Experimental Protocol

Adult rat left ventricular myocytes (ARVMs) were obtained from female Sprague Dawley rats (250–300 g) (7). Animal studies were reviewed and approved by University of Florence and University of Colorado Institutional Animal Care and Use Committee (IACUC) thereby meeting the standards set by the Directive 2010/63/EU of the European Parliament on the protection of animals used for scientific purposes and the NIH standards for the care and use of laboratory animals. The heart was rapidly removed and retrograde perfused with perfusion buffer (120.5 mM NaCl, 14.7 mM KCl, 0.6 mM $KH_2PO_4$, 0.6 mM $Na_2HPO_4$, 1.2 mM $MgSO_4$, 4.6 mM $NaHCO_3$, 10 mM Na-HEPES, 30 mM Taurine, 10 mM 2,3-butanedione monoxime, 5.5 mM Glucose, pH 7.2) for 10 min at 37°C. A small section of the left ventricular apex was cut at the end of the pre-digestion perfusion. The small apical tissue was skinned in Triton X-100. The remainder of the heart was enzymatically digested to make ARVMs (**Figure 1**).

## Cardiomyocyte Culture

The heart was digested with Liberase DH (Roche, 0.33 mg/ml) for 8 min, cut into small pieces, and a slurry was filtered through sterile 150-nm mesh. The filtrate was centrifuged at 400 g for 4 min to separate myocytes from non-myocytes. The myocyte suspension was layered over 60 μg/ml of BSA and allowed to settle for 15 min to separate myocytes from non-myocytes. Myocyte concentration was determined and plated on 100 mm laminin-coated plastic culture dishes at a density of 100 to 150 cells/mm$^2$. The ARVM culture was maintained in serum-free DMEM supplemented with albumin (2 mg/ml), carnitine (2 mmol/l), creatine (5 mmol/l), taurine (5 mmol/l), BDM (1 mg/ml), and penicillin-streptomycin (100 μg/ml).

## Myofibrils From Cardiomyocyte Culture

ARVMs were washed in sterile PBS (room temperature) twice then collected one of two ways. (1) The cells were collected in 1 ml of cold 20% sucrose in relaxing solution (pCa 9.0) with protease inhibitor cocktail (10 μM leupeptin, 5 μM pepstatin, 200 μM phenyl-methylsuphonylfluoride, 10 μM E64, 500 μM NaN3, 2 mM dithioerythritol). The demembraned ARVM slurry was vortexed (30 s then settled on ice for 10 min. The cell suspension was centrifuged (300 g for 15 min in 4°C) and the pellet was resuspended in fresh relaxing solution with protease inhibitor cocktail to remove the sucrose. The resuspension/wash cycle was repeated twice. The final demembraned ARVMs were resuspended in relaxing solution with protease inhibitor cocktail and homogenized at medium speed (Tissue Tearer) for 15–20 s to make the final myofibril suspension. (2). Cells were collected in 1 ml of cold 0.01% Triton-X in relaxing solution (pCa9.0) with protease inhibitor cocktail. The ARVM slurry was treated as described above.

## Myofibrils From Apical Tissue

The left ventricular apex was cut into thin slices and bathed in 0.05% Triton X-100 and protease inhibitor cocktail in rigor solution overnight at 4°C. The skinned tissue was then washed twice in rigor solution with protease inhibitor cocktail with gentle shaking. The skinned tissue was resuspended in 1 ml rigor solution with protease inhibitor cocktail and homogenized at medium speed for 15–20 s to make the final myofibril suspension (8, 9).

## Myofibril Mechanical Study

We used previously published techniques to measure and control the force and length of isolated myofibrils activated and relaxed by fast solution switching (8, 9). Briefly, a small volume of myofibril suspension was transferred to a temperature controlled chamber (15°C) filled with relaxing solution (pCa 9.0). A small bundle of myofibrils were mounted between two microtools. One tool was connected to a motor that could produce rapid length changes (Mad City Labs). The second tool was a calibrated cantilevered force probe (4–8 μm/μN; frequency response 2–5 KHz). Myofibrils were set 5–10% above slack myofibril length in relaxed conditions (pCa 9). Average sarcomere length and myofibril diameter were measured using ImageJ. Mounted myofibrils were activated and relaxed by rapidly translating the

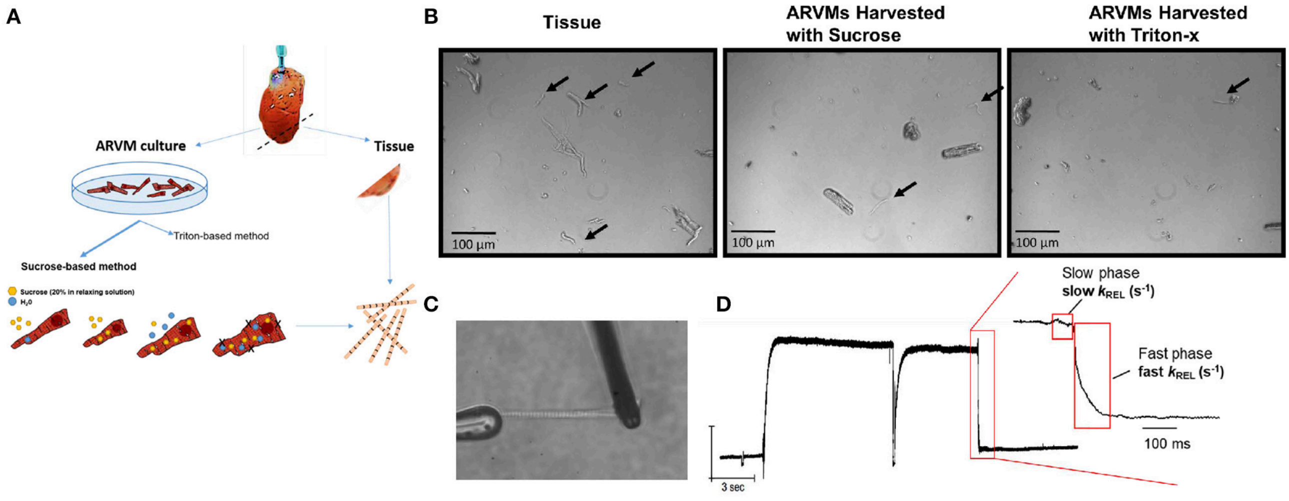

**FIGURE 1 | (A)** Experimental scheme: hearts from Sprague Dawley rats are retrograde perfused. Before enzymatic digestion, a small section of the apex is cut to obtain myofibrils by skinning in Triton-X100. Remaining heart was digested in Liberase DH to obtained primary ARVM culture. Myofibrils from ARVM culture were obtained by sucrose based osmotic shock method. **(B)** Representative images of 10x magnification demonstrating the different quantity and quality of myofibrils isolated using the different techniques. Black arrows indicate useable myofibrils in each field. The myocyte fragments shown in the panel of ARVMs harvested using Triton-x show a morphology distinct from the fragments of the other harvest techniques. **(C)** Representative image of a myofibril isolated from ARVMs using the sucrose-based method. **(D)** Representative trace from an ARMV-derived myofibril activated and relaxed by fast solution switching. ARVM, adult rat ventricular myocyte.

interface between two flowing streams of solutions of different pCa (9, 10). Data was collected and analyzed using a customized LabView software. Measured mechanical and kinetic parameters were defined as follows: resting tension ($mN/mm^2$)—myofibril basal tension in fully relaxing condition (pCa 9.0); maximal tension ($mN/mm^2$)—maximal tension generated at full calcium activation (pCa 4.5); the rate constant of tension development following maximal calcium activation ($k_{ACT}$); the rate constant of tension redevelopment following a release-restretch applied to the activated myofibril ($k_{TR}$) (11); rate constant of early slow force decline (slow $k_{REL}$)—the slope of the linear regression normalized to the amplitude of relaxation transient, duration of early slow force decline—measured from onset of solution change to the beginning of the exponential force decay, the rate constant of the final exponential phase of force decline (fast $k_{REL}$). To determine force-pCa relationship, peak isometric force was recorded at maximal (pCa 4.5) and submaximal (pCa 5.2, 5.4, 5.6, 5.8, 7) calcium concentrations and fitted to the Hill equation ($P/P0 = 1/(1 + 10^{(-nh(pCa50-pCa))})$).

## Myofilament Protein Analysis

To determine the level of phosphorylated myofilament proteins, the myofibril slurry was spun down and protein pellet was resuspended in isoelectric focusing buffer (IEF; 8 M Urea, 2.5 M Thiourea, 4% Chaps, 2 mM EDTA, 1 mM DTT, 1% TBP, phosphatase, and protease inhibitors). Twenty micrograms of protein was resolved by SDS-PAGE using a 10% gel and stained with ProQ Diamond. The gel was washed in methanol and restained with commassie brilliant blue (CBB) to determine total protein abundance. Gels were scanned and densitometry was measured using ImageJ. To determine the site-specific phosphorylation of troponin I, Western blots were performed. Site specific phospho-antibodies directed to serine 23/24 (Phosphosolutions p2010–2324, 1:1,000) and serine 43/44 (Phosphosolutions 9056, 1:1,000) of troponin I were used for Western blotting. TnI antibody (Fitzgerald 10R-T123K, 1:1,000) was used to determine the relative abundance of phosphorylated proteins. Densitometry data was used to normalize the phospho-specific signal over the total TnI signal.

## Statistical Analysis

Statistical analyses were performed using Prism Version 6 (GraphPad Software, San Diego, CA). Mean ± SEM values are presented. Data were checked for normality by Shapiro-Wilks test and if normal, compared by Student *t*-test (2 unpaired groups) or one-way ANOVA (>2 groups) with Newman-Keuls post-test. If not normal, data were log-transformed before statistical testing. Probability values of $p < 0.05$ were considered significant.

# RESULTS

## Myofibrils From Cultured Cardiomyocytes Permeabilized Using Sucrose Are Viable

Our initial aim was to determine the cardiomyocyte skinning buffer and homogenization protocol to harvest myofibrils from ARVMs. We began with low concentrations of Triton X-100 in rigor or relaxing solutions. 0.1% Triton X-100 caused complete lysis of cardiomyocytes in either buffer. We were able to harvest myofibrils from cardiomyocytes skinned in 0.01% Triton X-100 in rigor solutions but yielded poor quality and lower quantity of myofibrils. These myofibrils tended to be shorter, more fragmented, and difficult to mount on our force recording machine (**Figure 1B**). Sucrose (20% by volume) in relaxing solution was able to disrupt the cellular membrane without affecting the integrity of the myofibrils (**Figures 1B–D**).

## Mechanical Parameters From Myofibrils From ARVM Are Comparable to the Mechanical Parameters From Myofibrils From Tissue

Next mechanical parameters of myofibrils from ARVM culture harvested with sucrose or frozen tissue were compared. Myofibrils were isolated from frozen rat LV as a comparison since this is the standard source of myofibrils used to assess disease-specific differences in human hearts or animal models. The isometric sarcomere length measured was similar. The mechanical and kinetic behavior of ARVM myofibrils was not statistically different from tissue-derived myofibrils for most parameters (**Table 1**). The kinetics of force redevelopment ($k_{TR}$) were, however, slower in myofibrils from tissue. Mechanical run-down, the decrement of force generation, and its kinetics with successive activation-relaxation cycles was comparable between myofibrils isolated from ARVMs and tissue (data not shown). Force-pCa curves were constructed from myofibrils obtained from ARVMs in culture or from tissue. $Ca^{2+}$-sensitivity and the Hill coefficients (nH) were similar between myofibrils from ARVM and tissue (**Figure 2A**).

**TABLE 1 |** Comparison of mechanical parameters between myofibrils obtained from ARVM culture vs. traditional small tissue section.

| | ARVM (N, *n*) | Tissue (N, *n*) | *P* |
|---|---|---|---|
| Sarcomere length (μm) | 2.24 ± 0.09 (6, 19) | 2.28 ± 0.07 (6, 15) | ns |
| Resting tension (mN/mm$^2$) | 6.8 ± 3.5 (6, 17) | 6.6 ± 3.8 (6, 13) | ns |
| Maximal tension (mN /mm$^2$) | 146.8 ± 51.7 (6, 14) | 139.6 ± 51.3 (6, 15) | ns |
| $K_{ACT}$ (s$^{-1}$) | 5.37 ± 0.95 (6, 18) | 4.97 ± 1.14 (6, 14) | ns |
| $K_{TR}$ (s$^{-1}$) | 5.20 ± 0.89 (6, 17) | 4.52 ± 0.82 (6, 15) | $p < 0.05$ |
| Linear relaxation duration (ms) | 53.4 ± 17.7 (6, 16) | 52.0 ± 16.2 (6, 12) | ns |
| Exponential relaxation rate (s$^{-1}$) | 10.8 ± 4.8 (6, 14) | 14.6 ± 6.5 (6, 12) | ns |

*Myofibrils are fully calcium activated (pCa 4.5) and fully relaxed (pCa 9) by fast solution switching. Data presented with mean ± SEM. (N,n), (N# of rats, n # of myofibrils).*

## Duration of Cultured Cells Affects Kinetics of Activation and Relaxation but Not Calcium Sensitivity

In order to understand how prolonged culture affects the mechanical properties of cardiac myofibrils, we compared myofibrils isolated using sucrose from cardiomyocyte culture at day 1 and day 3. Myofibrils from day 1 group were isolated from cardiomyocytes that were kept in serum-free media in a 37°C incubator between 2 and 8 h. The 3-day-old cardiomyocytes were kept in a serum-free culture environment for an additional 48 h. Although magnitude of tension generation was unaffected by long-term culture, 3 days of culture showed changes in kinetics of activation and relaxation (**Table 2**). Using Pro-Q Diamond staining to assess for phosphorylation of sarcomeric proteins, we did not see a significant change in the degree of phosphorylation of key contractile and regulatory proteins of the

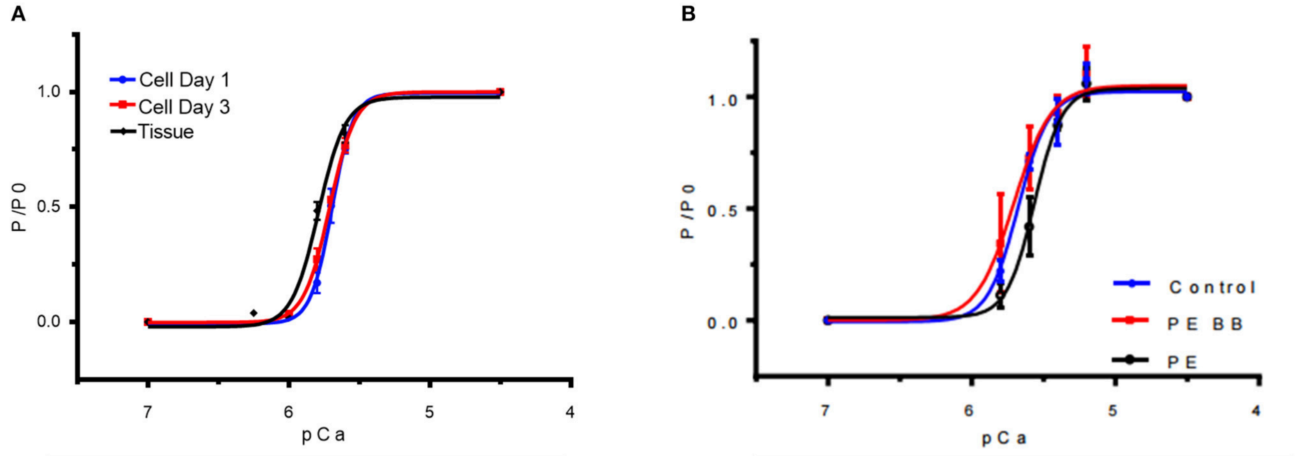

| | Tissue | ARVM Day 1 | ARVM Day 3 |
|---|---|---|---|
| pCa50 | 5.79 ± 0.01 | 5.69 ± 0.01 | 5.71 ± 0.01 |
| Hill Slope | 4.55 ± 0.55 | 5.74 ± 0. 72 | 4.74 ± 0.51 |

| | Control | PE | PE + BB |
|---|---|---|---|
| pCa50 | 5.67 ± 0.03 | 5.56 ± 0.03 | 5.71 ± 0.06 |
| Hill Slope | 4.09 ± 0.88 | 4.51 ± 1.16 | 3.35 ± 1.49 |

**FIGURE 2 | (A)** Force-pCa relationship of myofibrils obtained from cardiomyocyte culture day 1 (blue), culture day 3 (red) vs. myofibrils isolated from cardiac tissue (black). At each pCa, maximal tension was normalized to tension generated at pCa 4.5 ($P_0$). Data points are mean ± SEM. Lines are drawn according to the parameters estimated by fitting to the Hill equation ($P/ P_0 = 1/)(1 + 10^{(-nh(pCa50-pCa))}$). N = 4 rats, 16–20 myofibrils. **(B)** Force-pCa relationship of myofibrils obtained from ARVMs that were PE-treated (black), myofibrils treated with PE and the β-blocker propranolol (BB) (red) vs. vehicle treated control (blue). *N* = 6 rats, 16–22 myofibrils. ARVM, adult rat ventricular myocyte; PE, phenylephrine; BB, β-blocker propranolol.

**TABLE 2 |** Comparison of mechanical parameters between myofibrils obtained from ARVMs cultured for 1 day and ARVMs maintained in serum-free medium for 3 days.

| | **ARVM Day 1 (N, *n*)** | **ARVM Day 3 (N, *n*)** | ***P*** |
|---|---|---|---|
| Sarcomere length (μm) | 2.24 ± 0.09 (6, 19) | 2.25 ± 0.07 (8, 9) | ns |
| Resting tension (mN/mm$^2$) | 6.8 ± 3.5 (6, 17) | 7.3 ± 3.2 (8, 19) | ns |
| Maximal tension (mN /mm$^2$) | 146.8 ± 51.7 (6, 14) | 135.8 ± 47.6 (8, 18) | ns |
| $K_{ACT}$ (s$^{-1}$) | 5.37 ± 0.95 (6, 18) | 4.05 ± 0.98 (8, 19) | $P < 0.05$ |
| $K_{TR}$ (s$^{-1}$) | 5.20 ± 0.89 (6, 17) | 4.90 ± 0.95 (8, 19) | ns |
| Linear relaxation duration (ms) | 53.4 ± 17.7 (6, 16) | 34.2 ± 8.5 (8, 14) | $P < 0.05$ |
| Exponential relaxation rate (s$^{-1}$) | 10.8 ± 4.8 (6, 14) | 10.2 ± 5.2 (8, 16) | ns |

*Myofibrils are fully calcium activated (pCa 4.5) and fully relaxed (pCa 9) by fast solution switching. Data presented with mean ± SEM.*

sarcomere (**Figure 3**). The duration that ARVMs were kept in primary culture had no impact on $Ca^{2+}$-sensitivity or the Hill coefficient (**Figure 2A**).

## Treating ARVMs With Phenylephrine Leads to Decreased Calcium Sensitivity in Myofibrils Due to Phosphorylation of Troponin I

To demonstrate the applicability of culture based cardiomyocyte myofibrils to study the effect of manipulating the adrenergic signaling pathway, we treated ARVMs with phenylephrine (PE; 20 μM) for 48 h and performed myofibril mechanical measurements and sarcomeric protein analysis. Myofibrils were harvested using the sucrose method. We and others have shown that prolonged PE treatment leads to significant cardiomyocyte hypertrophy, induction of the pathologic gene profile, and deterioration of intact cardiomyocyte function (12, 13). The kinetics of activation and relaxation, and tension generation were unchanged with PE treatment (**Table 3**). Treatment with PE led to a significant decrease in calcium sensitivity (**Figure 2B**). Using CBB protein staining, we did not see a change in the expression level of sarcomeric proteins between vehicle vs. PE treated ARVMs (**Figure 3**). Global phosphorylation status was examined using Pro-Q Diamond stain. PE treatment led to increased phosphorylation of troponin I (TnI) (**Figure 3**). Western blot analysis confirmed the change in phosphorylation of serine 23/24 while serine 44 was not affected (**Figure 4A**). Decreased calcium sensitivity due to phosphorylation of TnI at serine 23/24 is consistent with previously published studies. To confirm our hypothesis that PE was also activating PKA via β-adrenergic signaling pathway, we treated ARVMs with PE with or without propranolol (2 μM). Propranolol treatment was sufficient to inhibit the increased phosphorylation of Serine 23/24 TnI (**Figure 4**) and the shift in pCa50 (**Figure 2B**). Propranolol treatment alone did not have any effect in basal expression of TnI or phosphorylation (**Figure 4**).

## DISCUSSION

We report a novel method of obtaining myofibrils from cultured ARVMs which are suitable for myofibril mechanical experiments. We establish that myofibrils obtained from an ARVM culture system are equivalent in mechanical properties to myofibrils prepared by skinning small cardiac tissue with Triton-X100. Demonstrating applicability of this method, we show that PE treatment does not significantly affect activation kinetics and tension generation, but PE treatment increases phosphorylation of TnI contributing to decreased myofilament calcium sensitivity when compared to vehicle treated controls. These findings show that primary ARVM culture system can be used for myofibril mechanical studies, and will expand the utility of myofibril mechanical experiment by providing a wider palette of experimental conditions.

The major advantage of myofibrils obtained from a primary culture system over the traditional Triton X-100 method is that primary culture system allows manipulation of specific cellular processes using widely available experimental techniques. The traditional method of obtaining myofibrils from a small heart section can be viewed as "as-is" with limited potential for *ex-vivo* manipulation. The combination of myofibril mechanical experiments and the wide array of biochemical techniques available to manipulate cultured cells provides a flexible experimental system to study the mechanical consequences of altering a specific cellular function. ARVM based myofibril studies provides additional advantages. ARVM are relatively inexpensive when compared to the need for generating mutant animals. For example, if you consider a potential experiment studying how protein x impacts myofibril mechanics, the cost and time to generate a transgenic or knockout animal is roughly $7,000 and can take up to 14 weeks. From there, there are costs associated with breeding and maintenance of a colony where animal costs can exceed $250 a month not including the salary of the staff necessary to oversee the colony. This total quickly reaches $10,000 or more and takes at least 6 months. In contrast, consider purchasing 6 adult rats at roughly $50 each and generating ARVMs. From here, the cells can be treated with inhibitors or ectopically expressed proteins and myofibril mechanics studied. On a practical level, we found that homogenizing intact cardiomyocytes to small bundles of myofibrils was easier to achieve from ARVMs than from small cardiac tissue. Our ARVM based method is complementary to the current standard and provides an additional source of experimental material. Importantly, our results show that myofibrils from ARVMs are mechanically comparable to myofibrils derived from tissue.

One difference in mechanical properties that we noted between tissue and ARVMs harvested using sucrose was that $k_{TR}$ was faster in ARVMs. This difference could be due to structural changes in the sarcomeres that occur following plating (14, 15) or it may be an experimental difference in isolation techniques (Triton X-100 compared to sucrose). It is important to recognize that these factors affect the mechanical parameters and experimental conditions should be considered appropriately. To further explore how plating impacts sarcomere function, we determined how duration of primary culture impacts myofibril function. Cardiomyocytes have been found to undergo transformation when maintained in primary culture. Although maintaining cardiomyocytes for up to 15 days has

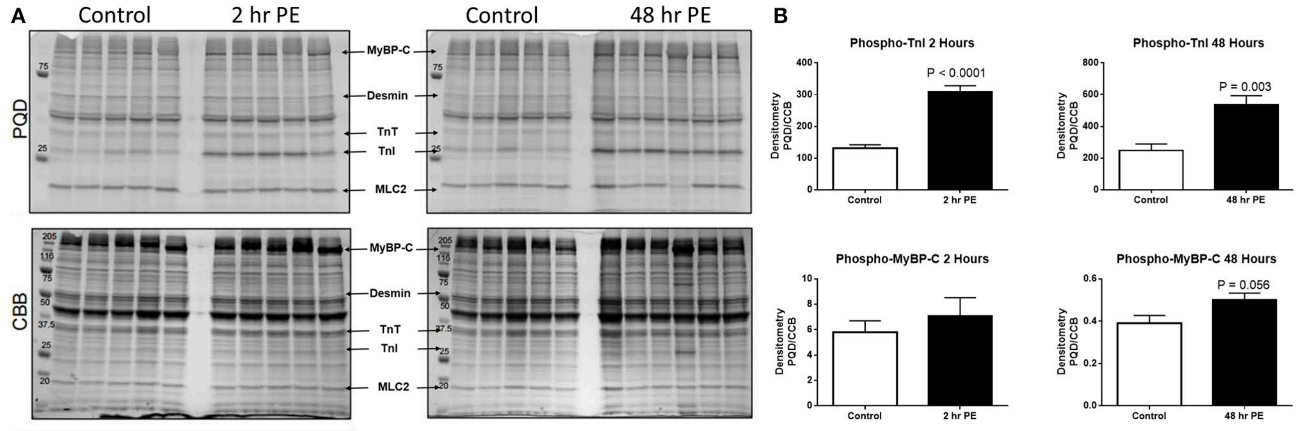

**FIGURE 3 | (A)** Myofilament protein phosphorylation from ARVMs treated with PE for 2 and 48 h. ProQ Diamond® stain (PQD) was used to determine the global phosphorylation status of myofilament proteins. The same gel was stained with commassie brilliant blue (CBB) to determine relative abundance of proteins. **(B)** Quantification of PQD over CBB densitometries. Only those sarcomeric proteins with significant change in global phosphorylation are shown. Phosphorylation of TnI is significantly increased in ARVMs after 2 h ($p < 0.0001$) and 48 h ($p = 0.003$) of PE treatment. Myosin binding protein C (MyBP-C) trends to increased phosphorylation at 48 h of treatment ($p = 0.056$) but not at 2 h. $N = 5$ rats. ARVM, adult rat ventricular myocyte; PE, phenylephrine; CBB, commassie brilliant blue; TnI, troponin I; MyBP-C, myosin binding protein C.

**TABLE 3 |** Comparison of mechanical parameters between myofibrils from ARVMs treated with PE for 48 h.

| | Vehicle (N, *n*) | PE (N, *n*) | *P* |
|---|---|---|---|
| Sarcomere length (μm) | 2.21 ± 0.1 (6, 19) | 2.21 ± 0.1 (6, 22) | ns |
| Resting tension (mN /mm$^2$) | 7.6 ± 2.8 (6, 18) | 6.7 ± 2.5 (6, 17) | ns |
| Maximal Tension (mN /mm$^2$) | 135.8 ± 47.6 (6, 17) | 118.8 ± 38.6 (6, 17) | ns |
| $K_{ACT}$ (s$^{-1}$) | 4.05 ± 0.98 (6, 19) | 3.95 ± 0.94 (6, 19) | ns |
| $K_{TR}$ (s$^{-1}$) | 4.90 ± 0.95 (6, 19) | 4.37 ± 1.02 (6, 19) | $P = 0.059$ |
| Linear Relaxation Duration (ms) | 34.2 ± 8.5 (6, 15) | 43.8 ± 17.1 (6, 15) | ns |
| Linear Relaxation Rate (s$^{-1}$) | 1.27 ± 0.91 (6, 6) | 1.35 ± 0.65 (6, 8) | ns |
| Exponential Relaxation Rate (s$^{-1}$) | 9.04 ± 3.3 (6, 15) | 10.0 ± 5.1 (6, 19) | ns |

*Myofibrils are fully calcium activated (pCa 4.5) and fully relaxed (pCa 9) by fast solution switching. Data presented with mean ± SEM. (N,n), (N# of rats, n # of myofibrils).*

been described (15), we and other investigators report an optimal culture time frame of up to 5–8 days (7). It is believed that the limited life-span of ARVMs in culture is due to dedifferentiation. Eppenberger et al. (16) demonstrated that over time cultured ARVMs have extensive morphological changes so that they look more like fetal myofibril and therefore achieve a less differentiated state (16). Dedifferentiation of cardiomyocytes in long-term culture is inevitable, but serum-free culture media decreases the rate of dedifferentiation (14). The culture media is critical to maintain healthy cells, and the culture media additives for ARVMs are albumin, creatine, carnitine, taurine, BDM, penicillin, and streptomycin. We have set 5 days as the upper limit for maintaining ARVMs in culture, and have designed our experiments around this time frame. We and others have previously shown and show additional data in this report that key functional and regulatory proteins of the sarcomere are unchanged in the level of expression and modification (12, 13, 17). The half-life of sarcomeric proteins ranges between 3 and 10 days (18, 19). Our data shows that there is no significant change in the expression level or global phosphorylation of sarcomeric proteins obtained from ARVMs in short vs. long term culture. Although we do not report qualitative or quantitative changes of sarcomeric proteins, we report significant changes in activation and relaxation kinetics between day 1 and day 3. This degree of change in biomechanical properties is not unexpected considering that ARVMs in primary culture are dedifferentiating. We hypothesize that routine biochemical assays used in this study to evaluate for the abundance and the post-translational modification status of sarcomeric proteins are not sensitive enough to detect subtle changes. These small changes appear to be sufficient to exert significant change in myofilament function. In this regard, experiments that compare myofibril mechanics between freshly isolated ARVM to one that is several days old would be inappropriate. In our experimental protocol, treated groups are always compared to age-matched vehicle treated controls, thereby allowing us to evaluate the effects of the treatment group while taking into account the unavoidable changes that are inherent in a primary culture based experiment.

Adult rat ventricular cardiomyocytes treated with PE (20 μM) for 48 h demonstrate that TnI phosphorylation is an important effector of sarcomeric protein function. Previously, we and others have shown that treating ARVMs with 48 h of PE caused contractile dysfunction (7, 13). This report builds on the previous study and provides new data showing that cardiomyocyte dysfunction does not require dysfunction of myofibril contractile machinery. This observation suggests a hierarchy of cardiomyocyte dysfunction by showing that the contractile machinery remains capable even in the face of

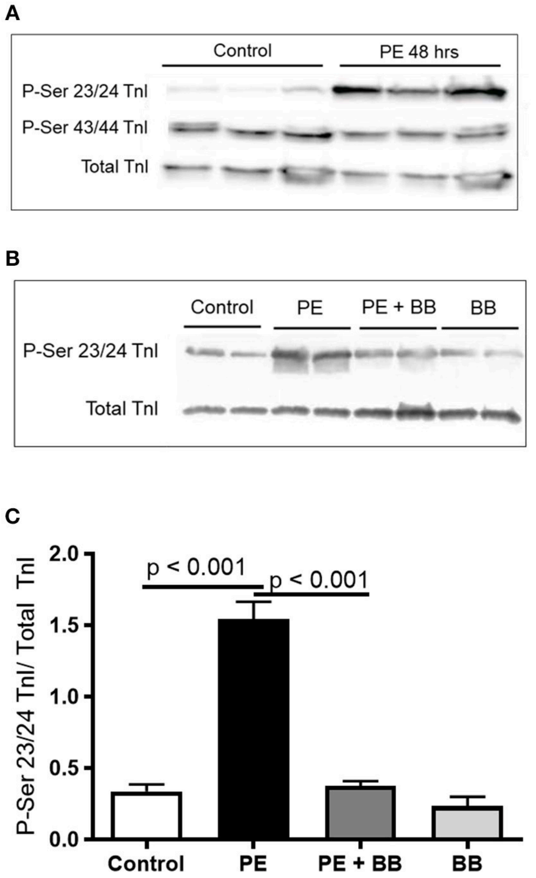

**FIGURE 4 | (A)** Representative Western blot demonstrating serine 23/24 is preferentially phosphorylated with PE treatment. Each lane is protein isolated from different experiments. These conditions were repeated in ARVMs cultured from 5 different rat hearts. **(B)** Representative image of a Western blot showing pre-treatment of ARVMs with the β-blocker propranolol (BB) leadsto inhibition of TnI phosphorylation at serine 23/24. Experiment was repeated in ARVMs cultured from 3 different rat hearts. **(C)** Quantification of TnI serine 23/24 phosphorylation normalized to total TnI. PE significantly increases phosphorylation of TnI at Ser 23/24 ($p < 0.001$). Treatment with PE and a β-blocker (BB) propranolol, normalizes TnI phosphorylation (PE tx v PE+BB $p < 0.001$). Each lane is protein isolated from different experiments. These conditions were repeated in ARVMs cultured from 3 different rat hearts. TnI, troponin I; PE, phenylephrine; ARVM, adult rat ventricular myocyte; BB, β-blocker propranolol.

cellular dysfunction. If the basic contractile unit from a dysfunctional cardiomyocyte is functioning normally, then can we target the basic contractile unit to normalize the whole cell function? We have previously published data showing that targeted inhibition of histone deacetylase 6 can augment contractility of myofibrils to normalize whole heart function in an angiotensin model of rodent heart failure (20). This strategy of targeting the myofibril to augment inotrope may offer benefits over currently available agents such as dobutamine or milrinone which targets the upstream receptor or enzymatic cascade immediately below the receptor. Clinical data may support this hypothesis since in adult heart failure literature, prolonged use of dobutamine or milrinone, while having positive inotropic effects, leads to increased mortality from side effects (21, 22). If our observation can be applied to human heart failure, perhaps targeting the myofibrillar proteins directly may provide a more direct and less toxic inotropic support.

We also report that PE, an α-adrengeric and β-adrenergic agonist (23), modifies TnI at serine 23/24. TnI serine 23/24 is predominantly under the control of protein kinase A (PKA), the down-stream effector of β-adrenergic receptor cascade. This observation provides insight into the role of PKA in modulating troponin I phosphorylation, the kinetics of cross-bridge cycle, and calcium sensitivity of cardiac myofibrils. We show that increased phosphorylation of serine 23/24 TnI decreases the calcium sensitivity without affecting the kinetics of activation or relaxation. Our results are in agreement with previous work performed in human myofibrils treated with PKA (24). Others, using rodent myofibrils, showed that activation of PKA resulted in both right shift in calcium sensitivity and changes in activation and relaxation kinetics (25, 26). Specifically, Rao et al. (25) exchanged TnI with targeted mutations in serine 23/24 into myofibrils to illustrate that phosphorylation status of TnI can control both relaxation duration and calcium sensitivity of activation. While both studies show the regulatory role of serine 23/24 in calcium sensitivity of activation, PE treatment of ARVMs leads to different results in relaxation kinetics. This difference may be due to the experimental condition. In our experiment, we stimulated cardiomyocytes with an upstream agonist thereby activating myriad of other secondary effectors. In Rao's work, exchanging mutant TnI into myofibrils would avoid the effects of signaling cascade that results from receptor activation (25). Regardless of the experimental protocol, we are in agreement that serine 23/24 is an important effector in changing sensitivity to calcium activation. Additional conclusions about the role of serine 23/24 in regulating relaxation remains, however, unsettled. The ability to obtain viable myofibrils from ARVMs presents an opportunity to use established myofibril mechanical assays in an *in vitro* model system which will be a valuable tool to inform mechanisms driving mechanical alterations.

In conclusion, we report that myofibrils obtained from ARVM culture are similar in mechanical properties to myofibrils isolated by skinningsmall sections of heart tissue.. While the traditional method of Triton X-100 based myofibrils will remain germane to myofibril mechanical research, we are confident that the primary ARVM culture based myofibrils will prove to be a powerful research tool complementing the time proven traditional method.

## AUTHOR CONTRIBUTIONS

MJ, CFa, JM, BS, KW, and NP performed myofibril mechanical experiments. MJ, JP, RC, and CFi isolated adult rat ventricular myocytes and myofibrils. MJ and CP designed and built the photodiode motion detector. MJ, CFi, and RC wrote the data acquisition program. MJ and JM performed protein analysis. MJ, KW, CT, and CP designed the experiments and analyzed all data. All authors contributed to writing the manuscript.

## FUNDING

This work was supported by Sarnoff Endowment [Fellow to Faculty Transition 379 Award (MJ)]; the National Institute of Health [2K12HD057022-11 (KW); 380 5KL2TR001080-02 (MJ)]; EU [STREP project 241577 BIG HEART, seventh 381 European Framework Program (CP)]; and the Italian Ministry of Health [WFR GR-2011-382 02350583 (CFi)].

## ACKNOWLEDGMENTS

The authors acknowledge Amit Patel for his assistance with writing the data acquisition program, Ted Anderson (Original Code Consultants) for his assistance in writing the data analysis program, and Allistair Moses for his assistance in designing the photodiode motion detector.

## REFERENCES

1. Tesi C, Piroddi N, Colomo F, Poggesi C. Relaxation kinetics following sudden Ca(2+) reduction in single myofibrils from skeletal muscle. *Biophys J*. (2002) 83:2142–51. doi: 10.1016/S0006-3495(02)73974-X
2. Stehle R, Kruger M, Pfitzer G. Force kinetics and individual sarcomere dynamics in cardiac myofibrils after rapid ca(2+) changes. *Biophys J*. (2002) 83:2152–61. doi: 10.1016/S0006-3495(02)73975-1
3. Stehle R, Solzin J, Iorga B, Poggesi C. Insights into the kinetics of Ca2+-regulated contraction and relaxation from myofibril studies. *Pflugers Arch*. (2009) 458:337–57. doi: 10.1007/s00424-008-0630-2
4. Stehle R, Iorga B. Kinetics of cardiac sarcomeric processes and rate-limiting steps in contraction and relaxation. *J Mol Cell Cardiol*. (2010) 48:843–50. doi: 10.1016/j.yjmcc.2009.12.020
5. Piroddi N, Belus A, Scellini B, Tesi C, Giunti G, Cerbai E, et al. Tension generation and relaxation in single myofibrils from human atrial and ventricular myocardium. *Pflugers Arch*. (2007) 454:63–73. doi: 10.1007/s00424-006-0181-3
6. Piroddi N, Belus A, Eiras S, Tesi C, van der Velden J, Poggesi C., et al. No direct effect of creatine phosphate on the cross-bridge cycle in cardiac myofibrils. *Pflugers Arch*. (2006) 452:3–6. doi: 10.1007/s00424-005-0008-7
7. Jeong MY, Walker JS, Brown RD, Moore RL, Vinson CS, Colucci WS., et al. AFos inhibits phenylephrine-mediated contractile dysfunction by altering phospholamban phosphorylation. *Am J Physiol Heart Circ Physiol*. (2010) 298:H1719–26. doi: 10.1152/ajpheart.00937.2009
8. Colomo F, Nencini S, Piroddi N, Poggesi C, Tesi C. Calcium dependence of the apparent rate of force generation in single striated muscle myofibrils activated by rapid solution changes. *Adv Exp Med Biol*. (1998) 453:373–81; discussion: 381–2. doi: 10.1007/978-1-4684-6039-1_42
9. Tesi C, Colomo F, Nencini S, Piroddi N, Poggesi C. The effect of inorganic phosphate on force generation in single myofibrils from rabbit skeletal muscle. *Biophys J*. (2000) 78:3081–92. doi: 10.1016/S0006-3495(00)76845-7
10. Tesi C, Colomo F, Nencini S, Piroddi N, Poggesi C. Modulation by substrate concentration of maximal shortening velocity and isometric force in single myofibrils from frog and rabbit fast skeletal muscle. *J Physiol*. (1999) 516 (Pt 3):847–53. doi: 10.1111/j.1469-7793.1999.0847u.x
11. Brenner B. Effect of Ca2+ on cross-bridge turnover kinetics in skinned single rabbit psoas fibers: implications for regulation of muscle contraction. *Proc Natl Acad Sci USA*. (1988) 85:3265–9. doi: 10.1073/pnas.85.9.3265
12. Jeong MY, Kinugawa K, Vinson C, Long CS. AFos dissociates cardiac myocyte hypertrophy and expression of the pathological gene program. *Circulation* (2005) 111:1645–51. doi: 10.1161/01.CIR.0000160367.99928.87
13. Satoh N, Suter TM, Liao R, Colucci WS. Chronic alpha-adrenergic receptor stimulation modulates the contractile phenotype of cardiac myocytes *in vitro*. *Circulation* (2000) 102:2249–54. doi: 10.1161/01.CIR.102.18.2249
14. Bugaisky LB, Zak R. Differentiation of adult rat cardiac myocytes in cell culture. *Circ Res*. (1989) 64:493–500. doi: 10.1161/01.RES.64.3.493
15. Volz A, Piper HM, Siegmund B, Schwartz P. Longevity of adult ventricular rat heart muscle cells in serum-free primary culture. *J Mol Cell Cardiol*. (1991) 23:161–73. doi: 10.1016/0022-2828(91)90103-S
16. Eppenberger ME, Hauser I, Baechi T, Schaub MC, Brunner UT, Dechesne CA, et al. Immunocytochemical analysis of the regeneration of myofibrils in long-term cultures of adult cardiomyocytes of the rat. *Dev Biol*. (1988) 130:1–15. doi: 10.1016/0012-1606(88)90408-3
17. Rust EM, Westfall MV, Metzger JM. Stability of the contractile assembly and Ca2+-activated tension in adenovirus infected adult cardiac myocytes. *Mol Cell Biochem*. (1998) 181:143–55. doi: 10.1023/A:1006802719136
18. Martin AF. Turnover of cardiac troponin subunits. Kinetic evidence for a precursor pool of troponin-I. *J Biol Chem*. (1981) 256:964–8.
19. Zak R, Martin AF, Prior G, Rabinowitz M. Comparison of turnover of several myofibrillar proteins and critical evaluation of double isotope method. *J Biol Chem*. (1977) 252:3430–5.
20. Demos-Davies KM, Ferguson BS, Cavasin MA, Mahaffey JH, Williams SM, Spiltoir JI, et al. HDAC6 contributes to pathological responses of heart and skeletal muscle to chronic angiotensin-II signaling. *Am J Physiol Heart Circ Physiol*. (2014) 307:H252–8. doi: 10.1152/ajpheart.00149.2014
21. O'Connor CM, Gattis WA, Uretsky BF, Adams KF, McNulty SE, Grossman SH, et al. Continuous intravenous dobutamine is associated with an increased risk of death in patients with advanced heart failure: insights from the Flolan International Randomized Survival Trial (FIRST). *Am Heart J*. (1999) 138 (1 Pt 1):78–86. doi: 10.1016/S0002-8703(99)70250-4
22. Packer M, Carver JR, Rodeheffer RJ, Ivanhoe RJ, DiBianco R, Zeldis SM, et al. Effect of oral milrinone on mortality in severe chronic heart failure. The PROMISE study research group. *N Engl J Med*. (1991) 325:1468–75. doi: 10.1056/NEJM199111213252103
23. Endoh M, Shimizu T, Yanagisawa T. Characterization of adrenoceptors mediating positive inotropic responses in the ventricular myocardium of the dog. *Br J Pharmacol*. (1978) 64:53–61. doi: 10.1111/j.1476-5381.1978.tb08640.x
24. Walker JS, Walker LA, Margulies K, Buttrick P, de Tombe P. Protein kinase A changes calcium sensitivity but not crossbridge kinetics in human cardiac myofibrils. *Am J Physiol Heart Circ Physiol*. (2011) 301:H138–46. doi: 10.1152/ajpheart.00838.2010
25. Rao V, Cheng Y, Lindert S, Wang D, Oxenford L, McCulloch AD, et al. PKA phosphorylation of cardiac troponin I modulates activation and relaxation kinetics of ventricular myofibrils. *Biophys J*. (2014) 107:1196–204. doi: 10.1016/j.bpj.2014.07.027
26. Vikhorev PG, Song W, Wilkinson R, Copeland O, Messer AE, Ferenczi MA., et al. The dilated cardiomyopathy-causing mutation ACTC E361G in cardiac muscle myofibrils specifically abolishes modulation of Ca(2+) regulation by phosphorylation of troponin I. *Biophys J*. (2014) 107:2369–80. doi: 10.1016/j.bpj.2014.10.024

**Conflict of Interest Statement:** The authors declare that the research was conducted in the absence of any commercial or financial relationships that could be construed as a potential conflict of interest.

frontiers
in Cardiovascular Medicine

ORIGINAL RESEARCH
published: 10 April 2019
doi: 10.3389/fcvm.2019.00036

# Assessment of PEEP-Ventilation and the Time Point of Parallel-Conductance Determination for Pressure-Volume Analysis Under β-Adrenergic Stimulation in Mice

***Lucas Bacmeister*** [1,2*†], ***Sebastian Segin*** [1,2], ***Rebekka Medert*** [1,2], ***Diana Lindner*** [3,4], ***Marc Freichel*** [1,2] ***and Juan E. Camacho Londoño*** [1,2*]

*[1] Pharmakologisches Institut, Ruprecht-Karls-Universität Heidelberg, Heidelberg, Germany, [2] Partner Site Heidelberg/Mannheim, DZHK (German Centre for Cardiovascular Research), Heidelberg, Germany, [3] Allgemeine und Interventionelle Kardiologie, Universitäres Herzzentrum Hamburg, Hamburg, Germany, [4] Partner Site Hamburg/Kiel/Lübeck, DZHK (German Centre for Cardiovascular Research), Hamburg, Germany*

**Aim:** Cardiac pressure-volume (PV loop) analysis under β-adrenergic stimulation is a powerful method to simultaneously determine intrinsic cardiac function and β-adrenergic reserve in mouse models. Despite its wide use, several key approaches of this method, which can affect murine cardiac function tremendously, have not been experimentally investigated until now. In this study, we investigate the impact of three lines of action during the complex procedure of PV loop analysis: (i) the ventilation with positive end-expiratory pressure, (ii) the time point of injecting hypertonic saline to estimate parallel-conductance, and (iii) the implications of end-systolic pressure-spikes that may arise under β-adrenergic stimulation.

**Methods and Results:** We performed pressure-volume analysis during β-adrenergic stimulation in an open-chest protocol under Isoflurane/Buprenorphine anesthesia. Our analysis showed that (i) ventilation with 2 $cmH_2O$ positive end-expiratory pressure prevented exacerbation of peak inspiratory pressures subsequently protecting mice from macroscopic pulmonary bleedings. (ii) Estimations of parallel-conductance by injecting hypertonic saline prior to pressure-volume recordings induced dilated chamber dimensions as depicted by elevation of end-systolic volume (+113%), end-diastolic volume (+40%), and end-diastolic pressure (+46%). Further, using this experimental approach, the preload-independent contractility (PRSW) was significantly impaired under basal conditions (−17%) and under catecholaminergic stimulation (−14% at 8.25 ng/min Isoprenaline), the β-adrenergic reserve was alleviated, and the incidence of ectopic beats was increased >5-fold. (iii) End-systolic pressure-spikes were observed in 26% of pressure-volume recordings under stimulation with 2.475 and 8.25 ng/min Isoprenaline, which affected the analysis of maximum pressure (+11.5%), end-diastolic volume (−8%), stroke volume (−10%), and cardiac output (−11%).

OPEN ACCESS

**Edited by:**
*Gabriela Kania,*
*University Hospital Zürich, Switzerland*

**Reviewed by:**
*Hirotsugu Tsuchimochi,*
*National Cerebral and Cardiovascular Center, Japan*
*Praphulla C. Shukla,*
*Indian Institute of Technology Kharagpur, India*

***Correspondence:**
*Lucas Bacmeister*
*lucas.bacmeister@pharma.uni-heidelberg.de*
*Juan E. Camacho Londoño*
*juan.londono@pharma.uni-heidelberg.de*

**†Present Address:**
*Lucas Bacmeister,*
*Allgemeine und Interventionelle Kardiologie, Universitäres Herzzentrum Hamburg, Hamburg, Germany*

**Specialty section:**
*This article was submitted to Cardiovascular Biologics and Regenerative Medicine, a section of the journal Frontiers in Cardiovascular Medicine*

**Received:** *06 January 2019*
**Accepted:** *18 March 2019*
**Published:** *10 April 2019*

**Citation:**
*Bacmeister L, Segin S, Medert R, Lindner D, Freichel M and Camacho Londoño JE (2019) Assessment of PEEP-Ventilation and the Time Point of Parallel-Conductance Determination for Pressure-Volume Analysis Under β-Adrenergic Stimulation in Mice. Front. Cardiovasc. Med. 6:36. doi: 10.3389/fcvm.2019.00036*

**Conclusions:** Our results (i) demonstrate the advantages of positive end-expiratory pressure ventilation in open-chest instrumented mice, (ii) underline the perils of injecting hypertonic saline prior to pressure-volume recordings to calibrate for parallel-conductance and (iii) emphasize the necessity to be aware of the consequences of end-systolic pressure-spikes during β-adrenergic stimulation.

**Keywords: pressure-volume analysis, parallel-conductance, β-adrenergic stimulation, hypertonic saline, positive end-expiratory pressure, end-systolic pressure-spikes, catheter entrapment, hemodynamics**

# INTRODUCTION

Cardiac pressure-volume (PV) analysis during incremental β-adrenergic stimulation in mice is capable of precisely determining ventricular function and adrenergic reserve in mice. This species offers advantages like the feasibility of genetic modifications and short generation times. Established since 1998 (1), PV analysis in mice revealed numerous novel regulators of cardiac function and is still regarded as the gold standard characterizing ventricular function (2, 3).

PV analysis is performed by advancing a pressure-conductance catheter into the left ventricle. A piezo-electrical pressure transducer continuously detects intra-ventricular pressure. Ventricular volume is measured by generating an electrical field using the catheter's two outer electrodes. Conductance-alterations within the blood-filled chamber are detected by two inner electrodes. Assuming a cylindrically shaped left ventricle, conductance can be converted into volume (4). However, the measured overall conductance (G) reflects of the blood-conductance within the ventricle ($G_b$) and the conductance of surrounding tissue (parallel-conductance, $G_p$). To obtain $G_b$, $G_p$ needs to be subtracted from G. $G_p$ may be estimated by injecting hypertonic saline into the left ventricle and by subsequent analysis of PV recordings during the wash-in phase as first described in canine (4, 5) and later validated for mice (6–8).

Several PV protocols assessing murine cardiac function have been published (1, 2, 9, 10). Moreover, the influence of several steps during the procedure, such as approaches using open-chest or closed-chest surgery (9, 11), the choice of anesthetics (11) as well as the genetic background (12) have already been examined regarding their impact on cardiac function. However, other factors potentially affecting basal cardiac function and adrenergic reserve have not been investigated until now. In this study, we performed PV analysis during incremental Isoprenaline stimulation following open-chest access to the heart and evaluated three key methodological aspects during the procedure of PV loop analysis in mice. We (i) ventilated mice with or without positive-end-expiratory pressure (PEEP), (ii) we estimated $G_p$ by injecting hypertonic saline either prior to or after PV recordings, and (iii) we analyzed which PV parameters are affected upon appearance of end-systolic pressure-spikes (ESPS), a common phenomenon observed in PV analysis under adrenergic stimulation (1, 8, 13–15).

Our findings (i) demonstrate the advantages of PEEP ventilation under β-adrenergic stimulation in open-chest instrumented mice, (ii) reveal multiple adverse effects of estimating $G_p$ by injecting hypertonic saline prior to PV recordings, and (iii) show ESPS occurring under β-adrenergic stimulation do affect both pressure- and volume-related parameters in the analysis of cardiac function.

# MATERIALS AND METHODS

## Animals

All experimental procedures fulfilled the EU-legislation guidelines for protection of animals used for scientific purposes and were approved by the Karlsruhe regional council (G131/15 and G121/17). Recordings from 48 male C57Bl/6N mice aged 19.4 ± 1.4 weeks were analyzed. Animals were obtained from Charles River Laboratories and housed in a 12 h light cycle under specified pathogen-free conditions (SPF) at the animal facility (IBF) of the Heidelberg Medical Faculty. Rodent food (LasVendi Rod18) and drinking water were supplied *ad libitum*.

## Anesthesia

Anesthesia was induced in a plexiglas-chamber pre-saturated with 2.5% Isoflurane, vaporized with 80 ml/min $O_2$ (Vapor 19.3, Abbot). Subsequently an anesthetic-mixture (7 ml/kg) containing 0.1 mg/kg Buprenorphine as analgesic (Bayer AG), 1,200 IU/kg Heparin (Ratiopharm GmbH) and 10 mg/kg Etomidate-Lipuro (B. Braun Melsungen AG) was injected intraperitoneally (i.p.). Anesthetized animals were endotracheally intubated using the shortened (3 cm) plastic cannula of an intravenous 20 Gauge catheter. After fixation on a heating plate (Hotplate 062, Labotect) a rectal probe (Hugo Sachs Elektronik) was inserted. Body temperature was maintained at 37 ± 0.5°C by manually adjusting heating plate temperature to 38.5 ± 1.5°C. A small rodent respirator (MiniVent 845, Harvard Apparatus) was, connected to the endotracheal tube. On-line airway pressures were monitored in LabChart 7.3 Pro (AD Instruments) by connecting a MPX-Transducer (Hugo Sachs Elektronik) to the respiratory tube. Ventilation was performed by setting respiratory rates to $53.5 \times M^{0.26}$ [$\text{min}^{-1}$] (M = BW in g) (9) and adjusting tidal volumes to peak inspiratory pressures of 11 ± 1 $cmH_2O$. After set once at the beginning, tidal volume was not altered during experiments. Adequate anesthesia depth was proved with a tail pinch and the absence of reflexes at the hind paws. Hereafter, 1 mg/kg Pancuronium (Sigma Life Science) was injected i.p. to prevent respiratory artifacts during recordings. The range of Heart Rate as an indicator for anesthesia depth (16) was monitored on-line in LabChart 7.3 Pro with a subcutaneous 1-lead ECG (Bio Amp, AD Instruments).

## Surgery

During surgery, anesthesia was maintained by ventilating with 2% Isoflurane vaporized with 80 ml/min $O_2$. All surgical procedures were performed under magnification (1.5- to 4-fold) via a surgical microscope (Stemi 2000-C, Carl Zeiss). Access to the central venous system was established by cannulation of the left femoral vein (LFV, **Figure S1A**).

In all experimental groups, fluid-loss was counteracted by infusing 15 μl/min 0.9% sodium-chloride (NaCl) with a syringe pump (11Plus, Harvard Apparatus). Hereafter, a thoracotomy, as adapted and modified from others (2, 9), was performed (**Figure S1B**). Two $cmH_2O$ positive end-expiratory pressure (PEEP) was established in 38 of 48 mice just before diaphragm incision by placing the expiratory ventilation hose 2 cm beneath the water-surface. To validate the established PEEP, on-line airway-pressures were monitored in LabChart 7.3 Pro. After diaphragm incision, a limited costotomy was performed (**Figure S1B**). The pericardium was bluntly dissected and a suture (8.0, Suprama) was positioned beneath the inferior caval vein (ICV). Finally, the left ventricular apex was pricked with a 25 gauge needle, and a 1.4-F pressure-conductance catheter (SPR-839, Millar) was inserted (**Figure S1C**). Intra-ventricular catheter position was optimized under on-line visualization until rectangular-shaped loops were obtained.

## Pressure-Volume Measurements

Isoflurane was reduced to 1.5% and animals were allowed to reach steady state conditions as indicated by constant heart rate and stroke volume, which was observed within 3–5 min. If the stabilization period extended 10 min, animals were not included into the analysis. The first two cycles of recording were performed while infusing 15 μl/min 0.9% NaCl. PV loops were recorded during two cycles of inferior caval vein (ICV) occlusion for each Isoprenaline (ISO) dose, after a new steady state was reached. To maintain constant infusion rates of 15 μl/min, increasing doses of 0.2475, 0.825, 2.475 and 8.25 ng/min Isoprenaline (ISO, Sigma Life Science) dissolved in 0.9% NaCl were infused by switching syringes. As the respiratory status has a significant impact on murine cardiac function during PV recordings (**Figure S2**), ventilation was suspended strictly at the end-expiration time point. Preload dependent parameters were recorded during the first 2 s of a measurement (**Figure S3**). To obtain preload-independent parameters, the suture around the ICV was gently lifted for the following 2 s of each measurement (**Figure S3**).

## Calibration

To estimate $G_p$, 10 μl hypertonic saline (15% NaCl) were rapidly injected into the left femoral vein (4, 5, 8). In 33 animals, this was performed after measurements (late saline group), whereas 15 mice received hypertonic saline prior to measurements (early saline group). Each experiment was completed by sampling left ventricular blood 5 min after saline-injection in the late saline group, or directly after the last measurement in the early saline group. Subsequently, mice were euthanized by massive bleeding after removal of the heart under anesthesia and Buprenorphin analgesia. Hereafter, blood conductance was measured in pre-warmed (37°C) cylinders of known volume (Millar).

## Pressure-Volume Analysis

All analytical steps were performed in LabChart 7.3 Pro. A factor for conductance-to-volume conversion (conversion-factor, CF) was enabled for each dataset by calibrating the known volumes of the calibration cuvette against blood-conductance. Subsequently, PV recordings during hypertonic saline's left ventricular wash-in phase were analyzed. $G_p$ was then subtracted from G.

For baseline analysis, 5–10 consecutive loops during end-expirational ventilation pause were selected (**Figure S3**). Preload-independent parameters were analyzed by selecting loops during ICV-occlusion (**Figure S3**). To ensure standardized calculation of preload independent parameters, solely the first five consecutive loops showing decreasing $V_{ed}$ were analyzed (**Figure S3**).

Parameters used to characterize general cardiac function were heart rate (HR), stroke work (SW), stroke volume (SV), cardiac output (CO), maximum pressure ($P_{max}$), end-diastolic pressure ($P_{ed}$), end-diastolic volume ($V_{ed}$) and end-systolic volume ($V_{es}$). Preload independent cardiac contractility was analyzed by Preload Recruitable Stroke Work (PRSW) (17). Preload dependent cardiac contractility was analyzed by maximum dP/dt ($dP/dt_{max}$). Isovolumetric relaxation was analyzed by Tau (Weiss Equation) (18) and minimum dP/dt ($dP/dt_{min}$). Diastolic filling was analyzed by End-diastolic Pressure-Volume Relationship (EDPVR, alpha-coefficient).

## Analysis of Airway Pressures

Peak inspirational airway pressures (Peak $P_{insp}$), were first determined when the conductance-catheter was inserted into the ventricle ($t_0$) and followed up 5, 10, and 15 min after catheter insertion ($t_5$, $t_{10}$, and $t_{15}$). Five consecutive Peak $P_{insp}$ were averaged for each time point.

## Analysis of Ectopic Beats

Ectopic beats were analyzed by dividing each experiment into sections of 1 min intervals, starting after steady state conditions were reached until the last ICV occlusion. If ectopic beats occurred during a section, this section was considered as "section with ectopic beat." Ectopic beats occurring timely associated with ICV occlusions were excluded from analysis, as these could have been ectopically driven by a contact between occlusion-suture and cardiac structures. **Figure S4** depicts how ectopic beats were detected in the PV analysis and in the simultaneous ECG.

## Statistical Analysis

Statistical analysis and figures were done in OriginPro 2016 and Excel. Two-sided, unpaired Student's *t*-tests were performed, and heteroskedastic variances were assumed (Microsoft Excel 2011). For analysis of increases of Peak $P_{insp}$ within groups two-sided, paired Student's *t*-tests assuming heteroskedastic variances were performed (Microsoft Excel 2011). *P*-values $< 0.05$ were considered statistically significant. All data is presented as mean ± standard deviation.

# RESULTS

## The Effect of Positive End-Expiratory Pressure (PEEP) Ventilation

To analyse the effect of positive end-expiratory airway pressure (PEEP) on open-chest PV loop recordings under β-adrenergic stimulation, we measured two groups of adult C57Bl6/N mice. The experimental protocol in both groups did not differ except for the ventilation, which was performed either with or without PEEP (2 $cmH_2O$, **Figure 1A**). The course of events after intubation including ventilation, venous catheterisation, incremental β-adrenergic stimulation and hypertonic saline injection is indicated in **Figure 1A**.

As PEEP-ventilation may alter airway pressures during open-chest PV loop analysis, we examined peak inspirational pressures (Peak $P_{insp}$) immediately after catheter insertion and 5, 10, and 15 min thereafter. Representative traces indicate the increase in end-expiratory airway pressures in PEEP-ventilated animals (**Figure 1B**). Interestingly, a time-dependent increase of Peak $P_{insp}$ was observed in animals that were not ventilated with PEEP (**Figures 1C,D**). Following 15 min of PV loop recording, Peak $P_{insp}$ increased by 36.2 ± 15.2% in the non-PEEP ventilated group as compared to 10.5 ± 3.6% in the PEEP-ventilated group ($p = 0.0004$, **Figure 1D**). Notably, macroscopic pulmonary bleedings were exclusively observed in 5 out of 10 (50%) non-PEEP-ventilated animals but in none of the PEEP-ventilated animals (**Figure 1E**), suggesting that pulmonary lesions develop along with exacerbated Peak $P_{insp}$. In contrast, body temperature, calibration factors and hypertrophy indices did not differ between the two groups (**Table S1**).

Since a stop in end-inspirational ventilation may affect cardiac function due to increased lung volume and airway pressure in PV analysis (**Figure S2**), we examined the effect of 2 $cmH_2O$ positive airway pressure in PEEP ventilated animals on PV loop parameters in comparison to the non-PEEP ventilated group. PEEP ventilation did not affect basal systolic, diastolic cardiac performance, or β-adrenergic reserve (**Table 1**).

## The Influence of the Time Point of Calibration Using Hypertonic Saline Injection

Estimation of parallel-conductance by injecting hypertonic saline may be performed prior to or after PV recordings. We hypothesized that injection of hypertonic saline prior to PV-loop recordings may adversely affect murine cardiac function. Hence, we compared these two time points of hypertonic saline injections concerning their effects on PV analysis under β-adrenergic stimulation.

Fifteen animals received 10 μl of 15% NaCl prior to (early saline group) and 23 animals after the PV recordings (late saline group) (**Figure 2A**). Except for the time point of saline application, protocols did not differ between groups (**Figure 2A**). Since PEEP ventilation proved beneficial, both groups were ventilated with 2 $cmH_2O$ PEEP (**Figure 2A**).

As we often observed ectopic beats during on-line visualization of PV recordings in the early saline group, ectopic beat frequency was quantified. The observation period for ectopic beats was defined over the time period depicted in **Figure 2A** and subsequently divided into sections of 1 min. If an ectopic beat occurred within a section, this section was defined as section with ectopic beat. The numbers of sections analyzed for ectopic beats was similar between the groups (15.5 ± 1.9 vs. 15.4 ± 1.5, $p = 0.0744$). Strikingly, early saline calibration induced a >5-fold increase in the occurrence of sections with ectopic beats as compared to late saline calibration (21.8 ± 20.0 vs. 4.2 ± 4.6%, $p = 0.0043$, **Figure 2B**) suggesting that the application of hypertonic saline operates as a pro-arrhythmic stimulus.

Concerning the actual calibration parameters, parallel-conductance was increased when early as compared to late saline injection was applied (19.6 ± 2.2 vs. 17.0 ± 2.0 RVU; $p = 0.0008$, **Figure 2C**). We checked for heart weight as a potential interfering variable, which was similar between groups (**Table S2**). Notably, the blood-conductance conversion factor at the end of the experiments did not differ between groups (late saline: 1.75 ± 0.30 μl/RVU, early saline: 1.77 ± 0.16 μl/RVU, $p = 0.6813$, **Figure 2D**), suggesting late saline does not alter blood-conductance if blood sampling is performed 5 min after saline injection.

Analysis of basal left-ventricular function revealed multiple alterations between the two calibration regimens. Five minutes after early saline injection, PV loops showed a prominent right shift (**Figure 3A**) toward dilated chamber dimensions, similarly as in acute heart failure-like phenotypes with a 46% increase in end-diastolic pressure ($P_{ed}$, $p = 0.0007$, **Figure 3B**), a 40% increase in end-diastolic volume ($V_{ed}$, $p < 0.0001$, **Figure 3C**) and a 113% increase in end-systolic volume ($V_{es}$, $p = 0.0001$, **Figure 3D**). The rise in volume load was accompanied by prolonged diastolic relaxation (Tau +17%, $p = 0.0080$, **Figure 3E**) and deteriorated cardiac contractility, as depicted by a 17% decrease in Preload Recruitable Stroke Work (PRSW, $p = 0.0081$, **Figure 3F**). Differences in cardiac chamber dimensions and diastolic relaxation diminished upon incremental β-adrenergic stimulation (**Figures 3B–E**). However, PRSW remained significantly impaired even at maximal β-adrenergic stimulation (**Figure 3F**), suggesting permanent effects of the hypertonic salt bolus independent of volume loading.

Although unaffected at basal conditions, the analysis of heart rate (**Figure 3G**) and maximum dP/dt (**Figure 3H**) revealed an alleviated adrenergic response as ISO-evoked increases in these parameters were also extenuated over the entire dose range. These results further emphasize that the adverse effects of early saline application on cardiac function are not transient.

To observe other potentially interfering parameters and conditions, we controlled for e.g., body temperature during PV recordings, as well as for hypertrophy indices, which did not differ between groups (**Table S2**). Detailed values for each analyzed parameter are given in **Table S3**.

## The Impact of End-Systolic Pressure-Spikes

End-systolic pressure-spikes (ESPS) describe artificial pressure increases at the very end of the systolic ejection phase. In the protocol with 2 $cmH_2O$ PEEP-ventilation and late saline calibration, ESPS were observed in 6 out of 23 recordings but only

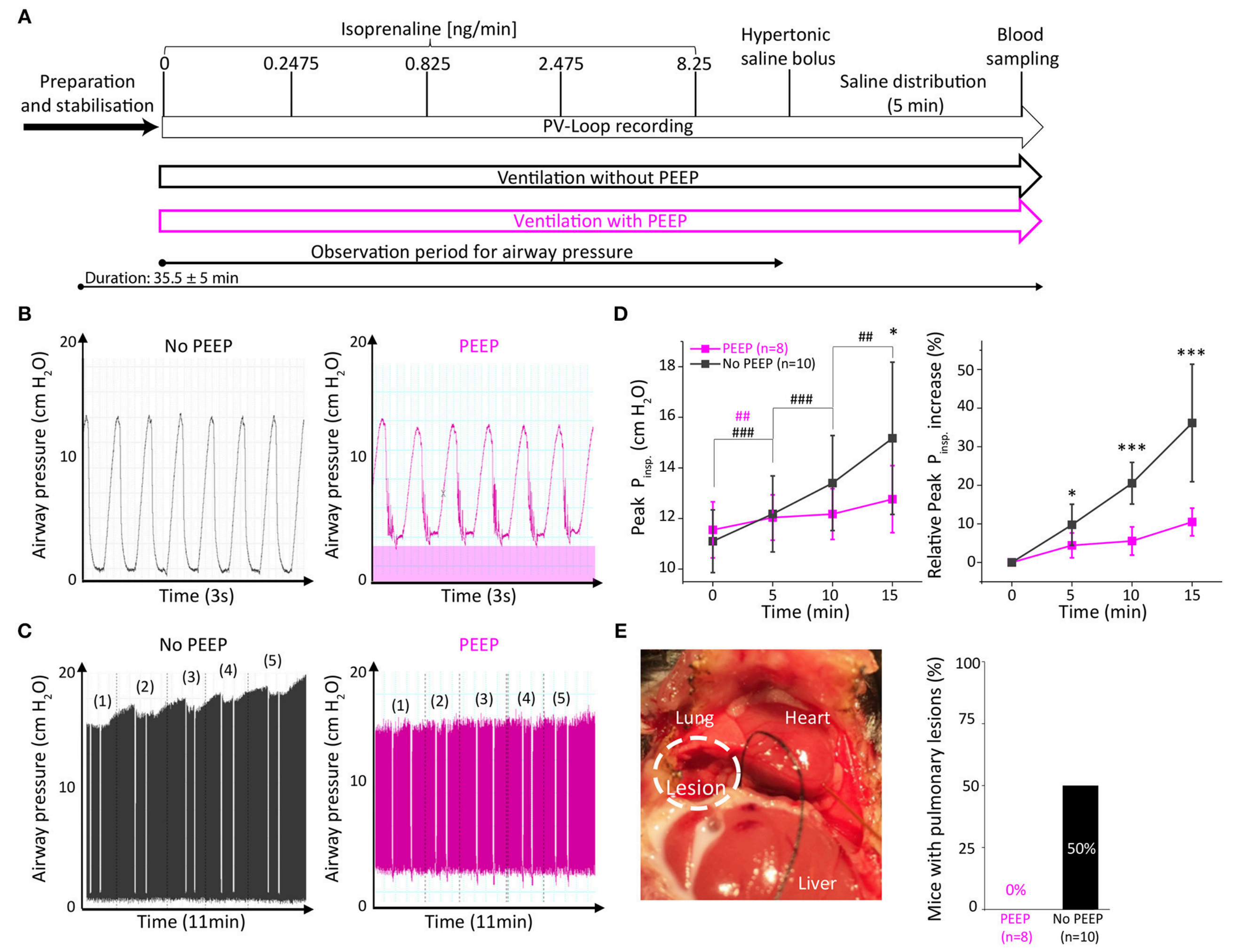

**FIGURE 1 |** Ventilation with positive end-expiratory pressure (PEEP) protected mice from exacerbated airway pressure and prevented pulmonary lesions. **(A)** Experimental design with two groups either ventilated without PEEP (black) or with PEEP of 2 $cmH_2O$ (purple). Comparison of representative traces of short-term **(B)** and long-term **(C)** PEEP-ventilation. In **(C)** white incisions depict end-expirational ventilation-stops during PV loop recordings. **(D)** Analysis of peak inspiratory pressure (Peak $P_{insp}$) during 15 min after catheter insertion (time 0). **(E)** Representative picture of a pulmonary lesion which occurred in 5 out of 10 non-PEEP-ventilated animals and quantitative assessment of pulmonary lesions. Data presented as mean ± standard deviation from $n = 10$ (No PEEP group) and $n = 8$ (PEEP group) mice. *n*, number of mice. $^*p < 0.05$, $^{***}p < 0.001$: *p*-value No PEEP vs. PEEP in an unpaired Student's *t*-test; $\#p < 0.05$, $\#\#p < 0.01$, $\#\#\#p < 0.001$: *p*-value vs. previous corresponding observation point in a paired Student's *t*-test within the groups (purple #: PEEP group, black #: No PEEP group).

at stimulation with doses at or above 2.475 ng/min Isoprenaline (**Figure 4A**). Hence, we divided PV loop recordings obtained with this protocol into two groups, which either presented ESPS upon β-adrenergic stimulation ($n = 6$) or not ($n = 17$) and examined the effect of ESPS on PV parameters.

Notably, PV recordings in mice that developed ESPS at higher ISO doses (≥2.475 ng/min) were otherwise morphologically not distinguishable at basal levels or at the lowest ISO dose (0.825 ng/min) from those that did not develop ESPS (**Figures 4B,C**). Furthermore, both groups showed comparable cardiac function at basal levels (**Figure 5**; **Table S4**), indicating similar catheter position prior to catecholamine stimulation.

ESPS artificially increase pressure near end-systole. Hence, PV loop analysis of recordings depicting ESPS comprises an artificially increased maximum pressure ($P_{max}$, **Figure 5A**). However, this "artificial $P_{max}$" could be corrected to "true $P_{max}$" by adjusting $P_{max}$ to the maximum value during auxotonic contractions, as depicted in **Figure 5A**. Following this maneuver, alterations in $P_{max}$ could be extinguished (**Figure 5A**).

Other pressure-derived contractility parameters that are potentially affected by increased pressure values close to the end-systole include diastolic relaxation parameters. Hence, we checked for alterations in diastolic function. Interestingly, ESPS had opposite effects on the two parameters characterizing diastolic relaxation: analysis of Tau in PV recordings depicting ESPS at 8.25 ng/min ISO indicated a deceleration of active diastolic relaxation by 11% ($p = 0.0445$, **Figure 5D**), whereas minimum dP/dt values revealed an acceleration by 18.4%

**TABLE 1 |** Pressure-volume analysis under β-adrenergic stimulation from mice with or without positive end-expiratory pressure ventilation.

| | **Systolic parameters** | | | **Diastolic parameters** | | |
|---|---|---|---|---|---|---|
| **Isoprenaline (ng/min)** | **No PEEP (*n* = 10)** | **PEEP (*n* = 8)** | ***p*-Value** | **No PEEP (*n* = 10)** | **PEEP (*n* = 8)** | ***p*-Value** |
| | **Heart rate (bpm ± SD)** | | | **End-diastolic volume (μl ± SD)** | | |
| 0 | 498 ± 35 | 494 ± 33 | 0.7918 | 24.4 ± 5.8 | 24.9 ± 3.6 | 0.8034 |
| 0.2475 | 518 ± 34 | 514 ± 33 | 0.8115 | 23.6 ± 6,1 | 23.7 ± 3.6 | 0.9511 |
| 0.825 | 554 ± 26 | 546 ± 22 | 0.4704 | 21.4 ± 4.4 | 22.3 ± 3.2 | 0.6220 |
| 2.475 | 597 ± 22 | 612 ± 25 | 0.2008 | 21.4 ± 3.2 | 21 ± 3.2 | 0.7856 |
| 8.25 | 620 ± 20 | 620 ± 20 | 0.9985 | 22.7 ± 3.4 | 23.2 ± 2.6 | 0.7028 |
| | **Stroke volume (μl ± SD)** | | | **End-systolic volume (μl ± SD)** | | |
| 0 | 17.9 ± 2.9 | 18.9 ± 2.8 | 0.4707 | 7.78 ± 6.97 | 7.39 ± 4.03 | 0.8839 |
| 0.2475 | 18.7 ± 2.5 | 19.6 ± 2.5 | 0.4453 | 6.22 ± 7.56 | 5.33 ± 3.63 | 0.7459 |
| 0.825 | 19.9 ± 2.9 | 20.4 ± 2.5 | 0.6895 | 2.86 ± 3.7 | 2.94 ± 2.27 | 0.9515 |
| 2.475 | 21.9 ± 2.5 | 22.3 ± 1.9 | 0.6946 | 1.12 ± 1.18 | 0.43 ± 0.33 | 0.1023 |
| 8.25 | 23.5 ± 2.3 | 24.3 ± 1.8 | 0.4394 | 1.15 ± 1.04 | 0.4 ± 0.31 | 0.0532 |
| | **Cardiac output (μl/min ± SD)** | | | **End-diastolic pressure (mmHg ± SD)** | | |
| 0 | 8,872 ± 1,388 | 9,329 ± 1,600 | 0.5343 | 5.07 ± 1.46 | 5.52 ± 1.26 | 0.4920 |
| 0.2475 | 9,717 ± 1,558 | 10,115 ± 1,574 | 0.5993 | 4.94 ± 1.61 | 5.26 ± 1,12 | 0.6199 |
| 0.825 | 11,016 ± 1,755 | 11,141 ± 1,624 | 0.8780 | 4.95 ± 1.67 | 5.5 ± 0.93 | 0.3933 |
| 2.475 | 13,089 ± 1,648 | 13,646 ± 821 | 0.3668 | 4.44 ± 1.28 | 5.4 ± 0.84 | 0.0738 |
| 8.25 | 14,559 ± 1,311 | 15,046 ± 1,151 | 0.4136 | 4.65 ± 1.16 | 5.47 ± 0.78 | 0.0924 |
| | **Maximum pressure (mmHg ± SD)** | | | **EDPVR (α ± SD)** | | |
| 0 | 82.1 ± 6 | 85.5 ± 5.7 | 0.2389 | 1.68 ± 1.38 | 1.64 ± 1.04 | 0.9419 |
| 0.2475 | 84.5 ± 6.8 | 88.3 ± 8.1 | 0.3093 | 1.66 ± 1.7 | 1.54 ± 0.9 | 0.8461 |
| 0.825 | 87.7 ± 5.9 | 87.5 ± 8.1 | 0.9545 | 1.69 ± 1.47 | 1.88 ± 0.71 | 0.7258 |
| 2.475 | 89.2 ± 6.3 | 90.3 ± 7.5 | 0.7589 | 1.52 ± 0.91 | 2.41 ± 0.58 | **0.0249** |
| 8.25 | 90.2 ± 6 | 91.2 ± 5.8 | 0.7289 | 1.93 ± 1.03 | 1.96 ± 0.73 | 0.9368 |
| | **PRSW (mmHg ± SD)** | | | **Minimum dP/dt (mmHg/s ± SD)** | | |
| 0 | 80.6 ± 17.2 | 77.2 ± 7.3 | 0.5784 | −7,764 ± 955 | −8,515 ± 1,128 | 0.1562 |
| 0.2475 | 90.4 ± 20.9 | 86.6 ± 15.1 | 0.6621 | −8,309 ± 889 | −9,130 ± 1,280 | 0.1490 |
| 0.825 | 103.8 ± 25.4 | 94.3 ± 13.6 | 0.3291 | −8,415 ± 450 | −8,782 ± 1,086 | 0.3943 |
| 2.475 | 117.3 ± 21.2 | 112.9 ± 21.1 | 0.6708 | −8,383 ± 604 | −8,549 ± 1,344 | 0.7528 |
| 8.25 | 119.5 ± 17.3 | 118.6 ± 17 | 0.9186 | −8,264 ± 1,435 | −8,304 ± 815 | 0.9405 |
| | **Maximum dP/dt (mmHg/s ± SD)** | | | **Tau (weiss-equation ± SD)** | | |
| 0 | 7,514 ± 1,445 | 8,052 ± 1,528 | 0.4167 | 6.01 ± 0.73 | 6.29 ± 0.61 | 0.3889 |
| 0.2475 | 8,439 ± 1,686 | 9,120 ± 2,117 | 0.3944 | 5.74 ± 0.74 | 5.83 ± 0.42 | 0.7440 |
| 0.825 | 10,040 ± 1,609 | 9,787 ± 2,598 | 0.8858 | 5.44 ± 0.59 | 5.5 ± 0.4 | 0.7825 |
| 2.475 | 12,140 ± 1,597 | 13,027 ± 1,387 | 0.4199 | 5.3 ± 0.45 | 5.33 ± 0.54 | 0.8849 |
| 8.25 | 13,351 ± 1,130 | 14,074 ± 1,113 | 0.2565 | 5.43 ± 0.22 | 5.38 ± 0.69 | 0.8468 |

*PRSW, preload recruitable stroke work; EDPVR, end-diastolic pressure-volume relationship; n, number of mice; SD, standard deviation; p-values from unpaired Student's t-test between No PEEP and PEEP: Bold digits indicate significant p-values (<0.05).*

($dP/dt_{min}$, $p = 0.0453$, **Table S5**). ESPS were associated with slower relaxation in $dP/dt_{min}$ at 0.2475 and 0.825 ng/min ISO (**Table S5**).

In addition, ESPS also impaired volume-related parameters (**Figure 5B**), as depicted by an about 8.5% decrease in end-diastolic volume ($p = 0.0611$ and $p = 0.0407$ at 2.475 and 8.25 ng/min ISO, respectively). Stroke volume was reduced by 9–10% ($p = 0.0011$ and $p = 0.0112$ at 2.475 and 8.25 ng/min ISO, respectively) as well as cardiac output ($p = 0.0066$ and $p = 0.0177$ at 2.475 and 8.25 ng/min ISO, respectively). With regards to systolic cardiac function, we could not observe differences in parameters of cardiac contractility (**Figure 5C**), neither in preload-independent PRSW, nor in preload dependent $dP/dt_{max}$.

We also checked for body-weight, hypertrophy indices and body temperature during measurements, which were comparable between groups (**Table S4**). This further suggests these variables do not determine the likelihood of ESPS-development. Exact values for each PV parameter are given in **Table S5**.

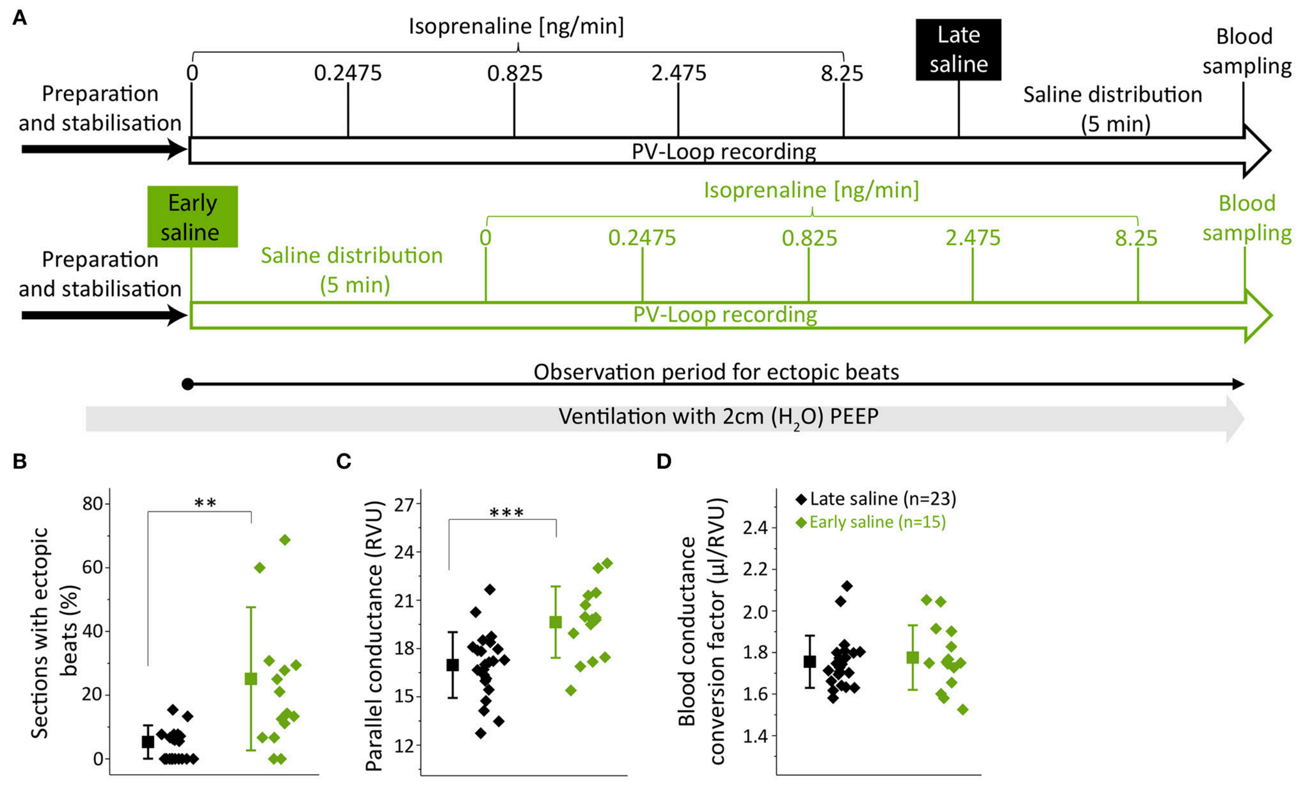

**FIGURE 2 |** Early hypertonic saline calibration increased ectopic beat frequency and parallel-conductance. **(A)** Experimental design indicating the application time points of the hypertonic saline bolus either after (late saline, black) or prior to (early saline, green) PV loop recordings; **(B)** Analysis of ectopic beats showing the percentual proportion of sections with ectopic beats; **(C)** Parallel-conductance (Gp) calculated in groups of early or late saline application; **(D)** Blood conductance conversion factor for volume conversion (µl/RVU) at the end of experiments. Saline-bolus: One-time injection of 10 µl saline (15%) into the left femoral vein. Data presented as mean ± standard deviation from $n = 23$ (late saline) and $n = 15$ (early saline) mice. PEEP, positive end-expiratory pressure, ISO, Isoprenaline, RVU, Relative volume units; *n*, number of mice. $^{**}p < 0.01$; $^{***}p < 0.001$: *p*-value of late saline vs. early saline in an unpaired Student's *t*-test.

## DISCUSSION

The salient findings of our study about key methodological factors in murine pressure-volume (PV) analysis under β-adrenergic stimulation were that (i) ventilation with 2 $cmH_2O$ positive end-expiratory pressure prevents pulmonary lesions and does not alter hemodynamic conditions, (ii) injections of hypertonic saline prior to pressure-volume recordings deteriorate cardiac function and facilitate the occurrence of ectopic beats, and (iii) end-systolic pressure-spikes (ESPS) impair not only pressure-derived, but also volumetric parameters and diastolic relaxation.

### Positive End-Expiratory Pressure

PEEP-ventilation most prominently protected mice from exacerbated increases of peak inspiratory pressure and macroscopic pulmonary lesions. Both could be observed most likely due to PEEP-ventilation reducing pulmonary atelectasis, subsequently improving pulmonary compliance and gas exchange as known in man and mice (19, 20). However, ventilation with 15 $cmH_2O$ PEEP in pigs can affect cardiac output due to preload reduction (21). This phenomenon is present during closed-chest conditions, but to a lesser degree also in open-chest instrumentation (21). However, ventilation with a moderate PEEP of 2 $cmH_2O$ during open-chest PV analysis did not affect murine left-ventricular function in our protocol. We therefore regard ventilation using 2 $cmH_2O$ PEEP as being safe in the context of murine open-chest PV analysis. Though ventilation with a PEEP of 5 $cmH_2O$ has already been used during open-chest PV analysis in mice, PEEP-ventilation has not been evaluated concerning its impacts on murine cardiac function in previous studies (10). However, it remains to be investigated whether and to which extent PEEP ventilation may affect murine cardiac performance in closed-chest PV analysis and/or in murine models of heart failure, e.g., myocardial infarction, pressure overload or myocarditis (22).

### Hypertonic Saline Calibration

Injecting hypertonic saline to calibrate for parallel-conductance 5 min prior to PV recordings deteriorated basal cardiac function as compared to its injection after PV recordings. Animals of the early saline group presented in an acute dilative heart failure-like phenotype depicting right shifted PV recordings and elevated end-diastolic pressure ($P_{ed}$). End-diastolic volume ($V_{ed}$) and end-systolic volume ($V_{es}$) alone could have been artificially

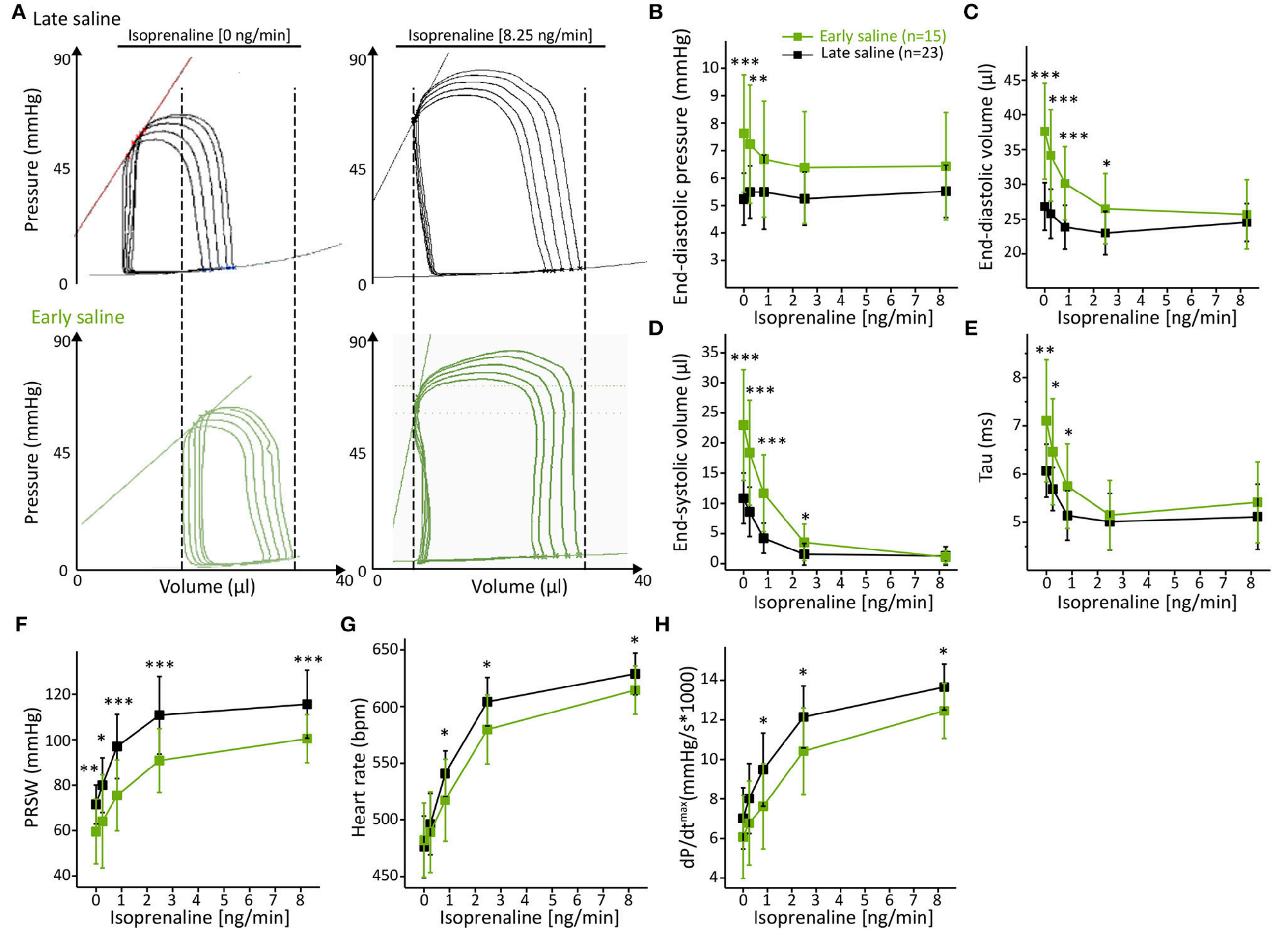

**FIGURE 3 |** Early hypertonic saline calibration increased cardiac preload, reduced cardiac contractility and ameliorated β-adrenergic reserve. **(A)** Representative PV loops during inferior caval vein occlusion of the late saline group as compared to the early saline group; **(B)** Cardiac preload as depicted by end-diastolic pressure **(B)**, end-diastolic volume **(C)**, and end-systolic volume **(D)**; **(E)** Analysis of the diastolic relaxation constant Tau; **(F)** Analysis of systolic contractility (PRSW); **(G)** maximum dP/dt and **(H)** heart rate. Data presented as mean ± standard deviation from $n = 23$ (late saline group) and $n = 15$ (early saline group) mice. Abbreviations: ISO, Isoprenaline, PRSW, Preload Recruitable Stroke Work; *n*, number of mice. $^*p < 0.05$; $^{**}p < 0.01$; $^{***}p < 0.001$: *p*-value of Late saline vs. Early saline in an unpaired Student's *t*-test.

enlarged by the 15% NaCl bolus increasing blood conductance. However, higher $P_{ed}$ points toward true volume overloading, as $P_{ed}$ is known to rise proportionally with cardiac preload (23). Potentially, early hyperosmolar saline application increased intra-vascular volume and concomitantly impaired also PRSW, a measure of preload-independent cardiac contractility, resulting in severe accumulation of blood proximal to the ventricle. These results are in line with findings in which impairment of maximum dP/dt was attributable to hypertonic saline injections in mice (6). As incremental β-adrenergic stimulation increased cardiac contractility in both groups, differences in cardiac volumes leveled off.

However, early hypertonic saline calibration also had non-recoverable effects on murine cardiac function, which were observed as permanent impairment of preload-independent contractility as well as in alleviated chronotropic and inotropic ISO-response. Possible explanations for the adverse effects on cardiac function include persisting effects following acute volume overload as well as severe electrolyte imbalance, such as hypernatremia and/or hyperchloremia. An increase in extracellular $Na^+$ levels may aggravate the electrochemical driving force for the $Na^+/Ca^{2x}$ Exchanger (NCX), thereby triggering trans-sarcolemmal $Ca^{2+}$-efflux, subsequently depleting sarcoplasmic reticulum stores, which can result in depressed contractility (24, 25). Other mechanisms could include the influence of high extracellular $Na^+$ on sodium-conducting channels that fine-tune cardiac contractility, such as TRPM4, which is known to be active under conditions of β-adrenergic stimulation (15, 26, 27). As animals had reached a new post-calibration steady state 5 min after early hypertonic saline calibration, we assume the observed effects of early hypertonic saline to be persistent. However, we cannot fully exclude that animals may further recover after a prolonged time of saline distribution prior to isoprenaline-challenge.

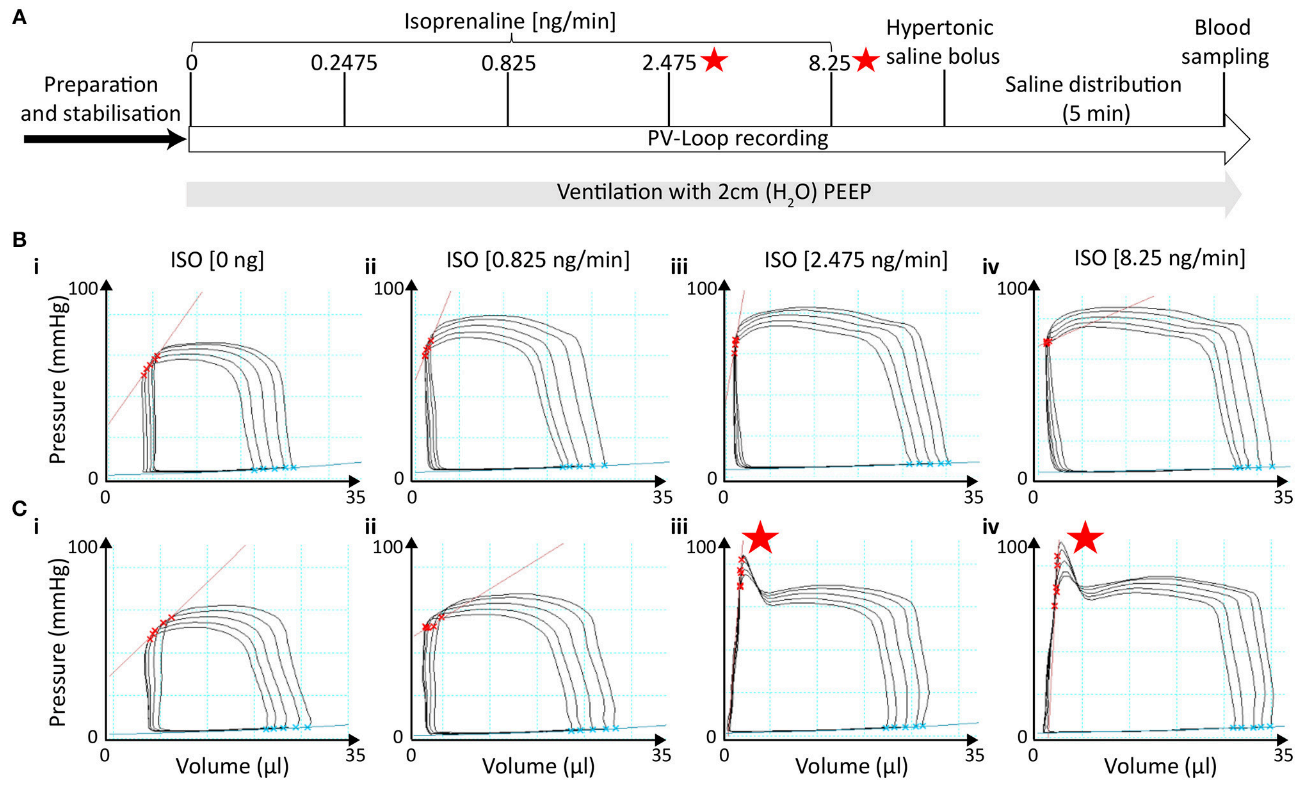

**FIGURE 4 |** End-systolic pressure-spikes under β-adrenergic stimulation occurred in measurements without initial signs of catheter entrapment. **(A)** Time of ESPS occurrence during the measurements labeled by red stars. (**B**$_{i-iv}$) Representative PV loops during ICV occlusion under incremental ISO stimulation in a measurement in which no ESPS were detected at any concentration. (**C**$_{i-iv}$) Representative PV loops during ICV occlusion in a measurement in which ESPS were detected during stimulation with 2.475 ng/min ISO or higher. ESPS, End-systolic pressure-spikes; ISO, Isoprenaline.

Moreover, dilated chamber dimensions that were observed in conditions applying early saline calibration increased ectopic beat frequency >5-fold most likely via elevation of intra-ventricular wall stretch, which is known to induce ectopic beats through stretch-activated channels (28–31). Furthermore, findings from contractility analysis in canine and human hearts, in which the relaxation constant Tau positively correlates with end-systolic volume ($V_{es}$) (32, 33), indicate that Tau was increased by enlarged intra-ventricular volumes. Minimum dP/dt ($dP/dt_{min}$) was not altered in our study, as it is known to correlate with end-systolic pressure (34, 35), which was indifferent between groups (data not shown).

Interestingly, $G_p$ was higher in the early saline group, though heart weight, which is known to positively correlate with $G_p$ (36), was unaltered between groups. However, alterations in contractility during the hypertonic saline's left ventricular wash-in phase can increase $G_p$ (36). These alterations in contractility were potentially less pronounced in the late saline group, as 8.25 ng/min ISO had already induced a higher contractile state at the time point of saline calibration.

## End-Systolic Pressure-Spikes

End-systolic pressure-spikes (ESPS) appeared following β-adrenergic stimulation using 2.475 ng/min ISO or higher. ESPS most likely resulted from a direct contact between the pressure transducer and papillary muscles and/or the left ventricular wall, as known from PV analysis and simultaneous echocardiography in rats (37). Strikingly, ESPS would potentially be rectifiable by catheter repositioning. However, in a longitudinal protocol, one cannot reposition the catheter if ESPS occur, since repositioning would significantly alter the parallel conductance within the catheter's electrical field. Thus, additional hypertonic saline calibrations would be required in recordings with ESPS, but not in those without ESPS, which would markedly affect the measurements. As one cannot reposition the catheter in this setting, we analyzed the impact of ESPS on PV parameters in order to optimize data analysis and reproducibility in this context.

In addition to the anticipated effects on pressure-derived parameters, which in case of maximum pressure were easily rectifiable, the occurrence of ESPS also impaired volume detection. As known from rats, the occurrence of ESPS correlates with a rather lateral catheter position (37), which increases the proportion of less conductive myocardium in the catheters electrical field. This may explain the reduced volume detection.

Unlike others in rats (37), we could not observe effects of ESPS on maximum dP/dt in PV analysis in mice. This

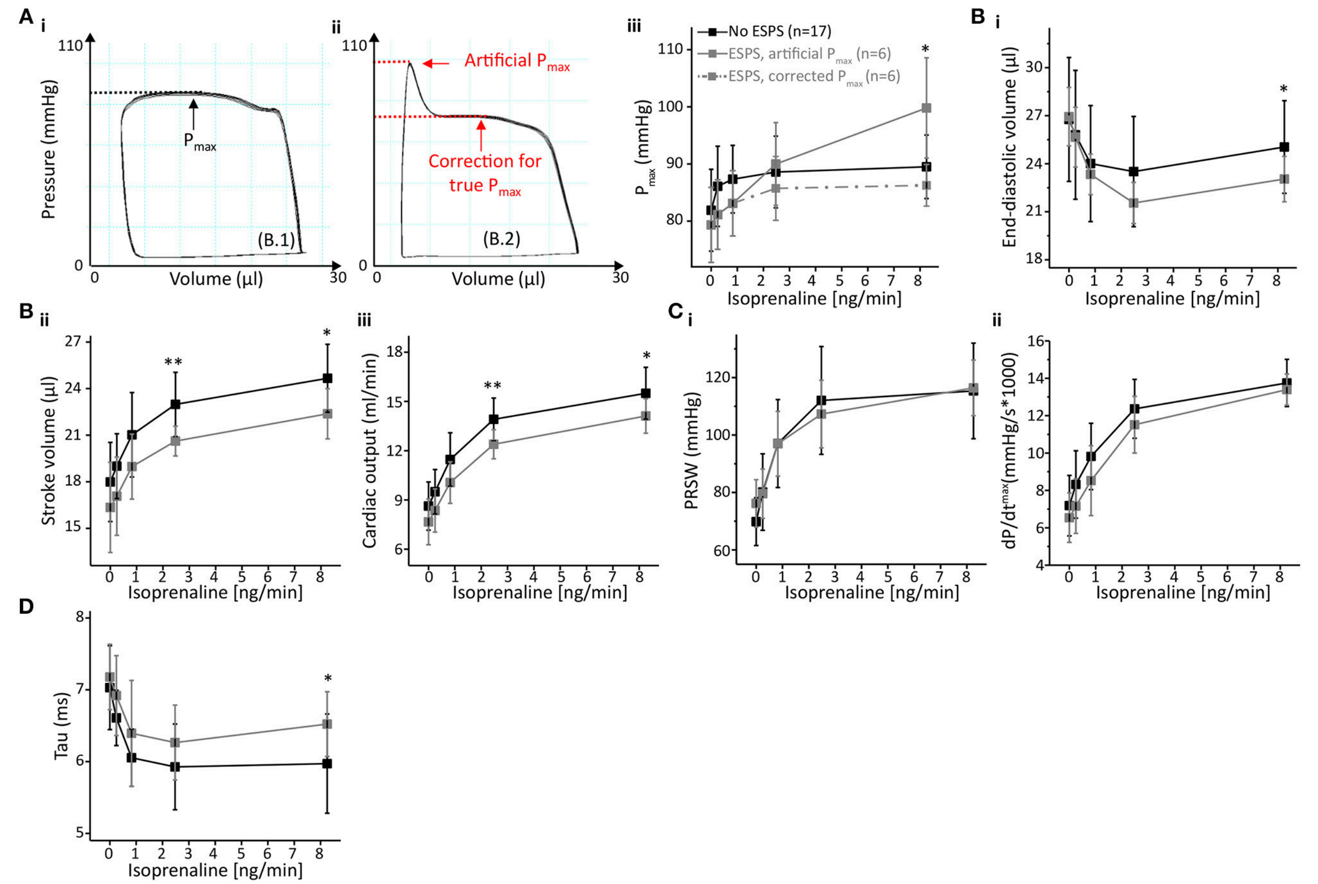

**FIGURE 5 |** End-systolic pressure-spikes impaired volume detection and diastolic relaxation but did not affect cardiac contractility. **(A)** Impact of ESPS on pressure detection with representative PV loops either without (**A**$_{i}$) or with ESPS (**A**$_{ii}$). Maximum pressure ($P_{max}$) could be corrected as depicted by red arrows and lines (**A**$_{ii}$); a comparison between $P_{max}$ in both groups, including corrected $P_{max}$ for measurements with ESPS (dashed line) is shown in (**A**$_{iii}$). **(B)** Volumetric parameters end-diastolic volume (**B**$_{i}$), stroke volume (**B**$_{ii}$) and cardiac output (**B**$_{iii}$). **(C)** Analysis of cardiac contractility showing preload recruitable stroke work (PRSW) (**C**$_{i}$) and maximum dP/dt (**C**$_{ii}$). **(D)** Diastolic relaxation constant Tau. Data presented as mean ± standard deviation from $n = 17$ (No ESPS group) and $n = 6$ (ESPS group) mice. ESPS, End-systolic pressure-spike; ISO, Isoprenaline; *n*, number of mice. $^{*}p < 0.05$; $^{**}p < 0.01$: *p*-values No ESPS vs. ESPS in an unpaired Student's *t*-test.

is in line with the common understanding that $dP/dt_{max}$ characterizes isovolumetric contraction (23) and ESPS in our protocol occurred at the end of auxotonic contraction. However, ESPS impaired the calculation of the diastolic relaxation parameters Tau and $dP/dt_{min}$. The calculation of both parameters positively correlates with the value for end-systolic pressure (34, 35, 38), which was artificially increased by the pressure spike near end-systole in PV recordings depicting ESPS. This may explain why ESPS artificially induced the contradictory finding of higher values, thus faster relaxation, in $dP/dt_{min}$, and higher values, thus slower relaxation, in Tau.

## Limitations

In our evaluation of PEEP-ventilation, we did not quantify pulmonary damage on a histological level by e.g., quantifying the formation of atelectasis. However, macroscopic hemorrhages, which were completely absent in PEEP-ventilated animals, depict even more severe forms of pulmonary injury. In line with this, others have previously shown protective effects of PEEP-ventilation on a histological level in mice (39), but not in the context of PV analysis. Moreover, we used the femoral vein as the injection site for hypertonic saline in our protocol, though estimation of parallel-conductance ($G_p$) by injecting hypertonic saline has previously been reported for the jugular vein or pulmonary artery (6, 7). Nonetheless, our $G_p$-values using the femoral vein as the central venous injection site are in the range of those reported using jugular vein injections (6, 7, 9).

## Conclusions

(i) Our results support the use of PEEP ventilation in murine open-chest pressure-volume (PV) analysis, as it prevents pulmonary lesions. (ii) They further endorse not to calibrate for parallel-conductance by injecting hypertonic saline prior to the actual PV recordings, due to its multiple adverse effects on murine cardiac function. (iii) We point out to consider that end-systolic pressure-spikes (ESPS), which may arise during incremental β-adrenergic stimulation, adversely affect specific parameters in murine PV analysis.

## AUTHOR CONTRIBUTIONS

LB, MF, and JCL conceived and planned the experiments. LB carried out the experiments. JCL and MF supervised the study. SS, RM, and DL contributed to the interpretation of the results. LB, MF, and JCL wrote the manuscript. All authors provided critical feedback and helped shape the research, analysis and manuscript.

## FUNDING

This work was supported by the DZHK (German Centre for Cardiovascular Research) and the BMBF (German Ministry of Education and Research) and by the Transregional Collaborative Research Center (TR-SFB) 152.

## ACKNOWLEDGMENTS

We thank Manuela Ritzal, Christin Matka, and the team from the Interfakultäre Biomedizinische Forschungseinrichtung (IBF) from the Heidelberg University for their excellent technical assistance. We acknowledge financial support by Deutsche Forschungsgemeinschaft (DFG) within the funding programme Open Access Publishing, by the Baden-Württemberg Ministry of Science, Research and the Arts and by Ruprecht-Karls-Universität Heidelberg.

## SUPPLEMENTARY MATERIAL

The Supplementary Material for this article can be found online at: https://www.frontiersin.org/articles/10.3389/fcvm.2019.00036/full#supplementary-material

## REFERENCES

1. Georgakopoulos D, Mitzner WA, Chen CH, Byrne BJ, Millar HD, Hare JM, et al. *In vivo* murine left ventricular pressure-volume relations by miniaturized conductance micromanometry. *Am J Physiol*. (1998) 274(4 Pt 2):H1416–22. doi: 10.1152/ajpheart.1998.274.4.H1416
2. Cingolani OH, Kass DA. Pressure-volume relation analysis of mouse ventricular function. *Am J Physiol Heart Circ Physiol*. (2011) 301:H2198–206. doi: 10.1152/ajpheart.00781.2011
3. Lindsey ML, Kassiri Z, Virag JAI, de Castro Bras LE, Scherrer-Crosbie M. Guidelines for measuring cardiac physiology in mice. *Am J Physiol Heart Circ Physiol*. (2018) 314:H733–52. doi: 10.1152/ajpheart.00339.2017
4. Baan J, van der Velde ET, de Bruin HG, Smeenk GJ, Koops J, van Dijk AD, et al. Continuous measurement of left ventricular volume in animals and humans by conductance catheter. *Circulation*. (1984) 70:812–23. doi: 10.1161/01.CIR.70.5.812
5. Lankford EB, Kass DA, Maughan WL, Shoukas AA. Does volume catheter parallel conductance vary during a cardiac cycle? *Am J Physiol*. (1990) 258(6 Pt 2):H1933–42. doi: 10.1152/ajpheart.1990.258.6.H1933
6. Georgakopoulos D, Kass DA. Estimation of parallel conductance by dual-frequency conductance catheter in mice. *Am J Physiol Heart Circ Physiol*. (2000) 279:H443–50. doi: 10.1152/ajpheart.2000.279.1.H443
7. Nielsen JM, Kristiansen SB, Ringgaard S, Nielsen TT, Flyvbjerg A, Redington AN, et al. Left ventricular volume measurement in mice by conductance catheter: evaluation and optimization of calibration. *Am J Physiol Heart Circ Physiol*. (2007) 293:H534–40. doi: 10.1152/ajpheart.01268.2006
8. Yang B, Larson DF, Beischel J, Kelly R, Shi J, Watson RR. Validation of conductance catheter system for quantification of murine pressure-volume loops. *J Invest Surg*. (2001) 14:341–55. doi: 10.1080/089419301753435710
9. Pacher P, Nagayama T, Mukhopadhyay P, Batkai S, Kass DA. Measurement of cardiac function using pressure-volume conductance catheter technique in mice and rats. *Nat Protoc*. (2008) 3:1422–34. doi: 10.1038/nprot.2008.138
10. Townsend D. Measuring pressure volume loops in the mouse. *J Vis Exp*. (2016) e53810. doi: 10.3791/53810
11. Lips DJ, van der Nagel T, Steendijk P, Palmen M, Janssen BJ, van Dantzig JM, et al. Left ventricular pressure-volume measurements in mice: comparison of closed-chest versus open-chest approach. *Basic Res Cardiol*. (2004) 99:351–9. doi: 10.1007/s00395-004-0476-5
12. Oosterlinck W, Vanderper A, Flameng W, Herijgers P. Glucose tolerance and left ventricular pressure-volume relationships in frequently used mouse strains. *J Biomed Biotechnol*. (2011) 2011:281312. doi: 10.1155/2011/281312
13. Westermann D, Knollmann BC, Steendijk P, Rutschow S, Riad A, Pauschinger M, et al. Diltiazem treatment prevents diastolic heart failure in mice with familial hypertrophic cardiomyopathy. *Eur J Heart Fail*. (2006) 8:115–21. doi: 10.1016/j.ejheart.2005.07.012
14. Nemoto S, DeFreitas G, Mann DL, Carabello BA. Effects of changes in left ventricular contractility on indexes of contractility in mice. *Am J Physiol Heart Circ Physiol*. (2002) 283:H2504–10. doi: 10.1152/ajpheart.0765.2001
15. Mathar I, Kecskes M, Van der Mieren G, Jacobs G, Camacho Londono JE, Uhl S, et al. Increased beta-adrenergic inotropy in ventricular myocardium from Trpm4$^{-/-}$ mice. *Circ Res*. (2014) 114:283–94. doi: 10.1161/CIRCRESAHA.114.302835
16. Gargiulo S, Greco A, Gramanzini M, Esposito S, Affuso A, Brunetti A, et al. Mice anesthesia, analgesia, and care, part I: anesthetic considerations in preclinical research. *ILAR J*. (2012) 53:E55–69. doi: 10.1093/ilar.53.1.55
17. Glower DD, Spratt JA, Snow ND, Kabas JS, Davis JW, Olsen CO, et al. Linearity of the frank-starling relationship in the intact heart: the concept of preload recruitable stroke work. *Circulation*. (1985) 71:994–1009. doi: 10.1161/01.CIR.71.5.994
18. Weiss JL, Frederiksen JW, Weisfeldt ML. Hemodynamic determinants of the time-course of fall in canine left ventricular pressure. *J Clin Invest*. (1976) 58:751–60. doi: 10.1172/JCI108522
19. Rusca M, Proietti S, Schnyder P, Frascarolo P, Hedenstierna G, Spahn DR, et al. Prevention of atelectasis formation during induction of general anesthesia. *Anesth Analg*. (2003) 97:1835–9. doi: 10.1213/01.ANE.0000087042.02266.F6
20. Thammanomai A, Hamakawa H, Bartolak-Suki E, Suki B. Combined effects of ventilation mode and positive end-expiratory pressure on mechanics, gas exchange and the epithelium in mice with acute lung injury. *PLoS ONE*. (2013) 8:e53934. doi: 10.1371/journal.pone.0053934
21. Kubitz JC, Annecke T, Kemming GI, Forkl S, Kronas N, Goetz AE, et al. The influence of positive end-expiratory pressure on stroke volume variation and central blood volume during open and closed chest conditions. *Eur J Cardiothorac Surg*. (2006) 30:90–5. doi: 10.1016/j.ejcts.2006.04.008
22. Bacmeister L, Schwarzl M, Warnke S, Stoffers B, Blankenberg S, Westermann D, et al. Inflammation and fibrosis in murine models of heart failure. *Basic. Res. Cardiol*. (2019) 114:19. doi: 10.1007/s00395-019-0722-5
23. Burkhoff D, Mirsky I, Suga H. Assessment of systolic and diastolic ventricular properties via pressure-volume analysis: a guide for clinical, translational, and basic researchers. *Am J Physiol Heart Circ Physiol*. (2005) 289:H501–12. doi: 10.1152/ajpheart.00138.2005

24. Aronsen JM, Swift F, Sejersted OM. Cardiac sodium transport and excitation-contraction coupling. *J Mol Cell Cardiol*. (2013) 61:11–9. doi: 10.1016/j.yjmcc.2013.06.003
25. Ottolia M, Torres N, Bridge JH, Philipson KD, Goldhaber JI. Na/Ca exchange and contraction of the heart. *J Mol Cell Cardiol*. (2013) 61:28–33. doi: 10.1016/j.yjmcc.2013.06.001
26. Uhl S, Mathar I, Vennekens R, Freichel M. Adenylyl cyclase-mediated effects contribute to increased isoprenaline-induced cardiac contractility in TRPM4-deficient mice. *J Mol Cell Cardiol*. (2014) 74:307–17. doi: 10.1016/j.yjmcc.2014.06.007
27. Freichel M, Berlin M, Schürger A, Mathar I, Bacmeister L, Medert R, et al. TRP channels in the heart. In: Emir TLR, editor. *Neurobiology of TRP Channels. 1*. New York, NY: CRC Press (2017). p. 149–86.
28. Franz MR, Burkhoff D, Yue DT, Sagawa K. Mechanically induced action potential changes and arrhythmia in isolated and *in situ* canine hearts. *Cardiovasc Res*. (1989) 23:213–23. doi: 10.1093/cvr/23.3.213
29. Franz MR, Cima R, Wang D, Profitt D, Kurz R. Electrophysiological effects of myocardial stretch and mechanical determinants of stretch-activated arrhythmias. *Circulation*. (1992) 86:968–78. doi: 10.1161/01.CIR.86.3.968
30. Kamkin A, Kiseleva I, Isenberg G. Stretch-activated currents in ventricular myocytes: amplitude and arrhythmogenic effects increase with hypertrophy. *Cardiovasc Res*. (2000) 48:409–20. doi: 10.1016/S0008-6363(00)00208-X
31. Taggart P, Sutton P, Lab M. Interaction between ventricular loading and repolarisation: relevance to arrhythmogenesis. *Br Heart J*. (1992) 67:213–5. doi: 10.1136/hrt.67.3.213
32. Courtois M, Mechem CJ, Barzilai B, Ludbrook PA. Factors related to end-systolic volume are important determinants of peak early diastolic transmitral flow velocity. *Circulation*. (1992) 85:1132–8. doi: 10.1161/01.CIR.85.3.1132
33. Udelson JE, Bacharach SL, Cannon RO III, Bonow RO. Minimum left ventricular pressure during beta-adrenergic stimulation in human subjects. Evidence for elastic recoil and diastolic "suction" in the normal heart. *Circulation*. (1990) 82:1174–82. doi: 10.1161/01.CIR.82.4.1174
34. Cohn PF, Liedtke AJ, Serur J, Sonnenblick EH, Urschel CW. Maximal rate of pressure fall (peak negative dP-dt) during ventricular relaxation. *Cardiovasc Res*. (1972) 6:263–7. doi: 10.1093/cvr/6.3.263
35. Weisfeldt ML, Scully HE, Frederiksen J, Rubenstein JJ, Pohost GM, Beierholm E, et al. Hemodynamic determinants of maximum negative dP-dt and periods of diastole. *Am J Physiol*. (1974) 227:613–21. doi: 10.1152/ajplegacy.1974.227.3.613
36. Feldman MD, Erikson JM, Mao Y, Korcarz CE, Lang RM, Freeman GL. Validation of a mouse conductance system to determine LV volume: comparison to echocardiography and crystals. *Am J Physiol Heart Circ Physiol*. (2000) 279:H1698–707. doi: 10.1152/ajpheart.2000.279.4.H1698
37. Wei AE, Maslov MY, Pezone MJ, Edelman ER, Lovich MA. Use of pressure-volume conductance catheters in real-time cardiovascular experimentation. *Heart Lung Circ*. (2014) 23:1059–69. doi: 10.1016/j.hlc.2014.04.130
38. Leite-Moreira AF, Gillebert TC. Nonuniform course of left ventricular pressure fall and its regulation by load and contractile state. *Circulation*. (1994) 90:2481–91. doi: 10.1161/01.CIR.90.5.2481
39. Cagle LA, Franzi LM, Linderholm AL, Last JA, Adams JY, Harper RW, et al. Effects of positive end-expiratory pressure and recruitment maneuvers in a ventilator-induced injury mouse model. *PLoS ONE*. (2017) 12:e0187419. doi: 10.1371/journal.pone.0187419

**Conflict of Interest Statement:** The authors declare that the research was conducted in the absence of any commercial or financial relationships that could be construed as a potential conflict of interest.

frontiers
in Cardiovascular Medicine

MINI REVIEW
published: 12 April 2019
doi: 10.3389/fcvm.2019.00046

# Mouse Models for Atherosclerosis Research—Which Is My Line?

*Sara Oppi [1], Thomas F. Lüscher [1,2] and Sokrates Stein [1]**

[1] *Center for Molecular Cardiology, University of Zurich, Zurich, Switzerland,* [2] *Heart Division, Royal Brompton & Harefield Hospitals and Imperial College, London, United Kingdom*

Atherosclerosis is one of the primary causes of cardiovascular disease and mortality. This chronic immunometabolic disease evolves during decades in humans and encompasses different organs and immune cell types, as well as local and systemic processes that promote the progression of the disease. The most frequently used animal model to study these atherogenic processes and inter-organ crosstalk in a short time frame are genetically modified mouse models. Some models have been used throughout the last decades, and some others been developed recently. These models have important differences in cholesterol and lipoprotein metabolism, reverse cholesterol transport pathway, obesity and diabetes as well as inflammatory processes. Therefore, the disease develops and progresses differently in the various mouse models. Since atherosclerosis is a multifaceted disease and many processes contribute to its progression, the choice of the right mouse model is important to study specific aspects of the disease. We will describe the different mouse models and provide a roadmap to facilitate current and future atherosclerosis researchers to choose the right model depending on their scientific question.

**Keywords: atherosclerosis, cardiovascular disease (CV disease), mouse models, immunometabolic disease, lipoprotein metabolism, inflammatory signaling, PCSK9 (proprotein convertase subtilisin kexin type 9), Fibrillin 1**

**Edited by:**
*Kenneth Boheler,*
*Johns Hopkins University,*
*United States*

**Reviewed by:**
*Soraya Taleb,*
*INSERM U970 Paris-Centre de Recherche Cardiovasculaire (PARCC),*
*France*
*Nasser M. Rizk,*
*Qatar University, Qatar*

***Correspondence:**
*Sokrates Stein*
*sokrates.stein@uzh.ch*

**Specialty section:**
*This article was submitted to Cardiovascular Biologics and Regenerative Medicine,*
*a section of the journal*
*Frontiers in Cardiovascular Medicine*

**Received:** *06 December 2018*
**Accepted:** *26 March 2019*
**Published:** *12 April 2019*

**Citation:**
*Oppi S, Lüscher TF and Stein S (2019)*
*Mouse Models for Atherosclerosis Research—Which Is My Line?*
*Front. Cardiovasc. Med. 6:46.*
*doi: 10.3389/fcvm.2019.00046*

## BACKGROUND

Atherosclerosis is a chronic immunometabolic disease and remains asymptomatic until a plaque becomes large enough to obstruct the lumen to cause ischemic pain or ruptures and causes a myocardial infarction, stroke, or peripheral artery disease. At the early stage, the disease is driven by the retention of cholesterol-rich, apolipoprotein B-containing lipoproteins at specific predilection sites such as bifurcations. High level of plasma low-density lipoprotein (LDL)-cholesterol is the most important risk factor promoting the development and progression of atherosclerosis. Lipoproteins that accumulate in the arterial wall undergo various modifications, such as oxidation and carbamylation. These modified lipoproteins and other pro-inflammatory triggers mediate the activation of vascular endothelial cells (**Figure 1**). In turn, activated endothelial cells express adhesion molecules, which bind to and recruit circulating innate and adaptive immune cells, such as monocytes and T cells (**Figure 1**). Within the intima, monocytes differentiate into macrophages and ingest modified lipoproteins, becoming cholesterol-laden foam cells (1). Plaque macrophages express different scavenger receptors that recognize and mediate the uptake modified lipoprotein antigens, such as oxidized lipoproteins, hence promoting foam cell formation and a pro-inflammatory polarization (**Figure 1**) (2). The excessive storage of cholesterol esters leads to a defective esterification pathway, thus resulting in a consistent accumulation of free cholesterol

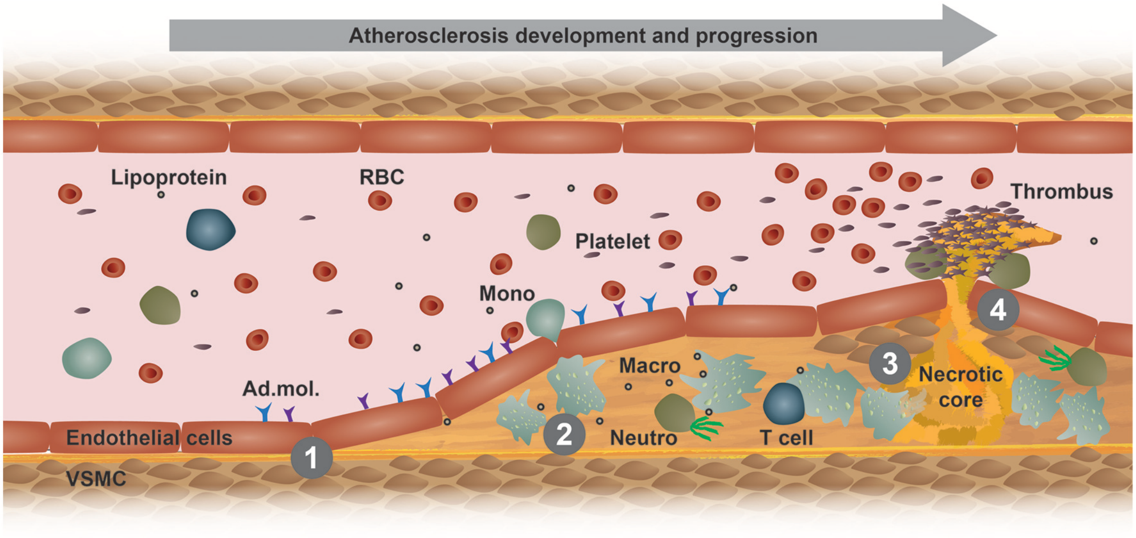

**FIGURE 1 |** Model of atherogenesis. This scheme illustrates the development of an atherosclerotic plaque from left to right in a longitudinal section of an arterial vessel. (**1**) Upon activation by metabolic or inflammatory triggers, endothelial cells express adhesion molecules (Ad. mol.) that promote the recruitment of immune cells, such as blood monocytes (Mono). These cells then infiltrate the arterial intima, where monocyte differentiate into macrophages (Macro) and interact with other immune cells, such as neutrophils (Neutro) and T cells. (**2**) Increased uptake of modified lipoproteins via scavenger receptors or decreased cholesterol efflux accelerates the accumulation of intracellular free cholesterol and cholesteryl ester-loaded lipid droplets that promote foam cell formation. (**3**) Macrophage foam cells eventually die and fall apart, thereby forming a necrotic core. (**4**) Advanced, vulnerable plaques can rupture and thereby form an arterial thrombus, which can lead to a myocardial infarction or stroke. RBC, red blood cell; VSMC, vascular smooth muscle cell.

that forms cholesterol crystals that damage the cells and activate apoptotic pathways. Efferocytosis, i.e., the phagocytosis of apoptotic and necrotic cells, gets impaired and promotes a further accumulation of foam cell debris and the release of inflammatory mediators that together potentiate the inflammation of the arterial wall (3). Additionally, foam cells release enzymes that degrade the extracellular matrix, thus increasing plaque vulnerability and the eventual risk of rupture, which would lead to platelet aggregation, blood coagulation and thrombus formation (**Figure 1**) (1). The development and stability of atherosclerotic plaques is also affected by inflammatory cytokines that are released by different immune cells, such as TNF-α and IFN-γ (4). These released cytokines induce an intra-plaque immune response and promote vascular smooth muscle cells (VSMCs) death, thus destabilizing the matrix of the plaques. Moreover, other cells and organs also contribute to the immunometabolic dysregulation happening during atherosclerosis development. Therefore, it is advisable to compare the different atherosclerosis mouse models and choose one that resembles the aspects of the human pathology as good as possible.

## ANIMAL MODELS

The pathophysiology of atherosclerosis in humans is a complex process that is triggered by various risk factors, including aging, hyperlipidemia, hypertension and diabetes, which lead to an immunometabolic dysregulation. The study of the immunometabolic processes and molecular mechanisms driving the disease requires animal models that mimic the human pathophysiology. Notably, there is no perfect animal model that recapitulate all the features of the human disease. Several animal models have been studied for atherosclerosis research over the last decades, and all of them show advantages and disadvantages. Different animal models can be chosen depending on the focus of the research. In terms of human physiology similarities and clinical relevance, non-human primates are the best model for atherosclerosis investigation. However, non-human primates are expensive to maintain, they develop the disease over a long time, there is a high risk of infections, and they have high ethical hurdles (5, 6). Alternative animal models should be cheaper, easier to handle and reproduce the human disease as good as possible (7). Moreover, they should be appropriate to perform genetic, pharmacological and/or interventional studies.

## OF MICE AND MEN

Mouse models meet these criteria at least in part and are thus are the most common animal model used for atherosclerosis studies. Nevertheless, mice also display major genetic and physiological differences compared to humans (8). One of the most evident difference between mice and humans resides in the lipoprotein metabolism. Mice are considered as a high-density lipoprotein (HDL) models since most of the cholesterol is transported in HDL particles, and not in LDL as in humans. Consequently, mice carry most plasma cholesterol in HDL particles and overall have massively lower cholesterol levels, which confers atherosclerosis protection due to an improved reverse cholesterol transport pathway (9). One reason for this difference is the lack of the cholesteryl ester transfer protein (CETP) in mice. In fact, CETP promotes the transfer of cholesterol ester from HDL to very low-density lipoproteins (VLDL) and of triglycerides from VDLD to HDL. Humans display a high expression CETP, which in turn leads to increased VLDL- and LDL-cholesterol levels.

Another important difference between mice and humans resides in the different bile acids composition. Additionally to the classical bile acid species that are synthesized in humans, mice produce α- and β-muricholic acids, which are more hydrophilic and thus reduce the uptake of cholesterol in the intestine (10). Moreover, the different composition of secondary and tertiary bile acids (e.g., tauro vs. glycin conjugation) and increased synthesis of bile acids is another reason for an improved reverse cholesterol transport and fecal cholesterol excretion in mice (11). These differences in lipoprotein metabolism and bile acids composition confer the mice a resistant to develop atherosclerosis.

To bypass these limitations and provide an appropriate model for the pathophysiology of the disease, dietary and genetic manipulations were developed to generate mouse models suitable for atherosclerosis studies. The standard chow diet of mice usually contains a low content of cholesterol (0.02–0.03%) and fats (5–6%). This low lipid content does not suffice to promote the development of atherosclerosis (12). Therefore, scientists use 'humanized diets', such as the Western-type, containing around 21% fat and 0.15% cholesterol, or the atherogenic diets, which contain more than 1% cholesterol but the same amount of fat. The administration of a high-fat-diet does not induce atherogenesis in most wild-type mouse strains, but it efficiently induces disease development in atherosclerosis-prone genetic mouse models.

These atherosclerosis-prone genetic mouse models were generated by targeting different genes, and they all trigger atherosclerosis development by altering the lipoprotein profile toward an increased VLDL- and LDL-cholesterol content, thus generating a lipoprotein profile that is comparable to humans (13–17).

Despite the disease development, the predisposed sites for lesion development differ between mice and humans. Plaques in humans preferentially develop in the coronary and carotid arteries, and progress to larger fibrous atheroma. In mice, lesions are mainly localized in the aortic sinus, proximal aorta and aortic arch and brachiocephalic trunk, and do not progress to very advanced stages (18). In fact, even genetically altered mice do not develop plaque rupture or coronary lesions leading to myocardial ischemia or infarction. In this review, we will describe the different transgenic mouse models and provide a roadmap to guide future researchers to choose an adequate model based on the scientific question that needs to be addressed (**Figure 2**).

## ATHEROGENIC MOUSE STRAINS

Although mice are classified as high-density lipoprotein models, there are important strain-specific differences in lipoprotein metabolism and inflammatory susceptibility. BALB/c, C3H strains have comparable HDL levels, while the C57Bl/6 strain has much lower HDL levels (19). Additionally, C57Bl/6 mice become obese, diabetic and susceptible to lesion development when fed with an atherogenic diet (20). Another important feature that makes the C57BI/6 mice an ideal model for the study of atherosclerosis and metabolic syndrome is the polarization toward the Th1 profile. C57Bl/6 mice contain T cells that mainly produce Th1 cytokines, especially high interferon-γ (IFN-γ), while other strains such as the BALB/c mice release more Th2 cytokines and less IFN-γ (21). The Th1 profile of C57Bl/6 mice makes the model even more pro-atherogenic. Indeed most of the pathogenic T cells in atherosclerosis show a Th1 profile, characterized by the production of high levels of IFN-γ that activate monocytes/macrophages and dendritic cells, increase the expression of matrix metalloproteinases and prevent the collagen disposition from VSMCs, thus destabilizing the fibrous cap and promoting lesion development (22).

## CHOLESTEROL AND LIPOPROTEIN METABOLISM

Despite of the propensity of the C57Bl/6 strain to develop the disease, different strategies were produced to increase LDL-cholesterol and thereby the atherosclerotic susceptibility of the C57Bl/6 strain, including the disruption of the *low-density lipoprotein receptor* (*Ldlr*-/-), the deletion of the *apolipoprotein E* (*Apoe*-/-), or the ectopic introduction of a mutant *protein convertase subtilisin/kexin type 9* (*Pcsk9*) gene.

APOE is part of the structure of chylomicrons remnants, VLDL and HDL, and it binds to the LDLR, VLDL receptor (VLDLR) and LDLR-related protein (LRP) in the liver to facilitate the clearance of plasma chylomicrons and VLDL remnants. Consequently, the genetic deletion of *Apoe* in mice results in increased levels of plasma cholesterol. *Apoe* knockout mice show a significant increase of total plasma cholesterol compared to wild-type mice under chow diet: 400–600 and 75–110 mg/dl, respectively (23). Of note, humans usually have total plasma cholesterol levels below 200 mg/dl; while levels over 240 mg/dl are considered to be high and are commonly related to familial hypercholesteremia (i.e., mutations in the LDL- or PCSK9 gene). That explains why the deletion of *Apoe* is sufficient to drive a massive hypercholesterolemia under normal diet and to develop spontaneous lesions. Feeding *Apoe*-/- mice with a high cholesterol diet additionally increases plasma cholesterol levels above 1,000 mg/dl, thus driving an extensive and accelerated atherosclerosis development. Lesion distribution in *Apoe*–/– mice are similar to humans, with a predominance in the aortic root, carotid artery, and aortic branches. However, the *Apoe*–/– model shows a different lipoprotein profile from humans since the majority of plasma cholesterol is carried by VLDL and chylomicrons particles, whereas it is mainly transported by LDL in humans. Another limitation of this mouse model is that despite the accelerated atherosclerosis development, the lesions rarely rupture and hence do not lead to thrombosis, whereas vascular occlusion is common in humans (24). In humans, different isoforms of *APOE* are linked to altered

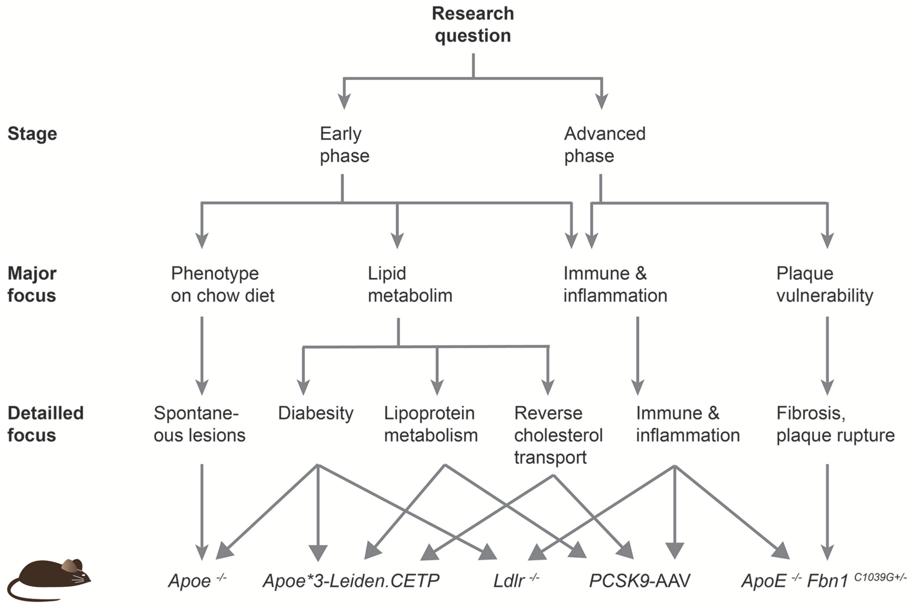

**FIGURE 2 |** Roadmap to facilitate the choice of an atherosclerotic mouse model. This scheme should help current and future researchers to choose the most appropriate atherosclerotic mouse model based on their specific research question.

lipoprotein profiles and increased cardiovascular mortality (25). Individuals carrying the APOE4 allele have more predisposition to develop cardiovascular disease compared to the APOE2 and APOE3 isoforms. In fact, the APOE4 isoform increases oxidative stress and inflammation, hence promoting disease development (26).

A model closer to the human situation to study altered cholesterol metabolism is the *Ldlr* knockout mouse. The LDLR is a membrane receptor located on the surface of many cell types and its function is to mediate the endocytosis of circulating LDL. The genetic deletion of the *Ldlr* increases cholesterol levels to 200–300 mg/dl on chow diet, and to about 1000 mg/dl on an atherogenic diet (15). The lesions preferentially develop in the proximal aorta at early stages and along the distal aorta at more advanced stages (27). The main aspect that makes *Ldlr* a favorable model to study cholesterol metabolism over the *Apoe* knockouts is its closer resemblance to human hypercholesterolemia since most cholesterol is transported by LDL particles (28). In humans, over 600 mutations of the *LDLR* gene have been reported, several of them causing familial hypercholesterolemia, a frequent genetic disorder associated with high levels of LDL-cholesterol and atherosclerosis development (29).

## REVERSE CHOLESTEROL TRANSPORT

In the reverse cholesterol transport (RCT) peripheral cholesterol is transferred to HDL particles and then transported to the liver. Within the liver it can then be further metabolized, be converted to bile acids, or be directly excreted via the bile. RCT is therefore regulated at various different sites, including the cholesterol efflux in peripheral tissues and cells, the exchange of lipids between lipoproteins in the blood, and the uptake, metabolization and biliary excretion in the liver (30).

APOE plays a central role in peripheral and hepatic RCT (31). Additionally, macrophages synthesize APOE and promote cholesterol efflux, and interestingly the macrophage-specific deletion of *Apoe* affects peripheral RCT *in vivo* (32–34). Moreover, APOE-positive macrophages promote proper RCT in Apoe knockout mice (34). Therefore, the *Apoe* deletion does affect both peripheral and hepatic RCT. Given the fact that the lipoprotein profile of *Ldlr*−/− mice is closer to humans and considering the presence of APOE in the system, the *Ldlr* knockout is the favored model for RCT and lipoprotein studies.

Another suitable model is the *Apoe**3-Leiden.CETP mouse line. This model has increased VLDL/LDL-cholesterol because of the expression of a human CETP, reduced peripheral cholesterol efflux, and severe atherosclerosis development (35). Moreover, *Apoe**3-Leiden.CETP mice fed a high-fat high-cholesterol diet for 6 months mimic changes in lipid profiles observed in humans suffering from the metabolic syndrome, and may therefore be the preferred model to study age-related changes in lipid metabolism and reverse cholesterol transport (36, 37).

## OBESITY AND TYPE-2 DIABETES

Obesity, insulin resistance and type-2 diabetes are reaching epidemic proportions world-wide, correlate with atherosclerosis development, and are strong predictors of cardiovascular mortality (38). Currently, there is no ideal mouse model that resembles all features of human diabetes, although several models have been established to study diabetes-accelerated atherosclerosis development, including genetic manipulations and specific diets (39). Diabetogenic diets that are rich in fats and sucrose induce obesity in C57Bl/6 mice, making this strain ideal to study the development of type-2 diabetes and atherosclerosis (40). *Ldlr*−/− mice are more susceptible to develop diabetes compared to the *Apoe*−/− mice and the control wildtype mice under diabetogenic diet feeding. In fact, *Ldlr*−/− mice have an increased body weight caused by an accumulation of subcutaneous adiposity, have high glucose levels and develop an insulin resistance upon diabetogenic diet challenge (41). This diabetic phenotype is not observed in *Apoe*−/− mice, possibly due to an increased rate of hepatic fatty acid oxidation (41). Conversely, on a high fat diet, both *Apoe*−/− and *Ldlr*−/− mice develop features of type 2 diabetes and promote atherosclerosis development (42, 43). Therefore, the choice of the diet is very important in this context.

Further models were generated by crossbreeding genetic models of type-2 diabetes, such as *leptin* (*ob/ob*) and *leptin receptor* (*db/db*) deficient mice, with atherosclerotic mouse models. These genetic models enable the study of the disease development under chow diet (39). Leptins are hormones synthesized by adipocytes, released into the bloodstream, and exerting their main functions by binding to leptin receptors at the hypothalamus to regulate the appetite and thus food intake. Moreover, leptins increase the energy expenditure that translate into an elevation in body temperature and increase in oxygen consumption. Therefore, deficiency of *leptin* or the *leptin receptor* leads an impaired energy expenditure and increased food intake, and thus to obesity (44, 45). Moreover, genetic deficiency of the leptin axis impairs the immune system and increases the susceptibility to infections (46). Thus, *leptin* or the *leptin receptor*-deficient mice display common features of the immuno-metabolic dysfunction that are observed in obesity and diabetes mellitus. Mice that develop both diabetes and atherosclerosis are a good model for the study diabetes-accelerated atherosclerosis development. For example, *Apoe*−/− *db/db* mice develop obesity, hyperinsulinemia, dyslipidemia and have a fast atherosclerosis development at 20 weeks of age compared to the control *Apoe*−/− mice (47). *Ldlr*−/− *ob/ob* mice get obese and show hyperglycemia, hypercholesterolemia and spontaneous lesions development under chow diet (48). In conclusion, multiple mouse models can be used to study diabetes-accelerated atherosclerosis, but the interpretation of the data has to be cautious given the various functions of leptin in many physiological processes. We refer to the review of Wu and Huan for further information on this topic (39).

## INFLAMMATORY PROCESSES

Inflammatory and immune processes play an important function in early steps of plaque formation, but also in advanced stages as reveal by the recent CANTOS trial (49). Lipoprotein oxidation, endothelial cell activation, macrophage activation and impaired efferocytosis, VSMCs proliferation, and platelet aggregation are some of the best characterized processes that contributes to the arterial wall inflammation, lesion expansion, and atherothrombosis. APOE is a multifunctional protein that affects each of these inflammatory processes. Functional APOE protein inhibits lipoproteins oxidation, while *Apoe*−/− mice display increased peroxidation of lipoproteins (50). *Apoe*−/− mice also show elevated levels of endothelial cell adhesion molecules, thus triggering the recruitment of monocytes and thymocytes into the subintimal space (23, 51). Moreover, APOE inhibits VSMC proliferation and migration, and consequently *Apoe*−/− mice display increases proliferation and migration of VSMCs (52). Additionally, APOE inhibits platelet aggregation, hence displaying an additional anti-atherogenic function (53). Efferocytosis, the phagocytic clearance of dead cells and cellular debris, plays important functions in the resolution of inflammation and is mainly mediated by macrophages and other immune phagocytes (54). The APOE protein has been shown to exert important functions in this process both *in vivo* and *in vitro* (55). Indeed, APOE promotes the ingestion of apoptotic cells in macrophages, and thus *Apoe*-deficient mice display impaired efferocytosis and an accumulation of apoptotic cells and cellular fragments in the vessel wall, further promoting lesion development. These anti-inflammatory properties of APOE, combined with its impact on lipoprotein metabolism, explain why *Apoe* knockout mice display a very strong development of atherosclerosis compared to other mouse models. Therefore, other models with a functional APOE protein, such as the *Ldlr*−/−, should be the primary choice to study inflammatory processes in atherosclerosis development.

## IMMUNOMETABOLIC REGULATION

Currently, one of the most interesting research questions is to assess the impact of inflammatory and immune processes on lipid and lipoprotein metabolism, and vice versa. The use of the *Apoe*−/− or *Ldlr*−/− models to address this question is limited due to their strong impact on inflammatory processes and/or lipoprotein metabolism. Another model that has been developed recently by two different groups are the *PCSK9*-AAV mouse lines (16, 17). These mice have no genetic modifications and express APOE and LDLR at normal levels. Nevertheless, the introduction of a mouse or human gain-of-function PCSK9 mutant leads to increased total plasma cholesterol (above 1,000 mg/dl) as well as VLDL- and LDL-cholesterol, and the development of atherosclerosis upon Western diet feeding. One further advantage of these lines is that a single adeno-associated virus (AAV) injection is sufficient to generate new mouse models in a much quicker time compared to conventional crossbreeding to *Apoe*−/− or *Ldlr*−/− mice. Another advantage is that immunometabolic processes can be studied without the confounding effects from the lack of APOE or LDLR. Although the use of AAVs seems to be pretty save and without pathogenicity, one might still consider a possible anti-viral host immune response of the organism (56).

## ATHEROTHROMBOTIC STUDIES

A clear limitation of the above described mouse models is that despite developing atherosclerotic lesions, these lesions rarely progress to advanced stages with atherothrombotic vascular occlusion that are observed in humans. Consequently, no spontaneous plaque rupture is observed in these mouse lines. To overcome this limitation a group of Belgium scientists developed and characterized a very interesting mouse model that displays many features of advanced atherosclerotic plaques (57). The mouse model was created by crossbreeding mice with a mutant fibrillin-1 allele (*Fbn1*$^{C1039G}$) with *Apoe* knockout mice, thus generating *Apoe*$^{-/-}$ *Fbn1*$^{C1039G+/-}$ mice. In these mice, the *Fbn1* mutation leads to the fragmentation of elastic fibers, which in turn promotes arterial stiffening and the development of large vulnerable atherosclerotic plaques that eventually rupture (58). Moreover, these mice display increased inflammation and degradation of the extracellular matrix within plaques, and an increased blood-brain barrier (BBB) permeability that leads to the development of xanthomas in the brain upon prolonged exposure to a Western diet (58, 59). Given its strong phenotype and clinical relevance, this line is currently the most interesting genetic mouse model to study advanced atherosclerosis and atherothrombosis in myocardial infarction or ischemic stroke.

Another mouse model that promotes plaque destabilization and stimulates plaque rupture as well as spontaneous atherothrombosis consists of *Apoe*-deficient mice fed with a high-fat diet for 4 weeks and a subsequent infusion of angiotensin II for 4 weeks. The continuous infusion of angiotensin II accelerates the destabilization and vulnerability of the plaques as well as abdominal aortic aneurysm (60). Angiotensin II increases the blood pressure, recruits monocytes, activates macrophages and increases the oxidative stress (61). Therefore, the *Apoe*-deficient mice fed with high-fat diet and subsequent angiotensin II infusion represents an alternative model to study advanced atherosclerosis.

## CONCLUSION

The mouse model continues to be the best model organism to decipher the underlying genetic, epigenetic and environmental-induced mechanisms leading to disease development and progression. The *Ldlr* knockout model resembles the human lipoprotein profile pretty well and is therefore a suitable model to study cholesterol and lipoprotein metabolism. Even closer to the human profile are the *Apoe**3-Leiden.CETP mice, which are certainly the model of choice to study human CETP but also changes in lipid profiles that are also observed in humans suffering from the metabolic syndrome. Obesity and insulin resistance are often associated with type 2 diabetes and increase the risk to develop atherosclerosis. *Ldlr* and *Apoe* knockout mice alone or in combination with a *leptin* or *leptin receptor* deficiency are appropriate to evaluate the metabolic syndrome in diet-induced studies or under normal chow, respectively. Inflammation is another important contributor of the disease development and the *Ldlr*–/– model should preferentially be used over the *Apoe*–/– mice, although other newer models such as the *PCSK9*-AAV approach offer an attractive alternative. Finally, the *Apoe* $^{-/-}$ *Fbn1*$^{C1039G+/-}$ mouse line is emerging as a new model to study atherothrombosis, myocardial infarction, and ischemic stroke. These mice form large and vulnerable atherosclerotic plaques that eventually rupture. In conclusions, the study of the diverse processes promoting atherosclerosis requires different mouse models, and the provided roadmap should facilitate current and future researchers to choose an adequate mouse model for their studies (**Figure 2**).

## PERSPECTIVE

Currently, a very exciting field is to explore the role of long non-coding RNA (lncRNA) in atherosclerosis and cardiovascular diseases (62). For example, the lncRNA *LeXis* regulates hepatic lipid accumulation and plasma cholesterol levels, and thereby decreases atherogenesis in *Ldlr* knockout mice (63), and MeXis, a lncRNA that is highly expressed in mouse macrophages, promotes macrophage cholesterol efflux, HDL-driven reverse cholesterol transport, and thus reduces macrophage foam cell formation and atherosclerosis development (64). Notably, another lncRNA, CHROME, has been identified as an alternatively regulator of the cholesterol efflux in primates and its levels are elevated in plasma and atherosclerotic lesions of individuals with coronary artery disease (65), highlighting the translational value of mouse studies.

Future studies aimed at identifying and describing new triggers and mechanisms regulating atherosclerosis development will develop novel mouse models to address their specific questions. Already now most studies are using tissue-specific overexpression or knockout mouse models, but also starting to address the function of specific mutations and not yet well-described posttranslational protein modifications, such as SUMOylation, in atherogenesis and cardiovascular diseases (66–70). Moreover, the incredibly fast development of the Crispr/Cas9 system led to the development of new mouse and also larger animal models to study atherogenesis and will continue to accelerate basic and translational cardiovascular research (71–76).

## AUTHOR CONTRIBUTIONS

SO and SS explored the literature. SO, TL, and SS wrote the manuscript.

## ACKNOWLEDGMENTS

We acknowledge support to SS by the Swiss National Science Foundation (PZOOP3_161521), The Novartis Foundation for medical-biological Research (#16B103), the Olga-Mayenfisch Foundation, the OPO foundation, and the Swiss Heart Foundation.

# REFERENCES

1. Libby P, Ridker PM, Hansson GK. Progress and challenges in translating the biology of atherosclerosis. *Nature.* (2011) 473:317–25. doi: 10.1038/nature10146
2. Moore KJ, Freeman MW. Scavenger receptors in atherosclerosis: beyond lipid uptake. *Arterioscler Thromb Vasc Biol.* (2006) 26:1702–11. doi: 10.1161/01.ATV.0000229218.97976.43
3. Moore KJ, Tabas I. Macrophages in the pathogenesis of atherosclerosis. *Cell.* (2011) 145:341–55. doi: 10.1016/j.cell.2011.04.005
4. Andersson J, Libby P, Hansson GK. Adaptive immunity and atherosclerosis. *Clin Immunol.* (2010) 134:33–46. doi: 10.1016/j.clim.2009.07.002
5. Mukhopadhyay R. Mouse models of atherosclerosis: explaining critical roles of lipid metabolism and inflammation. *J Appl Genet.* (2013) 54:185–92. doi: 10.1007/s13353-013-0134-4
6. Burm SM, Prins JB, Langermans J, Bajramovic JJ. Alternative methods for the use of non-human primates in biomedical research. *ALTEX.* (2014) 31:520–9. doi: 10.14573/altex.1406231
7. Emini Veseli B, Perrotta P, De Meyer GRA, Roth L, Van der Donckt C, Martinet W, et al. Animal models of atherosclerosis. *Eur J Pharmacol.* (2017) 816:3–13. doi: 10.1016/j.ejphar.2017.05.010
8. von Scheidt M, Zhao Y, Kurt Z, Pan C, Zeng L, Yang X, et al. Applications and limitations of mouse models for understanding human atherosclerosis. *Cell Metab.* (2017) 25:248–61. doi: 10.1016/j.cmet.2016.11.001
9. Barter PJ, Brewer HB, Jr., Chapman MJ, Hennekens CH, Rader DJ, Tall AR. Cholesteryl ester transfer protein: a novel target for raising HDL and inhibiting atherosclerosis. *Arterioscler Thromb Vasc Biol.* (2003) 23:160–7. doi: 10.1161/01.ATV.0000054658.91146.64
10. Takahashi S, Fukami T, Masuo Y, Brocker CN, Xie C, Krausz KW, et al. Cyp2c70 is responsible for the species difference in bile acid metabolism between mice and humans. *J Lipid Res.* (2016) 57:2130–7. doi: 10.1194/jlr.M071183
11. Xu Y, Li F, Zalzala M, Xu J, Gonzalez FJ, Adorini L, et al. Farnesoid X receptor activation increases reverse cholesterol transport by modulating bile acid composition and cholesterol absorption in mice. *Hepatology.* (2016) 64:1072–85. doi: 10.1002/hep.28712
12. Almeida-Suhett CP, Scott JM, Graham A, Chen Y, Deuster PA. Control diet in a high-fat diet study in mice: regular chow and purified low-fat diet have similar effects on phenotypic, metabolic, and behavioral outcomes. *Nutr Neurosci.* (2017) 22:1–10. doi: 10.1080/1028415X.2017.1349359
13. Zhang SH, Reddick RL, Piedrahita JA, Maeda N. Spontaneous hypercholesterolemia and arterial lesions in mice lacking apolipoprotein E. *Science.* (1992) 258:468–71. doi: 10.1126/science.1411543
14. Ishibashi S, Brown MS, Goldstein JL, Gerard RD, Hammer RE, Herz J. Hypercholesterolemia in low density lipoprotein receptor knockout mice and its reversal by adenovirus-mediated gene delivery. *J Clin Invest.* (1993) 92:883–93. doi: 10.1172/JCI116663
15. Ishibashi S, Goldstein JL, Brown MS, Herz J, Burns DK. Massive xanthomatosis and atherosclerosis in cholesterol-fed low density lipoprotein receptor-negative mice. *J Clin Invest.* (1994) 93:1885–93. doi: 10.1172/JCI117179
16. Bjorklund MM, Hollensen AK, Hagensen MK, Dagnaes-Hansen F, Christoffersen C, Mikkelsen JG, et al. Induction of atherosclerosis in mice and hamsters without germline genetic engineering. *Circ Res.* (2014) 114:1684–9. doi: 10.1161/CIRCRESAHA.114.302937
17. Roche-Molina M, Sanz-Rosa D, Cruz FM, Garcia-Prieto J, Lopez S, Abia R, et al. Induction of sustained hypercholesterolemia by single adeno-associated virus-mediated gene transfer of mutant hPCSK9. *Arterioscler Thromb Vasc Biol.* (2015) 35:50–9. doi: 10.1161/ATVBAHA.114.303617
18. Breslow JL. Mouse models of atherosclerosis. *Science.* (1996) 272:685–8. doi: 10.1126/science.272.5262.685
19. Paigen B, Holmes PA, Mitchell D, Albee D. Comparison of atherosclerotic lesions and HDL-lipid levels in male, female, and testosterone-treated female mice from strains C57BL/6, BALB/c, and C3H. *Atherosclerosis.* (1987) 64:215–21. doi: 10.1016/0021-9150(87)90249-8
20. Schreyer SA, Wilson DL, LeBoeuf RC. C57BL/6 mice fed high fat diets as models for diabetes-accelerated atherosclerosis. *Atherosclerosis.* (1998) 136:17–24. doi: 10.1016/S0021-9150(97)00165-2
21. Watanabe H, Numata K, Ito T, Takagi K, Matsukawa A. Innate immune response in Th1- and Th2-dominant mouse strains. *Shock.* (2004) 22:460–6. doi: 10.1097/01.shk.0000142249.08135.e9
22. Mallat Z, Taleb S, Ait-Oufella H, Tedgui A. The role of adaptive T cell immunity in atherosclerosis. *J Lipid Res.* (2009) 50(Suppl):S364–9. doi: 10.1194/jlr.R800092-JLR200
23. Nakashima Y, Plump AS, Raines EW, Breslow JL, Ross R. ApoE-deficient mice develop lesions of all phases of atherosclerosis throughout the arterial tree. *Arterioscler Thromb.* (1994) 14:133–40. doi: 10.1161/01.ATV.14.1.133
24. Smith JD, Breslow JL. The emergence of mouse models of atherosclerosis and their relevance to clinical research. *J Intern Med.* (1997) 242:99–109. doi: 10.1046/j.1365-2796.1997.00197.x
25. Mahley RW. Apolipoprotein E: from cardiovascular disease to neurodegenerative disorders. *J Mol Med.* (2016) 94:739–46. doi: 10.1007/s00109-016-1427-y
26. Jofre-Monseny L, Minihane AM, Rimbach G. Impact of apoE genotype on oxidative stress, inflammation and disease risk. *Mol Nutr Food Res.* (2008) 52:131–45. doi: 10.1002/mnfr.200700322
27. Tangirala RK, Rubin EM, Palinski W. Quantitation of atherosclerosis in murine models: correlation between lesions in the aortic origin and in the entire aorta, and differences in the extent of lesions between sexes in LDL receptor-deficient and apolipoprotein E-deficient mice. *J Lipid Res.* (1995) 36:2320–8.
28. Defesche JC. Low-density lipoprotein receptor–its structure, function, and mutations. *Semin Vasc Med.* (2004) 4:5–11. doi: 10.1055/s-2004-822993
29. Goldstein JL, Brown MS. Molecular medicine. The cholesterol quartet. *Science.* (2001) 292:1310–2. doi: 10.1126/science.1061815
30. Rosenson RS, Brewer HB, Jr., Davidson WS, Fayad ZA, Fuster V, Goldstein J, et al. Cholesterol efflux and atheroprotection: advancing the concept of reverse cholesterol transport. *Circulation.* (2012) 125:1905–19. doi: 10.1161/CIRCULATIONAHA.111.066589
31. Wagner T, Bartelt A, Schlein C, Heeren J. Genetic dissection of tissue-specific apolipoprotein E function for hypercholesterolemia and diet-induced obesity. *PLoS ONE.* (2015) 10:e0145102. doi: 10.1371/journal.pone.0145102
32. Basu SK, Brown MS, Ho YK, Havel RJ, Goldstein JL. Mouse macrophages synthesize and secrete a protein resembling apolipoprotein E. *Proc Natl Acad Sci USA.* (1981) 78:7545–9. doi: 10.1073/pnas.78.12.7545
33. Basu SK, Ho YK, Brown MS, Bilheimer DW, Anderson RG, Goldstein JL. Biochemical and genetic studies of the apoprotein E secreted by mouse macrophages and human monocytes. *J Biol Chem.* (1982) 257:9788–95.
34. Zanotti I, Pedrelli M, Poti F, Stomeo G, Gomaraschi M, Calabresi L, et al. Macrophage, but not systemic, apolipoprotein E is necessary for macrophage reverse cholesterol transport *in vivo*. *Arterioscler Thromb Vasc Biol.* (2011) 31:74–80. doi: 10.1161/ATVBAHA.110.213892
35. Westerterp M, van der Hoogt CC, de Haan W, Offerman EH, Dallinga-Thie GM, Jukema JW, et al. Cholesteryl ester transfer protein decreases high-density lipoprotein and severely aggravates atherosclerosis in APOE*3-Leiden mice. *Arterioscler Thromb Vasc Biol.* (2006) 26:2552–9. doi: 10.1161/01.ATV.0000243925.65265.3c
36. Kuhnast S, van der Tuin SJ, van der Hoorn JW, van Klinken JB, Simic B, Pieterman E, et al. Anacetrapib reduces progression of atherosclerosis, mainly by reducing non-HDL-cholesterol, improves lesion stability and adds to the beneficial effects of atorvastatin. *Eur Heart J.* (2015) 36:39–48. doi: 10.1093/eurheartj/ehu319
37. Paalvast Y, Gerding A, Wang Y, Bloks VW, van Dijk TH, Havinga R, et al. Male apoE*3-Leiden.CETP mice on high-fat high-cholesterol diet exhibit a biphasic dyslipidemic response, mimicking the changes in plasma lipids observed through life in men. *Physiol. Rep.* (2017) 5:e13376. doi: 10.14814/phy2.13376
38. Bhupathiraju SN, Hu FB. Epidemiology of obesity and diabetes and their cardiovascular complications. *Circ Res.* (2016) 118:1723–35. doi: 10.1161/CIRCRESAHA.115.306825
39. Wu KK, Huan Y. Diabetic atherosclerosis mouse models. *Atherosclerosis.* (2007) 191:241–9. doi: 10.1016/j.atherosclerosis.2006.08.030
40. Surwit RS, Kuhn CM, Cochrane C, McCubbin JA, Feinglos MN. Diet-induced type II diabetes in C57BL/6J mice. *Diabetes.* (1988) 37:1163–7. doi: 10.2337/diab.37.9.1163
41. Schreyer SA, Vick C, Lystig TC, Mystkowski P, LeBoeuf RC. LDL receptor but not apolipoprotein E deficiency increases diet-induced obesity and

diabetes in mice. *Am J Physiol Endocrinol Metab.* (2002) 282:E207–14. doi: 10.1152/ajpendo.2002.282.1.E207

42. Collins AR, Meehan WP, Kintscher U, Jackson S, Wakino S, Noh G, et al. Troglitazone inhibits formation of early atherosclerotic lesions in diabetic and nondiabetic low density lipoprotein receptor-deficient mice. *Arterioscler Thromb Vasc Biol.* (2001) 21:365–71. doi: 10.1161/01.ATV.21.3.365
43. Phillips JW, Barringhaus KG, Sanders JM, Yang Z, Chen M, Hesselbacher S, et al. Rosiglitazone reduces the accelerated neointima formation after arterial injury in a mouse injury model of type 2 diabetes. *Circulation.* (2003) 108:1994–9. doi: 10.1161/01.CIR.0000092886.52404.50
44. Hamrick MW. Role of the cytokine-like hormone leptin in muscle-bone crosstalk with aging. *J Bone Metab.* (2017) 24:1–8. doi: 10.11005/jbm.2017.24.1.1
45. Hussain Z, Khan JA. Food intake regulation by leptin: mechanisms mediating gluconeogenesis and energy expenditure. *Asian Pac J Trop Med.* (2017) 10:940–4. doi: 10.1016/j.apjtm.2017.09.003
46. La Cava A. Leptin in inflammation and autoimmunity. *Cytokine.* (2017) 98:51–8. doi: 10.1016/j.cyto.2016.10.011
47. Wu KK, Wu TJ, Chin J, Mitnaul LJ, Hernandez M, Cai TQ, et al. Increased hypercholesterolemia and atherosclerosis in mice lacking both ApoE and leptin receptor. *Atherosclerosis.* (2005) 181:251–9. doi: 10.1016/j.atherosclerosis.2005.01.029
48. Kennedy AJ, Ellacott KL, King VL, Hasty AH. Mouse models of the metabolic syndrome. *Dis Model Mech.* (2010) 3:156–66. doi: 10.1242/dmm.003467
49. Ridker PM, Everett BM, Thuren T, MacFadyen JG, Chang WH, Ballantyne C, et al. Antiinflammatory therapy with canakinumab for atherosclerotic disease. *N Engl J Med.* (2017) 377:1119–31. doi: 10.1056/NEJMoa1707914
50. Hayek T, Oiknine J, Brook JG, Aviram M. Increased plasma and lipoprotein lipid peroxidation in apo E-deficient mice. *Biochem Biophys Res Commun.* (1994) 201:1567–74. doi: 10.1006/bbrc.1994.1883
51. Tian J, Pei H, James JC, Li Y, Matsumoto AH, Helm GA, et al. Circulating adhesion molecules in apoE-deficient mouse strains with different atherosclerosis susceptibility. *Biochem Biophys Res Commun.* (2005) 329:1102–7. doi: 10.1016/j.bbrc.2005.02.090
52. Hui DY, Basford JE. Distinct signaling mechanisms for apoE inhibition of cell migration and proliferation. *Neurobiol Aging.* (2005) 26:317–23. doi: 10.1016/j.neurobiolaging.2004.02.030
53. Riddell DR, Vinogradov DV, Stannard AK, Chadwick N, Owen JS. Identification and characterization of LRP8 (apoER2) in human blood platelets. *J Lipid Res.* (1999) 40:1925–30.
54. Kasikara C, Doran AC, Cai B, Tabas I. The role of non-resolving inflammation in atherosclerosis. *J Clin Invest.* (2018) 128:2713–23. doi: 10.1172/JCI97950
55. Grainger DJ, Reckless J, McKilligin E. Apolipoprotein E modulates clearance of apoptotic bodies *in vitro* and *in vivo*, resulting in a systemic proinflammatory state in apolipoprotein E-deficient mice. *J Immunol.* (2004) 173:6366–75. doi: 10.4049/jimmunol.173.10.6366
56. Daya S, Berns KI. Gene therapy using adeno-associated virus vectors. *Clin Microbiol Rev.* (2008) 21:583–93. doi: 10.1128/CMR.00008-08
57. Van Herck JL, De Meyer GR, Martinet W, Van Hove CE, Foubert K, Theunis MH, et al. Impaired fibrillin-1 function promotes features of plaque instability in apolipoprotein E-deficient mice. *Circulation.* (2009) 120:2478–87. doi: 10.1161/CIRCULATIONAHA.109.872663
58. Van der Donckt C, Van Herck JL, Schrijvers DM, Vanhoutte G, Verhoye M, Blockx I, et al. Elastin fragmentation in atherosclerotic mice leads to intraplaque neovascularization, plaque rupture, myocardial infarction, stroke, and sudden death. *Eur Heart J.* (2015b) 36:1049–58. doi: 10.1093/eurheartj/ehu041
59. Van der Donckt C, Roth L, Vanhoutte G, Blockx I, Bink DI, Ritz K, et al. Fibrillin-1 impairment enhances blood-brain barrier permeability and xanthoma formation in brains of apolipoprotein E-deficient mice. *Neuroscience.* (2015a) 295:11–22. doi: 10.1016/j.neuroscience.2015.03.023
60. Sato K, Nakano K, Katsuki S, Matoba T, Osada K, Sawamura T, et al. Dietary cholesterol oxidation products accelerate plaque destabilization and rupture associated with monocyte infiltration/activation via the MCP-1-CCR2 pathway in mouse brachiocephalic arteries: therapeutic effects of ezetimibe. *J Atheroscler Thromb.* (2012) 19:986–98. doi: 10.5551/jat.13391
61. Matoba T, Sato K, Egashira K. Mouse models of plaque rupture. *Curr Opin Lipidol.* (2013) 24:419–25. doi: 10.1097/MOL.0b013e3283646e4d
62. Tontonoz P, Wu X, Jones M, Zhang Z, Salisbury D, Sallam T. Long noncoding RNA facilitated gene therapy reduces atherosclerosis in a murine model of familial hypercholesterolemia. *Circulation.* (2017) 136:776–8. doi: 10.1161/CIRCULATIONAHA.117.029002
63. Sallam T, Jones MC, Gilliland T, Zhang L, Wu X, Eskin A, et al. Feedback modulation of cholesterol metabolism by the lipid-responsive non-coding RNA LeXis. *Nature.* (2016) 534:124–8. doi: 10.1038/nature17674
64. Sallam T, Jones M, Thomas BJ, Wu X, Gilliland T, Qian K, et al. Transcriptional regulation of macrophage cholesterol efflux and atherogenesis by a long noncoding RNA. *Nat Med.* (2018) 24:304–12. doi: 10.1038/nm.4479
65. Hennessy EJ, van Solingen C, Scacalossi KR, Ouimet M, Afonso MS, Prins J, et al. The long noncoding RNA CHROME regulates cholesterol homeostasis in primates. *Nat Metab.* (2019) 1:98–110. doi: 10.1038/s42255-018-0004-9
66. Pascual G, Fong AL, Ogawa S, Gamliel A, Li AC, Perissi V, et al. A SUMOylation-dependent pathway mediates transrepression of inflammatory response genes by PPAR-gamma. *Nature.* (2005) 437:759–63. doi: 10.1038/nature03988
67. Venteclef N, Jakobsson T, Ehrlund A, Damdimopoulos A, Mikkonen L, Ellis E, et al. GPS2-dependent corepressor/SUMO pathways govern anti-inflammatory actions of LRH-1 and LXRbeta in the hepatic acute phase response. *Genes Dev.* (2010) 24:381–95. doi: 10.1101/gad.545110
68. Stein S, Oosterveer MH, Mataki C, Xu P, Lemos V, Havinga R, et al. SUMOylation-dependent LRH-1/PROX1 interaction promotes atherosclerosis by decreasing hepatic reverse cholesterol transport. *Cell Metab.* (2014) 20:603–13. doi: 10.1016/j.cmet.2014.07.023
69. Stein S, Lemos V, Xu P, Demagny H, Wang X, Ryu D, et al. Impaired SUMOylation of nuclear receptor LRH-1 promotes nonalcoholic fatty liver disease. *J Clin Invest.* (2017) 127:583–92. doi: 10.1172/JCI85499
70. Katafuchi T, Holland WL, Kollipara RK, Kittler R, Mangelsdorf DJ, Kliewer SA. PPARgamma-K107 SUMOylation regulates insulin sensitivity but not adiposity in mice. *Proc Natl Acad Sci USA.* (2018) 115:12102–11. doi: 10.1073/pnas.1814522115
71. Stein S, Matter CM. CardioPulse: translational research in cardiovascular disease. *Eur Heart J.* (2016) 37:1088–95. doi: 10.1093/eurheartj/ehw025
72. Huang L, Hua Z, Xiao H, Cheng Y, Xu K, Gao Q, et al. CRISPR/Cas9-mediated ApoE-/- and LDLR-/- double gene knockout in pigs elevates serum LDL-C and TC levels. *Oncotarget.* (2017) 8:37751–60. doi: 10.18632/oncotarget.17154
73. Jarrett KE, Lee CM, Yeh YH, Hsu RH, Gupta R, Zhang M, et al. Somatic genome editing with CRISPR/Cas9 generates and corrects a metabolic disease. *Sci Rep.* (2017) 7:44624. doi: 10.1038/srep44624
74. Fang B, Ren X, Wang Y, Li Z, Zhao L, Zhang M, et al. Apolipoprotein E deficiency accelerates atherosclerosis development in miniature pigs. *Dis Model Mech.* (2018) 11:dmm036632. doi: 10.1242/dmm.036632
75. Lu R, Yuan T, Wang Y, Zhang T, Yuan Y, Wu D, et al. Spontaneous severe hypercholesterolemia and atherosclerosis lesions in rabbits with deficiency of low-density lipoprotein receptor (LDLR) on exon 7. *EBioMedicine.* (2018) 36:29–38. doi: 10.1016/j.ebiom.2018.09.020
76. Wang X, Huang R, Zhang L, Li S, Luo J, Gu Y, et al. A severe atherosclerosis mouse model on the resistant NOD background. *Dis Model Mech.* (2018) 11:dmm033852. doi: 10.1242/dmm.033852

**Conflict of Interest Statement:** The authors declare that the research was conducted in the absence of any commercial or financial relationships that could be construed as a potential conflict of interest.

frontiers
in Cardiovascular Medicine

ORIGINAL RESEARCH
published: 16 May 2019
doi: 10.3389/fcvm.2019.00056

# Olive Leaf Extract Attenuates Inflammatory Activation and DNA Damage in Human Arterial Endothelial Cells

**Blaž Burja[1,2], Tadeja Kuret[1,3], Tea Janko[4], Dijana Topalović[5], Lada Živković[5], Katjuša Mrak-Poljšak[1], Biljana Spremo-Potparević[5], Polona Žigon[1], Oliver Distler[2], Saša Čučnik[1,3], Snezna Sodin-Semrl[1,4], Katja Lakota[1,4*†] and Mojca Frank-Bertoncelj[2*†]**

[1] Department of Rheumatology, University Medical Centre, Ljubljana, Slovenia, [2] Department of Rheumatology, Center of Experimental Rheumatology, University Hospital Zurich, Zurich, Switzerland, [3] Chair of Clinical Biochemistry, Faculty of Pharmacy, University of Ljubljana, Ljubljana, Slovenia, [4] Faculty of Mathematics, Natural Science and Information Technology, University of Primorska, Koper, Slovenia, [5] Department of Pathobiology, Faculty of Pharmacy, University of Belgrade, Belgrade, Serbia

Olive leaf extract (OLE) is used in traditional medicine as a food supplement and as an over-the-counter drug for a variety of its effects, including anti-inflammatory and anti-atherosclerotic ones. Mechanisms through which OLE could modulate these pathways in human vasculature remain largely unknown. Serum amyloid A (SAA) plays a causal role in atherosclerosis and cardiovascular diseases and induces pro-inflammatory and pro-adhesive responses in human coronary artery endothelial cells (HCAEC). Within this study we explored whether OLE can attenuate SAA-driven responses in HCAEC. HCAEC were treated with SAA (1,000 nM) and/or OLE (0.5 and 1 mg/ml). The expression of adhesion molecules VCAM-1 and E-selectin, matrix metalloproteinases (MMP2 and MMP9) and microRNA 146a, let-7e, and let-7g (involved in the regulation of inflammation) was determined by qPCR. The amount of secreted IL-6, IL-8, MIF, and GRO-α in cell culture supernatants was quantified by ELISA. Phosphorylation of NF-κB was assessed by Western blot and DNA damage was measured using the COMET assay. OLE decreased significantly released protein levels of IL-6 and IL-8, as well as mRNA expression of E-selectin in SAA-stimulated HCAEC and reduced MMP2 levels in unstimulated cells. Phosphorylation of NF-κB (p65) was upregulated in the presence of SAA, with OLE significantly attenuating this SAA-induced effect. OLE stabilized SAA-induced upregulation of microRNA-146a and let-7e in HCAEC, suggesting that OLE could fine-tune the SAA-driven activity of NF-κB by changing the microRNA networks in HCAEC. SAA induced DNA damage and worsened the oxidative DNA damage in HCAEC, whereas OLE protected HCAEC from SAA- and $H_2O_2$-driven DNA damage. OLE significantly attenuated certain pro-inflammatory and pro-adhesive responses and decreased DNA damage in HCAEC upon stimulation with SAA. The reversal of SAA-driven endothelial activation by OLE might contribute to its anti-inflammatory and anti-atherogenic effects in HCAEC.

**Keywords: OLE, SAA, HCAEC, inflammation, atherosclerosis, microRNA, DNA damage**

**Edited by:**
*Kenneth Boheler,*
*Johns Hopkins University,*
*United States*

**Reviewed by:**
*Ellen Poon,*
*The University of Hong Kong,*
*Hong Kong*
*Praphulla C. Shukla,*
*Indian Institute of Technology*
*Kharagpur, India*

***Correspondence:**
*Katja Lakota*
*katja.lakota@guest.arnes.si*
*Mojca Frank-Bertoncelj*
*mojca.frank@usz.ch*

*† These authors have contributed equally to this work*

**Specialty section:**
*This article was submitted to Cardiovascular Biologics and Regenerative Medicine, a section of the journal Frontiers in Cardiovascular Medicine*

**Received:** *14 December 2018*
**Accepted:** *16 April 2019*
**Published:** *16 May 2019*

**Citation:**
*Burja B, Kuret T, Janko T, Topalović D, Živković L, Mrak-Poljšak K, Spremo-Potparević B, Žigon P, Distler O, Čučnik S, Sodin-Semrl S, Lakota K and Frank-Bertoncelj M (2019) Olive Leaf Extract Attenuates Inflammatory Activation and DNA Damage in Human Arterial Endothelial Cells. Front. Cardiovasc. Med. 6:56. doi: 10.3389/fcvm.2019.00056*

# INTRODUCTION

Cardiovascular diseases, including coronary artery disease, are the leading cause of death globally, with atherosclerosis being the most common underlying reason for cardiovascular morbidity and mortality. In addition, systemic inflammation (present in a number of chronic diseases, including metabolic syndrome and rheumatoid arthritis) drives accelerated atherosclerosis (1) and patients with these diseases are at risk for developing atherosclerosis and its complications. Serum amyloid A (SAA), a major acute phase protein, is increased in chronic inflammatory diseases and coronary artery disease (2, 3). SAA was shown to be an early causal agent for atherosclerosis in animal models (4, 5). Serum levels of SAA have been reported to correlate with severity of atherosclerosis (6, 7) and have been utilized as a predictor of mortality following acute myocardial infarction (8, 9). In addition, SAA was shown to enhance monocyte and lymphocyte recruitment, directly stimulating foam cell formation, associating with HDL/LDL particles and compromising reverse cholesterol transport, among other processes (7). Furthermore, SAA was reported to induce matrix metalloproteinases (MMP), as well as increase biglycan synthesis and influence retention of lipoproteins by vascular proteoglycans (10). Early on, Ridker reported that even chronic low grade inflammation may lead to atherosclerosis and the development of cardiovascular diseases (11), emphasizing the importance of measuring systemic inflammatory markers, such as SAA.

Atherosclerotic lesions typically develop in coronary arteries and the activation of endothelium represents one of the crucial early steps in the development of atherosclerotic lesions in the coronary arterial system. Human coronary artery endothelial cells (HCAEC) therefore represent a suitable *in vitro* model to study the mechanisms of endothelial activation and atherosclerosis. HCAEC strongly respond to stimulation with SAA, activating a number of pro-inflammatory, pro-adhesive and pro-coagulant responses, as measured by increased expression of interleukin 6 (IL-6), interleukin 8 (IL-8), vascular cell adhesion molecule (VCAM1) and tissue factor (12). Elevated amounts of systemic SAA in patients with coronary artery disease may represent a potential pathophysiological link between inflammation, lipoprotein metabolism, oxidative stress and the development of atherosclerosis (2). DNA damage is emerging as a crucial player in accelerating the development and progression of atherosclerosis. In addition to microRNAs, which are important regulators of cellular processes leading to atherosclerosis (13–15), DNA damage has been reported to be a biomarker of atherosclerosis in monocytes (16). There is a lack of information concerning whether DNA damage and alterations in microRNA networks accompany or contribute to the SAA-driven endothelial activation.

Olive oil represents the basis of atheroprotective effects of the Mediterranean diet, and olive leaf extract (OLE) contains a much higher concentration of active polyphenol compounds compared with extra virgin olive oil (17). OLE from the olive tree (*Olea europaea* L.) is used as a food supplement or as an over-the-counter drug for a variety of benefits including its anti-arrhythmic, anti-atherosclerotic (18), anti-hypertensive, antioxidant, anti-tumor, anti-proliferative, anti-inflammatory (19, 20), and anti-fibrotic (20, 21) effects. The 80% alcoholic extract of olive leaves has also been included in the European Pharmacopeia (Ph. Eur.) based on a subset of its protective properties (20). The polyphenols of the olive tree activated major anti-oxidant pathways, including transcription factor Nrf2, as well as AMPK, IGF/Akt, and mTOR, thereby acting similarly to caloric restriction mimickers (20).

Dry OLE is rich in water-soluble phenolic compounds, specifically secoiridoid oleuropein (17%), whereas the remaining compounds [apigenine-7-O-glucoside, luteolin-7-O-glucoside, quercetin, and caffeic acid] are present in substantially smaller amounts [<0.1%] (22). Secoiridoid oleuropein consists of a polyphenolic molecule known as hydroxytyrosol, bound to elenolic acid and a glucose molecule. OLE and its compounds can repress the expression of a number of pro-inflammatory genes. Specifically, oleuropein decreased the expression of IL-6 and IL-1β in colon during DSS-induced colitis (23) and in LPS-stimulated macrophages (Raw264.7) (24). Peripheral blood mononuclear cells (PBMC) from healthy individuals, who consumed OLE on a single occasion, expressed less IL-8 when stimulated *ex vivo* with LPS (25), and serum IL-8 levels decreased in hypertensive individuals who consumed OLE for 6 weeks (26). IL-8 was also one of the most downregulated genes in PBMC from healthy subjects who consumed OLE for 8 weeks. The major contributors to these effects were downregulation of the arachidonic acid and NF-κB pathways by OLE (27). The inflammatory molecules MCP-1, VCAM-1, and TNF-α were down-regulated in thoracic aorta of rabbits on a high lipid diet supplemented with OLE, as compared to a high lipid diet alone (18). Oleuropein and hydroxytyrosol, the constituents of OLE, inhibited the expression of both VCAM-1 and ICAM-1 in human umbilical vein endothelial cells, further accompanied by a decreased activation of NF-κB and AP-1 and reduced monocyte adhesion (28). These studies suggest that OLE could affect pro-inflammatory and pro-adhesive cellular responses during the atherosclerotic process in the arterial wall.

In our present work, we show that OLE significantly attenuated the SAA-driven pro-inflammatory and pro-adhesive responses of HCAEC and modulated SAA-induced miR-146a and let-7e. OLE decreased SAA-induced phosphorylation of NF-κB and protected endothelial cells from SAA-induced DNA damage. This suggests that OLE might exhibit multiple athero-protective effects in coronary arterial vasculature.

# MATERIALS AND METHODS

## Materials

Lyophilized human recombinant SAA (Peprotech EC Ltd., London, UK) was reconstituted according to manufacturer's instructions to stock concentration and stored until usage at −20 or −80°C. The final concentration of SAA in experiments was 1,000 nM. Dry OLE EFLA®943 (Frutarom Switzerland Ltd., Wadenswil, Switzerland) was originally manufactured by applying an ethanol extraction procedure (80% m/m) from the dried leaves of olive tree, standardized to 16–24% of oleuropein.

Dry OLE powder was diluted in phosphate buffered saline (PBS) to a final concentration of 0.1 g/ml, unless otherwise indicated.

## Cell Culture

HCAEC from four different donors were purchased from Lonza (Walkesville, Maryland, USA). The cells were plated onto 25 $cm^2$ flasks and 6 or 24 well-plates (TPP, Trasadigen, Switzerland) and cultured at 37°C in a humidified atmosphere at 5% $CO_2$. HCAEC were grown in EGM-2M medium (CambrexBioScience, Walkesville, Maryland, USA) containing 5% fetal bovine serum. For experiments, subconfluent cell cultures were used between passages 4 and 6 in serum-free medium, with pretreatment of OLE for 45 min, followed by addition of SAA for 24 h, unless otherwise indicated. Prior to experiments, cells were incubated in serum-free medium for 2 h.

## RNA Isolation and Reverse Transcription Polymerase Chain Reaction Analysis

Prior to reverse transcription polymerase chain reaction (RT-PCR), total RNA from endothelial cell cultures was isolated using Total RNA Isolation System RNeasyPlus Micro (Qiagen, Germany), following manufacturer's instructions. The purity and amount of RNA were determined by measuring the OD at a ratio of 260 to 280 nm. One microgram of total RNA was transcribed into cDNA by Reverse Transcription System (Promega, Madison, WI, USA). For microRNA measurements, 5 ng of total RNA was reverse-transcribed using the TaqMan®MicroRNA Reverse Transcription Kit and miRNA-specific RT primers (Applied Biosystems).

## Real Time PCR

The expression of mRNA was measured with real time PCR ABI Step One (Applied Biosystems, Foster City, CA, USA) using Kapa Sybr master mix (Sigma-Aldrich, Germany), forward and reverse primers (200 nM each) and 10 ng cDNA per well. Primer sequences and conditions for RT-PCR are indicated for each primer set in **Supplementary Table 1**. Dissociation curves showed one peak in each PCR reaction. All experiments were performed in triplicates. GAPDH was used as an endogenous normalization control. The gene expression results were calculated with the $2^{Ct\Delta\Delta}$ method. The expression of microRNAs was determined with real-time PCR (7900HT Fast real-time PCR system) using TaqMan®probes and TaqMan Universal PCR Master Mix (all Applied Biosystems, Life Technologies Foster City, CA, USA). RNU48 was used as an endogenous control. Differences in microRNA expression were calculated with the $2^{Ct\Delta\Delta}$ method.

## Western Blot

Whole cell lysates were prepared from HCAEC using RIPA buffer containing Halt protease inhibitors (Pierce, Rockford, IL, USA) and phosphatase inhibitors (Cayman Chemical, Ann Arbor, MI, USA). The concentration of proteins was determined with the Bradford assay and equal amounts of proteins were loaded per gel pocket. $\alpha$-tubulin was used as a loading control. Whole cell lysates, mixed with loading buffer, were separated on 10% SDS polyacrylamide gels and electroblotted onto nitrocellulose membranes (Whatman). Membranes were blocked for 1 h in 5 % (w/v) non-fat milk in TBS-T. After blocking, the membranes were probed with rabbit anti-phospho NF-κB p65 and rabbit anti-NF-κB p65 (S536 and E498, respectively, both at dilutions of 1:1000 Cell Signaling Technology, Danvers, MA, USA). As secondary antibodies, horseradish peroxidase-conjugated goat anti-rabbit (Cell Signaling Technology, Danvers, MA, USA) were used. Signals were detected using Femto Luminol (ThermoFisher Scientific, Hempstead, UK) with G:Box (Syngene, Cambridge,UK). Densitometry analysis of protein bands was carried out using the Fusion FX software (Vilber Lourmat). For quantification of Western blots, the levels of phosphorylated NF-κB were normalized to the levels of total NF-κB.

## Protein Detection by ELISA

Supernatants from untreated and treated HCAEC were spun down (300 g, 5 min) and cell-free supernatants frozen at −80°C until usage. The assays were performed using commercial ELISA kits and were done in duplicates, according to the manufacturers‘ instructions. IL-6 and IL-8 ELISA kits were purchased from Invitrogen (Frederick, MD, USA), while GROa and MIF quantikine ELISA were from R&D Systems (Minneapolis, USA). Absorbance was measured at 450 nm with the microplate absorbance reader (Tecan, Groening, Austria). The concentrations of analytes were calculated from standard curves and multiplied by the dilution factor.

## Comet Assay

HCAEC were grown in 6 well-plates. After treatment with SAA ± OLE, cells were detached using Acutasse (Sigma Aldrich) and spun down (5 min, 300 g). COMET was performed as previously described (29). Briefly, cells were resuspended in 0.067% low melting agarose (Sigma Aldrich) at $37^0$C and were layered onto slides using a coverslip. Cells from each 6 well were layered onto 4 slides and after cooling at $4^0$C for 10 min, coverslips were removed. Two slides were treated with 3% $H_2O_2$ at 37°C and rinsed with PBS. The remaining two slides were immediately covered with an additional layer of 0.05% low melting agarose and were placed (after cooling) into fresh alkaline lysis buffer overnight. The lysis buffer was prepared from 89 ml of stock solution containing 2.5M NaCl, 100 mM EDTA, 10 mM Tris-base at pH 10, 10 ml DMSO and 1 ml Triton-X. Slides were then immersed into cold, alkaline electrophoresis buffer (300 mM NaOH, 1 mM EDTA freshly prepared from stock 10 M NaOH and stock 200 mM EDTA, pH 10) for 30 min, after which electrophoresis was run (30 min, 25 V, 300 mA). This was followed by 2 repeated rinses for 10 min with neutralization buffer (0.32 M Tris base at pH 7.5) and water. Slides were stained with Sybr Green I, and 100 cells per slide were scored under the fluorescence microscope (Nikon eclipse TE 300 and AxioImager Z1, Carl Zeiss, 400x magnification). The average of the duplicate slides was calculated and three biological replicates were performed per experimental condition (**Scheme 1**).

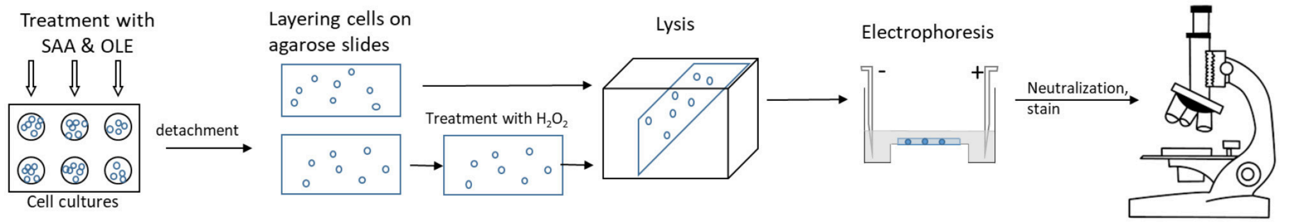

**SCHEME 1** | Scheme of COMET Analysis.

## Statistical Analysis

Data was presented as mean ± standard deviation (SD), unless otherwise indicated. The differences between the various treated and control groups were analyzed with RM one way ANOVA test with Tukey's method for multiple comparisons. All data was analyzed with the GraphPad Prism 7.0 software. A difference of $p < 0.05$ was considered statistically significant. DIANA-miRPath v3.0 software was used for assessment of miRNA regulatory roles and the identification of controlled pathways (30).

# RESULTS

## OLE Reduces the SAA-Driven Release of Pro-Inflammatory Cytokines and Chemokines From HCAEC

Treatment of HCAEC with OLE alone or in combination with SAA did not decrease the viability of HCAEC when compared to untreated cells (data not show). Inflammatory chemokines and cytokines play an important role in recruiting inflammatory cells and sustaining inflammation in chronic inflammatory diseases. To mimic the inflammatory milieu in the vasculature of patients with an activated systemic inflammatory response, we stimulated HCAEC with SAA (1000 nM or 12 mg/l). While high concentrations of SAA are commonly reached in the circulation of patients with infections, inflammatory and autoimmune diseases or trauma (31), chronically elevated low levels of SAA can already cause atherosclerosis (11). Stimulation of HCAEC with SAA significantly increased the release of IL-6, IL-8, and MIF (**Figures 1A,B**). Treatment with OLE reduced this SAA-induced release of IL-6 and IL-8 in a dose-dependent manner (**Figures 1A,B**). While 1 mg/ml OLE significantly decreased the release of IL-6 into supernatants of the SAA-stimulated HCAEC, the release of IL-8 returned to baseline levels. Additionally, similar effects of OLE were observed on the SAA-driven release of GROα, although significant changes were not observed (most probably due to large differences in the basal production of GROα in HCAEC). SAA-driven release of MIF was not affected (**Figures 1C,D**). Overall, this suggests that OLE can modulate the expression of a subset of the SAA-induced pro-inflammatory genes.

## OLE Alters the mRNA Expression of SAA-Induced E-Selectin in HCAEC

SAA significantly increased the expression of E-selectin mRNA in HCAEC, whereas VCAM-1 mRNA was up-regulated on average 4-fold above baseline with a notable variation between the donors (significance not reached) (**Figures 2A,B**). SAA-driven upregulation of E-selectin mRNA returned to baseline in the presence of OLE (**Figure 2B**). Moreover, OLE significantly down-regulated the constitutive expression of both E-selectin and VCAM-1 mRNAs (**Figures 2A,B**). While SAA strongly enhanced pro-inflammatory and pro-adhesive activities in HCAEC, it did not alter significantly the expression of MMP2, MMP9 and mRNAs (**Figures 2C,D**).

## SAA-Induced NF-κB Phosphorylation Is Reduced by OLE

The SAA-induced activation of gene expression coincided with the increase in the phosphorylation of NF-κB p65 (**Figure 3**). NF-κB is the central transcription factor in the expression of pro-inflammatory genes including those coding for cytokines, chemokines, and adhesion molecules (32). The SAA-increased phosphorylation of NF-κB was decreased in the presence of OLE (**Figure 3**). This shows that OLE could exert its anti-inflammatory and anti-adhesive effect also through modulation of NF-κB signaling.

## OLE Protects HCAEC From SAA-Induced and $H_2O_2$-Induced DNA Damage

Oxidative stress occurs when the formation of free radicals increases or when the antioxidant capacity of a cell is decreased, leading to DNA damage (33). COMET assay is a sensitive method to measure DNA damage in cells (34), where the relative amount of DNA in the COMET tail indicates the frequency of DNA breaks. Our results demonstrated that under basal conditions, on average 58% of HCAEC exhibited no COMET tails (condition A), whereas only 8% of the SAA-treated HCAEC were without COMET tails (**Figure 4A**). While 0.5 mg/ml OLE largely mimicked the background control in category A, a smaller percentage of cells, around 30%, exhibited no COMET tails when treated with 1 mg/ml OLE (**Figure 4A**). Nevertheless, the treatment with 0.5 mg/ml and 1 mg/ml OLE decreased DNA damage in the SAA-treated HCAEC, with 38% and 40% of HCAEC, respectively, exhibiting no DNA damage (no COMET tails) (**Figure 4A**). This data shows that SAA induces DNA damage in HCAEC, which can be largely prevented in the presence of OLE. Furthermore, OLE decreased the susceptibility of HCAEC to oxidative DNA damage, induced by treating the cells with 3% $H_2O_2$ (**Figure 4B**). Less than 10% of untreated cells and none of the SAA-stimulated cells were without COMET

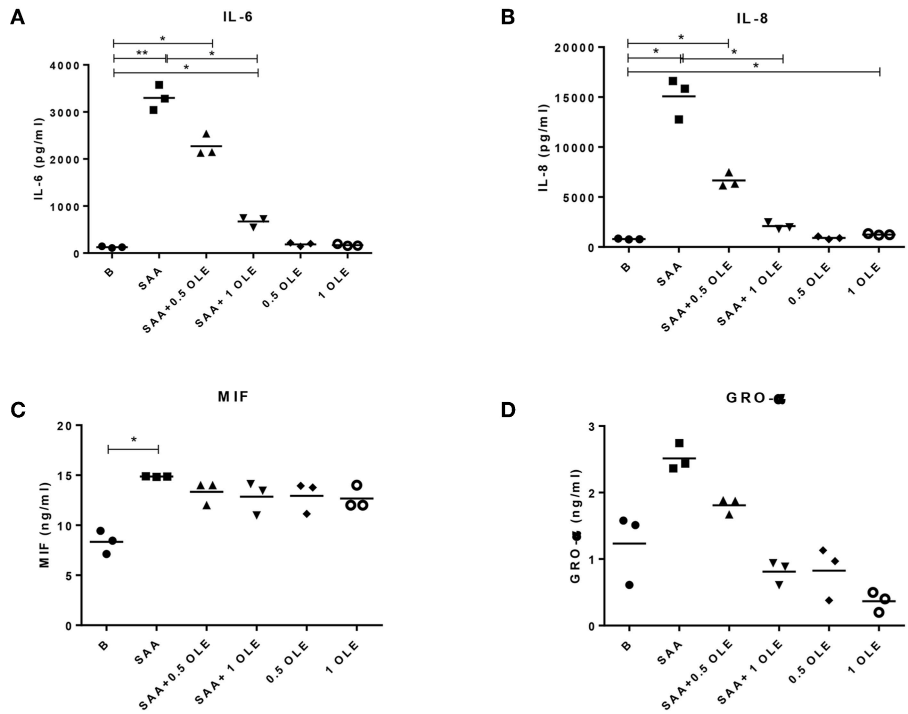

**FIGURE 1 |** OLE decreases SAA-driven release of pro-inflammatory cytokine IL-6 and chemokine IL-8 from HCAEC. The amount of IL-6 **(A)**, IL-8 **(B)**, MIF **(C)**, and GRO-α **(D)** in cell culture supernatants were measured by ELISA. The mean of 3 biological replicates is shown. HCAEC were treated with OLE (0.5 mg/ml, 1 mg/ml) 45 min prior to SAA addition (1,000 nM, 24 h). Data was analyzed using RM one-way ANOVA test with Tukey's multiple comparison test $^{*}p > 0.05$ $^{**}p > 0.01$.

tails (no DNA damage) upon exposure to $H_2O_2$, however the percentage of HCAEC without COMET tails increased upon treatment with OLE (**Figure 4B**). Furthermore, in presence of $H_2O_2$, 28% and 42% cells showed severe DNA damage (category E) in untreated and SAA-stimulated HCAEC, respectively. OLE alone or in the presence of SAA attenuated this damage (**Figure 4B**). Specifically, cells treated with OLE were evenly distributed in all categories, and the percentage of cells in category E was between 13 and 19% (**Figure 4B**). Collectively, treatment with OLE protected HCAEC from oxidative DNA damage, while the treatment of HCAEC with SAA worsened the oxidative DNA damage.

## Expression of the SAA-Induced miR-146a and Let-7e Is Altered by OLE

MicroRNA networks play a key role in regulating pro-inflammatory cell responses, as well as endothelial dysfunction. However, the expression and function of microRNAs during the SAA-driven endothelial activation remains largely unknown. Scarce evidence exists showing that OLE affects the microRNA profiles (35). To explore the alteration in microRNA networks during the SAA-driven endothelial activation, we measured the expression of miR-146a, let-7e, and let-7g with roles in inflammation (36) (**Figures 5A–C**). These measurements showed that SAA significantly increased the expression of miR-146a and OLE ameliorated the SAA-driven induction of miR-146a (**Figure 5A**) and let-7e (**Figure 5B**). The effects of SAA on the expression of let-7g (**Figure 5C**), however, were not changed from untreated HCAEC. Analysis of genes targeted with miR-146a and mirR-let-7e [using ≫Diana≪ tool mirPath v3 (30)] showed significant association with Toll like receptor signaling ($p =$ 0.005, n of genes targeted is 9), NF-kappa B signaling ($p =$ 0.009, number of genes targeted is 6, **Figure 5D**), ErbB signaling pathway ($p =$ 0.02, number of genes targeted is 7) and Cell cycle ($p =$ 0.03, number of genes targeted is 11) KEGG pathways (37).

## DISCUSSION

Our study provides novel data on the positive effects of olive leaf extract on the human coronary artery endothelium *ex vivo*. We show that OLE decreases levels of IL-6, IL-8 released protein and E-selectin mRNA in HCAEC in response to the endogenous inflammatory SAA, likely by reducing the SAA-driven phosphorylation of NF-κB p65. Furthermore, OLE changes the SAA-driven miR-146a and let-7e expression and decreases SAA-induced and $H_2O_2$-induced oxidative DNA damage in HCAEC, indicating protection at multiple levels. Using HCAEC *in vitro* cell culture model, we mimicked OLE's actions on the endothelial cell function. However, certain effects could be elucidated further only by using *in vivo* models or interventional human studies, e.g., the effects of OLE on the cholesterol/triglyceride profiles (18, 26).

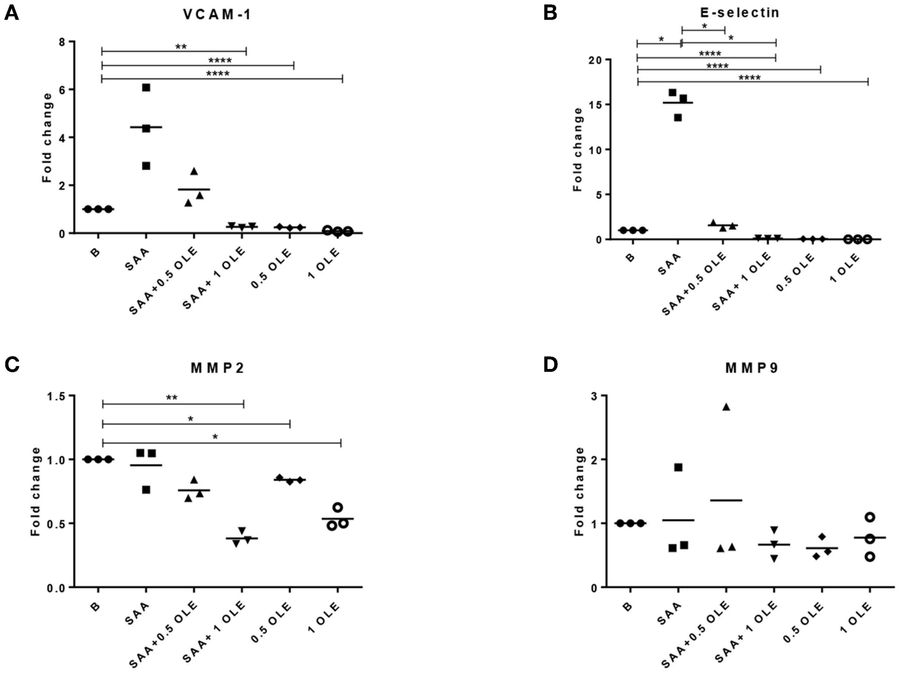

**FIGURE 2 |** OLE decreases mRNA expression of adhesion molecules and MMP2 in HCAEC. The expression of VCAM-1 **(A)**, E-selectin **(B)**, MMP2 **(C)**, and MMP9 **(D)** mRNA was determined by qPCR. Mean of 3 biological replicates is shown. HCAEC were treated with OLE (0.5 mg/ml, 1 mg/ml) 45 min prior to SAA addition (1,000 nM, 24 h). Data was analyzed using RM one way ANOVA test with Tukey's multiple comparison test *$p > 0.05$ **$p > 0.01$; ****$P < 0.0001$.

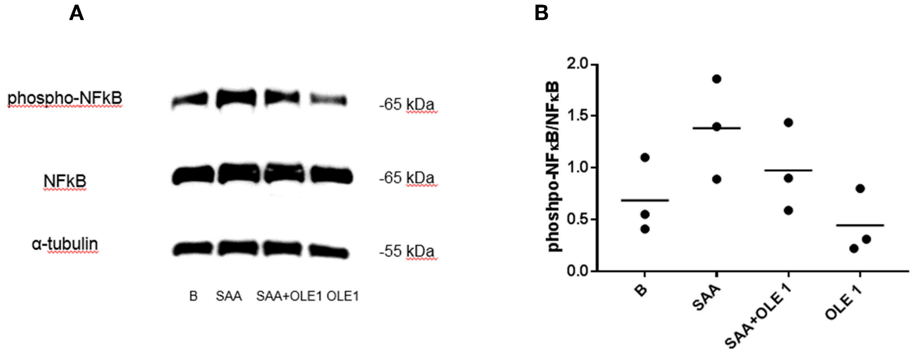

**FIGURE 3 |** OLE attenuates SAA-induced phosphorylation of NF-κB. **(A)** Western blot shows phosphorylation of NF-κB in HCAEC pretreated with OLE for 1 h and then treated with OLE ± SAA for 1 h (SAA 1,000 nM, OLE 1 mg/ml). Representative blot of $n = 3$ biological replicates. **(B)** Densitometry analysis of protein bands was carried out using the Fusion FX software (Vilber Lourmat), $n = 3$ biological replicates. For quantification of Western blots, the levels of phosphorylated NF-κB were normalized to the levels of total NF-κB. Equal amounts of protein were loaded per gel pocket. α-tubulin was used as a loading control.

Our results are in line with the human intervention study of olive leaf supplementation, which identified NF-κB as a central biological factor influenced by OLE (27). Similarly, a dietary intervention study showed that contrary to butter and walnut meals extra virgin olive oil did not elicit the phosphorylation of NF-κB in PBMC from healthy individuals (38). Moreover, OLE inhibited the phosphorylation of NF-κB and AP-1 in HUVEC and Raw264 macrophages (24, 28). Polyphenol compounds, such as oleuropein attenuated the phosphorylation of NF-κB in mouse models of ileum ischemia/reperfusion (39) and spinal cord injury (40). Overall, this suggests that active ingredients of OLE might have a therapeutic potential in regulating the activity of NF-κB.

We show that OLE decreases the SAA-induced release of IL-6 and attenuates the SAA-driven IL-8 and pro-adhesive E-selectin in HCAEC. Moreover, OLE decreased the basal expression of both pro-adhesive molecules, VCAM-1 and E-selectin, in HCAEC. All these molecules are critical effectors in the atherosclerosis process (41–44). The attenuation of pro-inflammatory responses causes a mediator-specific effect in

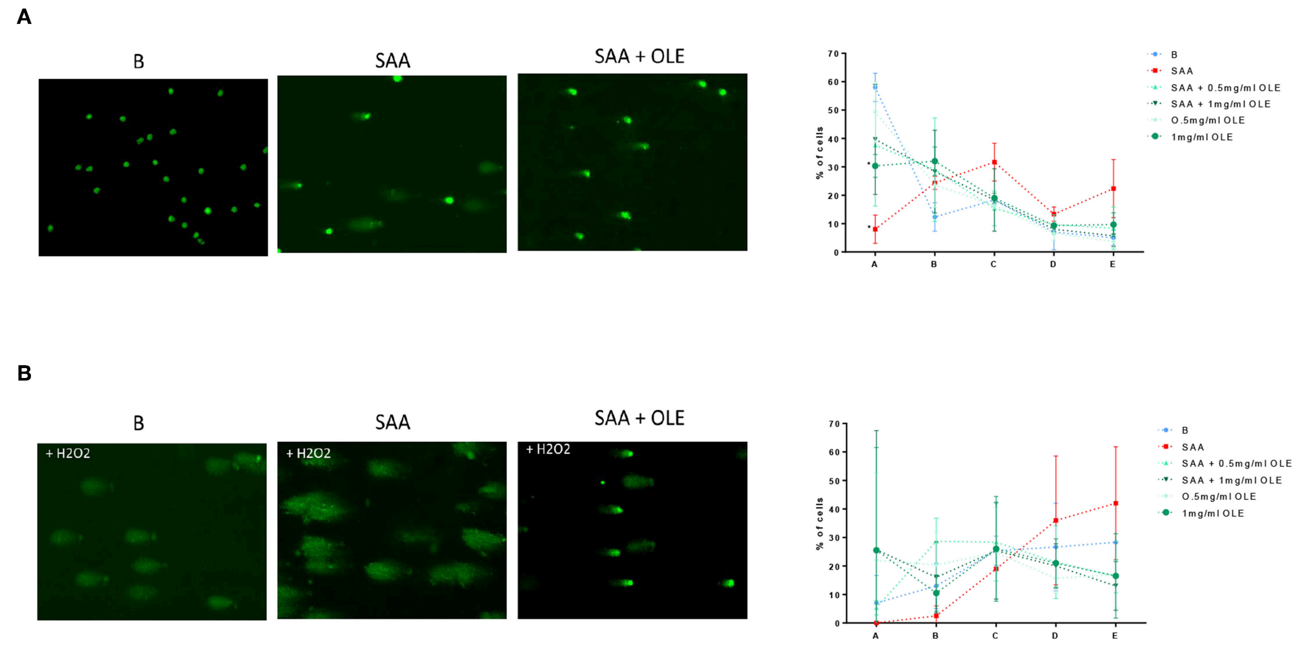

**FIGURE 4 |** OLE attenuates SAA-induced and $H_2O_2$-induced DNA damage in HCAEC. COMET assay was performed without **(A)** and with oxidative treatment (3% $H_2O_2$) **(B)**. Average from 3 biological replicates of the COMET assay for each experimental condition was performed on duplicate slides, 100 cells were evaluated per slide according to the following categories: A - no tail (no DNA damage), B - slight tail, C - strong signal in tail, but also in nucleus, D - majority of DNA in tail, E - no DNA in round nucleus.

HCAEC, since MIF released protein levels were not affected by OLE treatment. Our results are in line with the observed decrease in serum IL-8 in different human interventional studies upon OLE consumption (25–27) and the oleuropein-driven amelioration of IL-6 production in the LPS-induced Raw264 macrophages (24). Thus, OLE could have multiple beneficial effects via reducing the pro-inflammatory responses in different cell types participating in the atherosclerotic process. Additionally, oleuropein efficiently reduced the expression of VCAM-1 and E-selectin in HUVEC upon pro-inflammatory stimulation with LPS, TNF-α and PMA (28), when compared to other phytochemicals in the Mediterranean diet (e.g., elenolic acid and tyrosol in olive oil, resveratrol in wine). Healthy volunteers and subjects with hypertriglyceridemia who consumed extra virgin olive oil had significantly lower amounts of sICAM-1 and sVCAM-1 in comparison with subjects consuming refined olive oil, which contains no polyphenols and tocopherols (45). Nevertheless, the effects of dietary olive oil and extra virgin olive oil can partially be attributed to the incorporation of oleic acid or other fatty acids in cell membranes (46).

MMPs play an integral role in the atherosclerotic process via remodeling the extracellular matrix and regulating the migration of vascular smooth muscle cells. MMP2 and MMP9 decrease plaque stability and MMP2 appears to have a particular deleterious/pro-atherogenic role (47). While SAA did not affect the expression of MMP2 and MMP9 mRNAs in our experiments, OLE decreased the expression of MMP2 in HCAEC under basal conditions. This suggests that OLE might have additional (SAA-independent) beneficial effects on the MMP2-driven atherosclerosis-associated remodeling of the vascular wall.

In addition to its anti-inflammatory and antiadhesive activities, oleuropein acts as a potent free radical scavenger that suppresses the production of reactive oxygen species in different experimental systems including $H_2O_2$-induced cell damage (19, 29). Here, we report a novel observation that SAA (at 1,000 nM) induces DNA damage in HCAEC and increases the sensitivity of HCAEC to oxidative DNA damage. These SAA-driven effects were largely prevented in the presence of OLE. Importantly, OLE also reduced the $H_2O_2$-driven oxidative damage in the absence of SAA (**Figure 4**). The COMET assay we have utilized in this report is increasingly used in regulatory genotoxicity testing for the evaluation of DNA damage and repair in various tissues (48). It is one of a few assays that tests for both single stranded and double stranded DNA breaks, as opposed to γ-2HAX, which detects only dsDNA breaks. The COMET assay has become a well-established and well-accepted molecular technique in human biomonitoring and in clinical studies (49, 50). Moreover, COMET is one of the measuring techniques of European Standards Committee on Oxidative DNA Damage (ESCODD) (51). There are also several advantages of using the COMET assay, namely, the assay can be calibrated to give quantitative measures (52), it is a sensitive test (53), which is cost-effective and is becoming easier to perform, with the development of the high through-put Comet-Chip (54). More recently, an EpiComet-Chip was developed and validated for the assessment of DNA methylation status (55). There appear to be opposing activities of SAA, namely

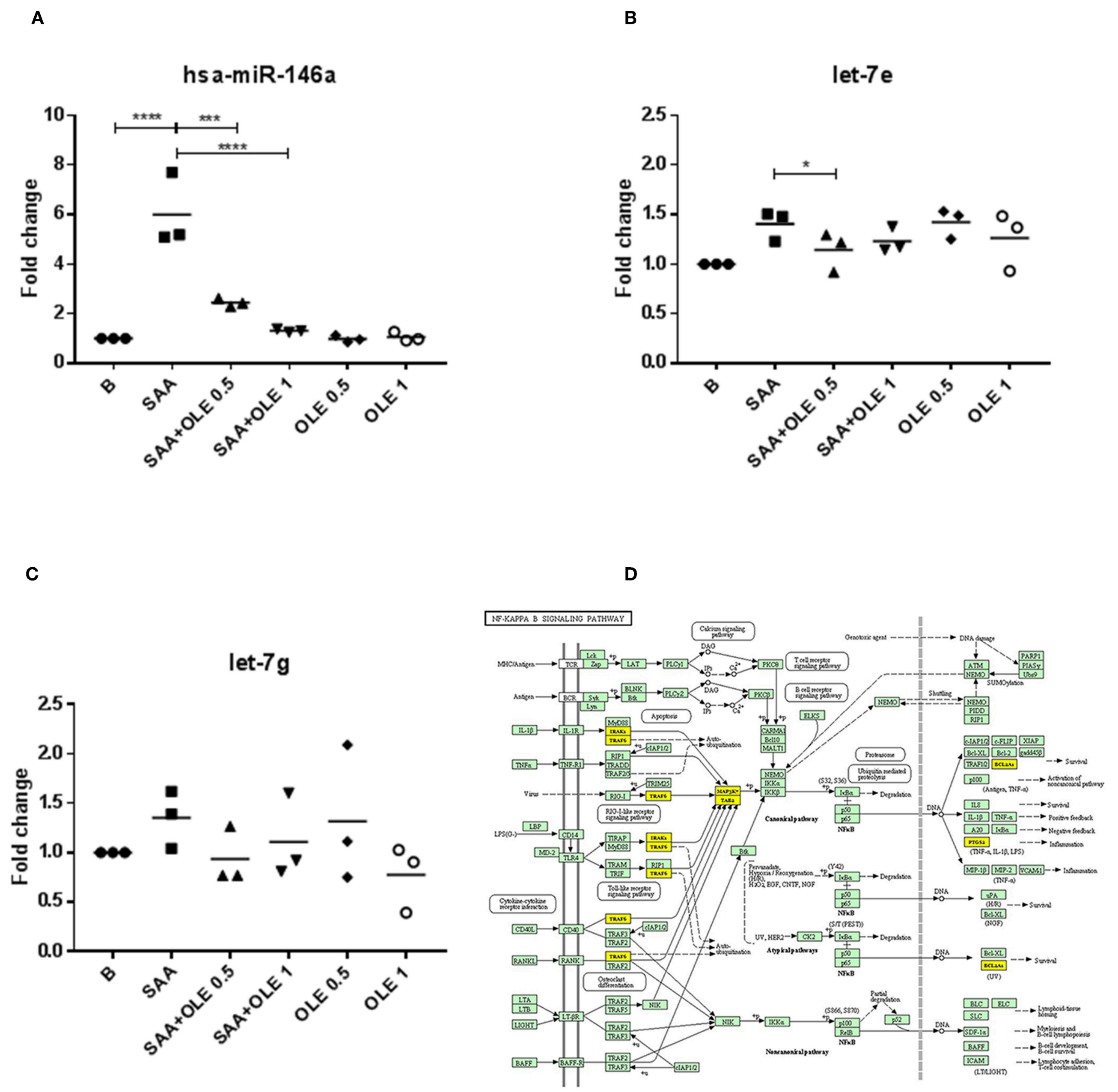

**FIGURE 5 |** OLE regulates SAA-induced miR-146a and let-7e. **(A–C)** represent fold changes of mRNA expression levels of miR-146a, let-7e and let-7g, respectively. The mean is shown of 3 biological replicates. Data was analyzed using RM one way ANOVA test with Tukey's multiple comparison test *p*-values are shown as follows $^{*}p > 0.05$, $^{***}P < 0.001$, $^{****}P < 0.0001$. **(D)** miR-146 and let-7e functional analysis showed significant influence on KEGG NF-κB signaling pathway ($p = 0.009$) (37) with 6 predicted target genes (marked yellow).

substantial DNA damage induction vs. slightly increased or stable viability (56, 57). This could be due to, on the one hand, SAA inflammatory events causing DNA damage in HCAEC, while on the other hand, viability might reflect the implication of elevated SAA in multiple types of cancers (e.g., esophageal squamous cell, ovarian, breast, lung, renal, and gastric) with increasing levels correlating with severity of cancer stages (58). The question then emerges whether SAA downregulates expression of genes, such as p53, thus elevating cell survival and cell cycle progression, which could be addressed in the future.

At the microRNA level, we show that SAA increases the expression of microRNA146a and let-7e in HCAEC, while OLE significantly attenuates these SAA-induced effects. The activation of NF-κB induces the expression of microRNA-146a, which acts as a negative feedback regulator of NF-κB via targeting TRAF6 and IRAK1/2. This controls the NF-κB transcriptional activity in the presence of excessive pro-inflammatory stimulation (36). Contrary to microRNA-146a, let-7e promotes the activation of NF-κB by inhibiting the expression of IκB β in endothelial cells (59). Thus, OLE could fine-tune SAA-driven activity of NF-κB by altering cellular microRNA networks (60).

In regard to the DIANA-miRPath v3 data (30) combining target prediction algorithms, with manually curated miRNA:gene interaction datasets to chart miR-146a and let-7e targets, the following genes and their involvement in processes most likely to be affected are, among others: TLR2 pathway (TLR2, TAB2, AKT2, JUN, TRAF6, STAT1, IRF7, IRAK1, MAP3K7), NF-κB pathway (TAB2, TRAF6, PTGS2, BCL2A1, IRAK1, MAP3K7), ErbB pathway (GSK3B, EGFR, STAT5B, AKT2, JUN, CDKN1A, ABL1) and cell cycle (GSK3B, CCNB1,CDC25B, SMAD4, RBL1, CDC23, CDKN1A, PRKDC, MDM2, ABL1, CDC25A). Among these genes, several are implicated in survival (BCL2A1, EGFR, STAT5B), ubiquitin-mediated proteolysis (TAB, TRAF6, IRAK1, MAP3K7, CDC23), anti-viral effects (IRF7), metabolism (AKT2, GSK3B). Interestingly, the cell cycle genes included both promoting (e.g., CDC23, CDC25A), as well as regulating (e.g., CDKN1A, CCNB1) genes of the cell cycle. In cells in general, it would be interesting to determine whether SAA downregulates PRKDC (elevating p53) and/or upregulates MDM2 (attenuating p53). While *in silico* analysis tools and applications, such as miRPath provide support to research, *in vitro* experimentation will further be necessary to confirm specific gene involvement.

Possible mechanisms of SAA activity could include changes in gene expression of pro-inflammatory cytokines, epigenetic events (e.g., miRNA-related), as well as induced reactive oxygen, nitrogen species, which may, in turn cause damage to cellular components (e.g., DNA), leading to chronic acceleration of chronic vascular disease, with OLE providing a counterbalance to these processes. In line with this, our data suggests that OLE exhibits multiple protective actions that could prevent or attenuate pro-inflammatory activation, influence vascular remodeling via modulation of MMP2 expression and may prevent DNA damage in the coronary arterial endothelium. This suggests that olive leaf extract, or its derivatives, might have athero-protective actions also *in vivo*, which would need to be further explored in the future.

## AUTHOR CONTRIBUTIONS

BB, KL, and MF-B designed the experiments, acquired, and analyzed the data, and wrote the manuscript. KL, BB, TK, TJ, KM-P, DT, and PŽ performed the experiments. DT, LŽ, and BS-P obtained OLE and advice on COMET. SS-S, SČ and OD coordinated the study. All authors participated in critical discussion of the data and drafting the manuscript. All authors have seen and approved the manuscript and its contents and are aware of the responsibilities connected to authorship.

## FUNDING

The study was supported by the Slovenian Research Agency ARRS with the bilateral project BU-RS/16-17-019, the National Research Program #P3-0314 and Be The Cure (BTCure).

## ACKNOWLEDGMENTS

The authors would like to thank A. Zupanic and S. Hernandez for assistance in editing this manuscript.

## SUPPLEMENTARY MATERIAL

The Supplementary Material for this article can be found online at: https://www.frontiersin.org/articles/10.3389/fcvm.2019.00056/full#supplementary-material

## REFERENCES

1. Lakota K, Artenjak A, Cučnik S, Brguljan J, Cegovnik B, Salobir B, et al. Atherogenesis, inflammation and autoimmunity - an overiew. In: Parthasarathy S, editor. *Atherogenesis.* Rijeka: InTech (2012). p. 187–202.
2. Hua S, Song C, Geczy CL, Freedman SB, Witting PK. A role for acute-phase serum amyloid A and high-density lipoprotein in oxidative stress, endothelial dysfunction and atherosclerosis. *Redox Rep*. (2009) 14:187–96. doi: 10.1179/135100009X12525712409490
3. Obici L, Raimondi S, Lavatelli F, Bellotti V, Merlini G. Susceptibility to AA amyloidosis in rheumatic diseases: a critical overview. *Arthritis Rheum*. (2009) 61:1435–40. doi: 10.1002/art.24735
4. Krishack PA, Bhanvadia CV, Lukens J, Sontag TJ, De Beer MC, Getz GS, et al. Serum amyloid A facilitates early lesion development in Ldlr-/- Mice. *J Am Heart Assoc.* (2015) 4:e001858. doi: 10.1161/JAHA.115.001858
5. Getz GS, Krishack PA, Reardon CA. Serum amyloid A and atherosclerosis. *Curr Opin Lipidol*. (2016) 27:531–5. doi: 10.1097/MOL.0000000000000331
6. Mezaki T, Matsubara T, Hori T, Higuchi K, Nakamura A, Nakagawa I, et al. Plasma levels of soluble thrombomodulin, C-reactive protein, and serum amyloid A protein in the atherosclerotic coronary circulation. *Jpn Heart J*. (2003) 44:601–12. doi: 10.1536/jhj.44.601
7. Thompson JC, Jayne C, Thompson J, Wilson PG, Yoder MH, Webb N, et al. A brief elevation of serum amyloid A is sufficient to increase atherosclerosis. *J Lipid Res*. (2015) 56:286–93. doi: 10.1194/jlr.M054015
8. Johnson BD, Kip KE, Marroquin OC, Ridker PM, Kelsey SF, Shaw LJ, et al. Serum amyloid A as a predictor of coronary artery disease and cardiovascular outcome in women: the National Heart, Lung, and Blood Institute-Sponsored Women's Ischemia Syndrome Evaluation (WISE). *Circulation*. (2004) 109:726–32. doi: 10.1161/01.CIR.0000115516.54550.B1
9. Katayama T, Nakashima H, Takagi C, Honda Y, Suzuki S, Iwasaki Y, et al. Prognostic value of serum amyloid A protein in patients with acute myocardial infarction. *Circ J*. (2005) 69:1186–91. doi: 10.1253/circj.69.1186
10. Sack GH Jr. Serum amyloid A - a review. *Mol Med*. (2018) 24:46. doi: 10.1186/s10020-018-0047-0
11. Ridker PM. Inflammation, atherosclerosis, and cardiovascular risk: an epidemiologic view. *Blood Coagul Fibrinol.* (1999) 10 (Suppl 1):S9–12.
12. Lakota K, Mrak Poljšak K, Rozman B, Kveder T, Tomšič M, Sodin-Šemrl S. Serum amyloid A activation of inflammatory and adhesion molecules in

human coronary artery and umbilical vein endothelial cells. *Eur J Inflam*. (2007) 5:73–81. doi: 10.1177/1721727X0700500203

13. Cervelli T, Borghini A, Galli A, Andreassi MG. DNA damage and repair in atherosclerosis: current insights and future perspectives. *Int J Mol Sci*. (2012) 13:16929–44. doi: 10.3390/ijms131216929
14. Zhang BK, Lai X, Jia SJ. Epigenetics in atherosclerosis: a clinical perspective. *Discov Med*. (2015) 19:73–80.
15. Khyzha N, Alizada A, Wilson MD, Fish JE. Epigenetics of atherosclerosis: emerging mechanisms and methods. *Trends Mol Med*. (2017) 23:332–47. doi: 10.1016/j.molmed.2017.02.004
16. Jacinto TA, Meireles GS, Dias AT, Aires R, Porto ML, Gava AL, et al. Increased ROS production and DNA damage in monocytes are biomarkers of aging and atherosclerosis. *Biol Res*. (2018) 51:33. doi: 10.1186/s40659-018-0182-7
17. Boss A, Bishop KS, Marlow G, Barnett MP, Ferguson LR. Evidence to support the anti-cancer effect of olive leaf extract and future directions. *Nutrients*. (2016) 8:E513. doi: 10.3390/nu8080513
18. Wang L, Geng C, Jiang L, Gong D, Liu D, Yoshimura H, et al. The anti-atherosclerotic effect of olive leaf extract is related to suppressed inflammatory response in rabbits with experimental atherosclerosis. *Eur J Nutr*. (2008) 47:235–43. doi: 10.1007/s00394-008-0717-8
19. Hassen I, Casabianca H, Hosni K. Biological activities of the natural antioxidant oleuropein: exceeding the expectation – a mini-review. *J Funct Foods*. (2015) 18:926–40. doi: 10.1016/j.jff.2014.09.001
20. Rigacci S, Stefani M. Nutraceutical properties of olive oil polyphenols. An itinerary from cultured cells through animal models to humans. *Int J Mol Sci*. (2016) 17:E843. doi: 10.3390/ijms17060843
21. Kim SW, Hur W, Li TZ, Lee YK, Choi JE, Hong SW, et al. Oleuropein prevents the progression of steatohepatitis to hepatic fibrosis induced by a high-fat diet in mice. *Exp Mol Med*. (2014) 46:e92. doi: 10.1038/emm.2014.10
22. Dekanski D, Janicijeic-Hudomal S, Tadic V, Markovic G, Arsic I, Mitrovic D. Phytochemical analysis and gastroprotective activity of an olive leaf extract. *J. Serbian Chem. Soc.* (2009) 74:367. doi: 10.2298/JSC0904367D
23. Giner E, Recio MC, Rios JL, Giner RM. Oleuropein protects against dextran sodium sulfate-induced chronic colitis in mice. *J Nat Prod*. (2013) 76:1113–20. doi: 10.1021/np400175b
24. Ryu SJ, Choi HS, Yoon KY, Lee OH, Kim KJ, Lee BY. Oleuropein suppresses LPS-induced inflammatory responses in RAW 264.7 cell and zebrafish. *J Agric Food Chem*. (2015) 63:2098–05. doi: 10.1021/jf505894b
25. Lockyer S, Corona G, Yaqoob P, Spencer JP, Rowland I. Secoiridoids delivered as olive leaf extract induce acute improvements in human vascular function and reduction of an inflammatory cytokine: a randomised, double-blind, placebo-controlled, cross-over trial. *Br J Nutr*. (2015) 114:75–83. doi: 10.1017/S0007114515001269
26. Lockyer S, Rowland I, Spencer JPE, Yaqoob P, Stonehouse W. Impact of phenolic-rich olive leaf extract on blood pressure, plasma lipids and inflammatory markers: a randomised controlled trial. *Eur J Nutr*. (2017) 56:1421–32. doi: 10.1007/s00394-016-1188-y
27. Boss A, Kao CH, Murray PM, Marlow G, Barnett MP, Ferguson LR. Human intervention study to assess the effects of supplementation with olive leaf extract on peripheral blood mononuclear cell gene expression. *Int J Mol Sci*. (2016) 17:E2019. doi: 10.3390/ijms17122019
28. Carluccio MA, Siculella L, Ancora MA, Massaro M, Scoditti E, Storelli C, et al. Olive oil and red wine antioxidant polyphenols inhibit endothelial activation: antiatherogenic properties of Mediterranean diet phytochemicals. *Arterioscler Thromb Vasc Biol*. (2003) 23:622–9. doi: 10.1161/01.ATV.0000062884.69432.A0
29. Cabarkapa A, Zivkovic L, Zukovec D, Djelic N, Bajic V, Dekanski D, et al. Protective effect of dry olive leaf extract in adrenaline induced DNA damage evaluated using in vitro comet assay with human peripheral leukocytes. *Toxicol in vitro*. (2014) 28:451–6. doi: 10.1016/j.tiv.2013.12.014
30. Vlachos IS, Zagganas K, Paraskevopoulou MD, Georgakilas G, Karagkouni D, Vergoulis T, et al. DIANA-miRPath v3.0: deciphering microRNA function with experimental support. *Nucleic Acids Res*. (2015) 43:W460–6. doi: 10.1093/nar/gkv403
31. De Buck M, Gouwy M, Wang JM, Van Snick J, Opdenakker G, Struyf S, et al. Structure and expression of different serum amyloid a (saa) variants and their concentration-dependent functions during host insults. *Curr Med Chem*. (2016) 23:1725–55. doi: 10.2174/0929867323666160418114600
32. Pahl HL. Activators and target genes of Rel/NF-kappaB transcription factors. *Oncogene*. (1999) 18:6853–66. doi: 10.1038/sj.onc.1203239
33. Birben E, Sahiner UM, Sackesen C, Erzurum S, Kalayci O. Oxidative stress and antioxidant defense. *World Allergy Organ J*. (2012) 5:9–19. doi: 10.1097/WOX.0b013e3182439613
34. Liao W, Mcnutt MA, Zhu WG. The comet assay: a sensitive method for detecting DNA damage in individual cells. *Methods*. (2009) 48:46–53. doi: 10.1016/j.ymeth.2009.02.016
35. Tezcan G, Tunca B, Bekar A, Budak F, Sahin S, Cecener G, et al. Olea europaea leaf extract improves the treatment response of GBM stem cells by modulating miRNA expression. *Am J Cancer Res*. (2014) 4:572–90.
36. Tahamtan A, Teymoori-Rad M, Nakstad B, Salimi V. Anti-inflammatory MicroRNAs and their potential for inflammatory diseases treatment. *Front Immunol*. (2018) 9:1377. doi: 10.3389/fimmu.2018.01377
37. Kanehisa M, Furumichi M, Tanabe M, Sato Y, Morishima K. KEGG: new perspectives on genomes, pathways, diseases and drugs. *Nucleic Acids Res.* (2017) 45:D353–61. doi: 10.1093/nar/gkw1092
38. Bellido C, Lopez-Miranda J, Blanco-Colio LM, Perez-Martinez P, Muriana FJ, Martin-Ventura JL, et al. Butter and walnuts, but not olive oil, elicit postprandial activation of nuclear transcription factor kappaB in peripheral blood mononuclear cells from healthy men. *Am J Clin Nutr*. (2004) 80:1487–91. doi: 10.1093/ajcn/80.6.1487
39. Campolo M, Di Paola R, Impellizzeri D, Crupi R, Morittu VM, Procopio A, et al. Effects of a polyphenol present in olive oil, oleuropein aglycone, in a murine model of intestinal ischemia/reperfusion injury. *J Leukoc Biol*. (2013) 93:277–87. doi: 10.1189/jlb.0712317
40. Impellizzeri D, Esposito E, Mazzon E, Paterniti I, Di Paola R, Bramanti P, et al. The effects of a polyphenol present in olive oil, oleuropein aglycone, in an experimental model of spinal cord injury in mice. *Biochem Pharmacol*. (2012) 83:1413–26. doi: 10.1016/j.bcp.2012.02.001
41. Papadopoulou C, Corrigall V, Taylor PR, Poston RN. The role of the chemokines MCP-1, GRO-alpha, IL-8 and their receptors in the adhesion of monocytic cells to human atherosclerotic plaques. *Cytokine*. (2008) 43:181–6. doi: 10.1016/j.cyto.2008.05.009
42. Shaposhnik Z, Wang X, Lusis AJ. Arterial colony stimulating factor-1 influences atherosclerotic lesions by regulating monocyte migration and apoptosis. *J Lipid Res*. (2010) 51:1962–70. doi: 10.1194/jlr.M005215
43. Hartman J, Frishman WH. Inflammation and atherosclerosis: a review of the role of interleukin-6 in the development of atherosclerosis and the potential for targeted drug therapy. *Cardiol Rev*. (2014) 22:147–51. doi: 10.1097/CRD.0000000000000021
44. Tousoulis D, Oikonomou E, Economou EK, Crea F, Kaski JC. Inflammatory cytokines in atherosclerosis: current therapeutic approaches. *Eur Heart J*. (2016) 37:1723–32. doi: 10.1093/eurheartj/ehv759
45. Pacheco YM, Bemudez B, Lopez S, Abia R, Villar J, Muriana FJ. Minor compounds of olive oil have postprandial anti-inflammatory effects. *Br J Nutr*. (2007) 98:260–3. doi: 10.1017/S0007114507701666
46. Perez-Jimenez F, Ruano J, Perez-Martinez P, Lopez-Segura F, Lopez-Miranda J. The influence of olive oil on human health: not a question of fat alone. *Mol Nutr Food Res*. (2007) 51:1199–208. doi: 10.1002/mnfr.200600273
47. Vacek TP, Rehman S, Neamtu D, Yu S, Givimani S, Tyagi SC. Matrix metalloproteinases in atherosclerosis: role of nitric oxide, hydrogen sulfide, homocysteine, and polymorphisms. *Vasc Health Risk Manag*. (2015) 11:173–83. doi: 10.2147/VHRM.S68415
48. Rothfuss A, O'Donovan M, De Boeck M, Brault D, Czich A, Custer L, et al. Collaborative study on fifteen compounds in the rat-liver Comet assay. *Mutat Res*. (2010) 702:40–69. doi: 10.1016/j.mrgentox.2010.07.006
49. Langie SAS, Azqueta A, Collins AR. The comet assay: past, present, and future. *Front Genet*. (2015) 6:266. doi: 10.3389/fgene.2015.00266
50. Turagam MK, Vuddanda V, Verberkmoes N, Ohtsuka T, Akca F, Atkins D, et al. Epicardial left atrial appendage exclusion reduces blood pressure in patients with atrial fibrillation and hypertension. *J Am Coll Cardiol*. (2018) 72:1346–53. doi: 10.1016/j.jacc.2018.06.066
51. Lorenzo Y, Costa S, Collins AR, Azqueta A. The comet assay, DNA damage, DNA repair and cytotoxicity: hedgehogs are not always dead. *Mutagenesis*. (2013) 28:427–32. doi: 10.1093/mutage/get018

52. Azqueta A, Collins AR. The comet assay: a sensitive and quantitative method for analysis of DNA damage. In: Meyers RA, editor. *Encyclopedia of Analytical Chemistry: Applications, Theory and Instrumentation*. Chichester: John Wiley (2011). doi: 10.1002/9780470027318.a9192
53. Ge J, Chow DN, Fessler JL, Weingeist DM, Wood DK, Engelward BP. Micropatterned comet assay enables high throughput and sensitive DNA damage quantification. *Mutagenesis*. (2015) 30:11–9. doi: 10.1093/mutage/geu063
54. Weingeist DM, Ge J, Wood DK, Mutamba JT, Huang Q, Rowland EA, et al. Single-cell microarray enables high-throughput evaluation of DNA double-strand breaks and DNA repair inhibitors. *Cell Cycle*. (2013) 12:907–15. doi: 10.4161/cc.23880
55. Townsend TA, Parrish MC, Engelward BP, Manjanatha MG. The development and validation of EpiComet-Chip, a modified high-throughput comet assay for the assessment of DNA methylation status. *Environ Mol Mutagen*. (2017) 58:508–21. doi: 10.1002/em.22101
56. Filippin-Monteiro FB, De Oliveira EM, Sandri S, Knebel FH, Albuquerque RC, Campa A. Serum amyloid A is a growth factor for 3T3-L1 adipocytes, inhibits differentiation and promotes insulin resistance. *Int J Obes*. (2012) 36:1032–9. doi: 10.1038/ijo.2011.193
57. Yu N, Zhang S, Lu J, Li Y, Yi X, Tang L, et al. Serum amyloid A, an acute phase protein, stimulates proliferative and proinflammatory responses of keratinocytes. *Cell Prolif*. (2017) 50:e12320. doi: 10.1111/cpr.12320
58. Zhou J, Sheng J, Fan Y, Zhu X, Tao Q, He Y, et al. Association between serum amyloid A levels and cancers: a systematic review and meta-analysis. *Postgrad Med J*. (2018) 94:499–507. doi: 10.1136/postgradmedj-2018-136004
59. Lin Z, Ge J, Wang Z, Ren J, Wang X, Xiong H, et al. Let-7e modulates the inflammatory response in vascular endothelial cells through ceRNA crosstalk. *Sci Rep*. (2017) 7:42498. doi: 10.1038/srep42498
60. Vasa-Nicotera M, Chen H, Tucci P, Yang AL, Saintigny G, Menghini R, et al. miR-146a is modulated in human endothelial cell with aging. *Atherosclerosis*. (2011) 217:326–30. doi: 10.1016/j.atherosclerosis.2011.03.034

**Conflict of Interest Statement:** The authors declare that the research was conducted in the absence of any commercial or financial relationships that could be construed as a potential conflict of interest.

frontiers
in Cardiovascular Medicine

REVIEW
published: 16 May 2019
doi: 10.3389/fcvm.2019.00064

# Myocarditis in Humans and in Experimental Animal Models

*Przemysław Błyszczuk* [1,2]*

[1] *Department of Clinical Immunology, Jagiellonian University Medical College, Cracow, Poland,* [2] *Department of Rheumatology, Center of Experimental Rheumatology, University Hospital Zurich, Zurich, Switzerland*

Myocarditis is defined as an inflammation of the cardiac muscle. In humans, various infectious and non-infectious triggers induce myocarditis with a broad spectrum of histological presentations and clinical symptoms of the disease. Myocarditis often resolves spontaneously, but some patients develop heart failure and require organ transplantation. The need to understand cellular and molecular mechanisms of inflammatory heart diseases led to the development of mouse models for experimental myocarditis. It has been shown that pathogenic agents inducing myocarditis in humans can often trigger the disease in mice. Due to multiple etiologies of inflammatory heart diseases in humans, a number of different experimental approaches have been developed to induce myocarditis in mice. Accordingly, experimental myocarditis in mice can be induced by infection with cardiotropic agents, such as coxsackievirus B3 and protozoan parasite *Trypanosoma cruzi* or by activating autoimmune responses against heart-specific antigens. In certain models, myocarditis is followed by the phenotype of dilated cardiomyopathy and the end stage of heart failure. This review describes the most commonly used mouse models of experimental myocarditis with a focus on the role of the innate and adaptive immune systems in induction and progression of the disease. The review discusses also advantages and limitations of individual mouse models in the context of the clinical manifestation and the course of the disease in humans. Finally, animal-free alternatives in myocarditis research are outlined.

**Keywords: myocarditis, animal models, coxsackievirus B3, Chagas disease, heart-specific autoimmunity, experimental autoimmune myocarditis**

***Edited by:***
*JeanSébastien Silvestre,*
*Institut National de la Santé et de la Recherche Médicale (INSERM), France*

***Reviewed by:***
*Sophie Van Linthout,*
*Charité Medical University of Berlin, Germany*
*Christian Zuppinger,*
*Bern University Hospital, Switzerland*

***Correspondence:***
*Przemysław Błyszczuk*
*przemyslaw.blyszczuk@uj.edu.pl*

***Specialty section:***
*This article was submitted to Cardiovascular Biologics and Regenerative Medicine, a section of the journal Frontiers in Cardiovascular Medicine*

***Received:*** *20 December 2018*
***Accepted:*** *30 April 2019*
***Published:*** *16 May 2019*

***Citation:***
*Błyszczuk P (2019) Myocarditis in Humans and in Experimental Animal Models.*
*Front. Cardiovasc. Med. 6:64.*
*doi: 10.3389/fcvm.2019.00064*

## INTRODUCTION

The World Heart Federation estimated that about 400,000 persons die annually worldwide because of inflammatory heart diseases. Epidemiologic post-mortem studies identified myocarditis as an important cause of unexpected and sudden death. Myocarditis has been implicated in cardiac sudden deaths in young adults at the rate of 8.6–12% (1, 2). The occurrence of myocarditis in sudden death in children was reported at the rate of 17% (3). Considering cardiovascular death in children and young adults, myocarditis was a major cause in 10–42% cases (4).

Myocarditis is classified as an inflammatory disease of the heart muscle. Traditionally, myocarditis is diagnosed based on endomyocardial biopsies. According to the widely used "Dallas" criteria published in 1987, a diagnosis of active myocarditis requires the presence of inflammatory infiltrates of non-ischemic origin in myocardial tissue associated with necrosis and/or degeneration of adjacent cardiomyocytes. Presence of inflammatory infiltrates in the absence of apparent myocyte damage is classified as borderline myocarditis (5). The definition of myocarditis has been more recently enumerated by the ESC Working Group on Myocardial and Pericardial Diseases, which proposed abnormal number of inflammatory infiltrates in myocardial tissue as $\geq$14 leucocytes/mm$^2$ including up to 4 monocytes/mm$^2$ with the presence of $\geq$7 cells/mm$^2$ CD3-positive T lymphocytes (6). These criteria have become widely accepted. Beside this common histological feature of inflammatory condition of the heart, there is a high diversity observed in the disease cause, characteristic of inflammatory infiltrates, clinical symptoms, course of inflammation, and the prognosis.

# PATHOPHYSIOLOGY OF MYOCARDITIS IN HUMAN

## From Myocarditis to Dilated Cardiomyopathy

Patients with myocarditis, proven via biopsies, show 55–80% 5-year transplantation-free survival (7–10). Mortality is observed not only during the acute phase, but also during the follow up. Myocarditis is a progressive disease with two post-acute clinical scenarios. In the first scenario, resolution of the inflammation is followed by complete recovery associated with improved heart function. It has been reported that myocarditis resolves spontaneously in ∼40–60% of cases (11, 12). In the second scenario, the acute phase is followed by development of stable dilated cardiomyopathy (DCM). Follow-up clinical studies showed development of DCM pathology over a period of several years in 14–52% patients with histologically proven myocarditis (12). DCM is referred to as left ventricular dilation associated with systolic dysfunction in the absence of coronary artery disease. Histologically, DCM is manifested by the extensive replacement of cardiac muscle cells with fibrotic tissue and deposition of collagen (13, 14). DCM patients develop not only heart pump weakening, but also heart valve problems, blood clots, and arrhythmias leading to heart and secondary organ failures. DCM patients show transplantation-free survival at the rate of 50–60% over 5 years in children (15) and in adults (7, 16, 17), however improved medication can increase the survival rate up to 80% (16). Particularly high mortality has been reported for patients with DCM due to Chagas disease (17). DCM can be associated with inflammation of the myocardium. Co-occurrence of myocarditis and DCM is referred to as inflammatory DCM (iDCM) (6). In fact, 16–30% of patients with chronic DCM show immunohistochemical evidences of myocardial inflammation (15, 18). Cardiac deaths in the follow-up myocarditis cohort were predominantly associated with DCM characteristic including systolic dysfunction and left ventricular dilation (9). Accordingly, ventricular dilatation and systolic dysfunction are associated with worse prognosis for myocarditis patients (8).

### Disease Etiology

In Europe and North America myocarditis is often idiopathic. Infections with cardiotropic enteroviruses such as coxsackievirus B3 (CVB3) have been associated with the disease and considered as a causative agent. The prevalence of enteroviruses detected in cardiac biopsies of myocarditis patients was reported at the rate of 14–57% (19). Other viruses such as parvovirus B19, adenoviruses or herpesviruses have also been detected in biopsies of myocarditis patients (19). Over decades, a shift in detection of enterovirus and adenovirus to parvovirus B19 and herpesviruses has been observed. However, the causative role of detected viruses in myocarditis patients is not evident. For example, surprisingly high prevalence of parvovirus B19 has been detected in myocarditis patients, suggesting its pathogenic role in the disease (20). More recent data showed, however, a high prevalence of parvovirus B19 also in myocarditis-negative hearts (21). Thus, the causative or associative role of individual viral infections in pathogenesis of myocarditis is still under investigation. Furthermore, it also remains to be elucidated, whether the persistence of the viral genome in the myocardium influences the clinical outcomes. So far, clinical studies resulted rather in contradicting conclusions (8, 22). In Europe and North America, myocarditis is also diagnosed in patients with Lyme disease (borreliosis). The disease is caused by bacteria *Borrelia burgdorferi*, which is transmitted by the bite of an infected ticks. It is estimated that up to 10% of Lyme disease patients develop myocarditis (23).

In Latin America, infections with protozoan *Trypanosoma cruzi* (Chagas disease) are the most common cause of inflammatory heart disease (24). The etiology of Chagas disease is quite well-established. Bites of blood-sucking triatomines (called also kissing bugs) spread the infective forms of the parasite. In humans, trypanosomal infection triggers the disease with two clinically distinct phases. The acute phase lasts several weeks and is usually asymptomatic or is associated with fever and local swelling or skin lesion. 10–30 years later about one third of the infected individuals develop a chronic form of the disease primarily manifested by DCM or iDCM, but also by neurological and/or gastrointestinal track pathologies. The chronic phase of the Chagas disease is usually progressive, leading to permanent heart failure (25). Cardiac dysfunction due to myocarditis and iDCM represents the most frequent and the most severe clinical manifestation of Chagas disease, which is associated with poor prognosis and high mortality rates (24, 26).

Non-infectious causes of myocarditis include mainly systemic autoimmune diseases and certain medications (27). Myocarditis has been observed for example in systemic lupus erythematosus (28) and in myasthenia gravis (29) patients. Recently, numerous cases of fatal myocarditis have been reported in cancer patients shortly after starting treatment with immune checkpoint inhibitors (30, 31). Immune checkpoint inhibitors refer to a category of drugs (antibodies) targeting negative regulators of T cell response, such as cytotoxic T-lymphocyte associated protein-4 (CTLA-4), programmed cell death protein-1 (PD-1), and PD-1 ligand (PD-L1). It is considered that immune checkpoint inhibitors may activate heart-specific autoimmunity in predisposed individuals (32). Today, it is widely accepted that autoimmune mechanisms are involved in the development and/or progression of myocarditis (33). Clinical evidences suggest active autoimmune response in human myocarditis on both, cellular and humoral levels. Initially, the concept of heart-specific autoimmunity came from the observation of high titers of heart-specific autoantibodies in CVB3 infected individuals. Accordingly, 30% of patients with myocarditis and DCM develop high titers of heart-specific autoantibodies (34). Cardiac myosin heavy chain (MyHC) has been identified as the most prominent autoantigen for circulating heart autoantibodies in myocarditis and cardiomyopathy patients (35). In fact, the presence of anti-MyHC autoantibodies has been associated with worse left ventricular systolic function and diastolic stiffness in patients with chronic myocarditis (36). There are strong indications that also antigen-presenting cells play an important role in the pathogenesis of myocarditis in humans by promoting autoimmune mechanisms. For example, histological analysis demonstrated increased levels of major histocompatibility complex (MHC) class I and II, known as human leukocyte antigen (HLA) complexes (37) and co-stimulatory molecules B7-1, B7-2, and CD40 (38) in hearts of myocarditis patients. More recent data pointed also to the importance of the humoral response in myocarditis (39).

## Clinical Assessment and Classifications of Myocarditis

### Diagnosis of Myocarditis

Clinical manifestation of myocarditis varies with a broad spectrum of symptoms, ranging from asymptomatic courses through shortness of breath, cardiac arrhythmias to chest pain resembling myocardial infarction (27, 40, 41). Myocarditis is often associated with left ventricular dysfunction (42), in some cases with cardiac arrhythmias (43) and elevated levels of certain biomarkers (6). These clinical symptoms are, however, not specific for myocarditis and the definitive diagnosis requires detection of inflammatory cells in the myocardium, typically on endomyocardial biopsy. In addition to histological analyses of cardiac biopsies, the assessment of myocarditis could be performed using a cardiac magnetic resonance imaging (44, 45). Improved imaging protocols confirmed usefulness of this modern, non-invasive technology in diagnosing myocarditis (46). Magnetic resonance imaging shows excellent diagnostic accuracy in patients with acute symptoms, while its usefulness is limited in patients with suspected chronic myocarditis (45, 47). On the one hand, histological evaluation of myocardial biopsies still represents a "gold standard," mainly because it allows not only to diagnose myocarditis, but also to identify infective agents and characterize the type of inflammatory cells. These data can be indicative for selection of the personalized treatment strategy and may be predictive for disease outcome (27, 40, 41, 48). In fact, endomyocardial biopsies confirm inflammation in 44–70% of patients with suspected myocarditis (49–51). On the other hand, due to the often patchy pattern of inflammation in the heart, endomyocardial biopsies-based diagnosis of myocarditis yields rather low sensitivity (52–54). Biopsies guided by non-invasive molecular imaging and/or electroanatomic mapping could increase the success rate. It seems, however, that the actual prevalence of myocarditis possibly remains underestimated. It is noteworthy that, incidental inflammation of the myocardium evaluated in a clinicopathological study reported that any inflammatory cells were present in 18% and multifocal inflammation in 9% of total cardiac and non-cardiac deaths (55).

### Clinical Classifications of Myocarditis

In the clinic, myocarditis can be classified based on the causative, histological, and clinicopathological criteria, which are summarized in **Table 1**. The causative criteria define infectious agents (virus, protozoa, or bacteria) or non-infectious condition (autoimmune diseases, medications etc.) associated with myocarditis. Identification of the infectious agent or potential non-infectious trigger may be indicative not only for disease etiology, but also helps to choose the most effective therapeutic strategy for the affected patients. In addition to identification of the causative agent, histological and immunohistological analyses are performed to categorize myocarditis based on the presence, morphology and type of inflammatory infiltrates in the myocardium. Lymphocytic myocarditis characterized by extensive infiltration of lymphocytes and monocytes with signs of cardiomyocyte necrosis (active lymphocytic myocarditis) represents the most frequent type of myocarditis (10). Lymphocytic myocarditis is often observed in myocardium tested

**TABLE 1** | Clinical classifications of myocarditis.

| Causative criteria | Histological criteria | Clinicopathological criteria |
|---|---|---|
| **Virus:** coxsackievirus B3, adenoviruses or herpesviruses and other | **Active myocarditis:** cardiac inflammation with apparent cardiomyocyte necrosis | **Fulminant myocarditis:** sudden onset, severe heart failure, cardiogenic shock or life-threatening arrhythmias |
| **Protozoa:** *Trypanosoma cruzi* (Chagas disease) | **Borderline myocarditis:** cardiac inflammation without evident cardiomyocyte necrosis | **Acute myocarditis:** highly variable from asymptomatic to cardiogenic shock, ventricular dysfunction, may progress to dilated cardiomyopathy |
| **Bacteria:** *Borrelia burgdorferi* (Lyme disease) and other | **Lymphocytic myocarditis:** extensive infiltration of lymphocytes and monocytes | **Chronic active myocarditis:** variable clinical symptoms, ventricular dysfunction, relapses of clinical symptoms and chronic myocardial inflammation on histology |
| **Immune checkpoint inhibitors:** anti-CTLA-4, anti-PD-1 or anti-PD-L1 therapy | **Giant cell myocarditis:** multinucleated giant cells and lymphocytes on heart biopsies | **Chronic persistent myocarditis:** persistent histologic infiltrate with myocyte necrosis, chest pain or palpitation without ventricular dysfunction |
| **Systemic autoimmune diseases:** Systemic lupus erythematosus, myasthenia gravis and other | **Eosinophilic myocarditis:** eosinophil-rich infiltrates with extensive myocyte necrosis | |

positive for viral persistence. Less common forms of myocarditis represent giant cell myocarditis and eosinophilic myocarditis. Giant cell myocarditis is characterized by the presence of multinucleated giant cells and lymphocytes on heart biopsies. Presence of giant cells within non-caseating granulomas, usually associated with myocardial fibrosis is referred to as cardiac sarcoidosis (56). The characteristic feature of eosinophilic myocarditis is the presence of eosinophil-rich infiltrates in the myocardium and extensive myocyte necrosis, which is accompanied with elevated level of circulating eosinophils (57). Giant cell myocarditis and eosinophilic myocarditis are associated with particularly poor prognosis (57–60).

Combination of the histologic data and clinical course of the disease resulted in clinicopathologic classification of myocarditis (61). Parameters such as onset of the disease, initial clinical and histological presentation, disease course and cardiac dysfunction define acute, fulminant, chronic active and chronic persistent subtypes of myocarditis. Acute myocarditis represents the most common type of myocarditis, in which symptoms last typically for days or weeks and the acute phase is followed by spontaneous improvement or development of stable DCM (62). In patients with fulminant myocarditis disease progresses rapidly resulting in severe heart failure and cardiogenic shock with mortality rate of 30–40% during the acute phase (63, 64). Patients diagnosed with fulminant myocarditis surviving the acute phase have been instead suggested to have excellent long-term prognosis (65), although a recently published study demonstrated contradictive findings (66). In its chronic form, myocarditis is detected over a period of three or more months. Clinical and histologic relapses and development of ventricular dysfunction is characteristic for chronic active myocarditis, whereas chronic persistent myocarditis is characterized by persistent presence of inflammatory cells in the myocardium, but it is usually not associated with ventricular dysfunction.

## MOUSE MODELS OF EXPERIMENTAL MYOCARDITIS

The need to understand cellular and molecular mechanisms of inflammatory heart diseases led to development of animal models for experimental myocarditis. In general, these models can be categorized based on the causative agents into two major classes: infectious and non-infectious. In infectious models, pathogens associated with myocarditis in humans are used to induce cardiac inflammation in animals. CVB3 and *T. cruzi* represent two classical infectious pathogens used for induction of experimental myocarditis in mice. In non-infectious models, myocarditis is typically triggered by an autoimmune response against heart-specific antigens. A comparative summary of the selected models is presented in the **Table 2**.

### Viral Models of Experimental Myocarditis

#### Experimental Myocarditis Induced With CVB3

CVB3 has been implicated to the pathogenesis of myocarditis in humans and therefore this virus was used to induce experimental myocarditis in animals. Coxackieviruses belonging to the *Picornaviridae* family represent positive-sense single-stranded RNA enteroviruses. Coxsackieviruses are typically transmitted by the oral route and for replication require host cells. Unlike other serotypes, CVB3 efficiently infects and replicates in cardiomyocytes leading to their death through apoptosis (181) or necroptosis (182). Effective CVB3 replication has been demonstrated also in cardiac fibroblasts (183). CVB3 infection begins by coupling the virus with host-cell coxsackievirus and adenovirus receptor (CAR), and decay-accelerating factor (DAF). Additionally, recent data pointed to the relevance of NOD2 in CVB3 uptake (184). After entering into the cytoplasm, viral RNA is translated and then transcribed. The viral genome is further translated into viral structural proteins, which assemble with the positive-strand RNA viral genome forming the complete infectious virion (185). Infected cardiomyocytes become ultimately lysed, which results in release of cytosolic proteins and virus progeny. Active viral replication as well as latent viral persistence have been described in hearts of myocarditis patients (186).

The first successful myocarditis induction in mice using purified CVB3 (Nancy strain) was reported in 1974 (67). The Nancy strain of CVB3 is the most commonly used virus to induce myocarditis in mice until today. The virus was passaged *in vitro* in the host cells. Inoculation of purified, *in vitro*-passaged CVB3 resulted in high viral replication in hearts of host mice. This model is characterized by substantial cardiomyocyte necrosis, moderate inflammation, pancreatitis, and often high mortality during the acute phase of disease in BALB/c, A/J, and C57BL/6 mice (67–74). Poor survival rate of mice infected with *in vitro*-passaged CVB3 led to development of the heart-passaged CVB3 model of experimental myocarditis (83). In this model, hearts of mice infected with CVB3 were used for preparation of the infective pathogen. Such heart-passaged CVB3 containing not only the virus, but also cardiac myosin is inoculated into host animals. In this model, viral replication peaks around day 7 and the pathogen is cleared around day 14, post-infection. Infected mice develop acute myocarditis around day 10–14, which is characterized by massive infiltration of cardiac tissue with primarily cells of myeloid lineage accompanied by T (mainly $CD4^+$) and some B lymphocytes in various mouse strains including BALB/c, A/J, ABY/SnJ, and C57BL/6 (83–89). In this model myocarditis is associated with left ventricular dysfunction during the acute phase. In contrast to high mortality rate observed in *in vitro*-passaged CVB3 model, typically all mice infected with heart-passaged CVB3 survive.

Following the acute myocarditis phase, disease course strongly depends on the genetic background of infected mice. Susceptible BALB/c, ABY/SnJ, and A/J mice progress to a phenotype of iDCM, characterized by chronic myocarditis, myocardial fibrosis, and cardiomyopathy, which is observed at day 28 post-infection and later (83, 89, 90). Whereas, mice with C57BL/6 genetic background do not develop DCM/iDCM phenotype (83, 91, 92), unless they are additionally treated with lipopolysaccharide (LPS) (93, 94). Infection with CVB3 leads to impaired cardiac functionality at later stages, which develops independently of the fibrotic phenotype in the heart (92, 94).

**TABLE 2 |** Characteristics of commonly used mouse models of experimental myocarditis.

| Mouse model | Susceptible mouse strains | Histological characteristic | Clinicopathological characteristic | Advantages and limitations | References |
|---|---|---|---|---|---|
| *In vitro*-passaged CVB3 or EMCV ($10^3$-$10^5$ $TCID_{50}$ or PFU) | BALB/c, A/J, DBA-2, C57BL/6 (4-9 weeks old) | Active myocarditis | Acute myocarditis | (+) use of clinically relevant virus<br>(+) suitable to study CVB3 replication<br>(–) high mortality<br>(–) high biosafety standards required | (67–82) |
| Heart-passaged CVB3 ($10^3$-$5x10^5$ PFU) | BALB/c, A/J, C57BL/6 (4-9 weeks old) | Active lymphocytic myocarditis, fibrosis | Acute myocarditis (C57BL/6) and chronic active myocarditis (BALB/c, A/J) | (+) use of clinically relevant virus<br>(+) allows to study disease progression<br>(–) involvement of immune system in CVB3 clearance and autoimmunity<br>(–) high biosafety standards required | (83–94) |
| Reovirus or MAV-1 ($10^4$-$10^7$ PFU) | BALB/c, C57BL/6, Swiss (2-7 days old) | Active myocarditis | Acute myocarditis | (+) suitable to study viral replication<br>(+) unique model of pediatric myocarditis<br>(–) clinically irrelevant viruses<br>(–) non-standard methodologies required | (95–98) |
| *T. cruzi* infection (50 – $10^6$ trypomastigotes) | BALB/c, A/J, C57BL/6, DBA-2, C3H/He, Swiss (4-12 weeks old) | Active lymphocytic myocarditis, fibrosis | Chronic active myocarditis | (+) use of clinically relevant pathogen<br>(+) recapitulate course of Chagas disease<br>(–) pathogen strain-dependent variability<br>(–) long-term model | (99–133) |
| Immunization with α-MyHC or troponin I peptide and CFA | BALB/c, A/J, A.SW (6-8 weeks old) | Active/borderline lymphocytic or eosinophilic* myocarditis, fibrosis | Acute myocarditis progressing to DCM | (+) biosafe<br>(+) suitable to study transition from myocarditis to DCM<br>(–) non-physiological disease induction<br>(–) immunization with CFA | (134–163) |
| Delivery of bmDCs loaded with α-MyHC peptide | BALB/c (6-8 weeks old) | Borderline lymphocytic myocarditis | Acute myocarditis | (+) biosafe<br>(+) suitable to study dendritic cells<br>(–) non-physiological disease induction<br>(–) culture of bmDCs in FCS-rich medium | (145, 164, 165) |
| TCR-M transgenic mice | BALB/c (≥4 weeks old) | Active/borderline lymphocytic myocarditis | Chronic persistent myocarditis | (+) biosafe<br>(+) suitable to study pathophysiology of heart-specific T cells<br>(–) non-physiological disease induction<br>(–) lack of heart non-specific T cells | (166) |
| CMy-mOVA mice injected with OT-I $CD8^+$ effector T cells ($2.5 \times 10^4$-$3 \times 10^6$) | C57BL/6 (6-20 weeks old) | Active lymphocytic myocarditis | Fulminant myocarditis | (+) biosafe<br>(+) suitable to study T cell-mediated cytotoxicity against cardiomyocytes<br>(–) reactivity against non-cardiac antigen<br>(–) *in vitro* T cell activation | (167–170) |
| PD-1/PD-L1-deficiency | BALB/c, MRL (≥4 weeks old) | Active/borderline lymphocytic myocarditis | Fulminant myocarditis | (+) biosafe<br>(+) suitable to study side effects of anti-PD-1/PD-1L therapy<br>(–) multiorgan involvement<br>(–) high mortality | (171–175) |
| HLA-DQ8 transgenic mice | BALB/c, NOD (≥4 weeks old) | Active/borderline lymphocytic myocarditis | Fulminant myocarditis | (+) biosafe<br>(+) suitable to study cardiac antigen presentation<br>(–) human-mouse chimeric system<br>(–) high mortality | (176–180) |

*α-MyHC, myosin heavy chain α; bmDCs, bone marrow-derived dendritic cells; CFA, complete Freund's adjuvant; CMy-mOVA - cardiac myocyte restricted membrane-bound ovalbumin; CVB3, coxsackievirus B3; EMCV, encephalomyocarditis virus; FCS, fetal calf serum; HLA, human leukocyte antigen; MAV-1, murine adenovirus type 1; OT-I, major histocompatibility complex class I-restricted ovalbumin-specific; PD-1, programmed cell death protein-1; PD-L1, PD-1 ligand; PFU, plaque forming unit; $TCID_{50}$, 50% tissue culture infectious dose; TCR-M, T cell receptor (TCR) specific to α-MyHC. * in $Ifng^{-/-} Il17a^{-/-}$ BALB/c mice.*

Infection with CVB3 triggers the respective innate and adaptive immune responses. Synthesis of antiviral cytokines such as type I interferons (IFNs) represent the first line of the innate immune defense against CVB3 infection, which aims to inhibit viral replication. Accordingly, treatments with IFN-α or IFN-β were reported to effectively eliminate virus in CVB3 infected mice (75) as well as in myocarditis patients (187). Following CVB3 entry into the target cell, the virus can engage intracellular nucleotide binding and oligomerization domain (NOD)-like receptors (NLRs) and activate certain Toll-like receptors (TLRs) (188). Activation of TRIF-dependent TLR3 has been recognized to be crucial for antiviral type I IFN production (76, 77). Interestingly, activation of other NLR and TLR pathways exacerbate myocarditis in CVB3 infected mice through negative regulation of type I IFN and stimulation of proinflammatory cytokines (73, 74, 184).

The innate immune response is usually followed by the adaptive response against the infective virus. In CVB3-mediated experimental myocarditis, the protective role of the adaptive immune response has been well-established. Studies using immunodeficient mice showed that lack of T and B cells led to viral persistence and enhanced myocarditis upon CVB3 infection (189, 190). Interestingly, in the CVB3 myocarditis model CD4$^+$, but not CD8$^+$ T cells play a pivotal role in viral clearance and thus protect infected mice from persistent cardiac inflammation (191, 192), whilst CD8$^+$ T cells have been implicated mainly in the autoimmune response (191, 193). These paradoxical observations can be explained by the findings that CD4$^+$ T cell response recognizes infected, but not uninfected myocytes, while CD8$^+$ effector T cells react only to uninfected myocytes through recognition of cardiac myosin (193). Furthermore, natural killer (NK) (78) and NK T cells (79, 80) were also reported to play protective roles in CVB3-induced myocarditis.

As stated above, heart-specific autoimmunity has been implicated in the pathogenesis of viral myocarditis. Early data indeed pointed to the development of functional heart-specific autoimmune response in CVB3 infected mice (81). Detection of circulating autoantibodies represents a basic diagnostic assay indicating ongoing autoimmune disorder. Following CVB3 infection, high titers of heart-specific autoantibodies have been detected in host A/J and BALB/c mice (194, 195). Heart-specific autoantibodies are commonly detected also in myocarditis patients (196) pointing to similarity between mouse models and clinical scenario. Infection with CVB3 activates also cardiac myosin reactive CD4$^+$ T cells in mice (69). Data from experimental model provided evidences that cardiac myosin reactive cells functionally contribute to cardiac pathology during chronic stage of the disease in CVB3 infected BALB/c mice (197). Heart specific autoimmunity seems to be a consequence of significant release of cardiac peptides from cardiomyocytes lysed during cardiotropic infection or molecular mimicry (epitope cross-reactivity) between the virus and cardiac proteins. Cardiac autoantigens in the presence of certain co-stimulatory, so called "third signal" cytokines can trigger the effector response of autoreactive T lymphocytes. It has been suggested that proinflammatory cytokines, mainly TNFα and IL-1β, produced during the innate response against viral infection play critical role in induction of the effector autoimmune response (33). Thus, myocarditis is likely a result of not only immune response against the infective virus, but also a consequence of boosted heart-specific autoimmune response. It seems that viral infection primary triggers myocarditis, while autoimmune response contributes to disease progression. In summary, myocarditis and iDCM phenotypes following CVB3 infection is the result of interplay between immune responses against the virus and heart-specific autoimmunity. Published data indicate that CVB3 infectious myocarditis mouse models accurately recapitulate principles of the immune responses in humans.

### Experimental Myocarditis Induced With Other Viruses

CVB3 represents the most common, but not the only virus used for induction of experimental myocarditis in mice. Cardiac inflammation associated with cardiomyocyte necrosis can be also induced with encephalomyocarditis virus (EMCV) (82). EMCV, like CVB3, are positive single-stranded RNA viruses belonging to the *Picornaviridae* family, which induce necrotic myocarditis with the similar mechanism of action (198). Enteroviruses CVB3 and EMVC are used to induce myocarditis in ≥4 weeks old mice. Whereas, the murine adenovirus type 1 (MAV-1) and reovirus 8B have been used to establish the mouse model for pediatric myocarditis. Depending on the delivery route, MAV-1 induces lethal [intraperitoneal injection (95)] or non-lethal [intranasal infection (96)] myocarditis in newborn mice. Infection of newborn mice with reovirus 8B also induces acute viral myocarditis. In this model myocarditis is characterized by marked cardiomyocyte necrosis and mild inflammation leading to death of infected BALB/c (97), but not C57BL/6 (98) mice. In contrast to the CVB3 model, autoimmunity seems not to be involved in myocarditis progression in reovirus 8B infected mice (97). Myocarditis in children is a deadly disease, particularly for newborns and infants and viral infections have been suggested as important causative agents in these young patients (199, 200). In that respect, MAV-1 and reovirus B8 models could be useful to study pathophysiological mechanisms of the disease in children.

## Experimental Models of Chagas Heart Disease

Trypanosomal infection can cause myocarditis and iDCM in mouse organisms. Experimental Chagas heart disease has been successfully established in a number of mouse lines using various *T. cruzi* strains including Colombian, Tulahuen, CL Brener Brazil, the Y, and SylvioX10, but so far, no model has been generally accepted as the classical one. Pathogenic trypanosome strains were isolated from Chagastic patients, insect vectors, and animal reservoir (99). *Trypanosoma cruzi* is typically passaged in mice and bloodstream trypomastigotes (infective form of the parasite) are transferred into experimental animals by different delivery routes including intraperitoneal, intradermal, and oral transmission. Inbred strains BALB/c, C57BL/6, A/J, DBA-2, or C3H/He are often used as hosts, however many laboratories use outbred Swiss mice to induce experimental Chagas heart disease. Disease course, organ involvement and survival rate in different models are characterized by high variability and strongly depend on the *T. cruzi* strain, delivery route and genetic background of the recipient mice (99–105). An example of the high variability in mouse Chagastic model was demonstrated in the experiment with Swiss mice infected with different clones of the Colombian strain, which showed mouse mortality ranging from 0 to 100% depending on the clone (102). Apparently, interplay between the host, parasite genetics and environmental factors ultimately determine the outcome of a mouse infection with *T. cruzi*. Trypanosomal infection may lead to myocarditis development in recipient mice within 1–3 weeks post-infection (101, 102). In the chronic form, experimental Chagas heart disease is associated with progressive inflammation, iDCM phenotype and heart dysfunction. This phenotype is observed several months post-infection (100, 104, 106–110). It seems that chronic models recapitulate not only the end stage heart phenotype, but also the course of the disease observed in Chagastic patients.

During the acute phase of Chagas disease, trypomastigotes spread with the bloodstream throughout the body and enter into target cells, in which they differentiate into amastigotes and multiply causing death of the host cells. Infection of myeloid cells and cardiomyocytes represent two important check points for the progression of the disease. Myeloid cells, like macrophages and dendritic cells actively internalize parasites by phagocytosis. The innate immune response of macrophages and dendritic cells represent the first line of defense against the parasite involving TLR-dependent and TLR-independent mechanisms. Trypomastigote cell surface membrane glycosylphosphatidylinositol-anchored mucin-like glycoproteins and glycoinositolphospholipids as well as secreted Tc52 proteins activate innate immune cells through TLR2-, TLR4-, and TLR9-dependent mechanisms (111–113). The classical TLR-dependent response activates NF-κb and MAPK pathways leading to production of proinflammatory cytokines including TNFα and Th1 polarizing IL-12. Such responses are indeed observed during trypanosomal infections in mice (114, 115). Furthermore, in response to IFN-γ (produced by Th1 cells, but also by activated NK cells) and TNFα macrophages produce nitric oxide. This short-lived free radical effectively suppresses parasite replication and represents the primary defense mechanism during the acute phase of the infection (116). During the acute trypanosomal infection, Th1 polarization is facilitated also through TLR-independent innate mechanisms. For example, a cysteine protease cruzipain released by trypomastigote generates short-lived kinins, which stimulate IL-12 production through the bradykinin $B_2$ receptor on the host cells and subsequently induce the protective Th1 response in infected mice (117).

Furthermore, *T. cruzi* triggers a robust adaptive immune response in the infected mouse organism. Phenotypically, infected mice show accumulation of lymphocytes in the spleen and subcutaneous lymph nodes associated with thymus atrophy (118). Early reports demonstrated persistent, non-specific polyclonal activation of T and B cells with phenotypic hypergammaglobulinemia (119, 120). Indeed, *T. cruzi* components such as DNA or glycoproteins have been shown to non-specifically activate T and B cells (121, 122), whereas more recent data pointed to the key role of antigen-specific response during parasite infection in mouse and in human (123, 124, 201). Importantly, the adaptive immune response plays a crucial role in pathogen clearance. Depletion of $CD4^+$ or $CD8^+$ T cells leads to an increase in parasite burden and exacerbation of myocarditis (125). Similarly, B cells and trypanosoma-specific antibodies have been shown to protect infected mice from uncontrolled parasite replication (126–128). Furthermore, interplay between T and B cells is needed for the effective adaptive immune response against trypanosomal infection (127, 128).

During the acute phase of the disease, the immune response eventually eliminates most of the infective pathogens, but not all. It has been suggested that a certain degree of parasite persistence, particularly in cardiac tissue correlates with the development of DCM phenotype and heart failure. Trypanosomal reactivation is commonly observed under immunosuppressive conditions in mouse models (129) and in humans (202) supporting the concept of parasite persistence. In the clinical scenario, Chagastic patients are treated with one of two anti-parasitic medications, benznidazole or nifurtimox, which generate free radicals, killing *T. cruzi* pathogens. In the chronic model of experimental Chagas heart disease, elimination of the pathogen during post-acute phase with benznidazole was shown to prevent development of severe chronic DCM in infected mice (110, 130). These results indicate that chronic experimental model can recapitulate incomplete eradication of *T. cruzi* observed in Chagastic patients. It is important to note that effectiveness of the anti-parasitic treatment decreases as the disease progresses. Ultimately, treatment with benznidazole fails to improve cardiac clinical outcomes in Chagastic patients with established DCM (203).

Heart-specific autoimmunity has been suggested as another disease progressing factor in Chagas heart disease. Heart-specific T cells and high titers of heart-specific autoantibodies have been identified in experimental mouse models (131, 204) as well as in Chagastic patients (205). In *T. cruzi* infected mice, development of heart-specific autoimmunity is associated with the genetic background of the host organism. Prominent humoral and cellular anti-cardiac myosin responses develop in A/J and BALB/c, but not in C57BL/6 mice (132, 206). Such an anti-cardiac myosin autoimmune response was shown to be non-essential for development of the acute phase of myocarditis (133), but has been implicated in the progression of post-acute cardiomyopathy during chronic phase of experimental Chagas heart disease (132). In mouse model of Chagas disease, the adaptive immune response, which plays a crucial role in the host defense against the infecting parasite, seems to contribute also to disease progression.

## Mouse Models of Experimental Autoimmune Myocarditis

As presented above, clinical observations and experimental data from infectious models provide strong evidences for involvement of autoimmune mechanisms in the development and progression of myocarditis. In infectious models, T and B cells are primary involved in pathogen clearance. It is therefore practically impossible to uncouple the defense from autoimmune mechanisms using commonly available technologies. The need to understand contribution and molecular mechanisms of autoimmunity led to development of rodent models of experimental autoimmune myocarditis (EAM), in which myocarditis is induced by heart-reactive T cells in the absence of infectious pathogen.

In the context of autoimmune myocarditis, the question arises whether or not heart-specific T cells naturally occur in mouse and in human. In principle, vertebrates are protected from autoreactive T cells by the immune tolerance mechanisms.

In the thymus, central tolerance specifically eliminates newly developing T cells, recognizing body's own antigens in a process called "negative selection." In this process presentation of self-antigens by antigen-presenting medullary cells is essential for maintenance of a central tolerance. Surprisingly, α-isoform of MyHC (α-MyHC), unlike other cardiac proteins, is not expressed in cells implicated in T cell tolerance. This results in undisturbed development of α-MyHC-specific T cells and leads to their physiological presence in the periphery in mice and in human (207). Thus, α-MyHC represents the major cardiac self-antigen. In fact, many currently used EAM models take advantage of this and activate naturally existing α-MyHC-specific T cells in order to trigger autoimmune-mediated myocarditis. Data from experimental animal models clearly demonstrated that autoreactive $CD4^+$ T lymphocytes were able to trigger myocarditis and DCM.

### The "Classical" Model of Experimental Autoimmune Myocarditis

The first attempt to induce heart-specific autoimmunity in animals was reported in 1958 (208), but in 1987 Neu et al. published the basis for the currently most commonly used mouse model of EAM (134). In this publication, authors demonstrated that delivery of cardiac myosin together with the complete Freund's adjuvant (CFA) induced myocarditis with high prevalence and high titers of myosin autoantibodies in genetically predisposed mice (134). Currently, in this "classical" model of EAM susceptible mice are immunized with α-MyHC peptide together with CFA at day 0 and 7. Myocarditis in α-MyHC/CFA immunized mice is characterized by massive infiltration of mainly myeloid cells together with $CD4^+$ T cells and few B and $CD8^+$ T lymphocytes. Inflammation of cardiac tissue occurs typically 14–21 days after the first immunization. Resolution of the inflammation is followed by the progressive accumulation of fibrotic tissue in the myocardium, ventricular dilatation and impaired heart function in some mice (135–146). Thus, this model allows to study not only autoimmune mechanisms, but also transition from myocarditis to DCM phenotype. Of note, α-MyHC/CFA immunization of $Ifng^{-/-}Il17a^{-/-}$ mice results in myocarditis with extensive infiltration of eosinophils in the myocardium representing a unique model of eosinophilic myocarditis (147).

Published data point to a central role of $CD4^+$ T cells in the α-MyHC/CFA model. Depletion of $CD4^+$ T cells prevents induction of myocarditis and the adoptive transfer of purified $CD4^+$ T cells from immunized mice successfully transfers the disease into immunodeficient hosts (148, 149). A simple passive transfer of high-titer myosin autoantibodies failed to transfer myocarditis in the recipient mice (150), however monoclonal anti-myosin antibodies were shown to induce myocarditis in a predisposed mouse strain (151). $CD8^+$ T cells, instead, contribute mainly to myocarditis severity, but are not essential for disease induction (148). However, recent data showed that using the specific α-MyHC peptide for EAM induction, $CD8^+$ T cells were able to limited extends convey myocarditis (152).

Co-delivery of a strong adjuvant, such as CFA represents the second key element of EAM induction in the "classical" model. CFA contains heat-killed *Mycobacterium tuberculosis*, which can activate TLR2, TLR4, and TLR9 on host cells (209). Activation of TLRs on the innate immune cells triggers secretion of a broad range of cytokines. In the adaptive immune response, the "third signal" cytokines produced by dendritic cells program vitality and expansion potential of antigen-activated T lymphocytes (210). The "third signal" cytokines have been also shown to polarize differentiating T cells toward Th1, Th2, or Th17 lineages. The importance of the "third signal" cytokines in the development of EAM has been demonstrated in a number of studies. Genetic deletion or blockage of the "third signal" cytokine signaling, including TNF-α (153, 154), GM-CSF (155), IL-1 (156), IL-6 (157), or IL-23 (158) resulted in complete resistance or amelioration of EAM. It remains, however, unclear whether the acute response to adjuvant in mice reflects immune processes during myocarditis induction in humans.

Development of EAM is a multifactorial process, which depends not only on the presence of heart-specific T cells and TLR activation, but also strongly on genetic predisposition. α-MyHC/CFA immunization induces myocarditis in susceptible strains only. Mice on BALB/c, A/J or A.SW background are susceptible to EAM, while mice on C57BL/6 background are resistant (134, 159–161). From a practical point of view, the resistance to EAM of widely-used C57BL/6 strain limits use of numerous transgenic models without the need for back-crossing onto the susceptible background. Differences in MHC haplotypes (H-2) of susceptible and resistant strains have been suggested to determine susceptibility of mice to EAM (148, 162). However, differences in susceptibility of A.SW and B10.S mice, which share the same H-2 genes, pointed also to the importance of non-H-2 genes in EAM development (163). Summarizing, the "classical" EAM model offers a well-established, simple and safe method to study heart-specific autoimmunity and progression of cardiac inflammation to DCM phenotype, but is limited to few inbred strains only.

### Other Models of Experimental Autoimmune Myocarditis

The idea that activation of self-antigen presenting cells is critical for myocarditis induction led to development of "dendritic cell" EAM model. It has been demonstrated that myocarditis could be effectively induced by adoptive transfer of bone marrow-derived dendritic cells (bmDCs) loaded with α-MyHC peptide and activated with LPS - a major component of the outer membrane of Gram-negative bacteria and the anti-CD40 antibody. In the "dendritic cell" EAM model, adoptive transfer of activated α-MyHC-loaded bmDCs at days 0, 3 and 5 results in acute myocarditis at days 8–12 (145, 164, 165). In contrast to the "classical" model, mice receiving α-MyHC-loaded bmDCs develop moderate fibrosis on the follow up. However, additional administration of CFA significantly accelerates fibrosis and induces ventricular dilatation and heart dysfunction in this model (211).

The "classical" and the "dendritic cell" EAM models, both rely on activation of naturally existing α-MyHC-reactive $CD4^+$ T cells. Non-transgenic mice contain physiologically very low prevalence of α-MyHC-reactive T cells and TLRs stimulation with CFA or LPS is needed not only for polarization, but also for expansion of activated α-MyHC-reactive T helper cells. High prevalence of these autoreactive cells can be alternatively obtained by transgenic overexpression of T cell receptor (TCR) specific to α-MyHC (TCR-M). A consequence of the high number of circulating α-MyHC-reactive T cells in the TCR-M transgenic mice is spontaneous development of progressive myocarditis associated with ventricular wall thickening, but without evident systolic dysfunction (166). The TCR-M transgenic model is particularly useful to study pathogenesis of autoreactive T cells in the absence of exogenous TLR agonists.

In contrast to widely studied $CD4^+$ T cells, the role of $CD8^+$ T cells (known also as cytotoxic T lymphocytes) in heart-specific autoimmunity is less understood. Unlike $CD4^+$ T cells, $CD8^+$ T cells recognize antigens presented by MHC class I molecules and directly induce apoptosis of antigen presenting cells by secreting cytotoxins, such as perforins and granzymes. In order to develop $CD8^+$ T cell-dependent myocarditis model, transgenic mice (on C57BL/6 genetic background) expressing cardiomyocyte-restricted membrane-bound ovalbumin (OVA) were injected with *in vitro* expanded and polarized MHC class I-restricted, OVA-specific OT-I $CD8^+$ T cells. Adoptive transfer of high doses ($\geq 5 \times 10^5$) of effector OT-I $CD8^+$ T cells caused massive cardiomyocyte cell death associated with lymphocytic (both $CD4^+$ and $CD8^+$) and myeloid cell infiltration. Severe myocarditis caused death of affected mice 3–7 days post T cell transfer (167, 168). In this model, T cell polarizing factors, such as IL-12 (167) and T-bet (169) played a key role in disease pathogenesis. Disease severity in this model correlates with the number of injected lymphocytes. In contrast to high doses, low doses ($2.5 \times 10^4$) of effector OT-I $CD8^+$ T cells induce a transient and moderate myocarditis only (170). This model is particularly useful to study $CD8^+$ T cell-mediated cytotoxicity against cardiomyocytes. Reactivity against non-physiological antigen (OVA) seems to be, however, a major drawback of this method.

Under homeostatic conditions, effector functions of $CD4^+$ and $CD8^+$ T cells are controlled by regulatory T cells (Treg). Accordingly, adoptive transfer of Treg-depleted T cells induces multiorgan inflammation including fatal autoimmune myocarditis and high-titer anti-myosin autoantibodies in the recipient mice. Of note, inflamed myocardium displayed multinucleated inflammatory cells resembling giant cell myocarditis in humans (212).

Once T cells become activated, more regulatory mechanisms control their expansion and effector function. Immune checkpoint regulators, such as PD-1 represents an example of regulatory mechanisms. Mechanistically, PD-1-PD-1L signaling inhibits TCR signaling on activated T cells and thus suppresses autoimmune response. Accordingly, mice deficient of PD-1 or PD-1L spontaneously develop systemic or organ-specific inflammations. Progressive myocarditis, iDCM phenotype and heart failures have been described in PD-1- and PD-1L-deficient mice on BALB/c (171, 172) and MRL (173, 174) genetic backgrounds, although for BALB/c not in all housing conditions (175). In mice lacking PD-1, fatal myocarditis caused high mortality in particular on MRL genetic background. Cardiac inflammation in PD-1-deficient mice is entirely dependent on the adaptive immunity (autoimmunity) and could be transferred by splenocytes (171, 174). In mouse models, PD-1-PD-1L signaling protects from myocarditis mediated by $CD4^+$ T (175) and by $CD8^+$ T (170) cells. PD-1 deficiency results in myocarditis also in aged C57BL/6 mice, but these mice are characterized by multiorgan inflammation and represent rather a model of systemic lupus erythematosus (213). It seems that the use of PD-1- and PD-1L-deficient mice developing progressive myocarditis represents a suitable model to study mechanisms of cardiac side effects observed during anti-PD-1-PD-1L therapies in oncological patients.

Although α-MyHC represents a main cardioimmunogenic antigen, other cardiac proteins can also trigger heart-specific autoimmunity. Immunization of A/J mice with recombinant cardiac troponin I peptide together with CFA induces myocarditis, which is followed by myocardial fibrosis, ventricular dilatation, and impaired systolic function (214). Unlike α-MyHC, troponin I is expressed in medullary thymic epithelial cells (207). The occurrence of circulating troponin I-reactive T cells is, instead, a result of inefficient elimination of autoreactive T cells during the "negative selection." The "leakage" of autoreactive T cells into periphery is a physiological phenomenon and its degree depends on the affinity of the TCR to the antigen-presenting medullary cells. Clinical data show elevated levels of troponin I in around one third of myocarditis patients (215), but high titers of anti-troponin I antibodies were detected only in 7% of DCM patients (216). It seems that troponin I represents rather a secondary autoantigen in heart-specific autoimmunity in myocarditis patients.

Presentation of cardiac antigen represent another important element of autoimmunity. Clinical studies suggested that specific HLA haplotypes are associated with heart-specific autoimmunity. This idea was functionally confirmed by introducing specific HLA complexes into a mouse. Replacement of mouse MHC class II with the specific HLA-DQ8 in NOD or BALB/c mice resulted in spontaneous development of myocarditis and iDCM phenotype (without evident fibrosis), and were associated with cardiac arrhythmias and high mortality of the transgenic mice (176–180). This model resembles a course of fatal fulminant myocarditis in humans. Adoptive transfer experiments pointed to the key role of $CD4^+$ T cells in pathogenesis of the disease in this mouse model (178, 179). Interestingly, introduction of HLA-DR3 or HLA-DQ6 failed to induce cardiac pathology pointing the specific role of HLA-DQ8 in heart-specific autoimmunity (177, 178). The HLA-DQ8 transgenic mice seem to be particular useful to study mechanisms of cardiac antigen presentation and induction of heart-specific autoimmunity.

## A TRIPHASIC MODEL OF MYOCARDITIS

Taking together clinical observations as well as data from animal models, a triphasic model of myocarditis development and progression could be proposed (**Figure 1**). The initial phase

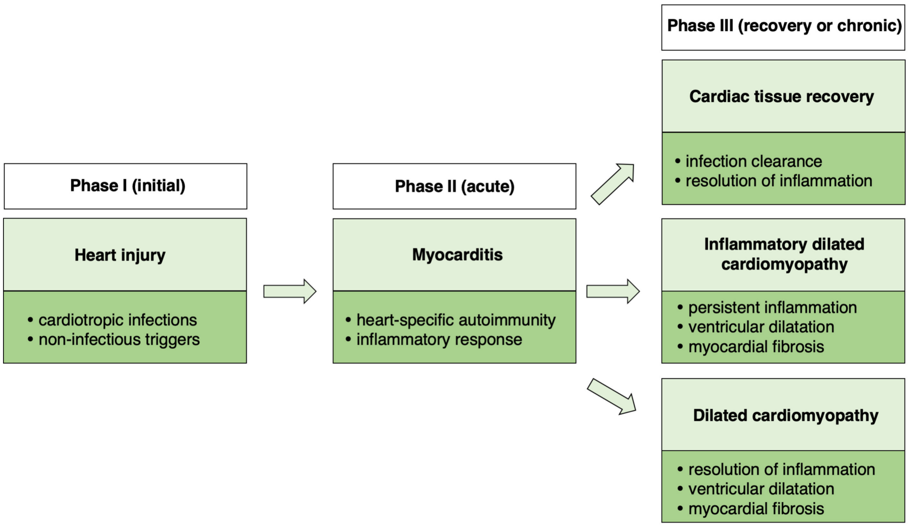

**FIGURE 1 |** Schematic presentation of a triphasic model of myocarditis.

is associated with heart injury, caused usually by cardiotropic infections or non-infectious triggers. Damaged myocardium induces primary inflammatory response and development of heart-specific autoimmunity, which results in the development of myocarditis. In certain cases, myocarditis can be directly induced by heart-specific autoimmunity. Cardiac inflammation can be transient or chronic. In the transient form, acute phase of myocarditis is followed by complete resolution of inflammation or development of stable DCM. In case of chronic myocarditis, many patients develop also DCM phenotype (iDCM). Cardiac dysfunction in DCM and in iDCM is in most cases progressive leading to end stage organ failure.

## WHICH MODEL OF EXPERIMENTAL MYOCARDITIS TO CHOOSE?

As presented above, a number of different animal models of myocarditis have been developed. Experimental myocarditis in mice can be induced with the whole spectrum of disease triggers ranging from clinically relevant agents, such as infective pathogens up to artificial models like transgenic animals. Depending on the model, myocarditis is characterized by different composition of inflammatory infiltrates and different extent of necrotic myocardium. In many models, DCM or iDCM phenotype associated with heart dysfunction represent the end stage of the disease. The question arises, which model reflects human myocarditis in the most relevant way. As myocarditis in humans shows high diversity in terms of causative agents, autoimmune response, course of inflammation, and progression to DCM/iDCM, it becomes evident that one animal model cannot mirror all aspects of the disease in humans.

For modeling of myocarditis with known etiology, as for example CVB3-mediated myocarditis or Chagas disease, use of the same infectious agent seems to be the most obvious choice. Infectious pathogens spread and induce myocarditis in mice and in humans using similar mechanisms, therefore these models are particularly useful to study early phase of disease. However, it is difficult to uncouple immune mechanisms involved in pathogen clearance and in autoimmune responses. Furthermore, handling the human infective pathogens is potentially dangerous for experimentators and requires exceptionally high biosafety standards.

In contrast, non-infectious models are safe for experimentators, but induce myocarditis in rather non-physiologic way. Nevertheless, lack of infectious agents allows to better study autoimmune mechanisms and involvement of the immune system to progression of myocarditis to DCM/iDCM phenotype. Summarizing, the usefulness of the respective mouse model is mostly limited to certain aspects of the disease in humans. It is therefore very important to address scientific question by choosing the relevant model.

## ALTERNATIVES FOR ANIMAL STUDIES IN MYOCARDITIS RESEARCH

In developed countries, public approval to conduct animal experimentations is today low as never before. Activists raise ethical concerns and appeal to minimize or even to stop performing experiments involving animals. Some of these postulates pointing to protocol optimization and to reduction of severity in animal experimentation are rational and have been already implemented in the form of 3R (replacement, reduction, and refinement) guidelines, but is there a realistic animal-free alternative in myocarditis research?

It seems that certain aspects of the disease, for example replication of cardiotropic pathogens, fibroblast-to-myofibroblast transition, endothelial cell activation, can be effectively addressed using conventional *ex vivo* or *in vitro* systems. These systems are suitable for molecular studies, but rather poorly reflect biomechanical and biochemical microenvironment of cardiac tissue. Dynamic development of three-dimensional cell culture methodologies, like organoids or microtissues represents a recent advancement, which can address some of these concerns. Furthermore, development of the human induced pluripotent stem cell (iPSC) technology represents another important milestone toward animal-free research. The use of human iPSC-derived cardiomyocytes in combination with other cell types allows today for a simplistic modeling of a human heart (217, 218). Furthermore, *de novo* tissue fabrication opens new possibilities to integrate bioscaffolds for improved architecture and microelectronics for live monitoring of cardiac tissue (219). These advances offer potentially very attractive replacements for animal models (220). However, generation of physiologically-relevant human cardiac tissue faces a number of serious problems, which include immature state of iPSC-derived cardiomyocytes, limited availability of non-cardiac primary cells (fibroblasts, endothelial cells) and high costs of *de novo* tissue fabrication. Moreover, in myocarditis active migration of inflammatory cells into the tissue plays a key role in the disease development. Currently, modeling of inflammatory response in terms of influx of inflammatory cells into cardiac tissue *in vitro* is not available.

Summarizing, it seems that the whole process of myocarditis is too complex to reproduce it outside of a body by using today's technologies. However, certain aspects of the disease can be reliably studied *in vitro* and upcoming advances may allow to reduce animal research in the future.

## CONCLUSIVE REMARKS

Animal models represent an important platform in preclinical research. As presented above, developed models of experimental myocarditis appear to reliably mirror many specific aspects of the disease in humans. Currently, these animal models are commonly used to get an insight into pathophysiology of myocarditis on molecular and cellular level and to test pharmaceutic compounds for treatment efficacy and safety. However, animal studies are commonly unicenter, involving mostly low group sizes and experiments are rarely reproduced by others. Furthermore, in some cases, published papers lack detailed description of used methodologies. Thus, the power of such exploratory studies is usually low.

In laboratory practice, typical large scale, multicenter animal studies are not possible due to ethical and economic reasons. It seems that synthetic research integrating data from independent studies is needed to increase the power of experimental findings. In this case, the use of the same or similar procedures is a basic prerequisite to analyse data from different laboratories. In the area of experimental myocarditis, some models show high reproducibility in terms of used protocols and obtained results. In particularly, published data by independent laboratories on disease course and severity of myocarditis induced in specific inbred strains by infection with CVB3 or by immunization with α-MyHC/CFA show high consistency. In contrast, other models like experimental Chagas disease show high variability due to inconsistencies in methodologies. The use of standardized procedures would allow to more effectively plan experimentations and more accurately interpret obtained data. Furthermore, the use of unified methodologies would be important to effectively share omics resources and to implement meta-analyses in animal research. Combined efforts are therefore needed to more efficiently use the potential of animal models in order to translate this knowledge into innovative, more effective treatment therapies.

## AUTHOR CONTRIBUTIONS

The author confirms being the sole contributor of this work and has approved it for publication.

## ACKNOWLEDGMENTS

This work has been supported by the National Science Centre (Poland) grants 2014/14/E/NZ5/00175 and 2016/21/B/NZ5/01397.

## REFERENCES

1. Fabre A, Sheppard MN. Sudden adult death syndrome and other non-ischaemic causes of sudden cardiac death. *Heart*. (2006) 92:316–20. doi: 10.1136/hrt.2004.045518
2. Doolan A, Langlois N, Semsarian C. Causes of sudden cardiac death in young Australians. *Med J Aust*. (2004) 180:110–2. doi: 10.5694/j.1326-5377.2004.tb05830.x
3. Noren GR, Staley NA, Bandt CM, Kaplan EL. Occurrence of myocarditis in sudden death in children. *J Forensic Sci*. (1977) 22:188–96. doi: 10.1520/JFS10385J
4. Basso C, Calabrese F, Corrado D, Thiene G. Postmortem diagnosis in sudden cardiac death victims: macroscopic, microscopic and molecular findings. *Cardiovasc Res*. (2001) 50:290–300. doi: 10.1016/S0008-6363(01)00261-9
5. Aretz HT, Billingham ME, Edwards WD, Factor SM, Fallon JT, Fenoglio JJ Jr, et al. Myocarditis. A histopathologic definition and classification. *Am J Cardiovasc Pathol*. (1987) 1:3–14.
6. Caforio AL, Pankuweit S, Arbustini E, Basso C, Gimeno-Blanes J, Felix SB, et al. Current state of knowledge on aetiology, diagnosis, management, and therapy of myocarditis: a position statement of the European Society of Cardiology Working Group on Myocardial and Pericardial Diseases. *Eur Heart J*. (2013) 34:2636–48:2648a–d. doi: 10.1093/eurheartj/eht210
7. Grogan M, Redfield MM, Bailey KR, Reeder GS, Gersh BJ, Edwards WD, et al. Long-term outcome of patients with biopsy-proved myocarditis: comparison with idiopathic dilated cardiomyopathy. *J Am Coll Cardiol*. (1995) 26:80–4. doi: 10.1016/0735-1097(95)00148-S
8. Kindermann I, Kindermann M, Kandolf R, Klingel K, Bultmann B, Muller T, et al. Predictors of outcome in patients with suspected myocarditis. *Circulation*. (2008) 118:639–48. doi: 10.1161/CIRCULATIONAHA.108.769489
9. Grun S, Schumm J, Greulich S, Wagner A, Schneider S, Bruder O, et al. Long-term follow-up of biopsy-proven viral myocarditis: predictors of mortality and incomplete recovery. *J Am Coll Cardiol*. (2012) 59:1604–15. doi: 10.1016/j.jacc.2012.01.007

10. Magnani JW, Danik HJ, Dec GW Jr, DiSalvo TG. Survival in biopsy-proven myocarditis: a long-term retrospective analysis of the histopathologic, clinical, and hemodynamic predictors. *Am Heart J*. (2006) 151:463–70. doi: 10.1016/j.ahj.2005.03.037
11. Dec GW Jr, Palacios IF, Fallon JT, Aretz HT, Mills J, Lee DC, et al. Active myocarditis in the spectrum of acute dilated cardiomyopathies. Clinical features, histologic correlates, and clinical outcome. *N Engl J Med*. (1985) 312:885–90. doi: 10.1056/NEJM198504043121404
12. D'Ambrosio A, Patti G, Manzoli A, Sinagra G, Di Lenarda A, Silvestri F, et al. The fate of acute myocarditis between spontaneous improvement and evolution to dilated cardiomyopathy: a review. *Heart*. (2001) 85:499–504. doi: 10.1136/heart.85.5.499
13. Jefferies JL, Towbin JA. Dilated cardiomyopathy. *Lancet*. (2010) 375:752–62. doi: 10.1016/S0140-6736(09)62023-7
14. Richardson P, McKenna W, Bristow M, Maisch B, Mautner B, O'Connell J, et al. Report of the 1995 World Health Organization/International Society and Federation of Cardiology Task Force on the Definition and Classification of cardiomyopathies. *Circulation*. (1996) 93:841–2. doi: 10.1161/01.CIR.93.5.841
15. Towbin JA, Lowe AM, Colan SD, Sleeper LA, Orav EJ, Clunie S, et al. Incidence, causes, and outcomes of dilated cardiomyopathy in children. *JAMA*. (2006) 296:1867–76. doi: 10.1001/jama.296.15.1867
16. Matsumura Y, Takata J, Kitaoka H, Kubo T, Baba Y, Hoshikawa E, et al. Long-term prognosis of dilated cardiomyopathy revisited: an improvement in survival over the past 20 years. *Circ J*. (2006) 70:376–83. doi: 10.1253/circj.70.376
17. Pereira Nunes Mdo C, Barbosa MM, Ribeiro AL, Amorim Fenelon LM, Rocha MO. Predictors of mortality in patients with dilated cardiomyopathy: relevance of chagas disease as an etiological factor. *Rev Esp Cardiol*. (2010) 63:788–97. doi: 10.1016/S1885-5857(10)70163-8
18. Wojnicz R, Nowalany-Kozielska E, Wojciechowska C, Glanowska G, Wilczewski P, Niklewski T, et al. Randomized, placebo-controlled study for immunosuppressive treatment of inflammatory dilated cardiomyopathy: two-year follow-up results. *Circulation*. (2001) 104:39–45. doi: 10.1161/01.CIR.104.1.39
19. Pankuweit S, Klingel K. Viral myocarditis: from experimental models to molecular diagnosis in patients. *Heart Fail Rev*. (2013) 18:683–702. doi: 10.1007/s10741-012-9357-4
20. Mahrholdt H, Wagner A, Deluigi CC, Kispert E, Hager S, Meinhardt G, et al. Presentation, patterns of myocardial damage, and clinical course of viral myocarditis. *Circulation*. (2006) 114:1581–90. doi: 10.1161/CIRCULATIONAHA.105.606509
21. Schenk T, Enders M, Pollak S, Hahn R, Huzly D. High prevalence of human parvovirus B19 DNA in myocardial autopsy samples from subjects without myocarditis or dilative cardiomyopathy. *J Clin Microbiol*. (2009) 47:106–10. doi: 10.1128/JCM.01672-08
22. Kuhl U, Pauschinger M, Seeberg B, Lassner D, Noutsias M, Poller W, et al. Viral persistence in the myocardium is associated with progressive cardiac dysfunction. *Circulation*. (2005) 112:1965–70. doi: 10.1161/CIRCULATIONAHA.105.548156
23. Kostic T, Momcilovic S, Perisic ZD, Apostolovic SR, Cvetkovic J, Jovanovic A, et al. Manifestations of Lyme carditis. *Int J Cardiol*. (2017) 232:24–32. doi: 10.1016/j.ijcard.2016.12.169
24. Hidron A, Vogenthaler N, Santos-Preciado JI, Rodriguez-Morales AJ, Franco-Paredes C, Rassi A Jr. Cardiac involvement with parasitic infections. *Clin Microbiol Rev*. (2010) 23:324–49. doi: 10.1128/CMR.00054-09
25. Parada H, Carrasco HA, Anez N, Fuenmayor C, Inglessis I. Cardiac involvement is a constant finding in acute Chagas' disease: a clinical, parasitological and histopathological study. *Int J Cardiol*. (1997) 60:49–54. doi: 10.1016/S0167-5273(97)02952-5
26. Bestetti RB, Muccillo G. Clinical course of Chagas' heart disease: a comparison with dilated cardiomyopathy. *Int J Cardiol*. (1997) 60:187–93. doi: 10.1016/S0167-5273(97)00083-1
27. Sagar S, Liu PP, Cooper LT Jr. Myocarditis. *Lancet*. (2012) 379:738–47. doi: 10.1016/S0140-6736(11)60648-X
28. Moder KG, Miller TD, Tazelaar HD. Cardiac involvement in systemic lupus erythematosus. *Mayo Clin Proc*. (1999) 74:275–84. doi: 10.4065/74.3.275
29. Suzuki S, Utsugisawa K, Yoshikawa H, Motomura M, Matsubara S, Yokoyama K, et al. Autoimmune targets of heart and skeletal muscles in myasthenia gravis. *Arch Neurol*. (2009) 66:1334–8. doi: 10.1001/archneurol.2009.229
30. Johnson DB, Balko JM, Compton ML, Chalkias S, Gorham J, Xu Y, et al. Fulminant Myocarditis with Combination Immune Checkpoint Blockade. *N Engl J Med*. (2016) 375:1749–55. doi: 10.1056/NEJMoa1609214
31. Mahmood SS, Fradley MG, Cohen JV, Nohria A, Reynolds KL, Heinzerling LM, et al. Myocarditis in patients treated with immune checkpoint inhibitors. *J Am Coll Cardiol*. (2018) 71:1755–64. doi: 10.1016/j.jacc.2018.02.037
32. Grabie N, Lichtman AH, Padera R. T Cell checkpoint regulators in the heart. *Cardiovasc Res*. (2019) 115:869–77. doi: 10.1093/cvr/cvz025
33. Rose NR. Myocarditis: infection versus autoimmunity. *J Clin Immunol*. (2009) 29:730–7. doi: 10.1007/s10875-009-9339-z
34. Caforio AL, Mahon NJ, Tona F, McKenna WJ. Circulating cardiac autoantibodies in dilated cardiomyopathy and myocarditis: pathogenetic and clinical significance. *Eur J Heart Fail*. (2002) 4:411–7. doi: 10.1016/S1388-9842(02)00010-7
35. Neumann DA, Burek CL, Baughman KL, Rose NR, Herskowitz A. Circulating heart-reactive antibodies in patients with myocarditis or cardiomyopathy. *J Am Coll Cardiol*. (1990) 16:839–46. doi: 10.1016/S0735-1097(10)80331-6
36. Lauer B, Schannwell M, Kuhl U, Strauer BE, Schultheiss HP. Antimyosin autoantibodies are associated with deterioration of systolic and diastolic left ventricular function in patients with chronic myocarditis. *J Am Coll Cardiol*. (2000) 35:11–8. doi: 10.1016/S0735-1097(99)00485-4
37. Herskowitz A, Ahmed-Ansari A, Neumann DA, Beschorner WE, Rose NR, Soule LM, et al. Induction of major histocompatibility complex antigens within the myocardium of patients with active myocarditis: a nonhistologic marker of myocarditis. *J Am Coll Cardiol*. (1990) 15:624–32. doi: 10.1016/0735-1097(90)90637-5
38. Seko Y, Takahashi N, Ishiyama S, Nishikawa T, Kasajima T, Hiroe M, et al. Expression of costimulatory molecules B7-1, B7-2, and CD40 in the heart of patients with acute myocarditis and dilated cardiomyopathy. *Circulation*. (1998) 97:637–9. doi: 10.1161/01.CIR.97.7.637
39. Caforio AL, Angelini A, Blank M, Shani A, Kivity S, Goddard G, et al. Passive transfer of affinity-purified anti-heart autoantibodies (AHA) from sera of patients with myocarditis induces experimental myocarditis in mice. *Int J Cardiol*. (2015) 179:166–77. doi: 10.1016/j.ijcard.2014.10.165
40. Cooper LT Jr. Myocarditis. *N Engl J Med*. (2009) 360:1526–38. doi: 10.1056/NEJMra0800028
41. Kindermann I, Barth C, Mahfoud F, Ukena C, Lenski M, Yilmaz A, et al. Update on myocarditis. *J Am Coll Cardiol*. (2012) 59:779–92. doi: 10.1016/j.jacc.2011.09.074
42. Felker GM, Boehmer JP, Hruban RH, Hutchins GM, Kasper EK, Baughman KL, et al. Echocardiographic findings in fulminant and acute myocarditis. *J Am Coll Cardiol*. (2000) 36:227–32. doi: 10.1016/S0735-1097(00)00690-2
43. Ukena C, Mahfoud F, Kindermann I, Kandolf R, Kindermann M, Bohm M. Prognostic electrocardiographic parameters in patients with suspected myocarditis. *Eur J Heart Fail*. (2011) 13:398–405. doi: 10.1093/eurjhf/hfq229
44. Friedrich MG, Sechtem U, Schulz-Menger J, Holmvang G, Alakija P, Cooper LT, et al. Cardiovascular magnetic resonance in myocarditis: a JACC White Paper. *J Am Coll Cardiol*. (2009) 53:1475–87. doi: 10.1016/j.jacc.2009.02.007
45. Lurz P, Luecke C, Eitel I, Fohrenbach F, Frank C, Grothoff M, et al. Comprehensive cardiac magnetic resonance imaging in patients with suspected myocarditis: the myoracer-trial. *J Am Coll Cardiol*. (2016) 67:1800–11. doi: 10.1016/j.jacc.2016.02.013
46. Ferreira VM, Schulz-Menger J, Holmvang G, Kramer CM, Carbone I, Sechtem U, et al. Cardiovascular magnetic resonance in nonischemic myocardial inflammation: expert recommendations. *J Am Coll Cardiol*. (2018) 72:3158–76. doi: 10.1016/j.jacc.2018.09.072
47. Lurz P, Eitel I, Adam J, Steiner J, Grothoff M, Desch S, et al. Diagnostic performance of CMR imaging compared with EMB in patients with suspected myocarditis. *JACC Cardiovasc Imaging*. (2012) 5:513–24. doi: 10.1016/j.jcmg.2011.11.022

48. Leone O, Veinot JP, Angelini A, Baandrup UT, Basso C, Berry G, et al. 2011 consensus statement on endomyocardial biopsy from the Association for European Cardiovascular Pathology and the Society for Cardiovascular Pathology. *Cardiovasc Pathol*. (2012) 21:245–74. doi: 10.1016/j.carpath.2011.10.001
49. Yilmaz A, Kindermann I, Kindermann M, Mahfoud F, Ukena C, Athanasiadis A, et al. Comparative evaluation of left and right ventricular endomyocardial biopsy: differences in complication rate and diagnostic performance. *Circulation*. (2010) 122:900–9. doi: 10.1161/CIRCULATIONAHA.109.924167
50. Chimenti C, Frustaci A. Contribution and risks of left ventricular endomyocardial biopsy in patients with cardiomyopathies: a retrospective study over a 28-year period. *Circulation*. (2013) 128:1531–41. doi: 10.1161/CIRCULATIONAHA.13.001414
51. Stiermaier T, Fohrenbach F, Klingel K, Kandolf R, Boudriot E, Sandri M, et al. Biventricular endomyocardial biopsy in patients with suspected myocarditis: Feasibility, complication rate and additional diagnostic value. *Int J Cardiol*. (2017) 230:364–70. doi: 10.1016/j.ijcard.2016.12.103
52. Hauck AJ, Kearney DL, Edwards WD. Evaluation of postmortem endomyocardial biopsy specimens from 38 patients with lymphocytic myocarditis: implications for role of sampling error. *Mayo Clin Proc*. (1989) 64:1235–45. doi: 10.1016/S0025-6196(12)61286-5
53. Chow LH, Radio SJ, Sears TD, McManus BM. Insensitivity of right ventricular endomyocardial biopsy in the diagnosis of myocarditis. *J Am Coll Cardiol*. (1989) 14:915–20. doi: 10.1016/0735-1097(89)90465-8
54. Khan T, Selvakumar D, Trivedi S, Rao K, Harapoz M, Thiagalingam A, et al. The value of endomyocardial biopsy in diagnosis and guiding therapy. *Pathology*. (2017) 49:750–6. doi: 10.1016/j.pathol.2017.08.004
55. Zhang M, Tavora F, Zhang Y, Ripple M, Fowler D, Li L, et al. The role of focal myocardial inflammation in sudden unexpected cardiac and noncardiac deaths–a clinicopathological study. *Int J Legal Med*. (2013) 127:131–8. doi: 10.1007/s00414-011-0634-x
56. Blauwet LA, Cooper LT. Idiopathic giant cell myocarditis and cardiac sarcoidosis. *Heart Fail Rev*. (2013) 18:733–46. doi: 10.1007/s10741-012-9358-3
57. Ginsberg F, Parrillo JE. Eosinophilic myocarditis. *Heart Fail Clin*. (2005) 1:419–29. doi: 10.1016/j.hfc.2005.06.013
58. Cooper LT Jr, Berry GJ, Shabetai R. Idiopathic giant-cell myocarditis–natural history and treatment. Multicenter Giant Cell Myocarditis Study Group Investigators. *N Engl J Med*. (1997) 336:1860–6. doi: 10.1056/NEJM199706263362603
59. Okura Y, Dec GW, Hare JM, Kodama M, Berry GJ, Tazelaar HD, et al. A clinical and histopathologic comparison of cardiac sarcoidosis and idiopathic giant cell myocarditis. *J Am Coll Cardiol*. (2003) 41:322–9. doi: 10.1016/S0735-1097(02)02715-8
60. Magnani JW, Dec GW. Myocarditis: current trends in diagnosis and treatment. *Circulation*. (2006) 113:876–90. doi: 10.1161/CIRCULATIONAHA.105.584532
61. Lieberman EB, Hutchins GM, Herskowitz A, Rose NR, Baughman KL. Clinicopathologic description of myocarditis. *J Am Coll Cardiol*. (1991) 18:1617–26. doi: 10.1016/0735-1097(91)90493-S
62. Dennert R, Crijns HJ, Heymans S. Acute viral myocarditis. *Eur Heart J*. (2008) 29:2073–82. doi: 10.1093/eurheartj/ehn296
63. Asaumi Y, Yasuda S, Morii I, Kakuchi H, Otsuka Y, Kawamura A, et al. Favourable clinical outcome in patients with cardiogenic shock due to fulminant myocarditis supported by percutaneous extracorporeal membrane oxygenation. *Eur Heart J*. (2005) 26:2185–92. doi: 10.1093/eurheartj/ehi411
64. Nakamura T, Ishida K, Taniguchi Y, Nakagawa T, Seguchi M, Wada H, et al. Prognosis of patients with fulminant myocarditis managed by peripheral venoarterial extracorporeal membranous oxygenation support: a retrospective single-center study. *J Intensive Care*. (2015) 3:5. doi: 10.1186/s40560-014-0069-9
65. McCarthy RE III, Boehmer JP, Hruban RH, Hutchins GM, Kasper EK, Hare JM, et al. Long-term outcome of fulminant myocarditis as compared with acute (nonfulminant) myocarditis. *N Engl J Med*. (2000) 342:690–5. doi: 10.1056/NEJM200003093421003
66. Ammirati E, Cipriani M, Lilliu M, Sormani P, Varrenti M, Raineri C, et al. Survival and left ventricular function changes in fulminant versus nonfulminant acute myocarditis. *Circulation*. (2017) 136:529–45. doi: 10.1161/CIRCULATIONAHA.117.026386
67. Woodruff JF, Woodruff JJ. Involvement of T lymphocytes in the pathogenesis of coxsackie virus B3 heart disease. *J Immunol*. (1974) 113:1726–34.
68. Nakamura H, Kunitsugu I, Fukuda K, Matsuzaki M, Sano M. Diverse stage-dependent effects of glucocorticoids in a murine model of viral myocarditis. *J Cardiol*. (2013) 61:237–42. doi: 10.1016/j.jjcc.2012.11.006
69. Gangaplara A, Massilamany C, Brown DM, Delhon G, Pattnaik AK, Chapman N, et al. Coxsackievirus B3 infection leads to the generation of cardiac myosin heavy chain-alpha-reactive CD4 T cells in A/J mice. *Clin Immunol*. (2012) 144:237–49. doi: 10.1016/j.clim.2012.07.003
70. Zheng C, Wu SM, Lian H, Lin YZ, Zhuang R, Thapa S, et al. Low-intensity pulsed ultrasound attenuates cardiac inflammation of CVB3-induced viral myocarditis via regulation of caveolin-1 and MAPK pathways. *J Cell Mol Med*. (2018) 23:1963–75. doi: 10.1111/jcmm.14098
71. Gou W, Zhang Z, Yang C, Li Y. MiR-223/Pknox1 axis protects mice from CVB3-induced viral myocarditis by modulating macrophage polarization. *Exp Cell Res*. (2018) 366:41–8. doi: 10.1016/j.yexcr.2018.03.004
72. Massilamany C, Gangaplara A, Basavalingappa RH, Rajasekaran RA, Vu H, Riethoven JJ, et al. Mutations in the 5' NTR and the non-structural protein 3A of the coxsackievirus B3 selectively attenuate myocarditogenicity. *PLoS ONE*. (2015) 10:e0131052. doi: 10.1371/journal.pone.0131052
73. Fuse K, Chan G, Liu Y, Gudgeon P, Husain M, Chen M, et al. Myeloid differentiation factor-88 plays a crucial role in the pathogenesis of Coxsackievirus B3-induced myocarditis and influences type I interferon production. *Circulation*. (2005) 112:2276–85. doi: 10.1161/CIRCULATIONAHA.105.536433
74. Valaperti A, Nishii M, Liu Y, Naito K, Chan M, Zhang L, et al. Innate immune interleukin-1 receptor-associated kinase 4 exacerbates viral myocarditis by reducing CCR5(+) CD11b(+) monocyte migration and impairing interferon production. *Circulation*. (2013) 128:1542–54. doi: 10.1161/CIRCULATIONAHA.113.002275
75. Matsumori A, Tomioka N, Kawai C. Protective effect of recombinant alpha interferon on coxsackievirus B3 myocarditis in mice. *Am Heart J*. (1988) 115:1229–32. doi: 10.1016/0002-8703(88)90013-0
76. Negishi H, Osawa T, Ogami K, Ouyang X, Sakaguchi S, Koshiba R, et al. A critical link between Toll-like receptor 3 and type II interferon signaling pathways in antiviral innate immunity. *Proc Natl Acad Sci USA*. (2008) 105:20446–51. doi: 10.1073/pnas.0810372105
77. Riad A, Westermann D, Zietsch C, Savvatis K, Becher PM, Bereswill S, et al. TRIF is a critical survival factor in viral cardiomyopathy. *J Immunol*. (2011) 186:2561–70. doi: 10.4049/jimmunol.1002029
78. Yuan J, Liu Z, Lim T, Zhang H, He J, Walker E, et al. CXCL10 inhibits viral replication through recruitment of natural killer cells in coxsackievirus B3-induced myocarditis. *Circ Res*. (2009) 104:628–38. doi: 10.1161/CIRCRESAHA.108.192179
79. Huber SA, Roberts B, Moussawi M, Boyson JE. Slam haplotype 2 promotes NKT but suppresses Vgamma4+ T-cell activation in coxsackievirus B3 infection leading to increased liver damage but reduced myocarditis. *Am J Pathol*. (2013) 182:401–9. doi: 10.1016/j.ajpath.2012.10.019
80. Liu W, Moussawi M, Roberts B, Boyson JE, Huber SA. Cross-regulation of T regulatory-cell response after coxsackievirus B3 infection by NKT and gammadelta T cells in the mouse. *Am J Pathol*. (2013) 183:441–9. doi: 10.1016/j.ajpath.2013.04.015
81. Nakamura H, Yamamura T, Umemoto S, Fukuta S, Shioi T, Matsumori A, et al. Autoimmune response in chronic ongoing myocarditis demonstrated by heterotopic cardiac transplantation in mice. *Circulation*. (1996) 94:3348–54. doi: 10.1161/01.CIR.94.12.3348
82. Yamada T, Matsumori A, Sasayama S. Therapeutic effect of anti-tumor necrosis factor-alpha antibody on the murine model of viral myocarditis induced by encephalomyocarditis virus. *Circulation*. (1994) 89:846–51. doi: 10.1161/01.CIR.89.2.846
83. Fairweather D, Rose NR. Coxsackievirus-induced myocarditis in mice: a model of autoimmune disease for studying immunotoxicity. *Methods*. (2007) 41:118–22. doi: 10.1016/j.ymeth.2006.07.009

84. Fairweather D, Frisancho-Kiss S, Yusung SA, Barrett MA, Davis SE, Steele RA, et al. IL-12 protects against coxsackievirus B3-induced myocarditis by increasing IFN-gamma and macrophage and neutrophil populations in the heart. *J Immunol*. (2005) 174:261–9. doi: 10.4049/jimmunol.174.1.261

85. Van Linthout S, Savvatis K, Miteva K, Peng J, Ringe J, Warstat K, et al. Mesenchymal stem cells improve murine acute coxsackievirus B3-induced myocarditis. *Eur Heart J*. (2011) 32:2168–78. doi: 10.1093/eurheartj/ehq467

86. Pappritz K, Savvatis K, Miteva K, Kerim B, Dong F, Fechner H, et al. Immunomodulation by adoptive regulatory T-cell transfer improves Coxsackievirus B3-induced myocarditis. *FASEB J*. (2018) 32:6066–78. doi: 10.1096/fj.201701408R

87. Savvatis K, Muller I, Frohlich M, Pappritz K, Zietsch C, Hamdani N, et al. Interleukin-6 receptor inhibition modulates the immune reaction and restores titin phosphorylation in experimental myocarditis. *Basic Res Cardiol*. (2014) 109:449. doi: 10.1007/s00395-014-0449-2

88. Miteva K, Pappritz K, El-Shafeey M, Dong F, Ringe J, Tschope C, et al. Mesenchymal stromal cells modulate monocytes trafficking in coxsackievirus B3-induced myocarditis. *Stem Cells Transl Med*. (2017) 6:1249–61. doi: 10.1002/sctm.16-0353

89. Kraft L, Erdenesukh T, Sauter M, Tschope C, Klingel K. Blocking the IL-1beta signalling pathway prevents chronic viral myocarditis and cardiac remodeling. *Basic Res Cardiol*. (2019) 114:11. doi: 10.1007/s00395-019-0719-0

90. Afanasyeva M, Georgakopoulos D, Belardi DF, Bedja D, Fairweather D, Wang Y, et al. Impaired up-regulation of CD25 on CD4+ T cells in IFN-gamma knockout mice is associated with progression of myocarditis to heart failure. *Proc Natl Acad Sci USA*. (2005) 102:180–5. doi: 10.1073/pnas.0408241102

91. Klingel K, Hohenadl C, Canu A, Albrecht M, Seemann M, Mall G, et al. Ongoing enterovirus-induced myocarditis is associated with persistent heart muscle infection: quantitative analysis of virus replication, tissue damage, and inflammation. *Proc Natl Acad Sci USA*. (1992) 89:314–8. doi: 10.1073/pnas.89.1.314

92. Becher PM, Gotzhein F, Klingel K, Escher F, Blankenberg S, Westermann D, et al. Cardiac function remains impaired despite reversible cardiac remodeling after acute experimental viral myocarditis. *J Immunol Res*. (2017) 2017:6590609. doi: 10.1155/2017/6590609

93. Lane JR, Neumann DA, Lafond-Walker A, Herskowitz A, Rose NR. LPS promotes CB3-induced myocarditis in resistant B10.A mice. *Cell Immunol*. (1991) 136:219–33. doi: 10.1016/0008-8749(91)90396-S

94. Heymans S, Pauschinger M, De Palma A, Kallwellis-Opara A, Rutschow S, Swinnen M, et al. Inhibition of urokinase-type plasminogen activator or matrix metalloproteinases prevents cardiac injury and dysfunction during viral myocarditis. *Circulation*. (2006) 114:565–73. doi: 10.1161/CIRCULATIONAHA.105.591032

95. Blailock ZR, Rabin ER, Melnick JL. Adenovirus endocarditis in mice. *Science*. (1967) 157:69–70. doi: 10.1126/science.157.3784.69

96. McCarthy MK, Procario MC, Twisselmann N, Wilkinson JE, Archambeau AJ, Michele DE, et al. Proinflammatory effects of interferon gamma in mouse adenovirus 1 myocarditis. *J Virol*. (2015) 89:468–79. doi: 10.1128/JVI.02077-14

97. Sherry B, Schoen FJ, Wenske E, Fields BN. Derivation and characterization of an efficiently myocarditic reovirus variant. *J Virol*. (1989) 63:4840–9.

98. Holm GH, Pruijssers AJ, Li L, Danthi P, Sherry B, Dermody TS. Interferon regulatory factor 3 attenuates reovirus myocarditis and contributes to viral clearance. *J Virol*. (2010) 84:6900–8. doi: 10.1128/JVI.01742-09

99. Sanchez-Guillen Mdel C, Bernabe C, Tibayrenc M, Zavala-Castro J, Totolhua JL, Mendez-Lopez J, et al. Trypanosoma cruzi strains isolated from human, vector, and animal reservoir in the same endemic region in Mexico and typed as T. cruzi I, discrete typing unit 1 exhibit considerable biological diversity. *Mem Inst Oswaldo Cruz*. (2006) 101:585–90. doi: 10.1590/S0074-02762006000600002

100. Michailowsky V, Silva NM, Rocha CD, Vieira LQ, Lannes-Vieira J, Gazzinelli RT. Pivotal role of interleukin-12 and interferon-gamma axis in controlling tissue parasitism and inflammation in the heart and central nervous system during Trypanosoma cruzi infection. *Am J Pathol*. (2001) 159:1723–33. doi: 10.1016/S0002-9440(10)63019-2

101. Camandaroba EL, Pinheiro Lima CM, Andrade SG. Oral transmission of Chagas disease: importance of Trypanosoma cruzi biodeme in the intragastric experimental infection. *Rev Inst Med Trop Sao Paulo*. (2002) 44:97–103. doi: 10.1590/S0036-46652002000200008

102. Camandaroba E, The TS, Pessina DH, Andrade SG. Trypanosoma cruzi: clones isolated from the Colombian strain, reproduce the parental strain characteristics, with ubiquitous histotropism. *Int J Exp Pathol*. (2006) 87:209–17. doi: 10.1111/j.1365-2613.2006.00476.x

103. Marino AP, Azevedo MI, Lannes-Vieira J. Differential expression of adhesion moleculesshaping the T-cell subset prevalence during the early phase of autoimmune and Trypanosoma cruzi-elicited myocarditis. *Mem Inst Oswaldo Cruz*. (2003) 98:945–52. doi: 10.1590/S0074-02762003000700015

104. Andrade LO, Machado CR, Chiari E, Pena SD, Macedo AM. Trypanosoma cruzi: role of host genetic background in the differential tissue distribution of parasite clonal populations. *Exp Parasitol*. (2002) 100:269–75. doi: 10.1016/S0014-4894(02)00024-3

105. Sanches TL, Cunha LD, Silva GK, Guedes PM, Silva JS, Zamboni DS. The use of a heterogeneously controlled mouse population reveals a significant correlation of acute phase parasitemia with mortality in Chagas disease. *PLoS ONE*. (2014) 9:e91640. doi: 10.1371/journal.pone.0091640

106. Bustamante JM, Rivarola HW, Fretes R, Paglini-Oliva PA. Weekly electrocardiographic pattern in mice infected with two different Trypanosoma cruzi strains. *Int J Cardiol*. (2005) 102:211–7. doi: 10.1016/j.ijcard.2004.05.014

107. Marinho CR, Nunez-Apaza LN, Bortoluci KR, Bombeiro AL, Bucci DZ, Grisotto MG, et al. Infection by the Sylvio X10/4 clone of Trypanosoma cruzi: relevance of a low-virulence model of Chagas' disease. *Microbes Infect*. (2009) 11:1037–45. doi: 10.1016/j.micinf.2009.07.011

108. Ponce NE, Sanmarco LM, Eberhardt N, Garcia MC, Rivarola HW, Cano RC, et al. CD73 inhibition shifts cardiac macrophage polarization toward a microbicidal phenotype and ameliorates the outcome of experimental chagas cardiomyopathy. *J Immunol*. (2016) 197:814–23. doi: 10.4049/jimmunol.1600371

109. Vilar-Pereira G, Carneiro VC, Mata-Santos H, Vicentino AR, Ramos IP, Giarola NL, et al. Resveratrol reverses functional chagas heart disease in mice. *PLoS Pathog*. (2016) 12:e1005947. doi: 10.1371/journal.ppat.1005947

110. Garcia S, Ramos CO, Senra JF, Vilas-Boas F, Rodrigues MM, Campos-de-Carvalho AC, et al. Treatment with benznidazole during the chronic phase of experimental Chagas' disease decreases cardiac alterations. *Antimicrob Agents Chemother*. (2005) 49:1521–8. doi: 10.1128/AAC.49.4.1521-1528.2005

111. Campos MA, Almeida IC, Takeuchi O, Akira S, Valente EP, Procopio DO, et al. Activation of Toll-like receptor-2 by glycosylphosphatidylinositol anchors from a protozoan parasite. *J Immunol*. (2001) 167:416–23. doi: 10.4049/jimmunol.167.1.416

112. Oliveira AC, Peixoto JR, de Arruda LB, Campos MA, Gazzinelli RT, Golenbock DT, et al. Expression of functional TLR4 confers proinflammatory responsiveness to Trypanosoma cruzi glycoinositolphospholipids and higher resistance to infection with T. cruzi. *J Immunol*. (2004) 173:5688–96. doi: 10.4049/jimmunol.173.9.5688

113. Bafica A, Santiago HC, Goldszmid R, Ropert C, Gazzinelli RT, Sher A. Cutting edge: TLR9 and TLR2 signaling together account for MyD88-dependent control of parasitemia in Trypanosoma cruzi infection. *J Immunol*. (2006) 177:3515–9. doi: 10.4049/jimmunol.177.6.3515

114. Huang H, Petkova SB, Cohen AW, Bouzahzah B, Chan J, Zhou JN, et al. Activation of transcription factors AP-1 and NF-kappa B in murine Chagasic myocarditis. *Infect Immun*. (2003) 71:2859–67. doi: 10.1128/IAI.71.5.2859-2867.2003

115. Huang H, Petkova SB, Pestell RG, Bouzahzah B, Chan J, Magazine H, et al. Trypanosoma cruzi infection (Chagas' disease) of mice causes activation of the mitogen-activated protein kinase cascade and expression of endothelin-1 in the myocardium. *J Cardiovasc Pharmacol*. (2000) 36:S148–50. doi: 10.1097/00005344-200036001-00046

116. Vespa GN, Cunha FQ, Silva JS. Nitric oxide is involved in control of Trypanosoma cruzi-induced parasitemia and directly kills the parasite *in vitro*. *Infect Immun*. (1994) 62:5177–82.

117. Monteiro AC, Schmitz V, Svensjo E, Gazzinelli RT, Almeida IC, Todorov A, et al. Cooperative activation of TLR2 and bradykinin B2 receptor

is required for induction of type 1 immunity in a mouse model of subcutaneous infection by Trypanosoma cruzi. *J Immunol*. (2006) 177:6325–35. doi: 10.4049/jimmunol.177.9.6325

118. de Meis J, Morrot A, Farias-de-Oliveira DA, Villa-Verde DM, Savino W. Differential regional immune response in Chagas disease. *PLoS Negl Trop Dis*. (2009) 3:e417. doi: 10.1371/journal.pntd.0000417
119. Minoprio PM, Eisen H, Forni L, D'Imperio Lima MR, Joskowicz M, et al. Polyclonal lymphocyte responses to murine Trypanosoma cruzi infection. I. Quantitation of both T- and B-cell responses. *Scand J Immunol*. (1986) 24:661–8. doi: 10.1111/j.1365-3083.1986.tb02185.x
120. Minoprio P, Bandeira A, Pereira P, Mota Santos T, Coutinho A. Preferential expansion of Ly-1 B and CD4- CD8- T cells in the polyclonal lymphocyte responses to murine T. cruzi infection. *Int Immunol*. (1989) 1:176–84. doi: 10.1093/intimm/1.2.176
121. Todeschini AR, Nunes MP, Pires RS, Lopes MF, Previato JO, Mendonca-Previato L, et al. Costimulation of host T lymphocytes by a trypanosomal trans-sialidase: involvement of CD43 signaling. *J Immunol*. (2002) 168:5192–8. doi: 10.4049/jimmunol.168.10.5192
122. Shoda LK, Kegerreis KA, Suarez CE, Roditi I, Corral RS, Bertot GM, et al. DNA from protozoan parasites Babesia bovis, Trypanosoma cruzi, and T. brucei is mitogenic for B lymphocytes and stimulates macrophage expression of interleukin-12, tumor necrosis factor alpha, and nitric oxide. *Infect Immun*. (2001) 69:2162–71. doi: 10.1128/IAI.69.4.2162-2171.2001
123. Kumar S, Tarleton RL. Antigen-specific Th1 but not Th2 cells provide protection from lethal Trypanosoma cruzi infection in mice. *J Immunol*. (2001) 166:4596–603. doi: 10.4049/jimmunol.166.7.4596
124. Martin DL, Tarleton RL. Antigen-specific T cells maintain an effector memory phenotype during persistent Trypanosoma cruzi infection. *J Immunol*. (2005) 174:1594–601. doi: 10.4049/jimmunol.174.3.1594
125. Tarleton RL, Sun J, Zhang L, Postan M. Depletion of T-cell subpopulations results in exacerbation of myocarditis and parasitism in experimental Chagas' disease. *Infect Immun*. (1994) 62:1820–9.
126. Kumar S, Tarleton RL. The relative contribution of antibody production and CD8+ T cell function to immune control of Trypanosoma cruzi. *Parasite Immunol*. (1998) 20:207–16. doi: 10.1046/j.1365-3024.1998.00154.x
127. Sullivan NL, Eickhoff CS, Sagartz J, Hoft DF. Deficiency of antigen-specific B cells results in decreased Trypanosoma cruzi systemic but not mucosal immunity due to CD8 T cell exhaustion. *J Immunol*. (2015) 194:1806–18. doi: 10.4049/jimmunol.1303163
128. Cardillo F, Postol E, Nihei J, Aroeira LS, Nomizo A, Mengel J. B cells modulate T cells so as to favour T helper type 1 and CD8+ T-cell responses in the acute phase of Trypanosoma cruzi infection. *Immunology*. (2007) 122:584–95. doi: 10.1111/j.1365-2567.2007.02677.x
129. Pereira ME, Santos LM, Araujo MS, Brener Z. Recrudescence induced by cyclophosphamide of chronic Trypanosoma cruzi infection in mice is influenced by the parasite strain. *Mem Inst Oswaldo Cruz*. (1996) 91:71–4. doi: 10.1590/S0074-02761996000100011
130. Santos DM, Martins TA, Caldas IS, Diniz LF, Machado-Coelho GL, Carneiro CM, et al. Benznidazole alters the pattern of Cyclophosphamide-induced reactivation in experimental Trypanosoma cruzi-dependent lineage infection. *Acta Trop*. (2010) 113:134–8. doi: 10.1016/j.actatropica.2009.10.007
131. Rizzo LV, Cunha-Neto E, Teixeira AR. Autoimmunity in Chagas' disease: specific inhibition of reactivity of CD4+ T cells against myosin in mice chronically infected with Trypanosoma cruzi. *Infect Immun*. (1989) 57:2640–4.
132. Pontes-de-Carvalho L, Santana CC, Soares MB, Oliveira GG, Cunha-Neto E, Ribeiro-dos-Santos R. Experimental chronic Chagas' disease myocarditis is an autoimmune disease preventable by induction of immunological tolerance to myocardial antigens. *J Autoimmun*. (2002) 18:131–8. doi: 10.1006/jaut.2001.0574
133. Leon JS, Wang K, Engman DM. Myosin autoimmunity is not essential for cardiac inflammation in acute Chagas' disease. *J Immunol*. (2003) 171:4271–7. doi: 10.4049/jimmunol.171.8.4271
134. Neu N, Rose NR, Beisel KW, Herskowitz A, Gurri-Glass G, Craig SW. Cardiac myosin induces myocarditis in genetically predisposed mice. *J Immunol*. (1987) 139:3630–6.
135. Blyszczuk P, Behnke S, Luscher TF, Eriksson U, Kania G. GM-CSF promotes inflammatory dendritic cell formation but does not contribute to disease progression in experimental autoimmune myocarditis. *Biochim Biophys Acta*. (2013) 1833:934–44. doi: 10.1016/j.bbamcr.2012.10.008
136. Blyszczuk P, Berthonneche C, Behnke S, Glonkler M, Moch H, Pedrazzini T, et al. Nitric oxide synthase 2 is required for conversion of pro-fibrogenic inflammatory CD133+ progenitors into F4/80+ macrophages in experimental autoimmune myocarditis. *Cardiovasc Res*. (2013) 97:219–29. doi: 10.1093/cvr/cvs317
137. Kania G, Blyszczuk P, Stein S, Valaperti A, Germano D, Dirnhofer S, et al. Heart-infiltrating prominin-1+/CD133+ progenitor cells represent the cellular source of transforming growth factor beta-mediated cardiac fibrosis in experimental autoimmune myocarditis. *Circ Res*. (2009) 105:462–70. doi: 10.1161/CIRCRESAHA.109.196287
138. Kania G, Blyszczuk P, Valaperti A, Dieterle T, Leimenstoll B, Dirnhofer S, et al. Prominin-1+/CD133+ bone marrow-derived heart-resident cells suppress experimental autoimmune myocarditis. *Cardiovasc Res*. (2008) 80:236–45. doi: 10.1093/cvr/cvn190
139. Kania G, Siegert S, Behnke S, Prados-Rosales R, Casadevall A, Luscher TF, et al. Innate signaling promotes formation of regulatory nitric oxide-producing dendritic cells limiting T-cell expansion in experimental autoimmune myocarditis. *Circulation*. (2013) 127:2285–94. doi: 10.1161/CIRCULATIONAHA.112.000434
140. van Heeswijk RB, De Blois J, Kania G, Gonzales C, Blyszczuk P, Stuber M, et al. Selective *in-vivo* visualization of immune-cell infiltration in a mouse model of autoimmune myocarditis by fluorine-19 cardiac magnetic resonance. *Circ Cardiovasc Imaging*. (2013) 6:277–84. doi: 10.1161/CIRCIMAGING.112.000125
141. Blyszczuk P, Muller-Edenborn B, Valenta T, Osto E, Stellato M, Behnke S, et al. Transforming growth factor-beta-dependent Wnt secretion controls myofibroblast formation and myocardial fibrosis progression in experimental autoimmune myocarditis. *Eur Heart J*. (2017) 38:1413–25. doi: 10.1093/eurheartj/ehw116
142. Baldeviano GC, Barin JG, Talor MV, Srinivasan S, Bedja D, Zheng D, et al. Interleukin-17A is dispensable for myocarditis but essential for the progression to dilated cardiomyopathy. *Circ Res*. (2010) 106:1646–55. doi: 10.1161/CIRCRESAHA.109.213157
143. Ma W, Wang Y, Lu S, Yan L, Hu F, Wang Z. Targeting androgen receptor with ASC-J9 attenuates cardiac injury and dysfunction in experimental autoimmune myocarditis by reducing M1-like macrophage. *Biochem Biophys Res Commun*. (2017) 485:746–52. doi: 10.1016/j.bbrc.2017.02.123
144. Thelemann C, Haller S, Blyszczuk P, Kania G, Rosa M, Eriksson U, et al. Absence of nonhematopoietic MHC class II expression protects mice from experimental autoimmune myocarditis. *Eur J Immunol*. (2016) 46:656–64. doi: 10.1002/eji.201545945
145. Machino-Ohtsuka T, Tajiri K, Kimura T, Sakai S, Sato A, Yoshida T, et al. Tenascin-C aggravates autoimmune myocarditis via dendritic cell activation and Th17 cell differentiation. *J Am Heart Assoc*. (2014) 3:e001052. doi: 10.1161/JAHA.114.001052
146. Martin R, Cordova C, San Roman JA, Gutierrez B, Cachofeiro V, Nieto ML. Oleanolic acid modulates the immune-inflammatory response in mice with experimental autoimmune myocarditis and protects from cardiac injury. Therapeutic implications for the human disease. *J Mol Cell Cardiol*. (2014) 72:250–62. doi: 10.1016/j.yjmcc.2014.04.002
147. Barin JG, Baldeviano GC, Talor MV, Wu L, Ong S, Fairweather D, et al. Fatal eosinophilic myocarditis develops in the absence of IFN-gamma and IL-17A. *J Immunol*. (2013) 191:4038–47. doi: 10.4049/jimmunol.1301282
148. Smith SC, Allen PM. Myosin-induced acute myocarditis is a T cell-mediated disease. *J Immunol*. (1991) 147:2141–7.
149. Valaperti A, Marty RR, Kania G, Germano D, Mauermann N, Dirnhofer S, et al. CD11b+ monocytes abrogate Th17 CD4+ T cell-mediated experimental autoimmune myocarditis. *J Immunol*. (2008) 180:2686–95. doi: 10.4049/jimmunol.180.4.2686
150. Neu N, Ploier B, Ofner C. Cardiac myosin-induced myocarditis. Heart autoantibodies are not involved in the induction of the disease. *J Immunol*. (1990) 145:4094–100.

151. Liao L, Sindhwani R, Rojkind M, Factor S, Leinwand L, Diamond B. Antibody-mediated autoimmune myocarditis depends on genetically determined target organ sensitivity. *J Exp Med*. (1995) 181:1123–31. doi: 10.1084/jem.181.3.1123
152. Massilamany C, Gangaplara A, Basavalingappa RH, Rajasekaran RA, Khalilzad-Sharghi V, Han Z, et al. Localization of CD8 T cell epitope within cardiac myosin heavy chain-alpha334-352 that induces autoimmune myocarditis in A/J mice. *Int J Cardiol*. (2016) 202:311–21. doi: 10.1016/j.ijcard.2015.09.016
153. Smith SC, Allen PM. Neutralization of endogenous tumor necrosis factor ameliorates the severity of myosin-induced myocarditis. *Circ Res*. (1992) 70:856–63. doi: 10.1161/01.RES.70.4.856
154. Bachmaier K, Pummerer C, Kozieradzki I, Pfeffer K, Mak TW, Neu N, et al. Low-molecular-weight tumor necrosis factor receptor p55 controls induction of autoimmune heart disease. *Circulation*. (1997) 95:655–61. doi: 10.1161/01.CIR.95.3.655
155. Sonderegger I, Iezzi G, Maier R, Schmitz N, Kurrer M, Kopf M. GM-CSF mediates autoimmunity by enhancing IL-6-dependent Th17 cell development and survival. *J Exp Med*. (2008) 205:2281–94. doi: 10.1084/jem.20071119
156. Eriksson U, Kurrer MO, Sonderegger I, Iezzi G, Tafuri A, Hunziker L, et al. Activation of dendritic cells through the interleukin 1 receptor 1 is critical for the induction of autoimmune myocarditis. *J Exp Med*. (2003) 197:323–31. doi: 10.1084/jem.20021788
157. Eriksson U, Kurrer MO, Schmitz N, Marsch SC, Fontana A, Eugster HP, et al. Interleukin-6-deficient mice resist development of autoimmune myocarditis associated with impaired upregulation of complement C3. *Circulation*. (2003) 107:320–5. doi: 10.1161/01.CIR.0000043802.38699.66
158. Wu L, Diny NL, Ong S, Barin JG, Hou X, Rose NR, et al. Pathogenic IL-23 signaling is required to initiate GM-CSF-driven autoimmune myocarditis in mice. *Eur J Immunol*. (2016) 46:582–92. doi: 10.1002/eji.201545924
159. Pummerer CL, Luze K, Grassl G, Bachmaier K, Offner F, Burrell SK, et al. Identification of cardiac myosin peptides capable of inducing autoimmune myocarditis in BALB/c mice. *J Clin Invest*. (1996) 97:2057–62. doi: 10.1172/JCI118642
160. Massilamany C, Gangaplara A, Steffen D, Reddy J. Identification of novel mimicry epitopes for cardiac myosin heavy chain-alpha that induce autoimmune myocarditis in A/J mice. *Cell Immunol*. (2011) 271:438–49. doi: 10.1016/j.cellimm.2011.08.013
161. Li HS, Ligons DL, Rose NR, Guler ML. Genetic differences in bone marrow-derived lymphoid lineages control susceptibility to experimental autoimmune myocarditis. *J Immunol*. (2008) 180:7480–4. doi: 10.4049/jimmunol.180.11.7480
162. Smith SC, Allen PM. Expression of myosin-class II major histocompatibility complexes in the normal myocardium occurs before induction of autoimmune myocarditis. *Proc Natl Acad Sci USA*. (1992) 89:9131–5. doi: 10.1073/pnas.89.19.9131
163. Guler ML, Ligons DL, Wang Y, Bianco M, Broman KW, Rose NR. Two autoimmune diabetes loci influencing T cell apoptosis control susceptibility to experimental autoimmune myocarditis. *J Immunol*. (2005) 174:2167–73. doi: 10.4049/jimmunol.174.4.2167
164. Eriksson U, Ricci R, Hunziker L, Kurrer MO, Oudit GY, Watts TH, et al. Dendritic cell-induced autoimmune heart failure requires cooperation between adaptive and innate immunity. *Nat Med*. (2003) 9:1484–90. doi: 10.1038/nm960
165. Van der Borght K, Scott CL, Martens L, Sichien D, Van Isterdael G, Nindl V, et al. Myocarditis elicits dendritic cell and monocyte infiltration in the heart and self-antigen presentation by conventional type 2 dendritic cells. *Front Immunol*. (2018) 9:2714. doi: 10.3389/fimmu.2018.02714
166. Nindl V, Maier R, Ratering D, De Giuli R, Zust R, Thiel V, et al. Cooperation of Th1 and Th17 cells determines transition from autoimmune myocarditis to dilated cardiomyopathy. *Eur J Immunol*. (2012) 42:2311–21. doi: 10.1002/eji.201142209
167. Grabie N, Delfs MW, Westrich JR, Love VA, Stavrakis G, Ahmad F, et al. IL-12 is required for differentiation of pathogenic CD8+ T cell effectors that cause myocarditis. *J Clin Invest*. (2003) 111:671–80. doi: 10.1172/JCI16867
168. Grabie N, Hsieh DT, Buono C, Westrich JR, Allen JA, Pang H, et al. Neutrophils sustain pathogenic CD8+ T cell responses in the heart. *Am J Pathol*. (2003) 163:2413–20. doi: 10.1016/S0002-9440(10)63596-1
169. Taqueti VR, Grabie N, Colvin R, Pang H, Jarolim P, Luster AD, et al. T-bet controls pathogenicity of CTLs in the heart by separable effects on migration and effector activity. *J Immunol*. (2006) 177:5890–901. doi: 10.4049/jimmunol.177.9.5890
170. Grabie N, Gotsman I, DaCosta R, Pang H, Stavrakis G, Butte MJ, et al. Endothelial programmed death-1 ligand 1 (PD-L1) regulates CD8+ T-cell mediated injury in the heart. *Circulation*. (2007) 116:2062–71. doi: 10.1161/CIRCULATIONAHA.107.709360
171. Nishimura H, Okazaki T, Tanaka Y, Nakatani K, Hara M, Matsumori A, et al. Autoimmune dilated cardiomyopathy in PD-1 receptor-deficient mice. *Science*. (2001) 291:319–22. doi: 10.1126/science.291.5502.319
172. Okazaki T, Tanaka Y, Nishio R, Mitsuiye T, Mizoguchi A, Wang J, et al. Autoantibodies against cardiac troponin I are responsible for dilated cardiomyopathy in PD-1-deficient mice. *Nat Med*. (2003) 9:1477–83. doi: 10.1038/nm955
173. Lucas JA, Menke J, Rabacal WA, Schoen FJ, Sharpe AH, Kelley VR. Programmed death ligand 1 regulates a critical checkpoint for autoimmune myocarditis and pneumonitis in MRL mice. *J Immunol*. (2008) 181:2513–21. doi: 10.4049/jimmunol.181.4.2513
174. Wang J, Okazaki IM, Yoshida T, Chikuma S, Kato Y, Nakaki F, et al. PD-1 deficiency results in the development of fatal myocarditis in MRL mice. *Int Immunol*. (2010) 22:443–52. doi: 10.1093/intimm/dxq026
175. Tarrio ML, Grabie N, Bu DX, Sharpe AH, Lichtman AH. PD-1 protects against inflammation and myocyte damage in T cell-mediated myocarditis. *J Immunol*. (2012) 188:4876–84. doi: 10.4049/jimmunol.1200389
176. Elliott JF, Liu J, Yuan ZN, Bautista-Lopez N, Wallbank SL, Suzuki K, et al. Autoimmune cardiomyopathy and heart block develop spontaneously in HLA-DQ8 transgenic IAbeta knockout NOD mice. *Proc Natl Acad Sci USA*. (2003) 100:13447–52. doi: 10.1073/pnas.2235552100
177. Taneja V, Behrens M, Cooper LT, Yamada S, Kita H, Redfield MM, et al. Spontaneous myocarditis mimicking human disease occurs in the presence of an appropriate MHC and non-MHC background in transgenic mice. *J Mol Cell Cardiol*. (2007) 42:1054–64. doi: 10.1016/j.yjmcc.2007.03.898
178. Hayward SL, Bautista-Lopez N, Suzuki K, Atrazhev A, Dickie P, Elliott JF. CD4 T cells play major effector role and CD8 T cells initiating role in spontaneous autoimmune myocarditis of HLA-DQ8 transgenic IAb knockout nonobese diabetic mice. *J Immunol*. (2006) 176:7715–25. doi: 10.4049/jimmunol.176.12.7715
179. Taylor JA, Havari E, McInerney MF, Bronson R, Wucherpfennig KW, Lipes MA. A spontaneous model for autoimmune myocarditis using the human MHC molecule HLA-DQ8. *J Immunol*. (2004) 172:2651–8. doi: 10.4049/jimmunol.172.4.2651
180. Boldizsar F, Tarjanyi O, Olasz K, Hegyi A, Mikecz K, Glant TT, et al. FTY720 (Gilenya) treatment prevents spontaneous autoimmune myocarditis and dilated cardiomyopathy in transgenic HLA-DQ8-BALB/c mice. *Cardiovasc Pathol*. (2016) 25:353–61. doi: 10.1016/j.carpath.2016.05.003
181. Saraste A, Arola A, Vuorinen T, Kyto V, Kallajoki M, Pulkki K, et al. Cardiomyocyte apoptosis in experimental coxsackievirus B3 myocarditis. *Cardiovasc Pathol*. (2003) 12:255–62. doi: 10.1016/S1054-8807(03)00077-2
182. Zhou F, Jiang X, Teng L, Yang J, Ding J, He C. Necroptosis may be a novel mechanism for cardiomyocyte death in acute myocarditis. *Mol Cell Biochem*. (2017) 442:11–8. doi: 10.1007/s11010-017-3188-5
183. Lindner D, Li J, Savvatis K, Klingel K, Blankenberg S, Tschope C, et al. Cardiac fibroblasts aggravate viral myocarditis: cell specific coxsackievirus B3 replication. *Mediators Inflamm*. (2014) 2014:519528. doi: 10.1155/2014/519528
184. Tschope C, Muller I, Xia Y, Savvatis K, Pappritz K, Pinkert S, et al. NOD2 (Nucleotide-Binding Oligomerization Domain 2) is a major pathogenic mediator of coxsackievirus B3-induced myocarditis. *Circ Heart Fail*. (2017) 10:e003870. doi: 10.1161/CIRCHEARTFAILURE.117.003870
185. Garmaroudi FS, Marchant D, Hendry R, Luo H, Yang D, Ye X, et al. Coxsackievirus B3 replication and pathogenesis. *Future Microbiol*. (2015) 10:629–53. doi: 10.2217/fmb.15.5
186. Pauschinger M, Doerner A, Kuehl U, Schwimmbeck PL, Poller W, Kandolf R, et al. Enteroviral RNA replication in the myocardium of patients with

left ventricular dysfunction and clinically suspected myocarditis. *Circulation*. (1999) 99:889–95. doi: 10.1161/01.CIR.99.7.889

187. Kuhl U, Pauschinger M, Schwimmbeck PL, Seeberg B, Lober C, Noutsias M, et al. Interferon-beta treatment eliminates cardiotropic viruses and improves left ventricular function in patients with myocardial persistence of viral genomes and left ventricular dysfunction. *Circulation*. (2003) 107:2793–8. doi: 10.1161/01.CIR.0000072766.67150.51
188. Epelman S, Liu PP, Mann DL. Role of innate and adaptive immune mechanisms in cardiac injury and repair. *Nat Rev Immunol*. (2015) 15:117–29. doi: 10.1038/nri3800
189. Chow LH, Beisel KW, McManus BM. Enteroviral infection of mice with severe combined immunodeficiency. Evidence for direct viral pathogenesis of myocardial injury. *Lab Invest*. (1992) 66:24–31.
190. Merkle I, Tonew M, Gluck B, Schmidtke M, Egerer R, Stelzner A. Coxsackievirus B3-induced chronic myocarditis in outbred NMRI mice. *J Hum Virol*. (1999) 2:369–79.
191. Henke A, Huber S, Stelzner A, Whitton JL. The role of CD8+ T lymphocytes in coxsackievirus B3-induced myocarditis. *J Virol*. (1995) 69:6720–8.
192. Leipner C, Borchers M, Merkle I, Stelzner A. Coxsackievirus B3-induced myocarditis in MHC class II-deficient mice. *J Hum Virol*. (1999) 2:102–14.
193. Huber SA, Sartini D, Exley M. Vgamma4(+) T cells promote autoimmune CD8(+) cytolytic T-lymphocyte activation in coxsackievirus B3-induced myocarditis in mice: role for CD4(+) Th1 cells. *J Virol*. (2002) 76:10785–90. doi: 10.1128/JVI.76.21.10785-10790.2002
194. Takata S, Nakamura H, Umemoto S, Yamaguchil K, Sekine T, Kato T, et al. Identification of autoantibodies with the corresponding antigen for repetitive coxsackievirus infection-induced cardiomyopathy. *Circ J*. (2004) 68:677–82. doi: 10.1253/circj.68.677
195. Latva-Hirvela J, Kyto V, Saraste A, Eriksson S, Vuorinen T, Pettersson K, et al. Development of troponin autoantibodies in experimental coxsackievirus B3 myocarditis. *Eur J Clin Invest*. (2009) 39:457–62. doi: 10.1111/j.1365-2362.2009.02113.x
196. Caforio AL, Tona F, Bottaro S, Vinci A, Dequal G, Daliento L, et al. Clinical implications of anti-heart autoantibodies in myocarditis and dilated cardiomyopathy. *Autoimmunity*. (2008) 41:35–45. doi: 10.1080/08916930701619235
197. Fousteri G, Dave A, Morin B, Omid S, Croft M, von Herrath MG. Nasal cardiac myosin peptide treatment and OX40 blockade protect mice from acute and chronic virally-induced myocarditis. *J Autoimmun*. (2011) 36:210–20. doi: 10.1016/j.jaut.2011.01.006
198. Hardarson HS, Baker JS, Yang Z, Purevjav E, Huang CH, Alexopoulou L, et al. Toll-like receptor 3 is an essential component of the innate stress response in virus-induced cardiac injury. *Am J Physiol Heart Circ Physiol*. (2007) 292:H251–8. doi: 10.1152/ajpheart.00398.2006
199. Bowles NE, Ni J, Kearney DL, Pauschinger M, Schultheiss HP, McCarthy R, et al. Detection of viruses in myocardial tissues by polymerase chain reaction. evidence of adenovirus as a common cause of myocarditis in children and adults. *J Am Coll Cardiol*. (2003) 42:466–72. doi: 10.1016/S0735-1097(03)00648-X
200. Kuhl U, Schultheiss HP. Myocarditis in children. *Heart Fail Clin*. (2010) 6:483–96, viii–ix. doi: 10.1016/j.hfc.2010.05.009
201. Wizel B, Palmieri M, Mendoza C, Arana B, Sidney J, Sette A, et al. Human infection with Trypanosoma cruzi induces parasite antigen-specific cytotoxic T lymphocyte responses. *J Clin Invest*. (1998) 102:1062–71. doi: 10.1172/JCI3835
202. Lattes R, Lasala MB. Chagas disease in the immunosuppressed patient. *Clin Microbiol Infect*. (2014) 20:300–9. doi: 10.1111/1469-0691.12585
203. Morillo CA, Marin-Neto JA, Avezum A, Sosa-Estani S, Rassi A Jr, Rosas F, et al. Randomized trial of benznidazole for chronic chagas' cardiomyopathy. *N Engl J Med*. (2015) 373:1295–306. doi: 10.1056/NEJMoa1507574
204. Tibbetts RS, McCormick TS, Rowland EC, Miller SD, Engman DM. Cardiac antigen-specific autoantibody production is associated with cardiomyopathy in Trypanosoma cruzi-infected mice. *J Immunol*. (1994) 152:1493–9.
205. Cunha-Neto E, Coelho V, Guilherme L, Fiorelli A, Stolf N, Kalil J. Autoimmunity in Chagas' disease. Identification of cardiac myosin-B13 Trypanosoma cruzi protein crossreactive T cell clones in heart lesions of a chronic Chagas' cardiomyopathy patient. *J Clin Invest*. (1996) 98:1709–12. doi: 10.1172/JCI118969
206. Leon JS, Godsel LM, Wang K, Engman DM. Cardiac myosin autoimmunity in acute Chagas' heart disease. *Infect Immun*. (2001) 69:5643–9. doi: 10.1128/IAI.69.9.5643-5649.2001
207. Lv H, Havari E, Pinto S, Gottumukkala RV, Cornivelli L, Raddassi K, et al. Impaired thymic tolerance to alpha-myosin directs autoimmunity to the heart in mice and humans. *J Clin Invest*. (2011) 121:1561–73. doi: 10.1172/JCI44583
208. Kaplan MH. Immunologic studies of heart tissue. I. Production in rabbits of antibodies reactive with an autologous myocardial antigen following immunization with heterologous heart tissue. *J Immunol*. (1958) 80: 254-67.
209. Rose NR. The adjuvant effect in infection and autoimmunity. *Clin Rev Allergy Immunol*. (2008) 34:279–82. doi: 10.1007/s12016-007-8049-7
210. Mitchell TC, Hildeman D, Kedl RM, Teague TK, Schaefer BC, White J, et al. Immunological adjuvants promote activated T cell survival via induction of Bcl-3. *Nat Immunol*. (2001) 2:397–402. doi: 10.1038/87692
211. Blyszczuk P, Kania G, Dieterle T, Marty RR, Valaperti A, Berthonneche C, et al. Myeloid differentiation factor-88/interleukin-1 signaling controls cardiac fibrosis and heart failure progression in inflammatory dilated cardiomyopathy. *Circ Res*. (2009) 105:912–20. doi: 10.1161/CIRCRESAHA.109.199802
212. Ono M, Shimizu J, Miyachi Y, Sakaguchi S. Control of autoimmune myocarditis and multiorgan inflammation by glucocorticoid-induced TNF receptor family-related protein(high), Foxp3-expressing CD25+ and CD25- regulatory T cells. *J Immunol*. (2006) 176:4748–56. doi: 10.4049/jimmunol.176.8.4748
213. Nishimura H, Nose M, Hiai H, Minato N, Honjo T. Development of lupus-like autoimmune diseases by disruption of the PD-1 gene encoding an ITIM motif-carrying immunoreceptor. *Immunity*. (1999) 11:141–51. doi: 10.1016/S1074-7613(00)80089-8
214. Goser S, Andrassy M, Buss SJ, Leuschner F, Volz CH, Ottl R, et al. Cardiac troponin I but not cardiac troponin T induces severe autoimmune inflammation in the myocardium. *Circulation*. (2006) 114:1693–702. doi: 10.1161/CIRCULATIONAHA.106.635664
215. Smith SC, Ladenson JH, Mason JW, Jaffe AS. Elevations of cardiac troponin I associated with myocarditis. Experimental and clinical correlates. *Circulation*. (1997) 95:163–8. doi: 10.1161/01.CIR.95.1.163
216. Leuschner F, Li J, Goser S, Reinhardt L, Ottl R, Bride P, et al. Absence of auto-antibodies against cardiac troponin I predicts improvement of left ventricular function after acute myocardial infarction. *Eur Heart J*. (2008) 29:1949–55. doi: 10.1093/eurheartj/ehn268
217. Mummery CL. Perspectives on the use of human induced pluripotent stem cell-derived cardiomyocytes in biomedical research. *Stem Cell Rep*. (2018) 11:1306–11. doi: 10.1016/j.stemcr.2018.11.011
218. Karakikes I, Ameen M, Termglinchan V, Wu JC. Human induced pluripotent stem cell-derived cardiomyocytes: insights into molecular, cellular, and functional phenotypes. *Circ Res*. (2015) 117:80–8. doi: 10.1161/CIRCRESAHA.117.305365
219. Zuppinger C. 3D culture for cardiac cells. *Biochim Biophys Acta*. (2016) 1863:1873–81. doi: 10.1016/j.bbamcr.2015.11.036
220. Nugraha B, Buono MF, von Boehmer L, Hoerstrup SP, Emmert MY. Human Cardiac Organoids for Disease Modeling. *Clin Pharmacol Ther*. (2019) 105:79–85. doi: 10.1002/cpt.1286

**Conflict of Interest Statement:** The author declares that the research was conducted in the absence of any commercial or financial relationships that could be construed as a potential conflict of interest.

frontiers
in Cardiovascular Medicine

REVIEW
published: 26 June 2019
doi: 10.3389/fcvm.2019.00087

# 3D Cardiac Cell Culture: A Critical Review of Current Technologies and Applications

*Christian Zuppinger**

*Cardiology, Department of Biomedical Research, Bern University Hospital, Bern, Switzerland*

OPEN ACCESS

**Edited by:**
*Maurizio Pesce,*
*Centro Cardiologico Monzino (IRCCS), Italy*

**Reviewed by:**
*Federico Quaini,*
*University of Parma, Italy*
*Antonio Paolo Beltrami,*
*University of Udine, Italy*

***Correspondence:**
*Christian Zuppinger*
*christian.zuppinger@dbmr.unibe.ch*

**Specialty section:**
*This article was submitted to Cardiovascular Biologics and Regenerative Medicine, a section of the journal Frontiers in Cardiovascular Medicine*

**Received:** *19 December 2018*
**Accepted:** *10 June 2019*
**Published:** *26 June 2019*

**Citation:**
*Zuppinger C (2019) 3D Cardiac Cell Culture: A Critical Review of Current Technologies and Applications. Front. Cardiovasc. Med. 6:87. doi: 10.3389/fcvm.2019.00087*

Three-dimensional (3D) cell culture is often mentioned in the context of regenerative medicine, for example, for the replacement of ischemic myocardium with tissue-engineered muscle constructs. Additionally, 3D cell culture is used, although less commonly, in basic research, toxicology, and drug development. These applications have recently benefited from innovations in stem cell technologies allowing the mass-production of hiPSC-derived cardiomyocytes or other cardiovascular cells, and from new culturing methods including organ-on-chip and bioprinting technologies. On the analysis side, improved sensors, computer-assisted image analysis, and data collection techniques have lowered the bar for switching to 3D cell culture models. Nevertheless, 3D cell culture is not as widespread or standardized as traditional cell culture methods using monolayers of cells on flat surfaces. The many possibilities of 3D cell culture, but also its limitations, drawbacks and methodological pitfalls, are less well-known. This article reviews currently used cardiovascular 3D cell culture production methods and analysis techniques for the investigation of cardiotoxicity, in drug development and for disease modeling.

**Keywords: 3D cell culture, induced pluripotent stem cells, cardiomyocyte, spheroid, engineered heart tissue, scaffold, high content screening**

## THE NEED FOR MORE TISSUE-LIKE CELL CULTURE MODELS

Standard cell culture using adherent cells on multi-well plastic plates, dishes and flasks is an effective technique for expanding cell lines, bioproduction, and inspection of cells in defined conditions. However, as soon as cultured cells are expected to respond to drugs, toxins or signaling modifiers like *in vivo*, cell culture on flat surfaces, i.e., two-dimensional (2D) culture, turns out to be an imperfect or downright misleading (1–4). Cells in an intact tissue are embedded in extracellular matrix proteins (ECM) and are exposed to an abundance of biochemical, mechanical, electrical and other types of stimuli that lead to appropriate responses and fine-tuned changes in gene expression. In the heart, cells undergo cyclic deformation, show rapid calcium transients and electrical signals or experience shear stress from blood flow (1). In order to retain organotypic functionality as much as possible, a straightforward approach is to use fully differentiated cells directly isolated from living tissue, as these are considered to be in a native state (2). Animal models, explanted hearts and later freshly isolated primary cells have been used for the assessments of various parameters of cardiac cell physiology and electrophysiology for more than a century, which has increased our knowledge of the basic mechanisms of the heart tremendously (5–7). Large animal models such as minipigs or goats are also still needed as they provide the essential anatomical structures to study surgical interventions and to observe *in situ* clinically relevant pathophysiological changes of heart and vessels, such as the response to pressure overload, myocarditis or atherosclerosis and infarcts (3). However, animal models are relatively expensive, need experienced personnel, long-term housing, strict quality control, and there are ethical concerns (4). Also, there are differences between the human heart and those of animals, and these differences can become more pronounced and limiting in pathological conditions (8). For these reasons, it would be advantageous to have access to *in vitro* screening models of the myocardium that allow the study of long-term effects of drugs, environmental factors and gene mutations, preferentially on a human genetic background.

Because of the above-mentioned limitations of classic models, three-dimensional (3D) culture systems have been developed that attempt to restore *in vivo* conditions in some sort of a multicellular micro-tissue (MT) with and without additional, natural or synthetic biomaterials, also called scaffolds. Historically, 3D cultures have first been used in a systematic manner for drug testing in cancer biology, which is explained in part by the fact that cellular aggregates with a hypoxic core show many similarities with avascular solid tumors (9). It has been repeatedly found, that only 3D technologies using co-cultures are able to mimic key aspects of the phenotypical and cellular heterogeneity as well as microenvironmental aspects of tumor growth (10). In the cardiovascular field, current 3D cell culture model systems that are in use for drug testing and toxicology applications mostly fall into two main categories: They contain A. a scaffold matrix, typically a hydrogel, which is mixed with and populated by cells and forms a strip or hourglass-shaped contracting MT between attachment sites, also called an engineered heart tissue (EHT) (**Figure 1**) (5), or B. smaller cellular aggregates (spheroids) forming by self-assembly without scaffold proteins in hanging drops or in multi-well plates with non-adhesive surfaces (**Figure 2**). An increasing number of studies making use of cardiac scaffold-free spheroids for drug testing and toxicology has been published in the last couple of years (6, 7) and frequently, a mix or co-culture of several cell types is used, such as rodent or human primary- or human induced pluripotent stem cell-derived cardiomyocytes (hiPSC-CMs), fibroblasts, stem cells, and endothelial cells (19–23). Additionally, microfluidic systems, micro-patterns, and microphysiological platforms, including various sensors, pumps and perfusion, and other technologies have been developed around the living components of such model systems (24). Larger tissue formats like multilayered cell sheets, re-cellularized hearts or large biomaterial patches usually are too expensive and slow in the making for drug screening purposes and are instead developed for regenerative medicine (25). Recently, the term "organoid" is more often used in the literature. However, this term should not be used for every 3D cell culture as it implies, at least by the original definition, self-organization of stem cells that leads to differentiated organotypic structures and functionality (26). In the cardiovascular field, self-organization *in vitro* has been observed in vascular networks (27), but for cardiac muscle cells, it is mostly limited to self-assembly of clusters by aggregation, alignment, concerted contractions and some degree of cellular maturation, while the actual embryonic development of a vascularized organ with chambers, working pump function and conduction system currently is not feasible to replicate *in vitro*.

## THE CELLULAR COMPONENTS OF CARDIAC 3D CULTURE AND DISEASE MODELS

The availability of differentiated cells for research is a challenge in the cardiac field as postnatal mammalian cardiomyocytes do not proliferate, and primary human cells are not available in significant quantities (28). The use of primary ventricular cardiomyocytes from adult animals or patients is not recommended for 3D culture as these rod-shaped cells do not integrate well in spherical aggregates and many cells become necrotic when kept floating for longer time (own observation). Fortunately, the development of hiPSC-CMs has helped to improve this issue and promoted research with human cardiomyocytes and 3D models in the cardiovascular field, even if the currently available hiPSC-CM are relatively immature (28–30). Also, the cell population is not entirely uniform as ventricular-type, nodal and atrial-like action potentials are found when single cells are analyzed using electrophysiological methods (29). Furthermore, there is heterogeneity in the expression of cytoskeleton and sarcomeric proteins such chamber-specific myosin light chains or troponins, and different grades of structural organization of sarcomeric proteins has been observed (30, 31). Another practical issue encountered with current protocols is the inconstant efficacy of the differentiation process and batch-to-batch variations that lead to baseline variations when cells from the same patient are repeatedly re-programmed (11, 32). The incomplete maturation of the cells may reduce the predictive power of the model system, considering that cardiovascular diseases predominantly occur in the elderly human population, although this demerit is not limited to hiPSC-CMs (33, 34). Several strategies, particularly with 3D cultures, have been employed to enhance the maturation of cultured hiPSC-CM such as novel iPSC reprogramming methods, changing the energy sources in specialized media, finding the ideal developmental time window for experiments, and electric and mechanical training of EHTs (35–38).

With the technology of hiPSC-CMs arrived the option of using patient-derived cell lines with disease-specific phenotypes and known mutations on a human genetic background, and with the full knowledge of the patient's medical history. This is an exciting prospect as it might enable new options in personalized medicine and gene therapies *in vitro* (39, 40). Similarly, hiPSC-CM technology has been used to model a number of inherited heart diseases, among them are Duchenne muscular dystrophy, Fabry disease, Danon disease, familial hypertrophic cardiomyopathy and others (41). Many of these hiPSC cell lines are publicly available in stem cell banks for use in different model systems including 3D culture approaches (42). The hypothesis that 3D culture models can provide tissue-like features was supported by using hiPSC-CMs with a disease-specific genotype in an EHT-model: The contractile deficit of

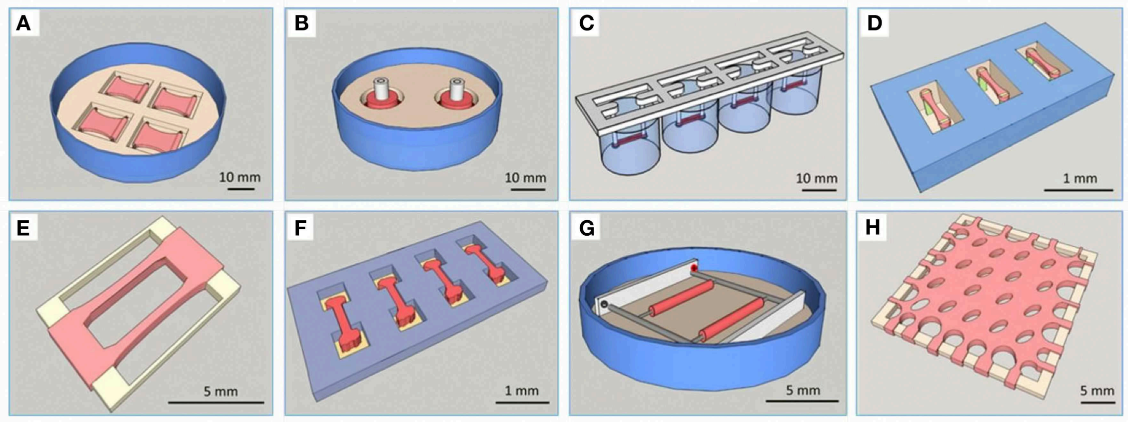

**FIGURE 1 |** Overview of different types of EHTs. Reprinted with permission from Weinberger et al. (11). **(A)** Plane EHT on Velcro-covered rods (5), **(B)** fabrication of ring-shaped EHTs (12), **(C)** fibrin-based mini-EHT on polydimethylsiloxane (PDMS) racks (13), **(D)** cardiac micro tissues (CMT) on fluorescent pillars (14), **(E)** cardiobundles on a PDMS frame (15), **(F)** micro heart muscle (16), **(G)** cardiac biowires (17), **(H)** cardiac patch (18).

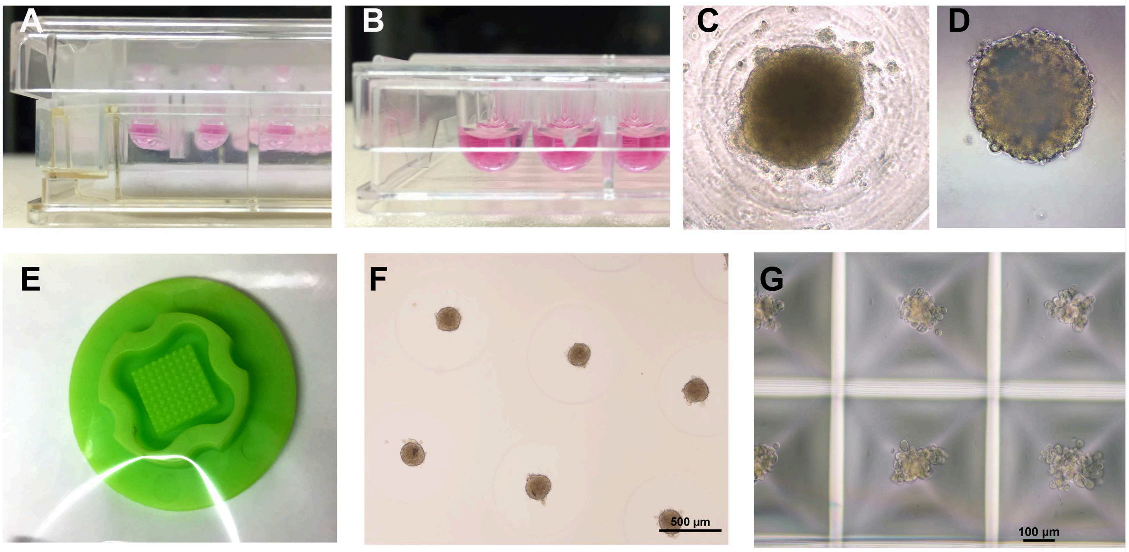

**FIGURE 2 |** Overview of different spheroid production methods. **(A)** Hanging drops (InSphero, GravityPlus), **(B)** U-shaped multi-well plate with non-adhesive coating (Greiner bio-one, Cellstar), **(C)** view inside a U-shaped well at day 2 of culture, **(D)** Spheroid made in hanging drop for 3 days was transferred to a non-adhesive multi-well plate for further culture (InSphero, GravityTrap), **(E)** Silicone micro-mold (3D Petri-dish, microtissues.com) for making an agarose cast for 81 spheroids, **(F)** Cardiac spheroids reside inside the 3D petri-dish agarose cast submerged in medium 4 days after seeding of the cell solution, **(G)** Small cardiac spheroids forming 3 days after seeding in a micro-patterned multi-well plate with 12 × 750 microwells (Kugelmeiers, Sphericalplate 5D). All photos by the author.

hiPSC-CMs with a truncation in the sarcomeric protein titin was not visible in 2D cultured cardiomyocytes but became obvious in EHTs working against the elastic resistance of PDMS or silicone pillars (39). Regarding disease models, applications in the field of cardio-oncology have motivated our lab to explore different cardiomyocyte model systems from primary adult rat cardiomyocytes to monolayers and cardiac spheroids made of hiPSC-CM and to study cancer therapy-associated changes of contractility and calcium handling (40, 43–45). Other cardiomyopathies that have been modeled in 3D cultures include cardiac fibrosis (46), hypertrophy (47), Chagas disease (48), atrial fibrillation (49), cardiotoxic cancer therapies, and other toxins (19, 20, 22, 44, 50).

## PRODUCTION METHODS

A number of different types of 3D culture models and production methods have been developed in the cardiovascular field (**Table 1**). The most basic form of 3D culture is the multicellular aggregate as it occurs by self-assembly of floating cells on low-attachment surfaces (also called liquid-overlay method). Such a suspension culture can be made in inexpensive ways, for example by using a sterile dish with a thin film of agarose. Spontaneous formation of this type of multicellular aggregate has already been observed at the time of early cardiomyocyte isolations from fetal or newborn animals (57). Many suppliers of cell culture products make variants of U-shaped bottom multi-well plates with special coating for ultra-low attachment that leads to self-assembly of spheroids (**Figures 2B,C**), or special formats for the mass-production of small aggregates (**Figure 2G**). Similarly, soft silicone molds can be used to make agarose-casts with many small wells for the production of microtissues (**Figures 2E,F**). The hanging drop technique has allowed producing uniform microtissues in a reliable way (44, 55), and sophisticated systems have been developed with hanging drops as part of microfluidic systems including perfusion and sensors (56). Overall, an advantage of the spheroid as 3D cell culture is the option of using semi-automatic methods to produce spheroids by using a pipetting robot for filling multi-well plates, exchanging medium, drug treatments, and finally analyzing the samples in high-content readers. Advantages and disadvantages of the spheroid culture vs. the EHT-models are listed in **Table 2**. The EHT model was conceived in the 90ies for the purpose of tissue engineering (5). Soon it was also used for drug testing and disease models with the option to measure contractile force, either directly or by the deflection of silicone poles, as well as calcium transients and electrical signals (13, 32, 61). Variants of the EHT model were developed that have in common the casting of a hydrogel, usually containing fibrin/thrombin and/or collagen and Matrigel components, with the addition of either primary newborn rodent cardiomyocytes or stem-cell derived cells as single and co-cultures and different geometries and analysis options (**Figure 1**). Elastic silicone posts deflect with the contractions and allow the tissue to contract auxotonically and perform contractile work, the physiological form of cardiac contraction (11). Smaller formats were developed for the purpose of drug treatment and optimization of maturation protocols (38, 41), while larger formats are suitable for regenerative therapies (11).

Vascular *in vitro* models have improved in recent years with the advent of microfluidic systems and the hope is, that these systems may partially replace animal experimentation that has been common in this field of research (62). Current vascular *in vitro* models apply different molding techniques, bioprinting, and combinations of these technologies for producing micro vessels on organ-on-chip platforms (51–53, 59). The challenge of oxygen supply in larger artificial tissues has been a matter of active research in tissue engineering for some time (24, 63). However, establishing a perfused vascular network *in vitro* turned out more difficult than initially anticipated since these processes are inherently multi-factorial and require a fine-tuned expression and post-translational processing of growth factors, a complex spatial localization of angiogenic signals in the ECM, and the collaboration of multiple cell types (organ-specific endothelial cells, pericytes, vascular smooth muscle cells) (64, 65). Instead of relying on cellular self-organization for establishing vascular networks, recent studies rather use pre-formed channels or bioprinting approaches to reach this goal (60). Additional concepts have been published that are making use of combined techniques, such as cell layers with pre-formed vascular trees obtained from animals, bioprinted and microcontact models as components of micro-physiological platforms and larger tissues for surgical applications (51, 66, 67).

## ANALYSIS METHODS

For endpoint analysis, classic lab methods like tissue fixation, paraffin embedding, histology, cryosectioning, immunolabeling, and cell viability/cytotoxicity assays are feasible with most types of 3D cultures where the cells are accessible. Protein chemistry, RNA isolation and histology usually require pooling of groups of smaller cellular aggregates (own observations). A number of cell viability/toxicology assays are commercially available that can be performed with either live MT or lysed material (67). Cell physiology methods for the investigation of cardiac features in living tissues such as contractions, force, calcium cycling or electric signals require specialized instrumentation depending on the sensitivity of the sensors and the desired temporal and spatial resolution (68). Although methods exist to directly measure contractile force in single cardiac cells and small muscle strips, these methods require a skilled workforce in order to provide good reproducibility and have a slow throughput (69). Instead, a variety of optical methods have been developed to measure length changes of the whole cells or sarcomers during the contractile cycle of mammalian cardiomyocytes (70–72). These video-based systems are either commercially available as complete bundles of hardware and software (IonOptix, Sony, EHT technologies), or as open access software for image analysis that can be used with existing microscopes and cameras (73, 74). Such a video-based analysis can be realized in inexpensive ways using modified consumer cameras (so-called action cameras with high frame rates up to 240 frames per second) and open source software (68). Optical measurement using white light has the advantage of being label-free and non-invasive, so the measurement can be repeated many times, even while the cell culture is in the incubator if a camera is placed inside an atmosphere- and temperature-controlled environment (68). Besides classic electrophysiology methods using patching and impaling with sharp microelectrode pipettes, multi-electrode arrays, and impedance spectroscopy have been used to measure electrical signals and contractile activity in cardiac 3D models (75–78). Calcium-binding fluorescent dyes and voltage-sensitive dyes have been used in 2D- and 3D-cultures as this method allows to measure a greater number of samples in relatively short time, and for some applications high-content readers can be used for this purpose (Hamamatsu Photonics, Molecular Devices, PerkinElmer) (50, 79). Although these optical methods provide good results for live 3D cultures as a whole tissue, obtaining data at (sub-)cellular level from inside these MT is challenging without relying on time-consuming histology methods. High optical resolution comes at the price of limited penetration depth and technical issues such as the permeability for fluorescent dyes and antibodies, the working distance of lenses and the geometry of sample holders limit these whole-mount microscopy applications. Recently, several approaches to "clearing" MTs (i.e., homogenizing the refractive index of the fixed tissue so that

**TABLE 1 |** Overview of cardiovascular 3D cell culture technologies.

| Type | Specific bio-functional properties | Companies | References |
|---|---|---|---|
| Molded natural or synthetic hydrogels populated by cells, attached to elastic micro-poles or a frame | Microtissues showing linearly aligned cardiomyocytes and improved tissue and cellular maturation after training, force measurements are feasible | EHT-technologies, novoheart | (5, 12, 13, 15, 17, 38) |
| Enclosed cells and hydrogels (in molds, tubing, or microfluidic channels), with perfusion | For microvascular models, self-organizing cells, may include shear-stress and stretch, measurement of barrier function | Mimetas, AlveoliX, TissUse | (51–54) |
| Self-assembling multicellular aggregates on low attachment plates, hanging drops or micropatterned surfaces | Small aggregates and spheroids showing spontaneous beating activity, can be mass-produced, treated and analyzed by semi-automatic systems | InSphero, microtissues.com, Corning, Kugelmeiers, Stemcell, Greiner, Nunclon, Cytoo | (6, 44, 55–57) |
| Magnetic levitation, bioprinting of larger structures, layering of sheets | Large tissues consisting of different cell types and biomaterials, making entire organs as the ultimate goal | n3D Biosciences, RegenHU, CellInk, Biolife4D | (58–60) |

*Literature references and companies represent a non-exhaustive list and the author apologizes for any omissions.*

**TABLE 2 |** Comparison of advantages and disadvantages of scaffold-based models and cardiac spheroids.

| Advantage | Features of cardiac spheroids | Disadvantage |
|---|---|---|
| Uses only a small number of potentially costly cells per data point | Small size of multicellular aggregates | Methods like protein chemistry and RNA extraction need pooling of spheroids |
| No interference of scaffold proteins with the development of the microtissue or the outcome of assays | Made without additional scaffold proteins | Some ECM factors could improve survival and self-organization of the tissue |
| Spheroid is quickly formed and ready for drug treatment and analysis | Assembles spontaneously by gravity or on non-adhesive surface | Little control over the distribution of cell types or overall shape, may result in multiple spheroids |
| Manipulation by pipetting and sedimentation, no touching | Spheroids are floating in culture | Spheroids may get lost or stuck on surfaces in pipetting steps |
| Mimics thicker tissues (and tumors) | Larger spheroids develop zones of $o_2$, PH, metabolites | Reduced viability, variable results, limited diffusion |
| Motion activity and calcium cycling correlates with cell viability and drug treatment | Show long-term spontaneous contractions | No direct force measurement, non-linear cell alignment |
| Miniaturized multi-well formats and compatible with plate readers | Spheroids can be cultured in single wells | - |
| **Advantage** | **Features of scaffold-based models (EHT)** | **Disadvantage** |
| Shape can be tailored for applications (screening, maturation, regen. Medicine) | Shape is determined by the scaffold/hydrogel mold | Uses large number of cells per tissue |
| Hydrogel can be adapted for organotypic functions and pathologies (vascularization, stiffness) | Made with scaffold biomaterial and ECM proteins | Limited diffusion, risk of breaking, unequal distribution of cells, potential interference with assays |
| Sensors can be integrated in microphysiological devices | Tissues attached to support structures | Manual steps necessary, small number of tissues of the same batch of cells |
| Mech. And electrical training, physiological function in disease models, force assessment | Linear alignment of muscle cells | - |
| Technology development toward tissue engineering applications | Training protocols show improved maturation of hiPSC-CM | - |

it becomes transparent) have been published, and commercial solutions have become available, especially for the use with spheroids and fluorescence high-content confocal imaging (80).

When it comes to choosing a 3D culture model system, the requirements of the project dictate crucial analysis methods. For a study of mechanical features of a muscle-construct, a hydrogel-based EHT model system might be chosen, where the cells experience mechanical load and have the ability to align longitudinally. Contractile force can then be measured either directly or using video methods by measuring the deflection of attached micro-posts or pillars of known strength (39, 40, 49, 50). Otherwise, if mainly the spontaneous or electrically paced beating pattern and viability of cardiac tissues is of interest in a larger number of samples, cardiac spheroids may be the model of choice. Cardiac functionality of these spheroids can be analyzed A) using label-free methods either by computational video analysis or electrical impedance spectroscopy methods, or B) using calcium- or voltage-sensitive dyes in multi-well plate readers, or by using more advanced microscope equipment for multiparametric assessment (19, 44, 56, 68, 81–84). A comparison of features and comparative advantages or disadvantages of these scaffold-containing or scaffold-free models is shown in **Table 2**. Finally, it could be summarized that spheroid models are easier to integrate in existing drug developmental pipelines and to upscale the number of tests in the same batch, while the ETH models provide a better physiological representation of the myocardium and thereby enable the analysis of advanced disease models.

## WHY IS 3D CELL CULTURE NOT USED MORE OFTEN?

Although many tools and reagents for making and analyzing 3D cell culture models are commercially available, and the number of publications in all fields of life science is increasing (85), the technology is infrequently used, outside of regenerative medicine, in academic research labs or industry several decades after the publication of the first studies (86). Reasons for this situation include that standard 2D culture is well established, with ample literature available, and previous studies to compare results (87). Furthermore, 2D culture has gained uncritical acceptance in the past, is less expensive, is more standardized, and is often easier and less time-consuming to analyze and to handle in the lab. When considering practical aspects of working with 3D culture, seemingly trivial tasks such as regular checking for culture health and growth are more difficult with most 3D models, because even smaller tissues usually are opaque and single cells not discernable unless stained (**Figures 2C,D**). Additionally, manual handling of the microtissues and culture medium can be challenging when the MTs are free floating, fragile or access to the tissue(s) is obstructed by surrounding containers and technical equipment. Some systems facilitate the handling of spheroids by trapping them in conical wells, in perfused chambers inside organ-on-chip designs or by incorporation of magnetic nanoparticles (88, 89) (**Table 1**). Fortunately, there are more technologies and products coming to the market that are targeted at 3D cell culture applications such as different formats of spheroid and EHT production systems, microfluidic technology and suitable ready-to-use equipment, reagents for the clarification of thicker tissues and adapted microscopes and software for live imaging. Finally, and despite the above-mentioned technological advancements, the research community has to agree to a set of standards and read-outs to use in efficacy and toxicity screening (90). Replacement of animal research by *in vitro* technologies using human cells is another substantial incentive for 3D cell culture, and already had a significant impact, for example, on how cosmetics are tested *in vitro* as the use of animals is banned for this purpose in Europe (4, 67). Still, it can be debated if existing 3D models already provide sufficient evidence for superior predictions of the clinical outcome of a new drug, and if these models show enough physiological relevance compared to animal or human tissue, or still lack complexity, for example regarding the role of the vasculature or the immune system (12, 90).

## CONCLUSIONS AND OUTLOOK

Each *in vitro* model has advantages and disadvantages for using it with certain assays, regarding organotypic features and production methods. Therefore, it needs to be decided upfront, which parameters and organotypic features are essential to be included in the study and if going 3D is making sense in the context of a particular project. Apparently, if the project deals with features of single cells isolated from its myocardial environment, then 2D cultured cardiomyocytes offer the option to use classic electrophysiology, high-resolution microscopy, and other methods. Instead 3D culture mimics features of larger tissues or entire organs and is the method of choice for co-culture models. 3D cardiac cell culture technologies hold great potential for applications in tissue engineering, drug development, cardio-toxicology and disease modeling. But a considerable effort is still needed to assure the accuracy, relevance, and reproducibility of these models and to improve automation and readout techniques. Instead of pushing many different systems to the market, careful analysis of core concepts may be instrumental for establishing 3D cell culture as a widespread and validated tool in life science.

## AUTHOR CONTRIBUTIONS

All content is prepared by the author CZ with the exception of **Figure 1** that is reprinted with permission from Wolters Kluwer Health, Inc.

## FUNDING

This work was supported by the Swiss Heart Foundation to CZ.

## ACKNOWLEDGMENTS

We thank Sarah Longnus Ph.D. (Cardiac Surgery Department, Univ. Hospital Bern) for support and discussions.

## REFERENCES

1. Tirziu D, Giordano FJ, Simons M. Cell communications in the heart. *Circulation*. (2010) 122:928–37. doi: 10.1161/CIRCULATIONAHA.108.847731
2. Louch WE, Sheehan KA, Wolska BM. Methods in cardiomyocyte isolation, culture, and gene transfer. *J Mol Cell Cardiol*. (2011) 51:288–98. doi: 10.1016/j.yjmcc.2011.06.012
3. Savoji H, Mohammadi MH, Rafatian N, Toroghi MK, Wang EY, Zhao Y, et al. Cardiovascular disease models: a game changing paradigm in drug discovery and screening. *Biomaterials*. (2019) 198:3–26. doi: 10.1016/j.biomaterials.2018.09.036
4. Hartung T. Look back in anger - what clinical studies tell us about preclinical work. *ALTEX*. (2013) 30:275–91. doi: 10.14573/altex.2013.3.275
5. Eschenhagen T, Fink C, Remmers U, Scholz H, Wattchow J, Weil J, et al. Three-dimensional reconstitution of embryonic cardiomyocytes in a collagen

matrix: a new heart muscle model system. *FASEB J*. (1997) 11:683–94. doi: 10.1096/fasebj.11.8.9240969

6. Kelm JM, Ehler E, Nielsen LK, Schlatter S, Perriard J-C, Fussenegger M. Design of artificial myocardial microtissues. *Tissue Eng*. (2004) 10:201–14. doi: 10.1089/107632704322791853
7. Figtree GA, Bubb KJ, Tang O, Kizana E, Gentile C. Vascularized cardiac spheroids as novel 3d *in vitro* models to study cardiac fibrosis. *Cells Tissues Organs*. (2017) 204:191–8. doi: 10.1159/000477436
8. Milani-Nejad N, Janssen PML. Small and large animal models in cardiac contraction research: advantages and disadvantages. *Pharmacol Ther*. (2014) 141:235–49. doi: 10.1016/j.pharmthera.2013.10.007
9. Inch WR, McCredie JA, Sutherland RM. Growth of nodular carcinomas in rodents compared with multi-cell spheroids in tissue culture. *Growth*. (1970) 34:271–82.
10. Thoma CR, Zimmermann M, Agarkova I, Kelm JM, Krek W. 3D cell culture systems modeling tumor growth determinants in cancer target discovery. *Adv Drug Deliv Rev*. (2014) 69–70:29–41. doi: 10.1016/j.addr.2014.03.001
11. Weinberger F, Mannhardt I, Eschenhagen T. Engineering cardiac muscle tissue: a maturating field of research. *Circ Res*. (2017) 120:1487–500. doi: 10.1161/CIRCRESAHA.117.310738
12. Zimmermann W-H, Schneiderbanger K, Schubert P, Didié M, Münzel F, Heubach JF, et al. Tissue engineering of a differentiated cardiac muscle construct. *Circ Res*. (2002) 90:223–30. doi: 10.1161/hh0202.103644
13. Hansen A, Eder A, Bönstrup M, Flato M, Mewe M, Schaaf S, et al. Development of a drug screening platform based on engineered heart tissue. *Circ Res*. (2010) 107:35–44. doi: 10.1161/CIRCRESAHA.109.211458
14. Boudou T, Legant WR, Mu A, Borochin MA, Thavandiran N, Radisic M, et al. A microfabricated platform to measure and manipulate the mechanics of engineered cardiac microtissues. *Tissue Eng Part A*. (2012) 18:910–9. doi: 10.1089/ten.tea.2011.0341
15. Jackman CP, Carlson AL, Bursac N. Dynamic culture yields engineered myocardium with near-adult functional output. *Biomaterials*. (2016) 111:66–79. doi: 10.1016/j.biomaterials.2016.09.024
16. Huebsch N, Loskill P, Deveshwar N, Spencer CI, Judge LM, Mandegar MA, et al. Miniaturized iPS-cell-derived cardiac muscles for physiologically relevant drug response analyses. *Sci Rep*. (2016) 6:24726. doi: 10.1038/srep24726
17. Nunes SS, Miklas JW, Liu J, Aschar-Sobbi R, Xiao Y, Zhang B, et al. Biowire: a platform for maturation of human pluripotent stem cell-derived cardiomyocytes. *Nat Methods*. (2013) 10:781–7. doi: 10.1038/nmeth.2524
18. Bian W, Jackman CP, Bursac N. Controlling the structural and functional anisotropy of engineered cardiac tissues. *Biofabrication*. (2014) 6:024109–9. doi: 10.1088/1758-5082/6/2/024109
19. Polonchuk L, Chabria M, Badi L, Hoflack J-C, Figtree G, Davies MJ, et al. Cardiac spheroids as promising *in vitro* models to study the human heart microenvironment. *Sci Rep*. (2017) 7:7005. doi: 10.1038/s41598-017-06385-8
20. Archer CR, Sargeant R, Basak J, Pilling J, Barnes JR, Pointon A. Characterization and validation of a human 3D cardiac microtissue for the assessment of changes in cardiac pathology. *Sci Rep*. (2018) 8:10160. doi: 10.1038/s41598-018-28393-y
21. Ravenscroft SM, Pointon A, Williams AW, Cross MJ, Sidaway JE. Cardiac non-myocyte cells show enhanced pharmacological function suggestive of contractile maturity in stem cell derived cardiomyocyte microtissues. *Toxicol Sci*. (2016) 152:99–112. doi: 10.1093/toxsci/kfw069
22. Verheijen M, Schrooders Y, Gmuender H, Nudischer R, Clayton O, Hynes J, et al. Bringing *in vitro* analysis closer to *in vivo*: Studying doxorubicin toxicity and associated mechanisms in 3D human microtissues with PBPK-based dose modelling. *Toxicol Lett*. (2018) 294:184–92. doi: 10.1016/j.toxlet.2018.05.029
23. Richards DJ, Coyle RC, Tan Y, Jia J, Wong K, Toomer K, et al. Inspiration from heart development: biomimetic development of functional human cardiac organoids. *Biomaterials*. (2017) 142:112–23. doi: 10.1016/j.biomaterials.2017.07.021
24. Mathur A, Ma Z, Loskill P, Jeeawoody S, Healy KE. *In vitro* cardiac tissue models: Current status and future prospects. *Adv Drug Deliv Rev*. (2016) 96:203–13. doi: 10.1016/j.addr.2015.09.011
25. Jackman CP, Ganapathi AM, Asfour H, Qian Y, Allen BW, Li Y, et al. Engineered cardiac tissue patch maintains structural and electrical properties after epicardial implantation. *Biomaterials*. (2018) 159:48–58. doi: 10.1016/j.biomaterials.2018.01.002
26. Lancaster MA, Knoblich JA. Organogenesis in a dish: modeling development and disease using organoid technologies. *Science*. (2014) 345:1247125–5. doi: 10.1126/science.1247125
27. Folkman J, Haudenschild C. Angiogenesis *in vitro*. *Nature*. (1980) 288:551–6. doi: 10.1038/288551a0
28. Mercola M, Ruiz-Lozano P, Schneider MD. Cardiac muscle regeneration: lessons from development. *Genes Dev*. (2011) 25:299–309. doi: 10.1101/gad.2018411
29. Veerman CC, Kosmidis G, Mummery CL, Casini S, Verkerk AO, Bellin M. Immaturity of human stem-cell-derived cardiomyocytes in culture: fatal flaw or soluble problem? *Stem Cells Dev*. (2015) 24:1035–52. doi: 10.1089/scd.2014.0533
30. Zuppinger C, Gibbons G, Dutta-Passecker P, Segiser A, Most H, Suter TM. Characterization of cytoskeleton features and maturation status of cultured human iPSC-derived cardiomyocytes. *Eur J Histochem*. (2017) 61:2763. doi: 10.4081/ejh.2017.2763
31. Bedada FB, Wheelwright M, Metzger JM. Maturation status of sarcomere structure and function in human iPSC-derived cardiac myocytes. *Biochim Biophys Acta*. (2015) 1863(7 Pt B):1829–38. doi: 10.1016/j.bbamcr.2015.11.005
32. Eschenhagen T, Mummery C, Knollmann BC. Modelling sarcomeric cardiomyopathies in the dish: from human heart samples to iPSC cardiomyocytes. *Cardiovasc Res*. (2015) 105:424–38. doi: 10.1093/cvr/cvv017
33. Bellin M, Marchetto MC, Gage FH, Mummery CL. Induced pluripotent stem cells: the new patient? *Nat Rev Mol Cell Biol*. (2012) 13:713–26. doi: 10.1038/nrm3448
34. Feric NT, Radisic M. Maturing human pluripotent stem cell-derived cardiomyocytes in human engineered cardiac tissues. *Adv Drug Deliv Rev*. (2016) 96:110–34. doi: 10.1016/j.addr.2015.04.019
35. Fong AH, Romero-López M, Heylman CM, Keating M, Tran D, Sobrino A, et al. Three-dimensional adult cardiac extracellular matrix promotes maturation of human induced pluripotent stem cell-derived cardiomyocytes. *Tissue Eng Part A*. (2016) 22:1016–25. doi: 10.1089/ten.TEA.2016.0027.
36. Correia C, Koshkin A, Duarte P, Hu D, Carido M, Sebastião MJ, et al. 3D aggregate culture improves metabolic maturation of human pluripotent stem cell derived cardiomyocytes. *Biotechnol Bioeng*. (2017) 87:521. doi: 10.1002/bit.26504
37. Ulmer BM, Stoehr A, Schulze ML, Patel S, Gucek M, Mannhardt I, et al. Contractile work contributes to maturation of energy metabolism in hiPSC-derived cardiomyocytes. *Stem Cell Rep*. (2018) 10:834–47. doi: 10.1016/j.stemcr.2018.01.039
38. Ronaldson-Bouchard K, Ma SP, Yeager K, Chen T, Song L, Sirabella D, et al. Advanced maturation of human cardiac tissue grown from pluripotent stem cells. *Nature*. (2018) 556:239–43. doi: 10.1038/s41586-018-0016-3
39. Hinson JT, Chopra A, Nafissi N, Polacheck WJ, Benson CC, Swist S, et al. HEART DISEASE. Titin mutations in iPS cells define sarcomere insufficiency as a cause of dilated cardiomyopathy. *Science*. (2015) 349:982–6. doi: 10.1126/science.aaa5458
40. Sawyer DB, Zuppinger C, Miller TA, Eppenberger HM. Modulation of anthracycline-induced myofibrillar disarray in rat ventricular myocytes by neuregulin-1β and anti-erbB2 Potential Mechanism for trastuzumab-induced cardiotoxicity. *Circulation*. (2002) 105:1551–4. doi: 10.1161/01.CIR.0000013839.41224.1C
41. Giacomelli E, Mummery CL, Bellin M. Human heart disease: lessons from human pluripotent stem cell-derived cardiomyocytes. *Cell Mol Life Sci*. (2017) 74:3711–39. doi: 10.1007/s00018-017-2546-5
42. Bellin M, Mummery CL. Inherited heart disease - what can we expect from the second decade of human iPS cell research? *FEBS Lett*. (2016) 590:2482–93. doi: 10.1002/1873-3468.12285
43. Timolati F, Ott D, Pentassuglia L, Giraud M-N, Perriard J-C, Suter TM, et al. Neuregulin-1 beta attenuates doxorubicin-induced alterations of excitation-contraction coupling and reduces oxidative stress in adult rat cardiomyocytes. *J Mol Cell Cardiol*. (2006) 41:845–54. doi: 10.1016/j.yjmcc.2006.08.002
44. Beauchamp P, Moritz W, Kelm JM, Ullrich ND, Agarkova I, Anson B, et al. Development and characterization of a scaffold-free 3D spheroid model of iPSC-derived human cardiomyocytes. *Tissue Eng Part C Methods*. (2015) 21:852–61. doi: 10.1089/ten.tec.2014.0376

45. Lim CC, Zuppinger C, Guo X, Kuster GM, Helmes M, Eppenberger HM, et al. Anthracyclines induce calpain-dependent titin proteolysis and necrosis in cardiomyocytes. *Am Soc Biochem Mol Biol*. (2004) 279:8290–9. doi: 10.1074/jbc.M308033200
46. Lee M-O, Jung KB, Jo S-J, Hyun S-A, Moon K-S, Seo J-W, et al. Modelling cardiac fibrosis using three-dimensional cardiac microtissues derived from human embryonic stem cells. *J Biol Eng*. (2019) 13:15. doi: 10.1186/s13036-019-0139-6
47. Hirt MN, Sörensen NA, Bartholdt LM, Boeddinghaus J, Schaaf S, Eder A, et al. Increased afterload induces pathological cardiac hypertrophy: a new *in vitro* model. *Basic Res Cardiol*. (2012) 107:307–16. doi: 10.1007/s00395-012-0307-z
48. Garzoni LR, Adesse D, Soares MJ, Rossi MID, Borojevic R, de Meirelles M de NL. Fibrosis and hypertrophy induced by Trypanosoma cruzi in a three-dimensional cardiomyocyte-culture system. *J Infect Dis*. (2008) 197:906–15. doi: 10.1086/528373
49. Zhao Y, Rafatian N, Feric NT, Cox BJ, Aschar-Sobbi R, Wang EY, et al. A platform for generation of chamber-specific cardiac tissues and disease modeling. *Cell*. (2019) 176:913–8. doi: 10.1016/j.cell.2018.11.042
50. Sirenko O, Grimm FA, Ryan KR, Iwata Y, Chiu WA, Parham F, et al. *In vitro* cardiotoxicity assessment of environmental chemicals using an organotypic human induced pluripotent stem cell-derived model. *Toxicol Appl Pharmacol*. (2017) 322:60–74. doi: 10.1016/j.taap.2017.02.020
51. Hasan A, Paul A, Vrana NE, Zhao X, Memic A, Hwang Y-S, et al. Microfluidic techniques for development of 3D vascularized tissue. *Biomaterials*. (2014) 35:7308–25. doi: 10.1016/j.biomaterials.2014.04.091
52. Sfriso R, Zhang S, Bichsel CA, Steck O, Despont A, Guenat OT, et al. 3D artificial round section micro-vessels to investigate endothelial cells under physiological flow conditions. *Sci Rep*. (2018) 8:5898. doi: 10.1038/s41598-018-24273-7
53. Bichsel CA, Hall SRR, Schmid RA, Guenat OT, Geiser T. Primary human lung pericytes support and stabilize *in vitro* perfusable microvessels. *Tissue Eng Part A*. (2015) 21:2166–76. doi: 10.1089/ten.tea.2014.0545
54. van Duinen V, Zhu D, Ramakers C, van Zonneveld AJ, Vulto P, Hankemeier T. Perfused 3D angiogenic sprouting in a high-throughput *in vitro* platform. *Angiogenesis*. (2018) 438:932–9. doi: 10.1007/s10456-018-9647-0
55. Kelm JM, Breitbach M, Fischer G, Odermatt B, Agarkova I, Fleischmann BK, et al. 3D microtissue formation of undifferentiated bone marrow mesenchymal stem cells leads to elevated apoptosis. *Tissue Eng Part A*. (2012) 18:692–702. doi: 10.1089/ten.tea.2011.0281
56. Frey O, Misun PM, Fluri DA, Hengstler JG, Hierlemann A. Reconfigurable microfluidic hanging drop network for multi-tissue interaction and analysis. *Nat Commun*. (2014) 5:4250. doi: 10.1038/ncomms5250
57. Halbert SP, Bruderer R, Lin TM. *In vitro* organization of dissociated rat cardiac cells into beating three-dimensional structures. *J Exp Med*. (1971) 133:677–95. doi: 10.1084/jem.133.4.677
58. Haisler WL, Timm DM, Gage JA, Tseng H, Killian TC, Souza GR. Three-dimensional cell culturing by magnetic levitation. *Nat Protoc*. (2013) 8:1940–9. doi: 10.1038/nprot.2013.125
59. Cui H, Miao S, Esworthy T, Zhou X, Lee S-J, Liu C, et al. 3D bioprinting for cardiovascular regeneration and pharmacology. *Adv Drug Deliv Rev*. (2018) 132:252–69. doi: 10.1016/j.addr.2018.07.014
60. Mironov V, Visconti RP, Kasyanov V, Forgacs G, Drake CJ, Markwald RR. Organ printing: tissue spheroids as building blocks. *Biomaterials*. (2009) 30:2164–74. doi: 10.1016/j.biomaterials.2008.12.084
61. Mannhardt I, Breckwoldt K, Letuffe-Brenière D, Schaaf S, Schulz H, Neuber C, et al. Human engineered heart tissue: analysis of contractile force. *Stem Cell Rep*. (2016) 7:29–42. doi: 10.1016/j.stemcr.2016.04.011
62. Suter-Dick L, Alves PM, Blaauboer BJ, Bremm K-D, Brito C, Coecke S, et al. Stem cell-derived systems in toxicology assessment. *Stem Cells Dev*. (2015) 24:1284–96. doi: 10.1089/scd.2014.0540
63. Kelm JM, Diaz Sanchez-Bustamante C, Ehler E, Hoerstrup SP, Djonov V, Ittner L, et al. VEGF profiling and angiogenesis in human microtissues. *J Biotechnol*. (2005) 118:213–29. doi: 10.1016/j.jbiotec.2005.03.016
64. Jain RK. Molecular regulation of vessel maturation. *Nat Med*. (2003) 9:685–93. doi: 10.1038/nm0603-685
65. Martino MM, Brkic S, Bovo E, Burger M, Schaefer DJ, Wolff T, et al. Extracellular matrix and growth factor engineering for controlled angiogenesis in regenerative medicine. *Front Bioeng Biotechnol*. (2015) 3:45. doi: 10.3389/fbioe.2015.00045
66. Lind JU, Busbee TA, Valentine AD, Pasqualini FS, Yuan H, Yadid M, et al. Instrumented cardiac microphysiological devices via multimaterial three-dimensional printing. *Nat Mater*. (2017) 16:303–8. doi: 10.1038/nmat4782
67. Rimann M, Graf-Hausner U. Synthetic 3D multicellular systems for drug development. *Curr Opin Biotechnol*. (2012) 23:803–9. doi: 10.1016/j.copbio.2012.01.011
68. Zuppinger C. Measurement of contractility and calcium release in cardiac spheroids. In: Heizmann CW, editor. *Calcium-Binding Proteins of the EF-Hand Superfamily. Methods in Molecular Biology*, Vol. 1929. New York, NY: Humana Press (2019). p. 41–52. doi: 10.1007/978-1-4939-9030-6_4
69. Palmer RE, Brady AJ, Roos KP. Mechanical measurements from isolated cardiac myocytes using a pipette attachment system. *Am J Physiol*. (1996) 270(2 Pt 1):C697–704. doi: 10.1152/ajpcell.1996.270.2.C697
70. Huebsch N, Loskill P, Mandegar MA, Marks NC, Sheehan AS, Ma Z, et al. Automated video-based analysis of contractility and calcium flux in human-induced pluripotent stem cell-derived cardiomyocytes cultured over different spatial scales. *Tissue Eng Part C Methods*. (2015) 21:467–79. doi: 10.1089/ten.tec.2014.0283
71. Kondo RP, Apstein CS, Eberli FR, Tillotson DL, Suter TM. Increased calcium loading and inotropy without greater cell death in hypoxic rat cardiomyocytes. *Am J Physiol*. (1998) 275(6 Pt 2):H2272–82. doi: 10.1152/ajpheart.1998.275.6.H2272
72. Timolati F, Anliker T, Groppalli V, Perriard J-C, Eppenberger HM, Suter TM, et al. The role of cell death and myofibrillar damage in contractile dysfunction of long-term cultured adult cardiomyocytes exposed to doxorubicin. *Cytotechnology*. (2009) 61:25–36. doi: 10.1007/s10616-009-9238-4
73. Sala L, van Meer BJ, Tertoolen LT, Bakkers J, Bellin M, Davis RP, et al. MUSCLEMOTION: a versatile open software tool to quantify cardiomyocyte and cardiac muscle contraction *in vitro* and *in vivo*. *Circ Res*. (2017) 122:e5–16. doi: 10.1161/CIRCRESAHA.117.312067
74. Laurila E, Ahola A, Hyttinen J, Aalto-Setälä K. Methods for *in vitro* functional analysis of iPSC derived cardiomyocytes - Special focus on analyzing the mechanical beating behavior. *Biochim Biophys Acta*. (2016) 1863(7 Pt B):1864–72. doi: 10.1016/j.bbamcr.2015.12.013
75. Schulze ML, Lemoine MD, Fischer AW, Scherschel K, David R, Riecken K, et al. Dissecting hiPSC-CM pacemaker function in a cardiac organoid model. *Biomaterials*. (2019) 206:133–45. doi: 10.1016/j.biomaterials.2019.03.023
76. Bürgel SC, Diener L, Frey O, Kim J-Y, Hierlemann A. Automated, multiplexed electrical impedance spectroscopy platform for continuous monitoring of microtissue spheroids. *Anal Chem*. (2016) 88:10876–83. doi: 10.1021/acs.analchem.6b01410
77. Bartholomä P, Gorjup E, Monz D, Reininger-Mack A, Thielecke H, Robitzki A. Three-dimensional *in vitro* reaggregates of embryonic cardiomyocytes: a potential model system for monitoring effects of bioactive agents. *J Biomol Screen*. (2005) 10:814–22. doi: 10.1177/1087057105280070
78. Frey U, Sanchez-Bustamante CD, Ugniwenko T, Heer F, Sedivy J, Hafizovic S, et al. Cell recordings with a CMOS high-density microelectrode array. *Conf Proc IEEE Eng Med Biol Soc*. (2007) 2007:167–70. doi: 10.1109/IEMBS.2007.4352249
79. Zeng H, Roman MI, Lis E, Lagrutta A, Sannajust F. Use of FDSS/μCell imaging platform for preclinical cardiac electrophysiology safety screening of compounds in human induced pluripotent stem cell-derived cardiomyocytes. *J Pharmacol Toxicol Methods*. (2016) 81:217–22. doi: 10.1016/j.vascn.2016.05.009
80. Boutin ME, Voss TC, Titus SA, Cruz-Gutierrez K, Michael S, Ferrer M. A high-throughput imaging and nuclear segmentation analysis protocol for cleared 3D culture models. *Sci Rep*. (2018) 8:11135. doi: 10.1038/s41598-018-29169-0
81. Jahnke H-G, Steel D, Fleischer S, Seidel D, Kurz R, Vinz S, et al. A novel 3D label-free monitoring system of hES-derived cardiomyocyte clusters: a step forward to *in vitro* cardiotoxicity testing. (2013) 8:e68971. doi: 10.1371/journal.pone.0068971
82. Sirenko O, Hancock MK, Crittenden C, Hammer M, Keating S, Carlson CB, et al. Phenotypic assays for characterizing compound effects on induced

pluripotent stem cell-derived cardiac spheroids. *Assay Drug Dev Technol*. (2017) 15:280–96. doi: 10.1089/adt.2017.792

83. Zuppinger C. Edge-detection for contractility measurements with cardiac spheroids. In: Clements M, Roquemore L, editors. *Stem Cell-Derived Models in Toxicology*. New York, NY: Humana Press (2017) p. 211–27. doi: 10.1007/978-1-4939-6661-5_11
84. Lemme M, Ulmer BM, Lemoine MD, Zech ATL, Flenner F, Ravens U, et al. Atrial-like engineered heart tissue: an *in vitro* model of the human atrium. *Stem Cell Rep*. (2018) 11:1378–90. doi: 10.1016/j.stemcr.2018.10.008
85. Simian M, Bissell MJ. Organoids: a historical perspective of thinking in three dimensions. *J Cell Biol*. (2017) 216:31–40. doi: 10.1083/jcb.201610056
86. Horvath P, Aulner N, Bickle M, Davies AM, Nery ED, Ebner D, et al. Screening out irrelevant cell-based models of disease. *Nat Rev Drug Discov*. (2016) 15:751–69. doi: 10.1038/nrd.2016.175
87. Antoni D, Burckel H, Josset E, Noel G. Three-dimensional cell culture: a breakthrough *in vivo*. *Int J Mol Sci*. (2015) 16:5517–27. doi: 10.3390/ijms16035517
88. Kim J-Y, Fluri DA, Marchan R, Boonen K, Mohanty S, Singh P, et al. 3D spherical microtissues and microfluidic technology for multi-tissue experiments and analysis. *J Biotechnol*. (2015) 205:24–35. doi: 10.1016/j.jbiotec.2015.01.003
89. Haisler WL, Timm DM, Gage JA, Tseng H, Killian TC, Souza GR. Three-dimensional cell culturing by magnetic levitation. *Nat Protoc*. (2013) 8:1940–9. doi: 10.1038/nprot.2013.125
90. Kelm JM, Lal-Nag M, Sittampalam GS, Ferrer M. Translational *in vitro* research: integrating 3D drug discovery and development processes into the drug development pipeline. *Drug Discov Today*. (2018) 24:26–30. doi: 10.1016/j.drudis.2018.07.007

**Conflict of Interest Statement:** The author declares that the research was conducted in the absence of any commercial or financial relationships that could be construed as a potential conflict of interest.

frontiers
in Cardiovascular Medicine

ORIGINAL RESEARCH
published: 01 August 2019
doi: 10.3389/fcvm.2019.00105

# Identification and Isolation of Cardiac Fibroblasts From the Adult Mouse Heart Using Two-Color Flow Cytometry

*Mara Stellato[1], Marcin Czepiel[2], Oliver Distler[1], Przemysław Błyszczuk[1,2] and Gabriela Kania[1]**

[1] *Department of Rheumatology, Center of Experimental Rheumatology, University Hospital Zurich, Zurich, Switzerland,*
[2] *Department of Clinical Immunology, Jagiellonian University Medical College, Cracow, Poland*

**Background:** Cardiac fibroblasts represent a main stromal cell type in the healthy myocardium. Activation of cardiac fibroblasts has been implicated in the pathogenesis of many heart diseases. Profibrotic stimuli activate fibroblasts, which proliferate and differentiate into pathogenic myofibroblasts causing a fibrotic phenotype in the heart. Cardiac fibroblasts are characterized by production of type I collagen, but non-transgenic methods allowing their identification and isolation require further improvements. Herein, we present a new and simple flow cytometry-based method to identify and isolate cardiac fibroblasts from the murine heart.

**Methods and Results:** Wild-type and reporter mice expressing enhanced green fluorescent protein (EGFP) under the murine alpha1(I) collagen promoter (Col1a1-EGFP) were used in this study. Hearts were harvested and dissociated into single cell suspensions using enzymatic digestion. Cardiac cells were stained with the erythrocyte marker Ter119, the pan-leukocyte marker CD45, the endothelial cell marker CD31 and gp38 (known also as podoplanin). Fibroblasts were defined in a two-color flow cytometry analysis as a lineage-negative (Lin: $Ter119^-CD45^-CD31^-$) and gp38-positive ($gp38^+$) population. Analysis of hearts isolated from Col1a1-EGFP reporter mice showed that cardiac $Lin^-gp38^+$ cells corresponded to type I collagen-producing cells. $Lin^-gp38^+$ cells were partially positive for the mesenchymal markers CD44, CD140a, Sca-1 and CD90.2. Sorted $Lin^-gp38^+$ cells were successfully expanded *in vitro* for up to four passages. $Lin^-gp38^+$ cells activated by Transforming Growth Factor Beta 1 (TGF-β1) upregulated myofibroblast-specific genes and proteins, developed stress fibers positive for alpha smooth muscle actin (αSMA) and showed increased contractility in the collagen gel contraction assay.

**Conclusions:** Two-color flow cytometry analysis using the selected cell surface antigens allows for the identification of collagen-producing fibroblasts in unaffected mouse hearts without using specific reporter constructs. This strategy opens new perspectives to study the physiology and pathophysiology of cardiac fibroblasts in mouse models.

**Keywords: cardiac fibroblast, collagen I, gp38/podoplanin, FACS sorting, flow cytometry**

***Edited by:***
*Antonio Paolo Beltrami,*
*University of Udine, Italy*

***Reviewed by:***
*Isotta Chimenti,*
*Sapienza University of Rome, Italy*
*Nikolaos G. Frangogiannis,*
*Albert Einstein College of Medicine,*
*United States*

****Correspondence:***
*Gabriela Kania*
*gabriela.kania@uzh.ch*

***Specialty section:***
*This article was submitted to Cardiovascular Biologics and Regenerative Medicine, a section of the journal Frontiers in Cardiovascular Medicine*

***Received:*** *07 April 2019*
***Accepted:*** *17 July 2019*
***Published:*** *01 August 2019*

***Citation:***
*Stellato M, Czepiel M, Distler O, Błyszczuk P and Kania G (2019) Identification and Isolation of Cardiac Fibroblasts From the Adult Mouse Heart Using Two-Color Flow Cytometry. Front. Cardiovasc. Med. 6:105. doi: 10.3389/fcvm.2019.00105*

# INTRODUCTION

Cardiac fibroblasts represent the main stromal cell type in the adult heart, which control extracellular matrix (ECM) turnover and maintain tissue structure (1–3). Fibroblasts are commonly defined as type I collagen-producing cells. For a long time, fibroblasts have been thought to be a homogenous cell population of mesenchymal origin with similar functions in different organs. However, several recent studies have demonstrated that fibroblasts present an extensive phenotypic heterogeneity (4–6). Disbalance in production and degradation of ECM components is associated with tissue remodeling. Activation of cardiac fibroblasts often leads to excessive accumulation of ECM proteins (mainly type I collagen) and proliferation of stromal cells in the myocardium. Fibrosis in the heart causes not only impaired mechanical contraction, but also can disturb conduction of electrical impulses. Progressive fibrosis is considered as one of the major causes of heart failures. This process is regulated by both, intrinsic mechanisms, such as transcriptional regulatory networks (7) and epigenetic processes, and by extrinsic factors, such as cell-to-cell signaling, soluble signaling mediators or ECM components. Transforming growth factor beta (TGF-β) represents a key profibrotic cytokine that activates and differentiates fibroblasts into pathological myofibroblasts. Myofibroblasts are characterized by excessive ECM production and enhanced contractility potentials and their presence is a key feature of cardiac fibrosis (8). Filaments positive for alpha smooth muscle actin (αSMA) is a commonly used marker of myofibroblasts.

A routine method to obtain cardiac fibroblasts is based on their selective adhesion and high expansion potential in cell cultures. Typically, outgrowing cells isolated from cardiac muscle are considered as fibroblasts. Indeed, while using optimized protocols, many cells obtained with this method show features of fibroblasts (2). This method is, however, not specific, and does not allow for analysis of freshly isolated cells.

Flow cytometry and fluorescence-activated cell sorting (FACS) represent widely used technologies to identify and isolate cells from a single cell suspension based on fluorescence. Antibodies conjugated with different fluorescent dyes allow detecting multiple markers simultaneously on a single cell. Analysis of living cells by flow cytometry and FACS requires, however, the use of antibodies recognizing cell membrane markers. Many cell types express specific cell membrane antigens, as for example haematopoietic cells (CD45) or endothelial cells (CD31). Cardiac fibroblasts were characterized by expression of certain cell surface antigens (9), but so far, the unique, fibroblast-defining cell surface marker is not available.

A subset of stromal cells recently identified in secondary lymphoid organs (SLOs) is defined by gp38 (called also podoplanin) positivity (4). At first, gp38 expression was found to be essential during development (10). In the developing heart, gp38 plays an important role in development of sinus venous myocardium (11). In the adult heart, gp38 is expressed in cardiac lymphatic vessels and in interstitial cells (12). Conversely, recent studies demonstrated that gp38 expression is limited to lymphatic endothelial cells and fibroblastic reticular cells, suggesting that gp38$^+$ cells may play an important role in different organs during homeostasis and disease processes such as inflammation or fibrosis (5, 13). Flow cytometry study in SLOs demonstrated that fibroblastic cells are negative for hematopoietic and endothelial lineage markers CD45 and CD31 defining a population of lymphatic fibroblasts (14). Characteristic of cardiac gp38$^+$ cells with flow cytometry has not been clarified yet. We hypothesized that lineage-negative and gp38$^+$ cells in the heart might specifically define a population of cardiac fibroblasts.

# METHODS

## Preparation of Single Cell Suspension From Mouse Heart

Wild-type C57BL/6 mice were purchased from Charles Rivers. Col1a1-EGFP (pCol9GFP-HS4,5) reporter mice (15) were kindly provided by Prof. D.A. Brenner, San Diego, USA. All mice were housed in pathogen-free conditions. Animal experiments were performed in accordance with the Swiss federal law and with the Guide for the Care and Use of Laboratory Animals published by the US National Institutes of Health (NIH Publication, 8th Edition, 2011). The Cantonal Veterinary Office in Zurich had approved animal experiments.

Hearts of 6–8-week-old wild-type and Col1a1-EGFP reporter mice were perfused with ice-cold phosphate buffered saline (PBS) through the left ventricle, were harvested and kept in PBS on ice. Hearts were cut into small pieces, resuspended in 0.025 mg/mL of Liberase TM solution (Roche) containing collagenase I and II and DNAse (40 ug/mL, Stemcell Technologies) in pure Dulbecco's modified Eagle's medium (DMEM, Sigma) and incubated for 45 min at 37°C. Enzymatic digestion was supported by mechanical tissue fragmentation using magnetic beads (VWR) and magnetic stirrer. Digested tissue was filtered through a 70 μm cell strainer followed by low speed centrifugation (50 g, 2 min) to remove cardiomyocytes, cell clumps and the remaining undigested tissue. Next, the supernatants were passed through a 40 μm cell strainer, centrifuged at 450 g for 4 min and washed with PBS. Single cell suspension for flow cytometry staining was obtained by resuspending cell pellet in FACS buffer: (PBS supplemented with 1% fetal bovine serum (FBS, ThermoScientific/Life Technology) and 1 mM EDTA (ThermoScientific/Invitrogen).

## Flow Cytometry and Cell Sorting

Cells in single cell suspensions were blocked with anti-mouse CD16/CD32 (1:200; Clone 93, Thermo Fisher Scientific) for 10 min at 4°C, followed by incubation on ice for 30 min with the appropriate combination of fluorochrome-conjugated antibodies diluted in FACS buffer: TER119-PE, (1:600, clone TER-11, eBioscience), CD45-PE (1:300, clone 30-F11, eBioscience), CD31-PE (1:300, clone 390, Thermo Fisher Scientific), gp38-APC (1:100, clone 8.1.1, eBioscience), CD90.2-eFluor 450 (1:300, clone 53-2.1, eBioscience), Sca-1- PerCP-Cy5.5 (1:300, clone D7, eBioscience), CD44-PE-Cy7 (1:300, clone IM7, eBioscience), CD140a-PE-Cy7 (1:300, clone APA5, eBioscience). 4′,6-diamidino-2-phenylindole (DAPI 1 μg/mL, Roche) was used to distinguish live/dead cells. Cells were analyzed with the BD

LSR Fortessa flow cytometer (BD Biosciences) and sorted with the FACSAria III 4L (BD Biosciences). FlowJo (version 10.08) was used for data analyses.

## Cell Culture

Sorted $\text{Lin}^{-}\text{gp38}^{+}$ cells were cultured in DMEM (Gibco) supplemented with 10% FBS, 50 U/mL penicillin, 50 μg/mL streptomycin (both Gibco) and 50 mM β-mercaptoethanol (Thermo Fisher Scientific). Cells were passaged up to 4 passages. Cells from passages 3 and 4 were used in differentiation experiments. Cell differentiation was induced with 10 ng/mL mouse recombinant TGF-β1 (Peprotech). All cells were cultured in humified incubators under standard culture conditions at 37°C and 5% $CO_2$.

## RNA Extraction and qPCR

Cells were washed with PBS, mixed with RNA lysis buffer (Zymo) and frozen at −80°C. Zymo Quick-RNA MicroPrep isolation kit was used to extract total RNA. 100% ethanol was added to the lysates and samples were than processed on the MicroPrep columns. DNA contamination was removed by DNAse I digestion. RNA was washed and eluted in 10 μl of water. RNA concentration and purity were assessed with Nanodrop 1000 (Thermo Fisher Scientific). Reverse transcription of 125 ng total RNA was performed using the Transcriptor First Strand cDNA Synthesis kit (Roche) and random hexamers, according to the manufacturer's protocol. qPCRs were performed with 2x SYBR Green master mix (Promega) and oligonucleotides for the genes of interest using an Agilent Technologies Stratagene Mx3005P qPCR system. *Acta2* oligonucleotides: forward (5′->3′): CGCTGTCAGGAACCCTGAGA, reverse (5′->3′): CGAAGCCGGCCTTACAGA; *Gapdh* (housekeeping gene) oligonucleotides: forward (5′->3′): CTGCACCACCAACTGCTTAGC, reverse (5′->3′): GGCATGGACTGTGGTCATGAG. Relative *Acta2* expression was normalized to *Gapdh* levels.

## Western Blotting

Cellular proteins were extracted with RIPA buffer (Sigma-Aldrich) supplemented with protease inhibitor cocktail (Complete ULTRA Tablets, Roche) and phosphatase inhibitors (PhosphoStop, Roche) from cultivated cells. Protein concentration was quantified by colorimetric bicinchoninic acid assay according to the manufacturer's protocol (Thermo Fisher Scientific). SDS-PAGE electrophoresis and wet-transfer method were used to separate and transfer proteins on nitrocellulose membranes followed by 45 min incubation in blocking solution: [tris buffered saline, Tween-20 (TBST, Thermo Fisher Scientific) containing 5% skim milk powder (Becton Dickinson AG)]. Membranes were incubated overnight with the following primary antibodies: anti-αSMA (1:1000, clone 1A4, Sigma-Aldrich) or GAPDH (1:10000, clone 14C10, Cell Signaling). Horseradish peroxidase (HRP)-conjugated secondary antibodies were used for detection with ECL substrate (SuperSignal West Pico Plus, Thermo Fisher Scientific) and development on the Fusion Fx (Vilber). Densitometric analyses were performed with ImageJ 1.47t. Fold changes were computed after normalization to GAPDH.

### ELISA

$\text{Lin}^{-}\text{gp38}^{+}$ cells were cultured for up to 4 passages and seeded with or without TGF-β1 (10 ng/mL) in 1% FBS medium for 7 days. Supernatants were collected and diluted 1:100 for assessing the amount of pro-collagen I alpha 1 using ELISA (Abcam) according to the manufacturer's instructions. The amount of pro-collagen I alpha 1 in the samples was calculated as interpolation of the standard curve.

## Immunofluorescent Staining

### Cells

Cells were seeded in 8-chamber slides (Lab-Tec) at the density of 2,500 cells/well, fixed in ice-cold methanol:acetone 7:3 (both Sigma-Aldrich) for 10 min at −20°C, washed with PBS and blocked with 10% FBS in PBS for 20 min at room temperature. Subsequently, incubation with the primary mouse anti-αSMA antibody (clone: clone 1A4, 1:100, Sigma-Aldrich) was performed for 1 h at room temperature followed by staining with the secondary Alexa 488 goat anti-mouse antibody (1:400, Thermo Fischer Scientific) and 50 μg/ml of fluorescent labeled phalloidin (Sigma-Aldrich) to visualize stress fibers for 45 min at room temperature. Nuclei were counterstained with DAPI solution (1 μg/ml, Roche). Images were acquired with an Olympus BX53 microscope equipped with a DP80 camera.

### Heart Tissue

Hearts were collected after PBS perfusion through the left ventricle, washed in cold PBS and incubated 24 h in 4% paraformaldehyde-PBS followed by incubating for another 24 h in 30% Sucrose-PBS at 4°C. Tissues were embedded in OCT and 15 μm sections were cut and kept in PBS at 4°C until used for immunohistochemical staining. First, cardiac sections were permeabilized with 0.1% TritonX-100 (Sigma-Aldrich) in PBS for 5 min, washed 3 times in PBS and blocked using 5% bovine serum albumin (BSA) together with 2% FBS in PBS for 30 min at room temperature (RT). Successively, golden syrian hamster anti-gp38 primary antibody (clone: 8.1.1., eBioscience; 1:50) was incubated overnight at 4°C. Sections were then washed three times in PBS and incubated with anti-hamster Alexa Fluor 546 secondary antibody (1:500, Thermo Fischer Scientific) for 45 min. Finally, after 3 washings in PBS, DAPI was used to label nuclei. Stained sections were transferred onto microscope slides and mounted with Vectashield mounting medium (Vector Laboratories). Images were acquired with an Olympus BX53 microscope equipped with a DP80 camera.

## Cell Contraction Assay

To assess contractile properties, the Contraction Assay Kit (Cell Biolabs) was used following the manufacturer's protocol. Cells were cultivated with or without 10 ng/mL TGF-β for 72 h and re-seeded in collagen gels for further 72 h. Each condition was analyzed in triplicates or quadruplicates. Images were taken at time 0, 24, 48, and 72 h after re-seeding in a collagen gel. Areas of the gels were measured by ImageJ. Percentage of contraction of all conditions was measured compared to the average of unstimulated cells at day 0.

## Bromodeoxyuridine (BrdU) ELISA Proliferation Assay

Cells were seeded in 96-well plates (5,000 cells/well), stimulated with 10 ng/mL TGF-β for 24 h and BrdU was added to the culture medium for the next 24 h. BrdU incorporation was measured by Colorimetric Cell Proliferation ELISA (Roche) according the manufacturer's protocol. Briefly, cells were fixed with a fixative/denaturing solution for 30 min and further incubated with anti-BrdU-POD antibodies for 90 min at room temperature followed by addition of the substrate solution. Absorbance was measured at 450 nm with correction at 690 nm with the Synergy HT microplate reader (BioTek). Each sample was measured in quadruplicates. Mean absorbance was calculated and unstimulated cells served as control. All experimental conditions were calculated as fold change to controls.

## Caspase Glo 3/7 Assay

For the detection of apoptosis, Caspase 3/7 activity was determined by using the Caspase-Glo® 3/7 Assay Systems (Promega) following the manufacturer's protocol. Briefly, Lin-gp38$^+$ cells were seeded in 96-well plates (5,000 cells/well), and stimulated with 10 ng/mL TGF-β for 24 h. Next, cells were incubated with the Caspase-Glo® reagent for 2 h in the dark at room temperature. Luminescent signals were measured with the Synergy HT microplate reader (BioTek). All conditions were analyzed in quadruplicates. Mean luminescence was calculated and unstimulated cells served as control. All experimental conditions were calculated as fold change to control.

### Statistics

Statistical significance of non-normally distributed data was analyzed by non-parametric Mann-Whitney *U*-test or Kruskal-Wallis test. For Western Blot data analysis, Dunn's *post-hoc* test was used for multiple comparisons. For ELISA data analysis, paired *t*-test was used. For contraction assays, all time-points were compared to each other using Sidak's multiple comparison test. All analyses were computed using the GraphPad Prism 8 software. Differences were considered statistically significant for $p < 0.05$; $n$ refers to the number of biological replicates.

# RESULTS

## Identification of a Stromal Cell Subset in the Mouse Heart

To isolate fibroblasts from the whole heart of wild-type mice, we established a protocol suitable for obtaining a single cell suspension to process and analyse by two-color flow cytometry. The single cell suspension was first gated in SSC-A, FSC-A plots to exclude cellular debris (below 50 k in FSC-A). Afterwards, live cells were selected as DAPI-negative in FSC-H/DAPI plots. In our two-color strategy, we combined antibodies against the stromal cell marker gp38 conjugated with one fluorescent dye (color 1) with three antibodies against markers of erythrocytes (Ter119), leukocytes (CD45) and endothelial cells (CD31) conjugated with another fluorescent dye (color 2). Anti-Ter119, anti-CD45 and anti-CD31 are thereafter referred to as lineage markers. Two-color flow cytometry analysis of cardiac tissue obtained from a healthy mouse showed a distinct population of gp38$^+$ cells negative for lineage markers called further Lin$^-$gp38$^+$ (**Figure 1**). Subsequently, we assessed the expression of gp38 in rest of the cell suspension. Lin$^-$gp38$^+$ cells represented a rare, but distinct population in hearts of wild-type mouse (median 4.2%, $Q_{1,3}$ 3.4%, 4.9% for $n = 5$ of positive cells gated on live, single cell total population; **Figure 2**).

## Cardiac Lin$^-$gp38$^+$ Cells Represent Type I Collagen-Producing Fibroblasts

Fibroblasts are characterized by collagen I production. In the next step, using Col1a1-EGFP reporter mice, we analyzed whether cardiac Lin$^-$gp38$^+$ cells produce collagen I. To this aim cardiac cells of Col1a1-EGFP mouse were stained with the two-color panel and analyzed by flow cytometry. As shown in **Figure 3**, the vast majority of EGFP-positive cells were Lin$^-$gp38$^+$ (median 95.4%, $Q_{1,3}$ 90%, 97% for $n = 5$, **Figures 3B,D**). Importantly, Lin$^-$gp38$^+$ cells were absent in the EGFP-negative population (median 1%, $Q_{1,3}$ 0.6%, 1.6% for $n = 5$, **Figures 3C,D**). These results demonstrated that type I collagen-producing cardiac fibroblasts could be specifically identified using indicated two-color panel and flow cytometry analysis. Moreover, we performed immunofluorescence staining for gp38 on heart sections from Col1a1-EGFP reporter mice. The pictures presented in **Figure 3E** show that most of EGFP$^+$ cells co-express gp38, and are localized between cardiomyocytes. In the next step, we further characterized cardiac Lin$^-$gp38$^+$ cells for expression of selected mesenchymal markers using flow cytometry. We found that the majority of Lin$^-$gp38$^+$ cells were positive for CD44 (median 94.5%, $Q_{1,3}$ 76.5%, 97.2% for $n = 5$) and CD140a (median 96.7%, $Q_{1,3}$ 94.7%, 99.8% for $n = 5$). Furthermore, our data demonstrated that only a subset of cardiac Lin$^-$gp38$^+$ cells expressed Sca-1 antigen (median 51.2%, $Q_{1,3}$ 50.5%, 57.4% for $n = 5$) and CD90.2 (median 30.6%, $Q_{1,3}$ 21.9%, 46.4% for $n = 5$, **Figure 4A**). These results confirm previous findings that cardiac fibroblasts are phenotypically heterogeneous.

## TGF-β1 Turns Cardiac Lin$^-$gp38$^+$ Cells Into Myofibroblast-Like Cells

In the next step, we established *in vitro* cultures of cardiac Lin$^-$gp38$^+$ cells. To this aim, Lin$^-$gp38$^+$ cells were sorted by FACS from the heart of adult wild-type mice and expanded *in vitro* for up to 4 passages. Cultivated Lin$^-$gp38$^+$ cells showed similar expression of mesenchymal markers upon 4 passages compared to freshly isolated cells for Sca-1 (median 50.2%, Q1,3 49.5%, 52.2% for $n = 5$), CD44 (median 98.1%, Q1,3 96.8%, 99.2% for $n = 5$), CD140α (median 43.3%, Q1,3 42.8%, 51.8%, for $n = 5$) and CD90.2 (median 42.3%, Q1,3 39.1%, 45.0% for $n = 5$, **Figure 4B**). The profibrotic cytokine TGF-β1 is known to enhance proliferation of cardiac fibroblasts and converse them into myofibroblast. We investigated how sorted and expanded cardiac Lin$^-$gp38$^+$ cells responded to

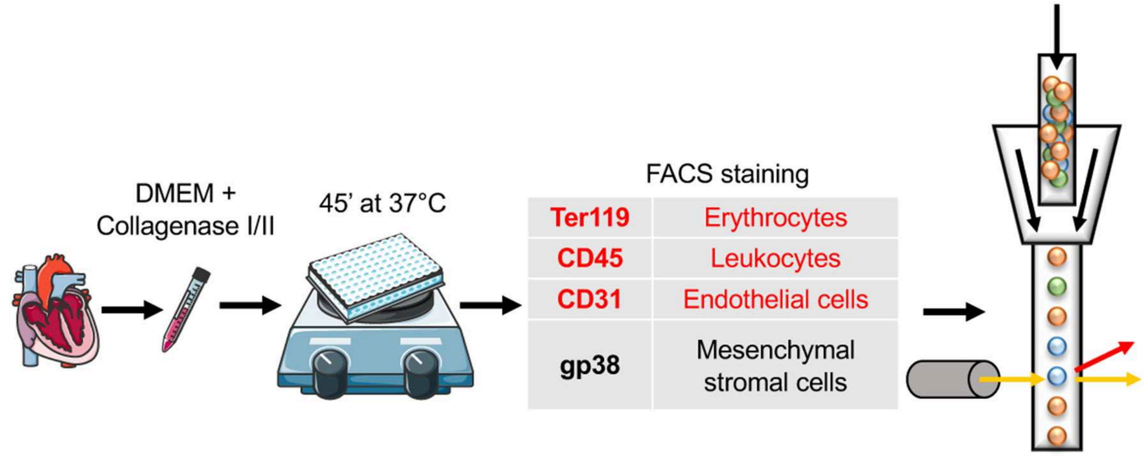

**FIGURE 1 |** Schematic protocol for stromal cell isolation from the mouse heart. Adult C57BL/6 mice were sacrificed and PBS perfusion via left ventricle was performed. Subsequently, hearts were cut with scissors and digested enzymatically, using pure DMEM complemented with a mixture of collagenase I, II, and DNAse. The incubation was performed for 45′ at 37°C in the presence of magnetic beads on a magnetic stirrer. Next, flow cytometry staining of antibodies included in the panel for stromal cell subset identification was implemented. Markers in red were used for the negative selection (Ter119, CD45, and CD31). In addition single cell suspension was evaluated for the expression of gp38 (in black). Cartoons adapted from SERVIER MEDICAL ART (https://smart.servier.com/), Creative Commons Attribution 3.0 License (https://creativecommons.org/licenses/by/3.0/legalcode).

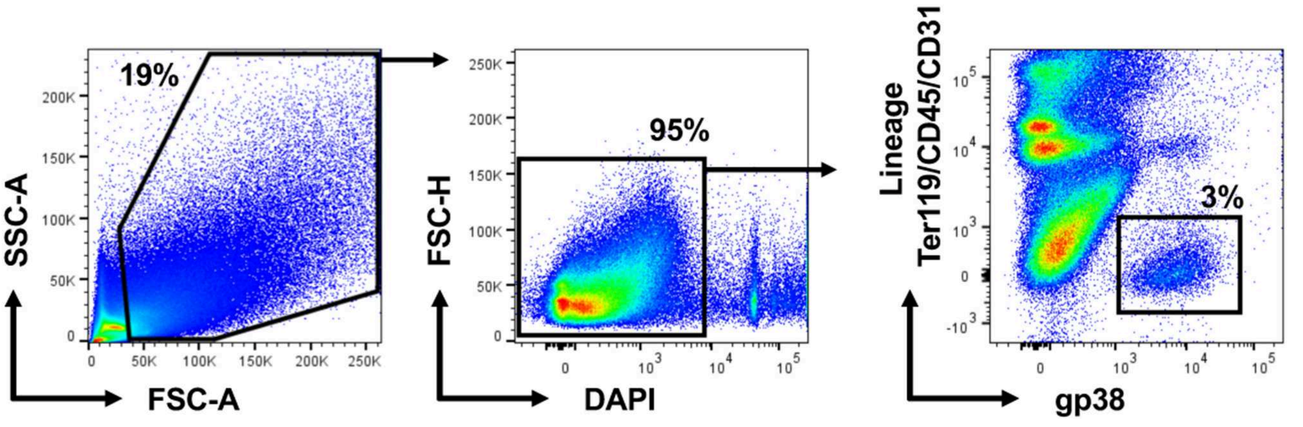

**FIGURE 2 |** Cardiac Lin$^-$gp38$^+$ represents a distinct stromal cell population in the mouse heart. Representative pictures and quantification of flow cytometry analysis of hearts from wild-type C57BL/6 mice. Mice of mixed gender were sacrificed, hearts were harvested and processed as described in **Figure 1**. Cellular debris below 50 k in FSC-A were excluded in SSC-A, FSC-A plots. After that, live cells were selected as DAPI-negative in FSC-H/DAPI plots. The percentage of Lin$^-$gp38$^+$ cells was quantified from the population of live cells (gated as DAPI-negative in FSC-H/DAPI plots) ($n = 5$).

stimulation with TGF-β1. As shown in **Figure 5A**, TGF-β1 up-regulated *Acta2* (gene encoding αSMA) expression 24 h after treatment induction. In line with this finding, αSMA protein was significantly up-regulated 72 h after TGF-β1 treatment (**Figure 5B**). Stimulation with TGF-β1 induced secretion of pro-collagen I by Lin$^-$gp38$^+$ cells (**Figure 5C**). Treatment with TGF-β1 induced also formation of well-structured αSMA-positive fibers, which co-localized with stress fibers (**Figure 5D**). αSMA protein incorporated into stress fibers has been implicated in increased isometric contraction of myofibroblasts. We measured the contraction strength of Lin$^-$gp38$^+$ cells using a collagen gel contraction assay. As shown in **Figure 5E**, treatment with TGF-β1 for 72 h increased contraction of Lin$^-$gp38$^+$ cells. Finally, we assessed the effect of TGF-β1 on proliferation and apoptosis of Lin$^-$gp38$^+$ cells. We observed increased proliferation of Lin$^-$gp38$^+$ cells treated with TGF-β1 in comparison to untreated control (**Figure 5F**). In contrast, TGF-β1 treatment did not affect apoptosis of Lin$^-$gp38$^+$ cells (**Figure 5G**). Altogether, these results indicate that TGF-β1 can effectively differentiate Lin$^-$gp38$^+$ cells into myofibroblasts-like cells.

## DISCUSSION

Several studies have investigated cellular composition of the adult mammalian heart. It is widely accepted that myocytes account for about 35% of the total number of cells in the

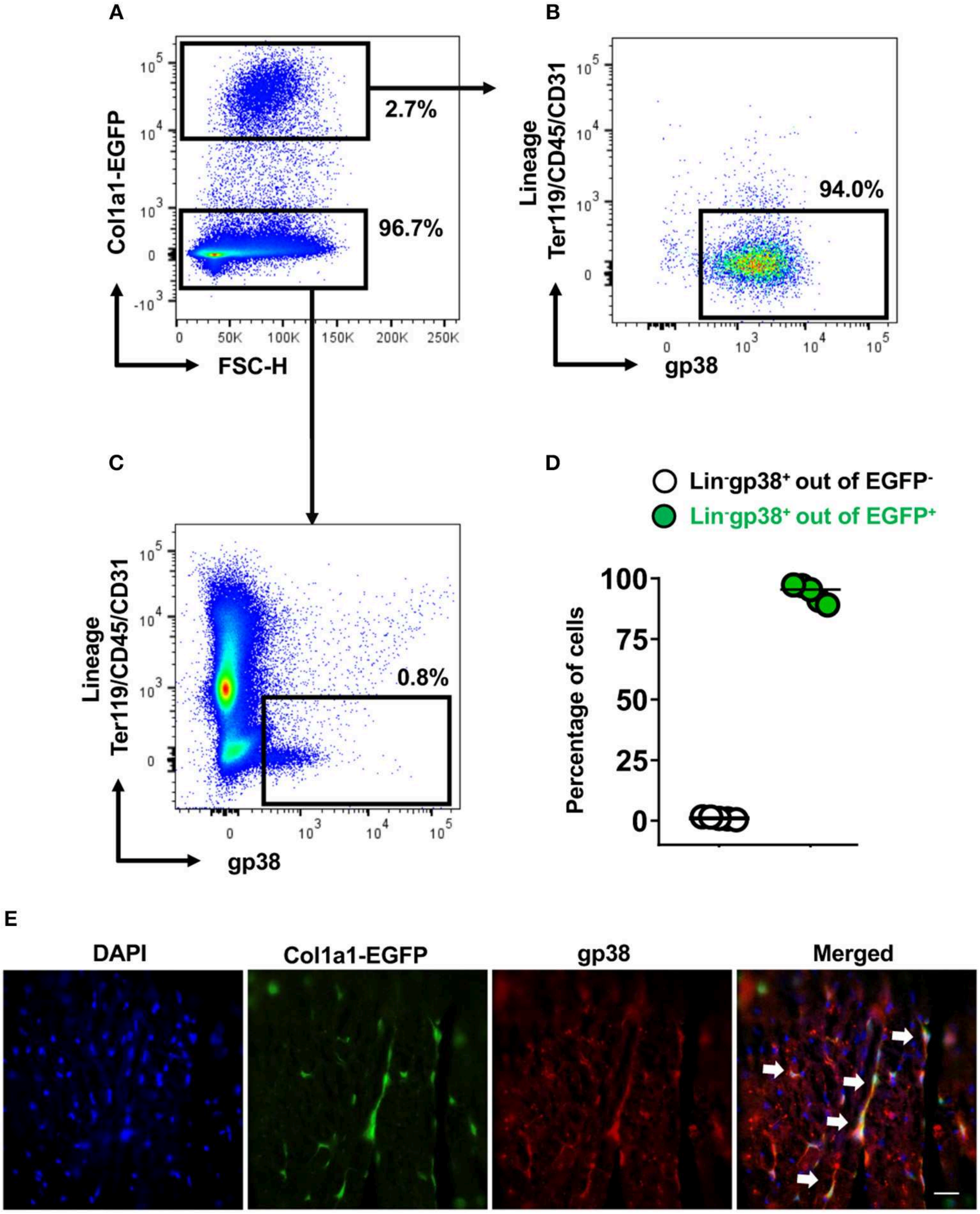

**FIGURE 3 |** Cardiac Lin$^-$gp38$^+$ cells represent collagen I producing cells. Representative flow cytometry analysis of cells isolated from hearts of Col1a1-EGFP tg mice. Cellular debris below 50 k in FSC-A were excluded in SSC-A/FSC-A plots. Live cells were first gated as Col1a1-EGFP$^+$ or Col1a1-EGFP$^-$ **(A)** and then analyzed for expression of Lin and gp38. The percentage of Lin$^-$gp38$^+$ cells was quantified from Col1a1-EGFP$^+$ cells **(B)** and Col1α1-EGFP$^-$ cells **(C)**. **(D)** Shows quantification of Lin$^-$gp38$^+$ cell percentages from EGFP$^-$ (white circles) and EGFP$^+$ (green circles) cells ($n = 5$). **(E)** Shows representative staining of gp38 (red) and EGFP expression (green) indicating the collagen I-producing cells in the cryosections from hearts of Col1a1-EGFP tg mouse. DAPI stains cell nuclei. Bar = 50 μm.

heart, while endothelial cells, fibroblasts, vascular smooth muscle and myeloid cells represent remaining fractions. Accordingly, endothelial cells account for up to 60%, myeloid cells for up to 10% and fibroblasts for up to 20% based on immunohistochemistry analyses (16, 17). A recent multiparametric flow cytometry analysis suggested that fibroblasts represent about 15% of non-cardiomyocyte cells (16). This analysis was, however, performed on cells obtained from ventricles only. Recently, these methods were overcome by more modern techniques, such as single cell RNAseq, which allowed a better understanding of the cellular frequencies in the heart (18). Fibroblasts seem to constitute the main stromal cell type in the myocardium (19). Nevertheless, the exact number of stromal cells and fibroblasts in particular in the heart is still debated. In fact, diverse studies have demonstrated that fibroblasts are not only phenotypically but also functionally different, according to their origin, localization in the body and tissues. Furthermore, the lack of reliable, specific

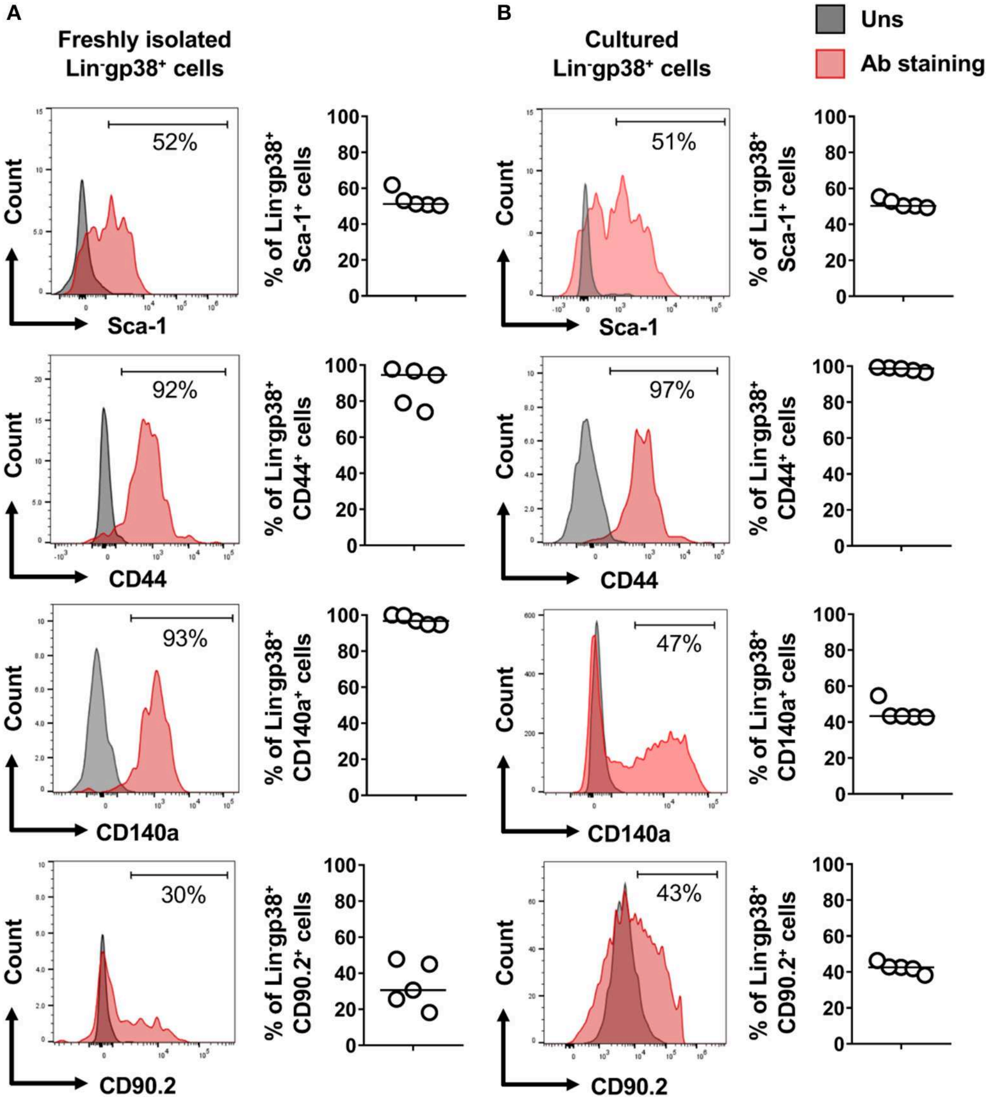

**FIGURE 4 |** Expression of mesenchymal cell markers on cardiac Lin$^-$gp38$^+$ cells. Representative flow cytometry histograms (data are representative for 1 out of 5 independent experiments; gray color indicates unstained controls) and quantification of the indicated mesenchymal markers on Lin$^-$gp38$^+$ cells of single cell suspension obtained from mouse heart **(A)** and cardiac Lin$^-$gp38$^+$ cells expanded *in vitro* for 3 passages **(B)** ($n = 5$).

and exclusive markers for fibroblasts has made their clear identification difficult.

To date, Fibroblast Specific Protein 1 (FSP1), CD90 (also named Thy-1), CD248 and others have been suggested as fibroblast-specific markers (9). However, subsequent studies demonstrated that endothelial cells and hematopoietic cells might share the expression of these markers. Moreover, several cell types might acquire or loose markers during disease-driven differentiation mechanisms. Kong et al used GFP-driven expression by FSP1 promoter in cardiac homeostasis and disease. The authors demonstrated that following myocardial infarction, half of the FSP1$^+$ cells were identified as hematopoietic cells and many endothelial cells were also positive for FSP1, indicating that FSP1 could not be considered exclusive for fibroblasts. CD90 was shown to be expressed in various cell types, including fibroblasts, ovarian cancer cells, endothelial cells, neurons, and hematopoietic cells (20). A recent study of single cell analyses revealed the up-regulation of fibrotic gene profiles: *Postn, Acta2, Adam12, Lox, Wisp1*, and *Ddr2* during cardiac remodeling in response to angiotensin II and after myocardial infarction (21, 22). Lineage tracing studies revealed that periostin-expressing myofibroblasts play a pivotal role during healing and fibrosis in the heart following myocardial infarction. These periostin-expressing myofibroblasts originated from Tcf21-expressing tissue-resident fibroblasts (21). However, the lack of specific monoclonal anti-mouse periostin antibodies, disables the use of this marker for the efficient isolation procedure.

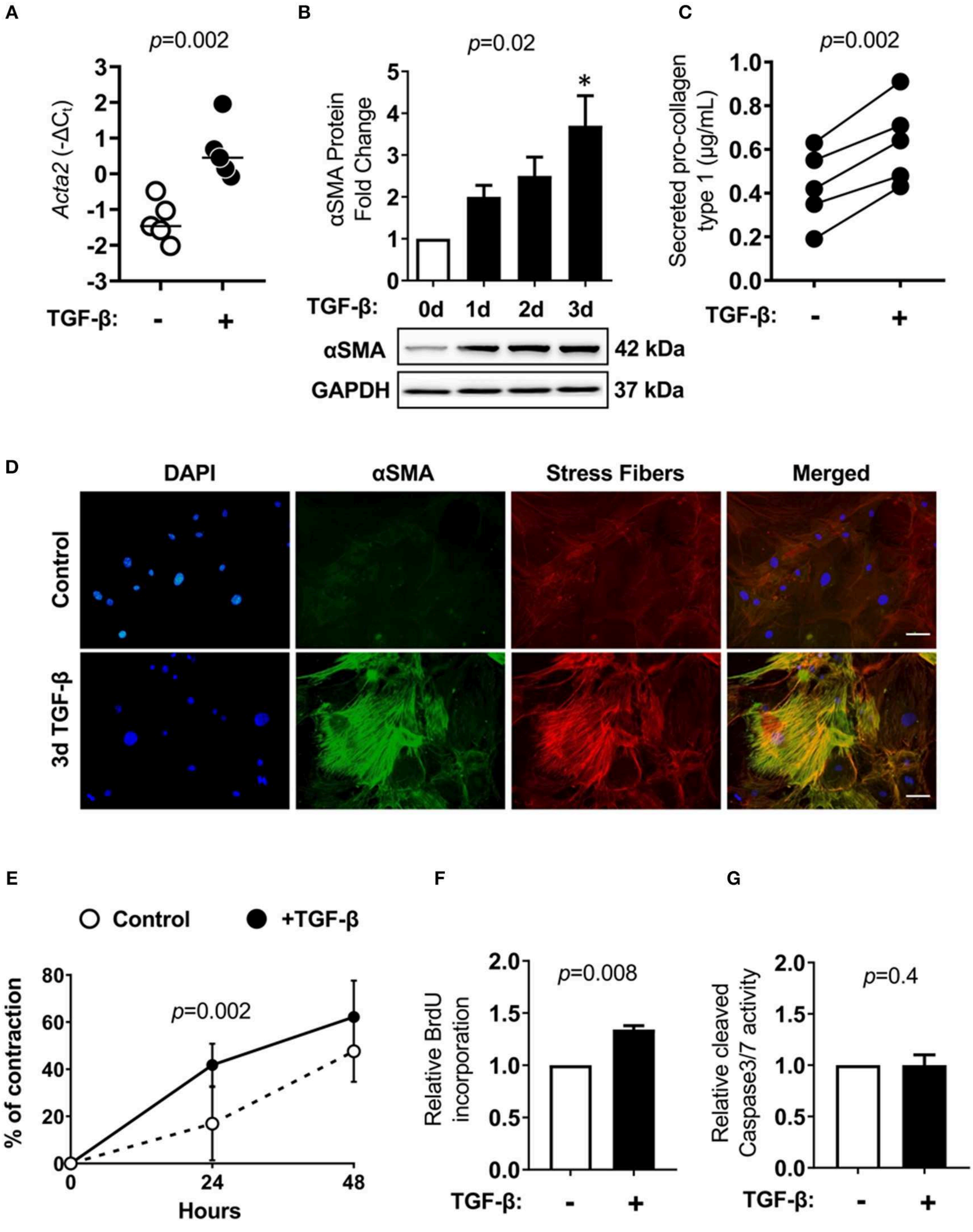

**FIGURE 5 |** Cardiac $Lin^-gp38^+$ cells response to TGF-β1 stimulation. Cardiac $Lin^-gp38^+$ cells were isolated from hearts of C57BL/6 mice as described in **Figure 1** and expanded *in vitro*. **(A)** Shows *Acta2* mRNA expression in cardiac $Lin^-gp38^+$ cells cultured in the presence or absence of TGF-β1 (10 ng/mL) for 24 h ($n = 5$, *p*-value calculated with Mann-Whitney *U*-test). **(B)** Shows quantification and representative immunoblots for αSMA protein levels in lysates of $Lin^-gp38^+$ cells cultured in the presence or absence of TGF-β1 (10 ng/mL) for the indicated time [$n = 5$, *p*-values computed using Kruskal-Wallis test followed by the Dunn's multiple comparisons test, $^*p < 0.05$ (*post-hoc* test vs. control)]. In **(C)**, results from ELISA for pro-collagen type 1 are presented. $Lin^-gp38^+$ cells were seeded at passage 3 and treated with or without TGF-β1 (10 ng/mL) for 7 days. Supernatants were used to assess the amount of pro-collagen type 1 secreted from $Lin^-gp38^+$ cells ($n = 5$, *p*-value calculated with paired *t*-test). **(D)** Shows representative staining of αSMA (green) and phalloidin (red) in $Lin^-gp38^+$ cells cultivated in the presence or absence of TGF-β1 (10 ng/mL) for 3 days. DAPI stains cell nuclei. Bar = 50 μm. **(E)** Shows quantification of $Lin^-gp38^+$ cells contractility precultured in the presence or absence of TGF-β1 (10 ng/mL) for 3 days ($n = 6$, *p*-value calculated with Sidak's multiple comparison test). **(F)** Indicates quantification of BrdU incorporation by $Lin^-gp38^+$ cells cultured in the presence or absence of TGF-β1 (10 ng/mL) for 24 h ($n = 5$, *p*-value calculated with Mann-Whitney *U*-test). **(G)** Shows quantification of cleaved caspase 3/7 activity in $Lin^-gp38^+$ cells cultured in the presence or absence of TGF-β1 (10 ng/mL) for 24 h ($n = 4$, *p*-value calculated with Mann-Whitney *U*-test).

Gp38 (podoplanin) is a mucin-type transmembrane glycoprotein receptor (10). This marker was recently described to stain a subset of stromal cells in SLOs. The gp38$^+$ stromal cells play a central role in the formation, reorganization and metabolism of ECM in SLOs as well as in liver, dermis and muscles (5) and are crucial in the functional regulation of T and B cell responses during immunity (23). Importantly, gp38$^+$ cells have been also identified in non-lymphoid organs such as pancreas, liver and spleen and were associated with chronic inflammation and fibrosis (24). In fibrosis, gp38$^+$ cells function as potent producers of ECM, hyaluronan and connective tissue growth factor, which is required for TGF-β-induced proliferation and differentiation into myofibroblasts (24). In mouse models of biliary and parenchymal liver fibrosis and in steatohepatitis, gp38 expression was linked with CD133 on newly characterized stromal cell population, which considerably expanded in all analyzed models of liver injury and returned to baseline levels during regression of inflammation (13). In the context of fibrotic disease, the gp38 marker has been reported to be expressed in CD34$^-$gp38$^+$CD90$^+$ reticular cells in the skin of the patients with systemic sclerosis and in mouse skin wounds (25) as well as a subset of ADAM12$^+$gp38$^+$PDGFRα$^+$ in skin and muscle acute injury stromal cells (5).

In this study, we demonstrated that lineage (Ter119, CD45 and CD31)-negative and gp38-positive cells represented a population of type I collagen-producing fibroblasts in the adult mouse heart. Accordingly, our results showed that the two-color staining strategy could successfully replace the use of Col1a1-EGFP reporter mice allowing for analysis of cardiac fibroblasts in non-transgenic mice. The two-color staining can be also used to isolate cardiac fibroblasts by FACS. Our proof-of-concept experiment confirmed that these cardiac Lin$^-$gp38$^+$ cells can be expanded *in vitro* for up to 4 passages and respond to TGF-β1 stimulation by inducing a myofibroblast-like phenotype. Currently, a commonly used method to isolate cardiac fibroblasts is based on differential adhesive properties of isolated cells. In this method, cardiac tissue is disintegrated by enzymatic digestion and obtained single cell suspension is plated onto a cell culture dish. Adherent (typically after 90 min) and proliferating (after days/weeks) cells showing a spindle shape phenotype are considered as fibroblasts (26). In this method no specific cell selection is performed, which may lead to impurity of isolated cells bringing potentially biased outcomes.

Flow cytometry analysis allows for the analysis on multiple markers on a single cell level. Our data showed expression of CD44 and CD140a on cardiac Lin$^-$gp38$^+$ cells. CD44 is a receptor for hyaluronic acid and other ECM ligands expressed on cardiac fibroblast in homeostasis and increased after heart infarction (27–29), while CD140a was demonstrated to be expressed in a sub-fraction of immature stromal cells with the qualities of mesenchymal stem cells (30). It is well-known that cardiac fibroblasts represent rather a heterogeneous cell population. In line with that, we found only a subset of cardiac Lin$^-$gp38$^+$ cells expressing Sca-1 and CD90, both well-known markers for mesenchymal stromal cells (31). Sca-1 has been used as a marker for fibroblastic cells, displaying a mesenchymal phenotype (32). Moreover, Sca-1 is expressed on cardiac progenitor cell populations, which attenuate the functional decline and adverse remodeling in post-infarction murine models showing beneficial effects for cardiac repair (33, 34). Interestingly, cardiac Lin$^-$gp38$^+$ cells resulted to be almost completely negative for the expression of CD29 (fibronectin receptor, not shown), which is considered as another mesenchymal marker (27).

Altogether, here we provide an easy and effective protocol for the identification and isolation of living cardiac fibroblast using two-color flow cytometry. We recommend to use this strategy specially to study the fibroblast populations in healthy or (and) diseased heart. We believe that this protocol will be used in various mouse models of cardiovascular diseases.

## DATA AVAILABILITY

The raw data supporting the conclusions of this manuscript will be made available by the authors, without undue reservation, to any qualified researcher.

## ETHICS STATEMENT

Animal experiments were performed in accordance with the Swiss federal law and with the Guide for the Care and Use of Laboratory Animals published by the US National Institutes of Health (NIH Publication, 8th Edition, 2011). The Cantonal Veterinary Office in Zurich had approved animal experiments. The Cantonal Veterinary Office in Zurich had approved all animal experiments (animal license number: 001/2017).

## AUTHOR CONTRIBUTIONS

GK, PB, MS, and MC: substantial contributions to the conception and design of the work, the acquisition, analysis or interpretation of data for the work. GK, PB, MS, MC, and OD: substantial contributions to drafting the work and revising it critically for important intellectual content, providing an approval for publication of the content, agree to be accountable for all aspects of the work in ensuring that questions related to the accuracy or integrity of any part of the work are appropriately investigated and resolved.

## FUNDING

This work has been supported by the Swiss National Foundation (Grants 310030_152876, 310030_175663), Swiss Heart Foundation, Hartmann Muller Foundation, Olga Mayenfisch Foundation, Hermann Klaus Foundation, Novartis Foundation, Forschungskredit UZH, Helmut Horten Foundation and Egli Foundation and the National Science Centre (Poland), grant 2014/14/E/NZ5/00175. The authors declare that this study received funding from Novartis Foundation. The funder had no role in study design, data collection and analysis, decision to publish, or preparation of the manuscript.

# REFERENCES

1. Vliegen HW, van der Laarse A, Cornelisse CJ, Eulderink F. Myocardial changes in pressure overload-induced left ventricular hypertrophy. A study on tissue composition, polyploidization and multinucleation. *Eur Heart J.* (1991) 12:488–94. doi: 10.1093/oxfordjournals.eurheartj.a059928
2. Agocha AE, Eghbali-Webb M. A simple method for preparation of cultured cardiac fibroblasts from adult human ventricular tissue. *Mol Cell Biochem.* (1997) 172:195–8. doi: 10.1007/978-1-4615-6353-2_19
3. Kanekar S, Hirozanne T, Terracio L, Borg TK. Cardiac fibroblasts form and function. *Cardiovasc Pathol.* (1998) 7:127–33. doi: 10.1016/S1054-8807(97)00119-1
4. Malhotra D, Fletcher AL, Astarita J, Lukacs-Kornek V, Tayalia P, Gonzalez SF, et al. Immunological Genome Project C. Transcriptional profiling of stroma from inflamed and resting lymph nodes defines immunological hallmarks. *Nat Immunol.* (2012) 13:499–510. doi: 10.1038/ni.2262
5. Dulauroy S, Di Carlo SE, Langa F, Eberl G, Peduto L. Lineage tracing and genetic ablation of ADAM12(+) perivascular cells identify a major source of profibrotic cells during acute tissue injury. *Nat Med.* (2012) 18:1262–70. doi: 10.1038/nm.2848
6. Fasnacht N, Huang HY, Koch U, Favre S, Auderset F, Chai Q, et al. Specific fibroblastic niches in secondary lymphoid organs orchestrate distinct Notch-regulated immune responses. *J Exp Med.* (2014) 211:2265–79. doi: 10.1084/jem.20132528
7. Davidson EH, Erwin DH. Gene regulatory networks and the evolution of animal body plans. *Science.* (2006) 311:796–800. doi: 10.1126/science.1113832
8. Moulin V, Larochelle S, Langlois C, Thibault I, Lopez-Valle CA, Roy M. Normal skin wound and hypertrophic scar myofibroblasts have differential responses to apoptotic inductors. *J Cell Physiol.* (2004) 198:350–8. doi: 10.1002/jcp.10415
9. Ivey MJ, Tallquist MD. Defining the cardiac fibroblast. *Circ J.* (2016) 80:2269–76. doi: 10.1253/circj.CJ-16-1003
10. Astarita JL, Acton SE, Turley SJ. Podoplanin: emerging functions in development, the immune system, and cancer. *Front Immunol.* (2012) 3:283. doi: 10.3389/fimmu.2012.00283
11. Mahtab EA, Wijffels MC, Van Den Akker NM, Hahurij ND, Lie-Venema H, Wisse LJ, et al. Cardiac malformations and myocardial abnormalities in podoplanin knockout mouse embryos: correlation with abnormal epicardial development. *Dev Dyn.* (2008) 237:847–57. doi: 10.1002/dvdy.21463
12. Cimini M, Cannata A, Pasquinelli G, Rota M, Goichberg P. Phenotypically heterogeneous podoplanin-expressing cell populations are associated with the lymphatic vessel growth and fibrogenic responses in the acutely and chronically infarcted myocardium. *PLoS ONE.* (2017) 12:e0173927. doi: 10.1371/journal.pone.0173927
13. Eckert C, Kim YO, Julich H, Heier EC, Klein N, Krause E, et al. Podoplanin discriminates distinct stromal cell populations and a novel progenitor subset in the liver. *Am J Physiol Gastrointest Liver Physiol.* (2016) 310:G1–12. doi: 10.1152/ajpgi.00344.2015
14. Fletcher AL, Malhotra D, Acton SE, Lukacs-Kornek V, Bellemare-Pelletier A, Curry M, et al. Reproducible isolation of lymph node stromal cells reveals site-dependent differences in fibroblastic reticular cells. *Front Immunol.* (2011) 2:35. doi: 10.3389/fimmu.2011.00035
15. Krempen K, Grotkopp D, Hall K, Bache A, Gillan A, Rippe RA, et al. Far upstream regulatory elements enhance position-independent and uterus-specific expression of the murine alpha1(I) collagen promoter in transgenic mice. *Gene Expr.* (1999) 8:151–63.
16. Pinto AR, Ilinykh A, Ivey MJ, Kuwabara JT, D'Antoni ML, Debuque R, et al. Revisiting cardiac cellular composition. *Circ Res.* (2016) 118:400–9. doi: 10.1161/CIRCRESAHA.115.307778
17. Souders CA, Bowers SL, Baudino TA. Cardiac fibroblast: the renaissance cell. *Circ Res.* (2009) 105:1164–76. doi: 10.1161/CIRCRESAHA.109.209809
18. Skelly DA, Squiers GT, McLellan MA, Bolisetty MT, Robson P, Rosenthal NA, et al. Single-cell transcriptional profiling reveals cellular diversity and intercommunication in the mouse heart. *Cell Rep.* (2018) 22:600–10. doi: 10.1016/j.celrep.2017.12.072
19. Gladka MM, Molenaar B, de Ruiter H, van der Elst S, Tsui H, Versteeg D, et al. Single-cell sequencing of the healthy and diseased heart reveals cytoskeleton-associated protein 4 as a new modulator of fibroblasts activation. *Circulation.* (2018) 138:166–80. doi: 10.1161/CIRCULATIONAHA.117.030742
20. Rege TA, Hagood JS. Thy-1, a versatile modulator of signaling affecting cellular adhesion, proliferation, survival, and cytokine/growth factor responses. *Biochim Biophys Acta.* (2006) 1763:991–9. doi: 10.1016/j.bbamcr.2006.08.008
21. Kanisicak O, Khalil H, Ivey MJ, Karch J, Maliken BD, Correll RN, et al. Genetic lineage tracing defines myofibroblast origin and function in the injured heart. *Nat Commun.* (2016) 7:12260. doi: 10.1038/ncomms12260
22. Kaur H, Takefuji M, Ngai CY, Carvalho J, Bayer J, Wietelmann A, et al. Targeted ablation of periostin-expressing activated fibroblasts prevents adverse cardiac remodeling in mice. *Circ Res.* (2016) 118:1906–17. doi: 10.1161/CIRCRESAHA.116.308643
23. Cremasco V, Woodruff MC, Onder L, Cupovic J, Nieves-Bonilla JM, Schildberg FA, et al. B cell homeostasis and follicle confines are governed by fibroblastic reticular cells. *Nat Immunol.* (2014) 15:973–81. doi: 10.1038/ni.2965
24. Peduto L, Dulauroy S, Lochner M, Spath GF, Morales MA, Cumano A, et al. Inflammation recapitulates the ontogeny of lymphoid stromal cells. *J Immunol.* (2009) 182:5789–99. doi: 10.4049/jimmunol.0803974
25. Nazari B, Rice LM, Stifano G, Barron AM, Wang YM, Korndorf T, et al. Altered dermal fibroblasts in systemic sclerosis display podoplanin and CD90. *Am J Pathol.* (2016) 186:2650–64. doi: 10.1016/j.ajpath.2016.06.020
26. Phan SH. Biology of fibroblasts and myofibroblasts. *Proc Am Thorac Soc.* (2008) 5:334–37. doi: 10.1513/pats.200708-146DR
27. Furtado MB, Costa MW, Pranoto EA, Salimova E, Pinto AR, Lam NT, et al. Cardiogenic genes expressed in cardiac fibroblasts contribute to heart development and repair. *Circ Res.* (2014) 114:1422–34. doi: 10.1161/CIRCRESAHA.114.302530
28. Alt E, Yan Y, Gehmert S, Song YH, Altman A, Gehmert S, et al. Fibroblasts share mesenchymal phenotypes with stem cells, but lack their differentiation and colony-forming potential. *Biol Cell.* (2011) 103:197–208. doi: 10.1042/BC20100117
29. Halfon S, Abramov N, Grinblat B, Ginis I. Markers distinguishing mesenchymal stem cells from fibroblasts are downregulated with passaging. *Stem Cells Dev.* (2011) 20:53–66. doi: 10.1089/scd.2010.0040
30. Farahani RM, Xaymardan M. Platelet-derived growth factor receptor alpha as a marker of mesenchymal stem cells in development and stem cell biology. *Stem Cells Int.* (2015) 2015:362753. doi: 10.1155/2015/362753
31. Dominici M, Le Blanc K, Mueller I, Slaper-Cortenbach I, Marini F, Krause D, et al. Minimal criteria for defining multipotent mesenchymal stromal cells. The International Society for Cellular Therapy position statement. *Cytotherapy.* (2006) 8:315–7. doi: 10.1080/14653240600855905
32. McQualter JL, Brouard N, Williams B, Baird BN, Sims-Lucas S, Yuen K, et al. Endogenous fibroblastic progenitor cells in the adult mouse lung are highly enriched in the sca-1 positive cell fraction. *Stem Cells.* (2009) 27:623–33. doi: 10.1634/stemcells.2008-0866
33. Wang X, Hu Q, Nakamura Y, Lee J, Zhang G, From AH, et al. The role of the sca-1+/CD31- cardiac progenitor cell population in postinfarction left ventricular remodeling. *Stem Cells.* (2006) 24:1779–88. doi: 10.1634/stemcells.2005-0386
34. Beltrami AP, Barlucchi L, Torella D, Baker M, Limana F, Chimenti S, et al. Adult cardiac stem cells are multipotent and support myocardial regeneration. *Cell.* (2003) 114:763–76. doi: 10.1016/S0092-8674(03)00687-1

**Conflict of Interest Statement:** The authors declare that the research was conducted in the absence of any commercial or financial relationships that could be construed as a potential conflict of interest.

frontiers
in Cardiovascular Medicine

ORIGINAL RESEARCH
published: 18 September 2019
doi: 10.3389/fcvm.2019.00118

# The Beneficial Effects of UM206 on Wound Healing After Myocardial Infarction in Mice Are Lost in Follow-Up Experiments

*Evangelos P. Daskalopoulos*†, *Kevin C. M. Hermans*†, *Jacques Debets*, *Agnieszka Strzelecka*, *Peter Leenders*, *Lily Vervoort-Peters*, *Ben J. A. Janssen* and *W. Matthijs Blankesteijn**

*Department of Pharmacology and Toxicology, Cardiovascular Research Institute Maastricht (CARIM), Maastricht University (UM), Maastricht, Netherlands*

**Edited by:**
*Przemyslaw Blyszczuk,*
*University of Zurich, Switzerland*

**Reviewed by:**
*Hirotsugu Tsuchimochi,*
*National Cerebral and Cardiovascular Center, Japan*
*Daphne Merkus,*
*Erasmus Medical Center, Netherlands*

***Correspondence:**
*W. Matthijs Blankesteijn*
*wm.blankesteijn@maastrichtuniversity.nl*

*†These authors have contributed equally to this work*

**Specialty section:**
*This article was submitted to Cardiovascular Biologics and Regenerative Medicine, a section of the journal Frontiers in Cardiovascular Medicine*

**Received:** *09 May 2019*
**Accepted:** *01 August 2019*
**Published:** *18 September 2019*

**Citation:**
*Daskalopoulos EP, Hermans KCM, Debets J, Strzelecka A, Leenders P, Vervoort-Peters L, Janssen BJA and Blankesteijn WM (2019) The Beneficial Effects of UM206 on Wound Healing After Myocardial Infarction in Mice Are Lost in Follow-Up Experiments. Front. Cardiovasc. Med. 6:118. doi: 10.3389/fcvm.2019.00118*

**Introduction:** An inadequate wound healing following myocardial infarction (MI) is one of the main etiologies of heart failure (HF) development. Interventions aiming at improving this process may contribute to preserving cardiac function after MI. Our group, as well as others, have demonstrated the crucial role of Wnt/frizzled signaling in post-MI remodeling. In this overview, we provide the results of different studies aimed at confirming an initial study from our group, in which we observed beneficial effects of administration of a peptide fragment of Wnt5a, UM206, on infarct healing in a mouse MI model.

**Methods:** Mice were subjected to permanent left coronary artery ligation, and treated with saline (control) or UM206, administered via osmotic minipumps. Cardiac function was assessed by echocardiography and hemodynamic measurements, while infarct size and myofibroblast content were characterized by (immuno)histochemistry.

**Results:** In total, we performed seven follow-up studies, but we were unable to reproduce the beneficial effects of UM206 on infarct healing in most of them. Variations in dose and timing of UM206 administration, its manufacturer and the genetic background of the mice could not restore the phenotype. An in-depth analysis of the datasets revealed that the absence of effect of UM206 coincided with a lack of adverse cardiac remodeling and HF development in all experimental groups, irrespective of the treatment.

**Discussion:** Irreproducibility of experimental observations is a major issue in biomedical sciences. It can arise from a relatively low number of experimental observations in the original study, a faulty hypothesis or a variation in the experimental model that cannot be controlled. In this case, the lack of adverse cardiac remodeling and lung weight increases in the follow-up studies point out to altered experimental conditions as the most likely explanation.

**Keywords: myocardial infarction, cardiac remodeling, heart failure, Wnt/frizzled signaling, receptor blockade, peptide fragment**

# INTRODUCTION

Heart failure (HF) is a devastating condition that frequently results from myocardial infarction (MI). The development of HF is generally thought to be the consequence of adverse cardiac remodeling (1). Although the initial remodeling of the infarct area after MI is generally considered to be beneficial, excessive remodeling leads to dilatation of the entire left ventricle, inducing a deleterious effect on cardiac function (2). This has resulted in the concept that interventions targeting post-MI wound healing can be cardioprotective.

In the past decades, extensive efforts have been made to study the post-MI wound healing process, in order to discover novel therapeutic targets. Several pathways have been identified and tested in animal models (2). Our lab has a longstanding interest in the role of Wnt signaling in cardiac remodeling following MI and the potential of this pathway for interventions aiming to improve wound healing. Following the initial description of the activation of Wnt signaling post-MI (3), several studies from our group and others have provided evidence for the beneficial effects of Wnt-signaling-related interventions on the wound healing post-MI (4). Our group has published data on an intervention with a peptide fragment of Wnt5a– named UM206– in a mouse MI model (5). UM206 was designed to interfere with the interaction between Wnt and its receptors, members of the frizzled protein family. In this study, subcutaneous administration of UM206 ($n = 26$) or saline ($n = 17$)–via an osmotic minipump–resulted in a reduction of the infarct size by almost 40% and a >3-fold increase in myofibroblast content in the infarct area, when compared to saline treatment. The end-diastolic volume of the LV more than doubled in saline-treated mice at 5 weeks post-MI, but only increased ∼35% in the UM206-treated animals. The ejection fraction (EF) was 31 ± 3% in the UM206-treated group, compared to 17 ± 3% in saline-treated animals. Furthermore, the increase in lung weight, a sign of fluid retention in the lung due to compromised pump function, was significantly reduced and the mortality, which amounted 35% in the saline-treated group at 5 weeks post-MI, was completely prevented in the UM206-treated group. These observations indicated that HF development was attenuated in this relatively large group of UM206-treated animals (5).

Following this successful study, we decided to test variations in the dosage regimen and timing and thus gain more insight into the cellular target(s) of UM206 and the phase(s) of the wound healing where the compound displays the optimal activity, in order to shed light onto its exact mechanism(s) of action. We initially observed that interventions with UM206 starting at 2 weeks post-MI were almost as successful as administration of UM206 for 5 weeks following MI. However, after two positive studies the beneficial effect of UM206 appeared to be lost. In this manuscript, we provide an overview of the available experimental data regarding the variable effects of UM206 on infarct healing and discuss the possible interpretations of our findings.

# METHODS

## Overview of the Studies

In this overview, we present the results from seven different studies in which we assessed the effects of UM206 on infarct healing. UM206 was administered subcutaneously via an osmotic minipump at a dose of 6 μg/kg/day, with the exception of study G where a higher dose (150 μg/kg/day) was used. In all studies except for study D, Swiss mice were used as they show a strong tendency to develop left ventricular (LV) dilatation and HF after MI (6). In all studies, the administration of UM206 started either directly or after a specified period following the induction of MI. The dosage regimens are graphically represented in **Table 1**, where the orange bars indicate the UM206-treatment periods and the gray bars indicate the saline-treatment periods.

In studies A and B, infarct healing was followed for 8 weeks with UM206 administered for the final 5 weeks (first 3 weeks were treatment-free). In study C, Swiss mice from two different suppliers (Charles River and Harlan) were subjected to a 5 weeks UM206 treatment (starting shortly after MI induction). In study D, the influence of the genetic background was explored by using BALB/c rather than Swiss mice. In study E, the oxidized (circular) form of UM206 was administered whereas in all other studies the linear (reduced) form was applied. Because UM206 obtained from different sources was used in the previous studies (see below), the UM206 from the batch used in the original study as well as in study A was used again in study F. Finally, in study G, UM206 was administered at a maximally soluble dose of 150 μg/kg/day.

## Origin and Administration of UM206

UM206 was produced either by ChemPep Inc., Miami FL, USA or by Pepscan Therapeutics, Lelystad, The Netherlands. UM206 is a 13 amino acid peptide derived from an area of high homology between multiple Wnt molecules. It has a molecular weight of 1,427 Da and the following sequence: Ac-CNKTSEGMDGCEL-$NH_2$. In previous experiments, this peptide was found to inhibit the frizzled-1 and−2 mediated canonical Wnt signaling induced by Wnt3a *in vitro* (5). The UM206 compound was administrated subcutaneously via osmotic minipumps (Alzet 2006; Durect, Cupertino CA, USA).

## Animal Surgery

An overview of the executed studies can be found in **Table 1**. Male Swiss mice were used (10–12 weeks of age at the start of the study) in all studies with the exception of study D, where male BALB/c mice were used. The animals were supplied by Charles River, Leiden, The Netherlands, but in study C, Swiss mice from Charles River and Harlan (Horst, The Netherlands) were compared to each other. Animals had free access to food and water. MI was induced under isoflurane gas anesthesia (2–3%) using a stereomicroscope (Leica MZ FL III, Leica Switzerland) as previously described (6). Briefly, animals were placed on a heating pad in supine position, endotracheal intubation was performed under direct laryngoscopy and mechanical ventilation

**TABLE 1 |** Schematic overview of the included studies, illustrating the treatment protocols with either UM206 (orange bars) or saline (gray bars).

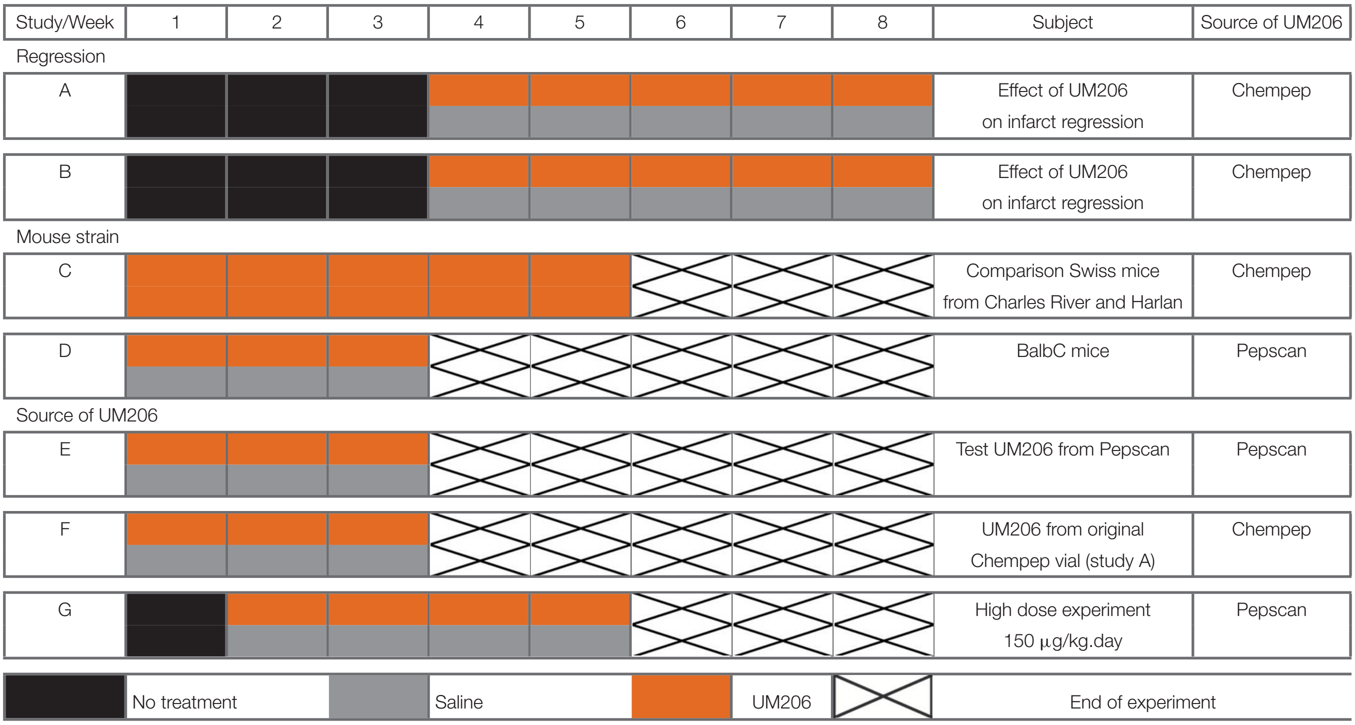

| Study/Week | 1 | 2 | 3 | 4 | 5 | 6 | 7 | 8 | Subject | Source of UM206 |
|---|---|---|---|---|---|---|---|---|---|---|
| Regression | | | | | | | | | | |
| A | ⬛ | ⬛ | ⬛ | 🟧<br>▒ | 🟧<br>▒ | 🟧<br>▒ | 🟧<br>▒ | 🟧<br>▒ | Effect of UM206 on infarct regression | Chempep |
| B | ⬛ | ⬛ | ⬛ | 🟧<br>▒ | 🟧<br>▒ | 🟧<br>▒ | 🟧<br>▒ | 🟧<br>▒ | Effect of UM206 on infarct regression | Chempep |
| Mouse strain | | | | | | | | | | |
| C | 🟧 | 🟧 | 🟧 | 🟧 | 🟧 | ☒ | ☒ | ☒ | Comparison Swiss mice from Charles River and Harlan | Chempep |
| D | 🟧<br>▒ | 🟧<br>▒ | 🟧<br>▒ | ☒ | ☒ | ☒ | ☒ | ☒ | BalbC mice | Pepscan |
| Source of UM206 | | | | | | | | | | |
| E | 🟧<br>▒ | 🟧<br>▒ | 🟧<br>▒ | ☒ | ☒ | ☒ | ☒ | ☒ | Test UM206 from Pepscan | Pepscan |
| F | 🟧<br>▒ | 🟧<br>▒ | 🟧<br>▒ | ☒ | ☒ | ☒ | ☒ | ☒ | UM206 from original Chempep vial (study A) | Chempep |
| G | ⬛ | 🟧<br>▒ | 🟧<br>▒ | 🟧<br>▒ | 🟧<br>▒ | ☒ | ☒ | ☒ | High dose experiment 150 μg/kg.day | Pepscan |

| | | | | | | | |
|---|---|---|---|---|---|---|---|
| ⬛ | No treatment | ▒ | Saline | 🟧 | UM206 | ☒ | End of experiment |

*Periods where no treatment was administered are represented by black bars. In total, data from seven different studies were included in this overview. The length of the studies, the specific subject of each study and the source of UM206 are indicated in the respective columns.*

was maintained with a small animal respirator (Hugo Sachs, MiniVent, tidal volume: 180–250 μl, rate: 200–250 breaths/min, depending on the strain). After thoracotomy, the lateral branch of the left anterior descending (LAD) coronary artery was ligated with a 6-0 prolene suture, just proximally to the main bifurcation. Successful ligation was verified by visual inspection of the LV apex for myocardial blanching, indicating interruption of the coronary blood flow. The chest cavity and skin were closed in layers with 5-0 polysorb sutures. Animals were gradually weaned from the respirator. All experimental procedures were approved by the Committee for Animal Research of Maastricht University and were performed by highly trained and experienced users that were blinded to the treatment groups.

## Echocardiography

Left ventricular (LV) dimensions and function were assessed under isoflurane anesthesia (2–3% for induction and 1–2% for maintenance) as previously described (5). B-mode echocardiographic recordings were made in midpapillary short-axis and parasternal long-axis using a Vevo 2100 imaging platform (VisualSonics, Toronto, ON, Canada) with a 30 MHz transducer. Data were derived from images in end diastole and peak systole and average values over at least three different cycles were used. From the long-axis images, LV area (LVA) as well as the length of the LV lumen from base to apex (LVL) were determined. The end-diastolic volume (EDV) and end-systolic volume (ESV) were calculated from the area and length measurements as $(8 \times \text{LVA}^2)/(3\pi \times \text{LVL})$ in diastole and systole, respectively, and ejection fraction (EF) was deducted. All measurements and analysis were performed by experienced users that were blinded to the treatment groups.

## Hemodynamics

Hemodynamic measurements were performed as previously described (7). Briefly, mice underwent urethane anesthesia (2.5 mg/kg i.p.), then a high-fidelity catheter tip micromanometer (Mikro-tip 1.4F; SPR-671, Millar Instruments, Houston TX, USA) was inserted through the right carotid artery into the LV cavity. The heart was then stimulated by an i.v. ramp infusion of dobutamine (Sigma Aldrich, Saint Louis, MO, USA) using a microinjection pump (model 200 Series, KdScientific, Boston, MA, USA). Every 2 min the infusion rate of dobutamine was increased by 2.5 ng/g body weight$^{-1}$ min$^{-1}$ up to 20 ng/g body weight$^{-1}$ min$^{-1}$ and contractility data were recorded.

## Histological Analysis

Histological analysis of the infarcted hearts was performed as previously described (6). Briefly, mouse hearts were longitudinally cut in half, perpendicular to the septum, fixed in 4% paraformaldehyde solution for 24 h and embedded in paraffin. Sections (4 μm) were cut and stained with the AZAN technique. Infarct size (percentage of the LV length) was measured using a computerized morphometry system (Qwin, Leica). Alpha smooth muscle actin (αSMA) monoclonal antibody (Sigma, dilution 1:1,000) was used to identify myofibroblasts in the infarct area. The relative myofibroblast area was determined using the Qwin morphometry system with manual exclusion of vascular smooth muscle cells and expressed as myofibroblast area/total tissue area (%).

## Statistical Analysis

Data are expressed as means ± SEM. For comparisons between individual groups, Student's *t*-test was used. A $P < 0.05$ (two-sided) was considered to be statistically significant. Comparisons of multiple groups were performed using one-way ANOVA with Dunnett's *post-hoc* test. Again, $P < 0.05$ (two-sided) were considered to be statistically significant. All statistical analyses were performed using GraphPad software (version 7).

# RESULTS

## Effects of UM206 Treatment on Mortality After MI

One of the most remarkable effects of the UM206 treatment in our previously published study was the complete prevention of mortality post-MI (5). In Swiss mice, mortality due to HF is typically around 30%, 5 weeks after induction of MI (6), a figure that was confirmed in the saline-treated group in our original study. An overview of the mortality rates of the mice in all seven studies is provided in **Table 2**. It is remarkable to note that in all studies the mortality was found to be considerably lower than in the previously published study, irrespective of whether the animals received UM206 or saline treatment.

**TABLE 2 |** Overview of mouse mortality in all follow-up studies.

| Study | % saline (dead/total) | % treated (dead/total) | Mortality before start of treatment | Total mouse number | Total mortality |
|---|---|---|---|---|---|
| **Regression** | | | | | |
| A | 0% (0/6) | 0% (0/9) | 11 | 26 | 11 |
| B | 0% (0/6) | 14% (2/14) | 2 | 22 | 4 |
| **Mouse strain** | | | | | |
| C | N/A | 5% (1/20) | N/A | 20 | 1 |
| D | 15% (2/13) | 0% (0/13) | N/A | 26 | 2 |
| **Source** | | | | | |
| E | 0% (0/10) | 13% (1/8) | N/A | 18 | 1 |
| F | 0% (0/7) | 0% (0/4) | N/A | 11 | 0 |
| G | 0% (0/6) | 0% (0/8) | 3 | 14 | 3 |

*N/A, "not available" (no deaths recorded).*

## Effects of Late Administration of UM206 (Studies A and B)

These experiments were designed to study the effects of UM206 on the later phases of infarct healing to explore whether this intervention could induce regression of the infarct size. To this end, the administration of UM206 started at 3 weeks after infarction and continued until 8 weeks post-MI. As shown in **Figure 1**, in the initial experiment (study A) an improved EF was observed (**Figure 1A**), which was accompanied by a significant reduction in EDV and ESV (**Table 3**). In study A, UM206 treatment also resulted in a significant reduction in lung weight. However, these findings were not paralleled by a smaller infarct size (**Figure 1B**), an increase in myofibroblast numbers (**Figure 1C**) or improved hemodynamics (**Table 3**), as observed in our original study (5). Moreover, a second experiment with an identical experimental setup (Study B) showed a significant decline in EF (**Figure 1A**) and no significant effects on any of the other parameters tested (**Figure 1B** and **Table 3**). Unfortunately, due to a technical failure in the tissue processing we could not determine the myofibroblast content in study B.

## Effect of Mouse Strain and Supplier (Studies C and D)

In previous studies, we observed profound effects of mouse strain and supplier on infarct healing (6). Therefore, we compared Swiss mice from two different suppliers (Charles River and Harlan, Study C) and studied the effects of UM206 on infarct healing in BalbC mice (study D). The EF was found to be significantly higher in the UM206-treated Swiss mice supplied by Harlan (**Figure 2A**), but this was not accompanied by a significant difference in infarct size (**Figure 2B**), myofibroblast content (**Figure 2C**) or any of the other parameters listed in **Table 4**. Along similar lines, no beneficial effects of UM206

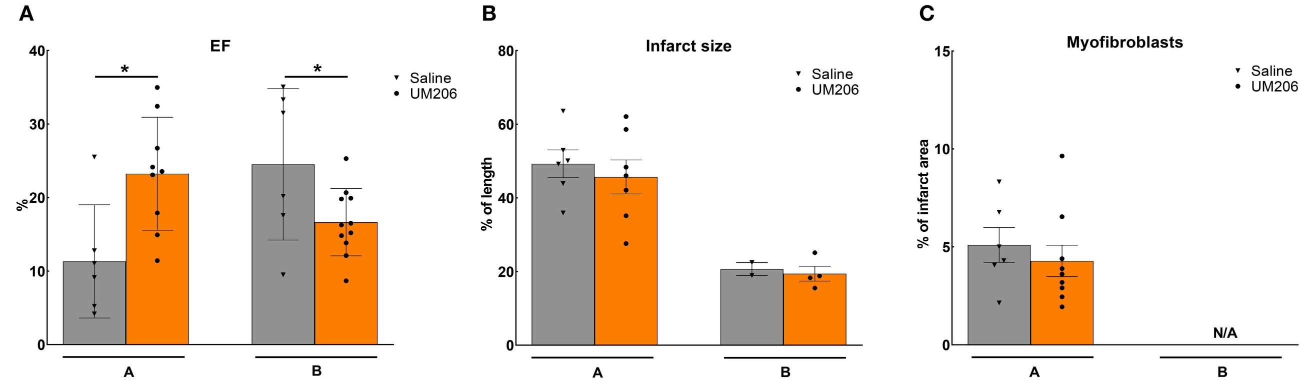

**FIGURE 1 |** Regression studies (Studies A and B): Cardiac function, infarct size, and myofibroblast counts. **(A)** Cardiac function (as measured by ejection fraction [EF%]), **(B)** Infarct size determination (measured by IHC and expressed as % of tissue length), and **(C)** Myofibroblast count (measured by IHC and expressed as % of infarct area). EF, ejection fraction; IHC, immunohistochemistry; N/A, not available. Data are presented as mean ± SEM. *$P < 0.05$.

**TABLE 3 |** Regression studies (Studies A and B): echocardiographic parameters (EDV and ESV), hemodynamic characteristics determination (dP/dt max and dP/dt min), and heart and lung weight measurements.

| | Study A | | Study B | |
|---|---|---|---|---|
| | **Saline** | **UM206** | **Saline** | **UM206** |
| EDV (cm$^3$) | 0.278 ± 0.024 | 0.195 ± 0.014*** | 0.192 ± 0.021 | 0.204 ± 0.012 |
| ESV (cm$^3$) | 0.250 ± 0.027 | 0.151 ± 0.015*** | 0.149 ± 0.023 | 0.171 ± 0.012 |
| dP/dt max (mmHg/sec)$^\dagger$ | 3345 ± 1210 | 5088 ± 942 | 5495 ± 620 | 3797 ± 326* |
| dP/dt min (mmHg/sec)$^\dagger$ | −2020 ± 500 | −2292 ± 472 | −2839 ± 353 | −2330 ± 149 |
| HW/BW | 0.0051 ± 0.0002 | 0.0047 ± 0.0002 | 0.0047 ± 0.0003 | 0.0047 ± 0.0001 |
| LW/BW | 0.0072 ± 0.0011 | 0.0050 ± 0.0001* | 0.0050 ± 0.0003 | 0.0060 ± 0.0005 |

*The dP/dt max$^\dagger$ and dP/dt min$^\dagger$ data represent the effect of dobutamine on the dP/dt corrected for the baseline (dP/dt max or min value minus the dP/dt baseline value respectively). EDV, end diastolic volume; ESV, end systolic volume; HW/BW, heart weight to body weight ration; LW/BW, lung weight to body weight ratio. Data are presented as mean ± SEM. *$P < 0.05$, ***$P < 0.001$.*

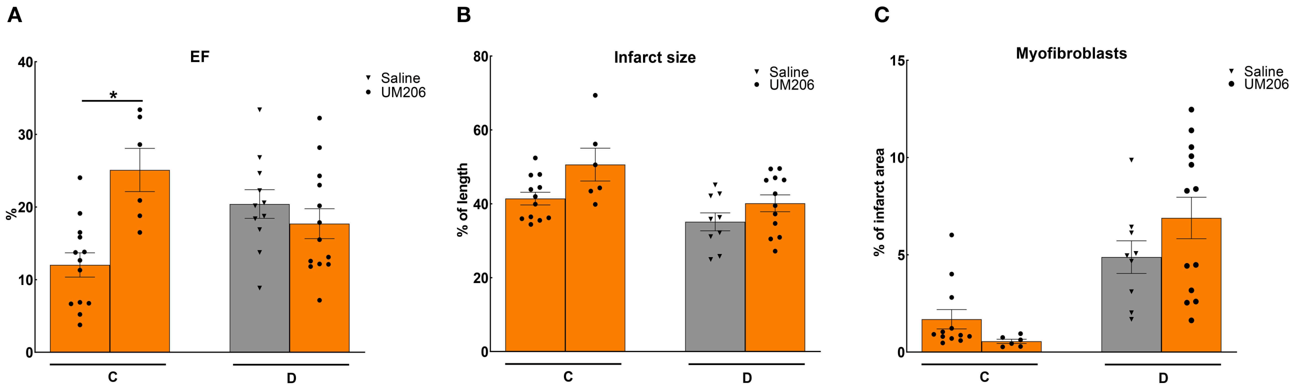

**FIGURE 2 |** Mouse strain studies (Studies C and D): Cardiac function, infarct size, and myofibroblast counts. **(A)** Cardiac function (as measured by ejection fraction [EF%]), **(B)** Infarct size determination (measured by IHC and expressed as % of tissue length), and **(C)** Myofibroblast count (measured by IHC and expressed as % of infarct area). EF, ejection fraction; IHC, immunohistochemistry. Data are presented as mean ± SEM. *$P < 0.05$.

administration were observed in BalbC mice for any of the tested parameters (**Figure 2** and **Table 4**).

## Effect of Oxidative State, Source, and Dose of UM206 (Studies E–G)

To rule out any effects of the oxidative state, source and dose of UM206, we performed three additional experiments; the results are presented in **Figure 3** and **Table 5**. UM206 contains two Cys residues which, when oxidized, can form a disulfide bond that circularizes the peptide. In study E, we compared the administration of this circular form of UM206 with saline treatment and did not observe any effect of the administration on the parameters tested. In study F, we administered UM206 from the original badge produced by Chempep, identical to the compound used in our original study (5). Again, no effect of this therapy was observed on any of the parameters tested. Finally, we decided to increase the dose of UM206 from 6 µg/kg/day, as used in all previous experiments, to 150 µg/kg/day (Study G). This dose was achieved by inserting a saturated solution of UM206 in the minipumps. Unfortunately, similarly to the previous experiments we did not observe any beneficial effects of this high-dose administration of UM206 when compared to saline administration.

# DISCUSSION

In this manuscript, we provide an overview of seven studies, performed in our laboratory, on the effects of UM206 on the wound healing after MI. These studies were performed to confirm the strong protective effect of this treatment on adverse cardiac remodeling, as previously illustrated by less dilatation of the left ventricle, improved cardiac function and lower lung weights, as well as improved survival (5). This beneficial effect of UM206 treatment on infarct healing could partially be confirmed in the first follow-up study, although the increase in myofibroblast numbers could not be reproduced. In the other studies, no significant differences have been observed in the infarct healing UM206-treated groups compared to saline-treated controls.

Irreproducibility of experimental data is a major issue in biomedical sciences. Researchers from the pharmaceutical companies Bayer and Amgen have systematically investigated this issue and found that the results of 75–91% of published experimental studies could not be reproduced in their own laboratories (8, 9). This illustrates that we are dealing with a considerable number of variables that are difficult to control, but that are of paramount importance for the outcome of an experiment. It is quite evident that when one is confronted

**TABLE 4 |** Mouse strain studies (Studies C and D): echocardiographic parameters (EDV and ESV), hemodynamic characteristics determination (dP/dt max and dP/dt min), and heart and lung weight measurements.

| | **Study C** | | **Study D** | |
|---|---|---|---|---|
| | **Swiss Harlan** | **Swiss C.-R** | **BalbC** | **BalbC** |
| | **UM206** | **UM206** | **Saline** | **UM206** |
| EDV (cm$^3$) | 0.228 ± 0.012 | 0.210 ± 0.017 | 0.123 ± 0.009 | 0.130 ± 0.006 |
| ESV (cm$^3$) | 0.202 ± 0.013 | 0.159 ± 0.018 | 0.099 ± 0.008 | 0.108 ± 0.007 |
| dP/dt max (mmHg/sec)$^\dagger$ | 2999 ± 499 | 4291 ± 861 | 5017 ± 876 | 4293 ± 656 |
| dP/dt min (mmHg/sec)$^\dagger$ | −1774 ± 310 | −2666 ± 775 | −2646 ± 436 | −2464 ± 330 |
| HW/BW | 0.0042 ± 0.0001 | 0.0046 ± 0.0001 | 0.0062 ± 0.0004 | 0.0065 ± 0.0005 |
| LW/BW | 0.0081 ± 0.0007 | 0.0058 ± 0.0005 | 0.0100 ± 0.0019 | 0.0106 ± 0.0017 |

*The dP/dt max$^\dagger$ and dP/dt min$^\dagger$ data represent the effect of dobutamine on the dP/dt corrected for the baseline (dP/dt max or min value minus the dP/dt baseline value respectively). EDV, end diastolic volume; ESV, end systolic volume; HW/BW, heart weight to body weight ration; LW/BW, lung weight to body weight ratio. Data are presented as mean ± SEM.*

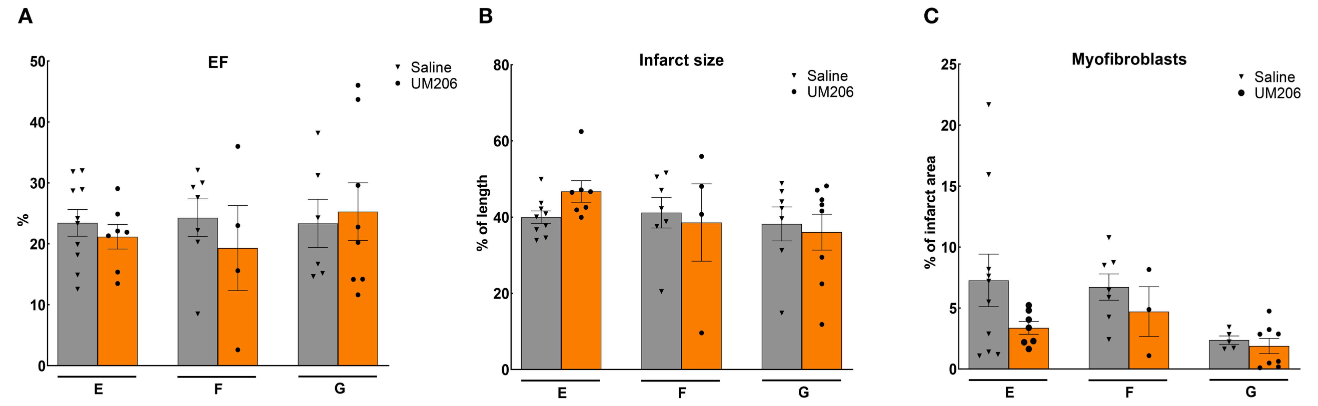

**FIGURE 3 |** Different source/dose of UM206 studies (Studies E, F, and G): **(A)** Cardiac function (as measured by ejection fraction [EF%]), **(B)** Infarct size determination (measured by IHC and expressed as % of tissue length), and **(C)** Myofibroblast count (measured by IHC and expressed as % of infarct area). EF, ejection fraction; IHC, immunohistochemistry. Data are presented as mean ± SEM.

with a discrepancy between subsequent studies, a scrutinous comparison of the experimental conditions is executed to identify potential differences. First, the surgical team that performed the operations is highly experienced and has not changed over the years so this is an unlikely factor. Originally, the Swiss mice were obtained from Charles River, but in order to exclude a possible effect of the genetic background we also tested Swiss mice from Harlan as well as BALB/c mice, with similar results. This excludes the animal background and surgery as a plausible explanation for the variations observed in the effects of UM206.

Another variable that we addressed was the source of UM206. In most of the studies, we made use of UM206 produced by ChemPep (Miami FL, USA) but we also tried UM206 produced by Pepscan (Lelystad, the Netherlands). No consistent differences in effects were observed between the peptides produced by these two companies, which is in complete agreement with the identical analytical data sheets provided with the compounds.

Since, UM206 is a peptide of 13 amino acids with two Cys residues located at positions 1 and 11, the peptide can form an internal disulfide bond when it is placed under oxidative conditions. Alternatively, dimeric or even multimeric complexes can also be–theoretically–formed, although this is obviously more likely to occur when the compound is dissolved at a high concentration. Given the low concentration of UM206 in the minipumps (4 µmol/l), the formation of multimers is unlikely. *In vitro* incubation of UM206 in osmotic minipumps under oxidative conditions revealed that virtually all of the UM206 will have formed disulfide bonds–mostly the internal variant–within 24 h (personal communication Dr. Nicolas Dailly and Dr. Peter Timmerman, Pepscan Lelystad). In previous *in vitro* studies, we have found the oxidized form of UM206 to be inactive as an antagonist, so this could explain the lack of effect observed in the follow-up studies. However, then the question remains unanswered how the compound could be administered in the active form in the initial studies, since the mode of administration (osmotic minipump) was the same.

A third issue is the position of the UM206 peptide in the Wnt/frizzled complex. The crystal structure of the *X*Wnt8/frizzled-8 cysteine-rich domain was published (10), showing that it is unlikely that the loop of the Wnt protein where UM206 is derived from is in direct physical contact with the frizzled protein. This finding obscures the pharmacological mechanism of action of this peptide. In the meantime, several researchers have provided evidence that Wnt and frizzled interact

**TABLE 5 |** Studies on different sources and dosing of UM206: echocardiographic parameters (EDV and ESV), hemodynamic characteristics determination (dP/dt max and dP/dt min), and heart and lung weight measurements.

| | Study E | | Study F | | Study G | |
|---|---|---|---|---|---|---|
| | Pepscan 6 μg/kg/day | | Chempep 6 μg/kg/day | | Pepscan 150 μg/kg/day | |
| | Saline | UM206 | Saline | UM206 | Saline | UM206 |
| EDV (cm$^3$) | 0.187 ± 0.011 | 0.182 ± 0.007 | 0.142 ± 0.008 | 0.137 ± 0.020 | 0.194 ± 0.020 | 0.190 ± 0.019 |
| ESV (cm$^3$) | 0.145 ± 0.012 | 0.144 ± 0.008 | 0.109 ± 0.010 | 0.115 ± 0.026 | 0.152 ± 0.021 | 0.148 ± 0.022 |
| dP/dt max (mmHg/sec)$^\dagger$ | 3915 ± 587 | 3349 ± 622 | 2201 ± 432 | 4039 ± 1711 | 3150 ± 561 | 3826 ± 446 |
| dP/dt min (mmHg/sec)$^\dagger$ | −1941 ± 302 | −1841 ± 335 | −924 ± 232 | −1861 ± 559 | −1537 ± 356 | −1767 ± 247 |
| HW/BW | 0.0044 ± 0.0001 | 0.0043 ± 0.0001 | 0.0051 ± 0.0004 | 0.0053 ± 0.0005 | 0.0048 ± 0.0003 | 0.0045 ± 0.0001 |
| LW/BW | 0.0057 ± 0.0005 | 0.0049 ± 0.0002 | 0.0070 ± 0.0019 | 0.0080 ± 0.0022 | 0.0065 ± 0.0011 | 0.0071 ± 0.0011 |

*The dP/dt max$^\dagger$ and dP/dt min$^\dagger$ data represent the effect of dobutamine on the dP/dt corrected for the baseline (dP/dt max or min value minus the dP/dt baseline value respectively). EDV, end diastolic volume; ESV, end systolic volume; HW/BW, heart weight to body weight ration; LW/BW, lung weight to body weight ratio. Data are presented as mean ± SEM.*

in a complex with other proteins, including the co-receptor LRP5/6 (11), and it is quite likely that UM206 interferes somehow with this complex formation. We cannot exclude that variations in the components involved in the formation of this complex determine the effectiveness of UM206, but it is unclear how this could have changed over time.

A remarkable observation in the current set of experimental data is that the lung weights in the saline-treated animals in the original study were considerably higher than the lung weights in the follow-up studies, despite similar infarct lengths. This suggests that overt HF induced by MI was only present in the first studies, but the development of the cardiac remodeling response was less severe in the latter ones. It is obvious that a therapy aiming at preventing adverse cardiac remodeling is ineffective when this adverse remodeling does not take place. This raises the question whether there have been any changes in the experimental conditions between the initial and follow-up studies that could explain these deviating outcomes. At this point, we can only speculate about experimental conditions, such as e.g., housing conditions, which could influence the infarct healing to the extent that heart failure development after MI was prevented. An alternative explanation could be that changes in the gut microbiome, which is increasingly recognized as factor regulating the wound healing after MI (12), have affected the heart failure development after MI over time.

A plausible explanation for irreproducible results can be that the underlying hypothesis is wrong and the positive results, observed in the initial experiment, are actually the result of chance. In this case, this explanation for the lack of reproducibility does not seem to hold. First of all, in the initial study, a relatively large number of animals (saline: $n = 17$, UM206-treated: $n = 26$) was included (5), supporting the robustness of the statistical analysis of these data. Moreover, we tested UM206 in a swine model of ischemia/reperfusion and one of the most prominent findings of this study was a reduced infarct size, similar to what we observed in our initial mouse study (13). In this context, it is relevant to note that several other authors have demonstrated beneficial effects on infarct healing of pharmacological inhibition of Wnt signaling (14). This includes interventions at the level of Wnt secretion (15–17), the β-catenin destruction complex (18), and the β-catenin transcription complex (19, 20). Repression of the methylation of the Wnt inhibitory factor 1 gene was shown to improve the differentiation of cardiac progenitor cells into cardiomyocytes, resulting in preserved LV wall thickening and improved LV functional parameters (21). In all of these studies, the inhibition of Wnt signaling induced a reduction in infarct size, similar to what we observed in our initial UM206 study. Furthermore, Foxy-5, a peptide derived from the same region of Wnt5a as UM206, has been shown to reduce metastatic spread of prostate cancer cells, underscoring the pharmacological potency of Wnt5a fragments (22). Taken together, explaining the inconsistent results from our mouse studies by an incorrect underlying hypothesis is becoming increasingly unlikely.

## CONCLUSIONS

The current overview of multiple studies on the effect of UM206 on infarct healing in mice suggests that changes in the experimental model had a profound effect on the results. In this case, the lack of HF development in the follow-up studies most likely has obscured the beneficial effects of the compound on wound healing post-MI. In the meantime, studies by several other groups have confirmed the beneficial effects of pharmacological Wnt inhibition on infarct healing by targeting the pathway at different levels. This supports the validity of the concept that inhibition of Wnt signaling after MI can be a promising novel approach to improve wound healing and preserve cardiac function.

## DATA AVAILABILITY

The raw data supporting the conclusions of this manuscript will be made available by the authors, without undue reservation, to any qualified researcher.

## AUTHOR CONTRIBUTIONS

ED and KH are the shared first authors and responsible for literature search, conduction of experiments, data analysis and interpretation, as well as manuscript preparation, and editing.

JD, AS, PL, and LV-P helped with data collection. BJ helped with data analysis and manuscript editing. WB is the senior author and was responsible for study conception, overseeing data collection and analysis, literature search, as well as manuscript preparation, and editing.

## FUNDING

The studies described in this manuscript were supported by grants from the Dutch Heart Foundation (2010B196) and Cyttron II (FES0908), Dutch Ministry of Economic Affairs.

## ACKNOWLEDGMENTS

We would like to thank Dr. Peter Timmerman and Dr. Nicolas Dailly, Pepscan Therapeutics B.V., Lelystad, Netherlands for their help in determining the effect of oxidation on the effect of UM206. The technical support of Gregorio Fazzi and Dennis Suylen is gratefully acknowledged.

## REFERENCES

1. Mcmurray JJ, Pfeffer MA. Heart failure. *Lancet.* (2005) 365:1877–89. doi: 10.1016/S0140-6736(05)66621-4
2. Daskalopoulos EP, Hermans KC, Blankesteijn WM. Cardiac (myo)fibroblast: novel strategies for its targeting following myocardial infarction. *Curr Pharm Des.* (2014) 20:1987–2002. doi: 10.2174/13816128113199990452
3. Blankesteijn WM, Essers-Janssen YPG, Verluyten MJA, Daemen MJP, Smits JFM. A homologue of Drosophila tissue polarity gene frizzled is expressed in migrating myofibroblasts in the infarcted rat heart. *Nat Med.* (1997) 3:541–4. doi: 10.1038/nm0597-541
4. Hermans KC, Blankesteijn WM. Wnt signaling in cardiac disease. *Compr Physiol.* (2015) 5:1183–209. doi: 10.1002/cphy.c140060
5. Laeremans H, Hackeng TM, Van Zandvoort MA, Thijssen VL, Janssen BJ, Ottenheijm HC, et al. Blocking of frizzled signaling with a homologous peptide fragment of wnt3a/wnt5a reduces infarct expansion and prevents the development of heart failure after myocardial infarction. *Circulation.* (2011) 124:1626–35. doi: 10.1161/CIRCULATIONAHA.110.976969
6. Van Den Borne SW, Van De Schans VA, Strzelecka AE, Vervoort-Peters HT, Lijnen PM, Cleutjens JP, et al. Mouse strain determines the outcome of wound healing after myocardial infarction. *Cardiovasc Res.* (2009) 84:273–82. doi: 10.1093/cvr/cvp207
7. De Celle T, Vanrobaeys F, Lijnen P, Blankesteijn WM, Heeneman S, Van Beeumen J, et al. Alterations in mouse cardiac proteome after *in vivo* myocardial infarction: permanent ischaemia versus ischaemia-reperfusion. *Exp Physiol.* (2005) 90:593–606. doi: 10.1113/expphysiol.2005.030296
8. Prinz F, Schlange T, Asadullah K. Believe it or not: how much can we rely on published data on potential drug targets? *Nat Rev Drug Discov.* (2011) 10:712. doi: 10.1038/nrd3439-c1
9. Begley CG, Ellis LM. Drug development: raise standards for preclinical cancer research. *Nature.* (2012) 483:531–3. doi: 10.1038/483531a
10. Janda CY, Waghray D, Levin AM, Thomas C, Garcia KC. Structural basis of Wnt recognition by Frizzled. *Science.* (2012) 337:59–64. doi: 10.1126/science.1222879
11. Joiner DM, Ke J, Zhong Z, Xu HE, Williams BO. LRP5 and LRP6 in development and disease. *Trends Endocrinol Metab.* (2013) 24:31–9. doi: 10.1016/j.tem.2012.10.003
12. Zununi Vahed S, Barzegari A, Zuluaga M, Letourneur D, Pavon-Djavid G. Myocardial infarction and gut microbiota: an incidental connection. *Pharmacol Res.* (2018) 129:308–17. doi: 10.1016/j.phrs.2017.11.008
13. Uitterdijk A, Hermans KC, De Wijs-Meijler DP, Daskalopoulos EP, Reiss IK, Duncker DJ, et al. UM206, a selective Frizzled antagonist, attenuates adverse remodeling after myocardial infarction in swine. *Lab Invest.* (2016) 96:168–76. doi: 10.1038/labinvest.2015.139
14. Foulquier S, Daskalopoulos EP, Lluri G, Hermans KCM, Deb A, Blankesteijn WM. WNT signaling in cardiac and vascular disease. *Pharmacol Rev.* (2018) 70:68–141. doi: 10.1124/pr.117.013896
15. Bastakoty D, Saraswati S, Joshi P, Atkinson J, Feoktistov I, Liu J, et al. Temporary, systemic inhibition of the WNT/β-catenin pathway promotes regenerative cardiac repair following myocardial infarct. *Cell Stem Cells Regen Med.* (2016) 2. doi: 10.16966/2472-6990.111
16. Moon J, Zhou H, Zhang LS, Tan W, Liu Y, Zhang S, et al. Blockade to pathological remodeling of infarcted heart tissue using a porcupine antagonist. *Proc Natl Acad Sci USA.* (2017) 114:1649–54. doi: 10.1073/pnas.1621346114
17. Yang D, Fu W, Li L, Xia X, Liao Q, Yue R, et al. Therapeutic effect of a novel Wnt pathway inhibitor on cardiac regeneration after myocardial infarction. *Clin Sci.* (2017) 131:2919–32. doi: 10.1042/CS20171256
18. Murakoshi M, Saiki K, Urayama K, Sato TN. An anthelmintic drug, pyrvinium pamoate, thwarts fibrosis and ameliorates myocardial contractile dysfunction in a mouse model of myocardial infarction. *PLoS ONE.* (2013) 8:e79374. doi: 10.1371/journal.pone.0079374
19. Sasaki T, Hwang H, Nguyen C, Kloner RA, Kahn M. The small molecule Wnt signaling modulator ICG-001 improves contractile function in chronically infarcted rat myocardium. *PLoS ONE.* (2013) 8:e75010. doi: 10.1371/journal.pone.0075010
20. Xie S, FuW, Yu G, Hu X, Lai KS, Peng X, et al. Discovering small molecules as Wnt inhibitors that promote heart regeneration and injury repair. *J Mol Cell Biol.* (2019). doi: 10.1093/jmcb/mjz023. [Epub ahead of print].
21. De Pauw A, Andre E, Sekkali B, Bouzin C, Esfahani H, Barbier N, et al. Dnmt3a-mediated inhibition of Wnt in cardiac progenitor cells improves differentiation and remote remodeling after infarction. *JCI Insight.* (2017) 2:91810. doi: 10.1172/jci.insight.91810
22. Canesin G, Evans-Axelsson S, Hellsten R, Krzyzanowska A, Prasad CP, Bjartell A, et al. Treatment with the WNT5A-mimicking peptide Foxy-5 effectively reduces the metastatic spread of WNT5A-low prostate cancer cells in an orthotopic mouse model. *PLoS ONE.* (2017) 12:e0184418. doi: 10.1371/journal.pone.0184418

**Conflict of Interest Statement:** The authors declare that the research was conducted in the absence of any commercial or financial relationships that could be construed as a potential conflict of interest.

frontiers
in Cardiovascular Medicine

ORIGINAL RESEARCH
published: 14 January 2020
doi: 10.3389/fcvm.2019.00189

# Fractional Flow Reserve Evaluated as Metric of Coronary Stenosis — A Mathematical Model Study

*Theo J. C. Faes*[1]*, *Romain Meer*[1], *Guy R. Heyndrickx*[2†] *and Peter L. M. Kerkhof*[1†]

[1] *Department of Radiology and Nuclear Medicine, Amsterdam University Medical Centers, Amsterdam, Netherlands,* [2] *Cardiovascular Center, Aalst, Belgium*

**Introduction:** Coronary arterial stenosis may impair myocardial perfusion with myocardial ischemia and associated morbidity and mortality as result. The myocardial fractional flow reserve (*FFR*) is clinically used as a stenosis-specific index.

**Aim:** This study aims to identify the relation between the *FFR* and the degree of coronary arterial stenosis using a simple mathematical model of the coronary circulation.

**Methods:** A mathematical model of the coronary circulation, including an arterial stenosis of variable degree, was developed. The relation between the *FFR* and the degree of stenosis (defined as the fractional cross sectional area narrowing) was investigated, including the influence of the aortic and venous pressures and the capillary resistance. An additional study concerning 22 patients with coronary artery disease permits comparison of clinical data and *in silico* findings.

**Results:** The *FFR* shows an S-shaped relationship with the stenosis index. We found a marked influence of venous and aortic pressure and capillary resistance. The *FFR* is accompanied by a clinically relevant co-metric ($FFR_C$), defined by the Pythagorean sum of the two pressures in the definition formula for *FFR*. In the patient group the $FFR_C$ is strongly related to the post-stenotic pressure ($R = 0.91$). The $FFR_C$ requires establishment of a validated cut-off point using future trials.

**Conclusion:** The S-shaped dependence of *FFR* on the severity of the stenosis makes the *FFR* a measure of the ordinal scale. The marked influences of the aortic and venous pressures and the capillary resistance on the *FFR* will be interpreted as significant variations in intra- and inter-individual clinical findings. These fluctuations are partly connected to the neglect of considering the $FFR_C$. At otherwise identical conditions the *FFR* as measured at baseline differs from the value obtained during hyperemic conditions. This expected observation requires further investigation, as the current hyperemia based evaluation fails to take advantage of available baseline data.

**Keywords: coronary circulation, coronary stenosis, degree of stenosis, fractional flow reserve, mathematical model, clinical metrics, *in silico* study**

***Edited by:***
*Gabriela Kania,*
*University Hospital Zürich, Switzerland*

***Reviewed by:***
*Daniele Torella,*
*University of Catanzaro, Italy*
*Francesco Tona,*
*University of Padova, Italy*

***Correspondence:***
*Theo J. C. Faes*
*tjc.faes@amsterdamumc.nl*

**†*ORCID:***
*Guy R. Heyndrickx*
*orcid.org/0000-0003-3553-3985*
*Peter L. M. Kerkhof*
*orcid.org/0000-0001-9488-633X*

***Specialty section:***
*This article was submitted to*
*Cardiovascular Biologics and*
*Regenerative Medicine,*
*a section of the journal*
*Frontiers in Cardiovascular Medicine*

***Received:*** *03 January 2019*
***Accepted:*** *11 December 2019*
***Published:*** *14 January 2020*

***Citation:***
*Faes TJC, Meer R, Heyndrickx GR and Kerkhof PLM (2020) Fractional Flow Reserve Evaluated as Metric of Coronary Stenosis — A Mathematical Model Study.*
*Front. Cardiovasc. Med. 6:189.*
*doi: 10.3389/fcvm.2019.00189*

## INTRODUCTION

A coronary artery stenosis may seriously affect myocardial perfusion with myocardial ischemia or even cardiac death as possible sequelae (1). Consequently, a function limiting coronary arterial stenosis is associated with a significant increase in morbidity and mortality, although the underlying mechanisms may partly differ for men and women (2–5). Traditionally, a stenosis has been evaluated by angiography leading to a preoccupation with coronary luminology (6). Inadequacy of this method led to a number of alternative approaches, both invasive such as pressure determinations, and non-invasive techniques including Doppler echocardiography. Often the fractional flow reserve (*FFR*) is clinically used as a stenosis-related index of maximum attainable local myocardial perfusion. By using pressure wires, the *FFR* is assessed by measuring invasively the coronary pressures proximal and distal of the stenosis. The *FFR* is defined as the ratio of mean coronary pressures measured directly distal and proximal of the stenosis, i.e., $FFR = \mathrm{P}_{\mathrm{Distal}}/\mathrm{P}_{\mathrm{Proximal}}$ [a dimensionless number in the numerical range from 0 (complete occlusion) through 1 (no occlusion)]; an *FFR*-value below 0.80 is considered to reflect a clinically significant stenosis. The *FFR* is thought to be a stenosis-specific index that reflects the effect of the coronary stenosis on the myocardial perfusion. Moreover, the *FFR* is reported to be independent of hemodynamic characteristics of the coronary circulation, such as blood pressure, heart rate, and cardiac contractility (7). In clinical practice, however, the use of the *FFR* is somewhat limited by the high costs, the extra time involved, and the need to administer adenosine to induce hyperemia with an associated risk and burden for the patient. Furthermore, the ratio *FFR* does not address its intrinsic companion, being the Pythagorean sum of $\mathrm{P}_{\mathrm{Distal}}$ and $\mathrm{P}_{\mathrm{Proximal}}$ (8) (see section Methods for details).

By using a simple mathematical model of the coronary circulation, this study aims to identify the relationship of the *FFR* on the degree of stenosis, while evaluating hemodynamic characteristics of the arterial coronary circulation. Recently, Duanmu et al. presented a lumped-parameter model of the coronary circulation (9). In their model, the coronary circulation is described by defining a number of compartments, and by characterizing the hemodynamics of each compartment with the use of a three-element Windkessel model (10). Each Windkessel consists of a dissipative Poiseuille resistance (*R*), a blood storing compliance (*C*), and a blood mass inertance (*L*). The values of these three elements (*R*, *C*, *L*) were calculated from the length and diameter of the coronary vessel using CT-images (9). To study the effect of a stenosis on the coronary hemodynamics and the *FFR*, we extended their model by including an extra dissipative resistance to more precisely mimic the stenosis. The focus of our present study is more limited than explored in Duanmu's model. Our plain model is used to gain insight in the fundamental characteristics of the *FFR* metric. This discernment will guide our future simulation studies employing the Duanmu model as a convenient starting point for both the left and right coronary artery.

Our present study aims are:

- To discuss the *FFR*'s definition with its assumptions and their theoretical consequences;
- To identify the relation of the *FFR* and the underlying degree of coronary arterial stenosis;
- To discuss the consequences of defining the *FFR* as a ratio of two pressures;
- To hint for an alternative for the *FFR*.

For verification of the outcomes, the theoretical issues will be related to available clinical data.

# METHODS

The *FFR* is determined by measuring the mean aortic pressure, $P_A^{(H)}$, and the mean pressure distal to the stenosis, $P_D^{(H)}$, during hyperemia, and by the subsequent calculation of the ratio $FFR = P_D^{(H)}/P_A^{(H)}$. In the following we will discuss: firstly, the rationale of *FFR* as ratio of distal-to-stenosis pressure to aortic pressure and, secondly, the mathematical relationship between this *FFR* and the stenosis's geometry (i.e., the ratio of the stenotic cross sectional area to the non-stenotic area) as determinant of the flow limitation.

## The Rationale of the FFR as Pressure Ratio

In their landmark study Pijls and De Bruyne start from the definition of *FFR* as the maximum myocardial blood flow in the presence of a stenosis, $F_{Smax}$, divided by the theoretical maximum myocardial blood flow in the absence of the stenosis, $F_{Nmax}$. Subsequently, they show that the *FFR* is approximately equal to the ratio of the mean pressure measured distal to the stenosis, $P_D^{(H)}$, and the mean aortic pressure $P_A^{(H)}$ both measured during hyperemia (as indicated by the letter *H* in the superscript), i.e.,

$$FFR = \frac{F_{S_{MAX}}}{F_{N_{MAX}}} \approx \frac{P_D^{(H)}}{P_A^{(H)}} \tag{1}$$

The maximum flows are achieved by the administration of a hyperemic agent, e.g., adenosine.

To accomplish this result, Pijls and De Bruyne use a two-compartment model to characterize the blood flow in the vascular bed of the coronary circulation: one compartment represents the coronary arteries, with or without stenosis, and the second compartment represents the remaining distal capillary network and venous vessels of the coronary circulation (**Figure 1**). This model defines the following quantities: Let $P_A$ and $P_V$ be the mean aortic and the venous pressure (mmHg), respectively, and let $P_D$ be the mean pressure (mmHg) distal of the epicardial artery stenosis. Moreover, let $R_A$ and $R_C$ be the hemodynamic resistances (mmHg.s/ml) of the arterial part (either non-stenotic or stenotic) and the capillary and venous part, respectively. Finally, after the administration of a hyperemic agent the capillary resistance reduces to $R_{C\min}$ and the flow

---

**Abbreviations:** α, degree of cross sectional area narrowing for a coronary artery stenosis; A, cross-sectional area; B, baseline; C, vascular compliance; CFD, computational fluid dynamics; *F*, myocardial blood flow; $F_N$, non-stenotic flow; *FFR*$_{(C)}$, fractional flow reserve (companion); H, hyperemia; *L*, full length of a coronary vessel; $L_S$, length of local stenosis; L, blood mass inertance; N, non-stenotic case; cf. S; $P_A$, coronary pressure proximal from the stenosis; $P_D$, coronary pressure distal of the stenosis; $P_V$, venous pressure; R, Poiseuille resistance; $R_A$, hemodynamic resistance (mmHg.s/ml) of the arterial part; $R_C$, hemodynamic resistance (mmHg.s/ml) of the capillary and venous parts; $R_0$, hemodynamic resistance (mmHg.s/ml) of the coronary artery without stenosis; RCA, right coronary artery; S, stenosis; cf. N; S (%), diameter-based percentage of stenosis; cf. α.

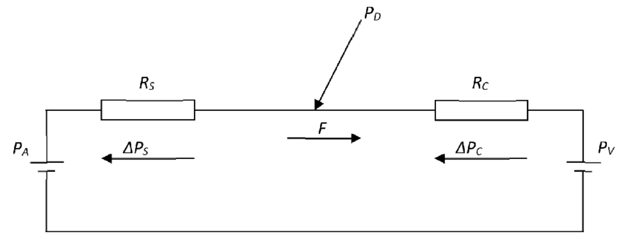

**FIGURE 1 |** Electrical analog of the coronary circulation. The model consists of an aortic pressure $P_A$ and a venous pressure $P_V$ with two resistances, serially connected between these pressure sources, to represent the stenotic $R_S$ and capillary $R_C$ fluid resistances. $F$ is the flow through the resistances, while $\Delta P_S$ and $\Delta P_C$ are the pressure drops over the resistances $R_S$ and $R_C$, respectively. $P_D$ is the pressure distal to the stenosis and proximal to the capillaries.

increases to $F_{\max}$, while the distal pressure $P_D$ decreases to $P_D^{(H)}$. Within this model, simple hemodynamic reasoning yields the following results:

1. By application of Poiseuille's law (i.e., flow equals pressure drop divided by fluid resistance; see Equation 11) to the capillary compartment, the baseline and maximum flows equal the perfusion pressures $P_D - P_V$ and $P_D^{(H)} - P_V$ divided by the capillary hemodynamic resistance $R_C$ and $R_{C\min}$, respectively. That is,

$$F = \frac{P_D - P_V}{R_C} \ \& \ F_{MAX} = \frac{P_D^{(H)} - P_V}{R_{C_{MIN}}} \tag{2}$$

2. For the non-stenotic case, the pressure drop over the arterial part is negligible compared to the capillary pressure drop, so, $P_D \approx P_A >> P_V$ and $P_D^{(H)} \approx P_A^{(H)} >> P_V$ (where $>>$ indicates: much larger). Hence, by substitution of $P_D^{(H)} \approx P_A$ in Equation (2), the non-stenotic flow $F_N$ becomes,

$$F_N = \frac{P_D - P_V}{R_C} \approx \frac{P_A - P_V}{R_C} \ \& \quad F_{N_{MAX}} = \frac{P_D^{(H)} - P_V}{R_{C_{MIN}}} \approx \frac{P_A^{(H)} - P_V}{R_{C_{MIN}}} \approx \frac{P_A - P_V}{R_{C_{MIN}}} \tag{3}$$

assuming an unchanged aortic pressure during hyperemia.

3. For the stenotic case, the pressure drop over the arterial part is non-negligible compared to the capillary pressure drop, so, $P_A > P_D > P_V$ and $P_A^{(H)} > P_D^{(H)} > P_V$. Hence, with Equation (2), the stenotic flow $F_S$ becomes,

$$F_S = \frac{P_D - P_V}{R_C} \ \& \ F_{S_{MAX}} = \frac{P_D^{(H)} - P_V}{R_{C_{MIN}}} \tag{4}$$

4. By substitution of these flows (Equations 3 and 4) in the definition of $FFR$ (Equation 1) yields,

$$FFR \overset{(1)}{=} \frac{F_{S_{MAX}}}{F_{N_{MAX}}} \overset{(2)}{=} \frac{\frac{P_D^{(H)}-P_V}{R_{C_{MIN}}}}{\frac{P_A^{(H)}-P_V}{R_{C_{MIN}}}} \overset{(3)}{=} \frac{P_D^{(H)} - P_V}{P_A^{(H)} - P_V} \overset{(4)}{\approx} \frac{P_D^{(H)}}{P_A^{(H)}} \tag{5}$$

with the following rationale applied at the numbered signs of equality: (1) definition of $FFR$ (Equation 1); (2) substitution of Equations (3, 4); (3) cancelation of the common term $R_{C\min}$; (4) neglecting $P_V$, as considered small compared to $P_D^{(H)}$ and $P_A$.

Note that, occasionally, the $FFR$ is measured as the ratio of the distal-to-stenosis pressure and the aortic pressure in *baseline* (B) instead of the *hyperemic* state. Let $FFR^{(H)}$ and $FFR^{(B)}$ refer to hyperemic and baseline state, respectively. Then, Equation (5) implies that $FFR^{(H)} \leq FFR^{(B)}$ since

$$FFR^{(H)} = \frac{P_D^{(H)}}{P_A^{(H)}} \approx \frac{P_D^{(H)}}{P_A} \leq \frac{P_D^{(B)}}{P_A} = FFR^{(B)} \tag{6}$$

as hyperemic $P_D^{(H)}$ is lower than the baseline $P_D^{(B)}$ and as hyperemic and baseline aortic pressure are approximately equal, $P_A^{(H)} \approx P_A$. Thus, the $FFR$ during hyperemia is smaller than $FFR$ during baseline.

To summarize: under the assumptions of the model with Poiseuillean resistances, the $FFR$ as ratio of the maximum stenotic blood flow and the theoretical maximum non-stenotic blood flow is approximated by the ratio of the mean hyperemic post-stenotic pressure $P_D^{(H)}$ and the mean aortic pressure $P_A^{(H)}$.

## Consequences of Defining the *FFR* as Ratio of Pressures

From a mathematical-physiologic viewpoint, one might interpret the $FFR$ as a summary of two pressures, $P_D$ and $P_A$, in only one number, being the ratio $P_D/P_A$. Subsequently, one might wonder whether relevant information is lost by summarizing two pressures in a single number which concerns a dimensionless ratio.

A convenient way to analyze the consequences of using the ratio, is to employ the analogy with the Cartesian and polar coordinate systems (see **Figure 2**). To be specific, consider the pressures ($P_A$, $P_D$) as a point in a graph with $P_A$ and $P_D$ on the abscissa and ordinate (horizontal and vertical axis), respectively. Hence, ($P_A$, $P_D$) act as the Cartesian coordinates. Alternatively, the same point can be defined by the polar coordinates: (i) the length of the line from the origin to the point ($P_A$, $P_D$); (ii) the angle between this line and the positive abscissa (or equivalently by the slope of this line). By using the Pythagorean theorem, the line's length, say $FFR_C$, equals $\sqrt{}(P_A{}^2 + P_D{}^2)$ and the tangent or slope of the angle $P_D/P_A$ equals $FFR$ (see **Figure 2**). Hence, $FFR_C = \sqrt{}(P_A{}^2 + P_D{}^2)$ and $FFR$ act as the polar coordinates. So, in the graph the point is characterized complete by either the Cartesian coordinates ($P_A$, $P_D$) or the polar coordinates $FFR_C = \sqrt{}(P_A{}^2 + P_D{}^2)$ and $FFR = P_D/P_A$.

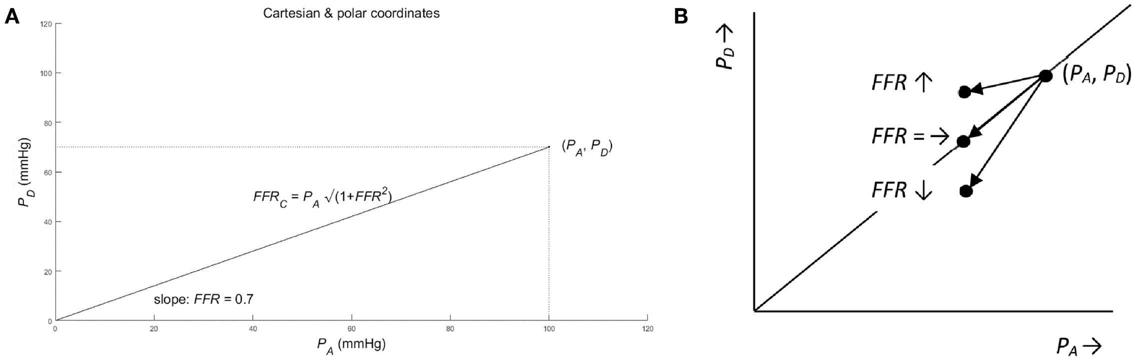

**FIGURE 2 | (A)** Cartesian and polar coordinates. The pressure $P_A$ and $P_D$ represented in Cartesian coordinates ($P_A$, $P_D$) (see dotted lines) and in polar coordinates ($P_A\sqrt{(1+FFR^2)}, FFR$). Note that the pair of pressure ($P_A$, $P_D$) define exactly one point in the graph, while the single *FFR* defines a complete line in the graph. So, mathematically speaking, the single *FFR* without the companion $FFR_C$ leaves ambiguity. As a result, all points on a line through the origin share the same value of *FFR*. (For details see Methods section). **(B)** Ambiguous change of *FFR* from point ($P_A$, $P_D$) for three different cases of a pressure decrease: The *FFR* is unchanged (see notation *FFR* =), if the change in $P_D$ is equal to the change of $P_A$ times *FFR*. Similarly, the *FFR* decreases (see FFR ↓) and increases (see FFR ↑), if the change in $P_D$ is smaller and larger than the change of $P_A$ times *FFR*, respectively (see section Methods for details).

For later use, note the following mathematical relations:

$$FFR = \frac{P_D}{P_A} \Rightarrow P_D = P_A\, FFR \text{ and } P_A = \frac{1}{FFR} P_D$$
$$FFR_C = \sqrt{P_A^2 + P_D^2} = \sqrt{P_A^2 + P_A^2 FFR^2} =$$
$$P_A\sqrt{1 + FFR^2} \approx P_A\,(1 + {}^{1}\!/_{2}\, FFR) \qquad (7)$$

where the approximation of the square root results from Newton's Binomial Series, and becomes more accurate for smaller values of *FFR*. Note: if two out of the four variables $P_D$, $P_A$, *FFR*, $FFR_C$ are known, then the remaining variables can be calculated.

Using these two coordinate systems, the original question—whether information is lost by using the *FFR*—can be answered from a mathematical point of view. By using the *FFR*, as a summary measure of $P_A$ and $P_D$, information is clearly lost, because only one of the two polar coordinates is used while the other polar coordinate is neglected. Thus, all points on the same line through the origin share the same *FFR* and, therefore, cannot be distinguished by the *FFR* alone. So, the *FFR* summarizes the information carried by $P_D$ and $P_A$ "one-dimensionally" along the lines passing the origin in the $P_A$-$P_D$-plot.

This mathematical result provides guidance to answer the remaining question whether the *FFR* can be interpreted as a sound measure of stenosis. As a counterexample, consider a patient developing a stenosis resulting in a decreased post-stenotic pressure, from $P_D$ to $\gamma P_D$ (direct result of increased stenotic fluid resistance), and a decreased aortic pressure, say from $P_A$ to $\beta P_A$ (indirect result of reduced cardiac performance due to a decreased perfusion of the cardiac muscle tissue). Then the *FFR* changes from $P_D/P_A$ to $\gamma P_D/\beta P_A$, that is a change from *FFR* to ($\gamma/\beta$) *FFR*. Depending on the actual numerical values of $\gamma$ and $\beta$, the *FFR* will decrease ($\gamma < \beta$), remain unchanged ($\gamma = \beta$), or will increase ($\gamma > \beta$) (see **Figure 2B**). Clearly, this ambiguity of the *FFR* is an undesired and unanticipated property for a sound measure of degree of stenosis.

The common clinical experience of a decreasing *FFR* with a worsening of the stenosis, may be explained by the assumption that the decrease in $P_D$ is often larger than the change in $P_A$ ($\gamma < \beta$) and, hence, the *FFR* will decrease with a worsening of the stenosis.

## Relationship Between FFR and Degree of Stenosis

In order to find the relationship between the *FFR* and the degree of narrowing in the stenosed artery, further modeling of the stenosis is required. Various approaches may be chosen: (1) a uniform narrowing of the vessel's cross-sectional area from the normal value $A_0$ to the "narrowed value" $A_S$ over the full vessel's length *L* and, then, using Poiseuille's law to calculate the narrowed vessel's hemodynamic resistance; or (2) a local narrowing of the vessel's cross-sectional area from the normal value $A_0$ to the "narrowed value" $A_S$ over the stenosis length $L_S$ and, then, using Bernoulli's law to calculate the hemodynamic resistance. The first approach will be used in this study.

### Degree of Stenosis

Let $A_S$ ($d_S$) and $A_0$ ($d_0$) be the cross-sectional area (diameter) of the coronary artery with and without a stenosis. Then, the degree of cross sectional area narrowing ($\alpha$) is defined as

$$\alpha = \frac{A_S}{A_0} = \left(\frac{d_S}{d_0}\right)^2, \text{ with: } 0 \leq A_S \leq A_0 \text{ and } 0 \leq d_S \leq d_0 \qquad (8)$$

with $\alpha$ in the range 0 (complete stenosis) to 1 (no stenosis). Alternatively, the stenosis degree *S* is defined as

$$S = 1 - \frac{d_s}{d_0} \qquad (9)$$

Clearly, both measures are related,

$$\alpha = (1 - S)^2 \text{ and } S = 1 - \sqrt{\alpha} \tag{10}$$

The advantage of using α is, however, that the subsequent formulae will be simpler.

### Poiseuille's Law Applied to a Uniform Narrowed Vessel

Let $R_S(\alpha)$ be the hemodynamic resistance (mmHg.s/ml) of the stenotic artery with a narrowing of degree α over the vessel's length $L$ (cm). Then, by applying Poiseuille's law, the resistance $R_S(\alpha)$ is,

$$R_S(\alpha) = \frac{\Delta P}{F} = \frac{8\pi\eta L}{A_S^2} = \frac{8\pi\eta L}{A_0^2}\frac{1}{\alpha^2} = \frac{R_0}{\alpha^2}, \quad \text{with: } R_0 = \frac{8\pi\eta L}{A_0^2} \tag{11}$$

where $\Delta P$ is the vessel's pressure difference (mmHg), $F$ is the flow (ml/s), η is the viscosity (mmHg.s/cm$^2$), $L$ is the vessel length (cm), and $A_S$ the cross-sectional area (cm$^2$) of the stenotic artery.

### Pressures and Flow

With reference to **Figure 1**, the flow ($F$) equals the perfusion pressure $P_A - P_V$ divided by the sum of the two resistances $R_S(\alpha)$ and $R_C$, i.e.,

$$F = \frac{P_A - P_V}{R_C + R_S(\alpha)} \tag{12}$$

Moreover, the distal pressure $P_D$ equals the aortic pressure $P_A$ minus the pressure drop over $R_S(\alpha)$, i.e., $R_S(\alpha)\, F$. Hence,

$$P_D = P_A - R_S(\alpha)\, F \tag{13}$$

and by substitution of Equation (12) in Equation (13) yields,

$$\begin{aligned} P_D &= P_A - \frac{R_S(\alpha)}{R_C + R_S(\alpha)}(P_A - P_V) \\ &= \left(1 - \frac{R_S(\alpha)}{R_C + R_S(\alpha)}\right) P_A + \frac{R_S(\alpha)}{R_C + R_S(\alpha)} P_V \\ &= \frac{R_C}{R_C + R_S(\alpha)} P_A + \frac{R_S(\alpha)}{R_C + R_S(\alpha)} P_V \end{aligned} \tag{14}$$

The dependence of $FFR$ upon the degree of narrowing α is found by first the substitution of Equation (14) in Equation (1), i.e.,

$$FFR = \frac{P_D}{P_A} = \frac{R_C}{R_C + R_S(\alpha)} + \frac{R_S(\alpha)}{R_C + R_S(\alpha)}\frac{P_V}{P_A} \tag{15}$$

and, subsequently, the substitution of Equation (11) in Equation (15), i.e.,

$$FFR = \frac{P_D}{P_A} = \frac{R_C}{R_C + \frac{R_0}{\alpha^2}} + \frac{\frac{R_0}{\alpha^2}}{R_C + \frac{R_0}{\alpha^2}}\frac{P_V}{P_A} \tag{16}$$

or, equivalently,

$$FFR = \frac{P_D}{P_A} = \frac{1}{1 + \frac{R_0}{R_C}\frac{1}{\alpha^2}} + \frac{\frac{R_0}{R_C}\frac{1}{\alpha^2}}{1 + \frac{R_0}{R_C}\frac{1}{\alpha^2}}\frac{P_V}{P_A} \tag{17}$$

Note: The $FFR$ in Equations (15) or (16) applies to both $FFR^{(H)}$ or $FFR^{(B)}$, depending on whether the pressures were measured under hyperemia or baseline conditions.

## Patient Study

This retrospective sub-study evaluates data from 22 patients (age 67 ± 11 years) from Aalst Cardiovascular Center (Belgium), having right coronary artery (RCA) stenosis in proximal (p, $N = 8$), medial (m, $N = 12$), or distal (d, $N = 4$) part of the vessel. $FFR$ was derived from the ratio of the average blood pressure distal to the coronary artery stenosis ($P_D$) and the average pressure in the aorta ($P_A$), both obtained during i.c. adenosine infusion or after an i.v. bolus injection. Technical details are described elsewhere (5). All patients gave permission to use their data in anonymized investigations by signing a consent form. This retrospective study was exempt from institutional review by the Clinical Review Board.

## RESULTS

## *In silico* Study

The dependence of the $FFR$, $FFR_C$ and $P_D$ on the degree-of-stenosis α (α = 1 is no stenosis, α = 0 is complete occlusion) is specified in Equation (17) combined with Equation (7) (see section Methods). To discuss the nature of the dependence of $FFR$, $FFR_C$, and $P_D$ on α, three graphs are created, and an additional graph is drawn to document $FFR$ vs. $P_D$ (**Figure 3**). In the following four points, the merits of each of these graphs is presented in detail:

1. The upper-left panel shows the clearly non-linear dependence of $FFR$ upon α (Equation 17), for various settings of the parameters: $R_0/R_C = 0.04$ or 0.1 with $P_V/P_A = 0$ or 0.1 (see legend in upper-left panel). Note the following:

- The four lines share a similar S-shape (which is common for a hyperbolic function of the form in Equation 17) but the S-shaped curves start and end at different levels. In particular, the curves start (α = 0) at $P_V/P_A$ [i.e., the origin for $P_V/P_A$= 0 and point (0, 0.1) for $P_V/P_A$= 0.1] and the lines end (α = 1) at approximately $(1+ R_0/R_C)^{-1}$ (i.e., approximately 0.96 and 0.83, almost independently of $P_V/P_A$). Note that $P_V/P_A$ dominates the starting values (left) while $R_0/R_C$ dominates the end values (right), resulting in a crossover of the dotted and dashed line. These four example curves can be used to predict other parameter settings. The lower left and upper right point is determined by the value of $P_V/P_A$ and $(1+ R_0/R_C)^{-1}$ while the steepness of the curve decreases with an increasing $R_0/R_C$. In summary: the dependence of $FFR$ on α is an S-shaped relation with the start and end points dependent upon the ratio of the aortic and the venous pressures, as well as the ratio of the non-stenotic arterial and capillary-venous resistances.

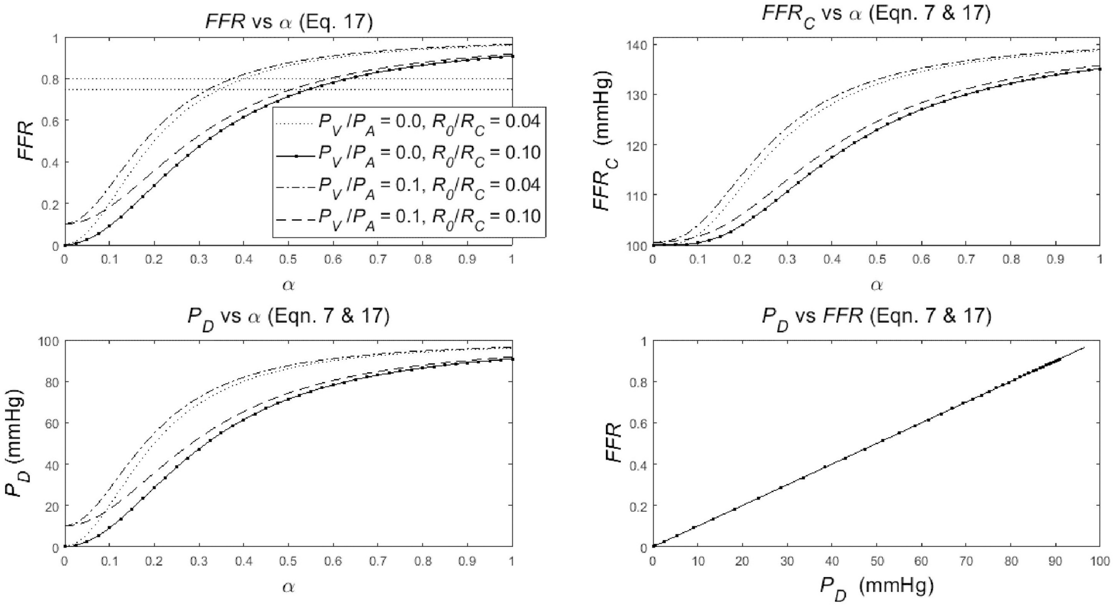

**FIGURE 3 |** Simulation results for the non-linear dependence of:

- the *FFR* with common reference values at 0.75 and 0.8 (upper-left panel),
- its companion $FFR_C$ (upper-right panel),
- the distal-to-stenosis pressure $P_D$ (lower-left panel),

to the degree of stenosis α (α = 1 is no stenosis, α = 0 means complete occlusion) for different values of $R_0/R_C$ and $P_V/P_A$ (see legend).

- The relation of *FFR* as function of $P_D$ (lower-right panel),

(The legend in upper-left panel applies also to the upper-right and lower-left panel). See section Results for details.

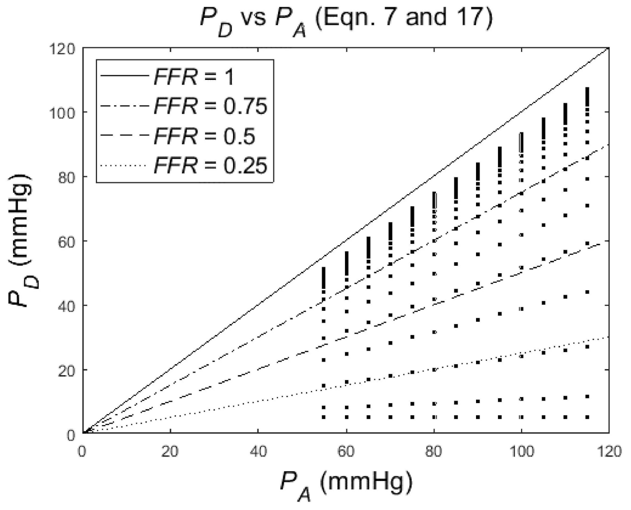

**FIGURE 4 |** Simulation of distal-to-stenosis pressure $P_D$ vs. mean aortic pressure $P_A$ (Equation 17) with each dot representing a case with $P_A$ running from 55 to 115 mmHg for different values of the degree of stenosis α (α running from 1 to 0), and with lines (Equation 7) indicating *FFR* at 1, 0.75, 0.5, and 0.25.

- The S-shaped form of the curves implicates that the change of the *FFR* for a change of α is strongly dependent on the particular location considered. In the steep middle part of the curve, a change of α results in a relatively large change in *FFR*, while a same sized change in α will result in much smaller change in *FFR* in the flat lower and upper parts of the curve. This notion is illustrated by the horizontal line with dots, where the dots are separated by an equal step size in *FFR* while the associated step size in α varies with the steepness of the curve. Thus, the sensitivity of the *FFR*, as a measure of stenotic narrowing, is strongly dependent upon the degree of stenotic narrowing. Technically speaking, this makes that *FFR* is a measure on an ordinal scale (i.e., equal changes in α yield unequal changes in *FFR*). This fact implies that common statistics like means and standard deviations, as well as parametric statistical tests, like Student's *t*-test, are here strictly speaking inappropriate. In summary, a unit change of *FFR* does not correspond to a unit change in α.
- The venous pressure is of influence on the *FFR*; the larger the $P_V/P_A$, the larger the *FFR* although this effect is more pronounced for lower α. This influence may lead to an overestimation of the actual value of the *FFR*. Technically speaking, the *FFR* is a biased measure of α. Similarly, the capillary resistance is of strong influence on the *FFR*; the larger $R_0/R_C$ (i.e., the smaller $R_C$) the less steep the *FFR*-curve is, with as result quite different values of *FFR*. In particular, the *FFR*s as measured during baseline and hyperemia are expected to differ significantly, where the baseline *FFR* is larger than the hyperemic *FFR* [see Equation (6) in section Methods]. In summary, the *FFR* is a biased measure of α, and the uncontrolled bias will present itself as random variations in inter-individual results.

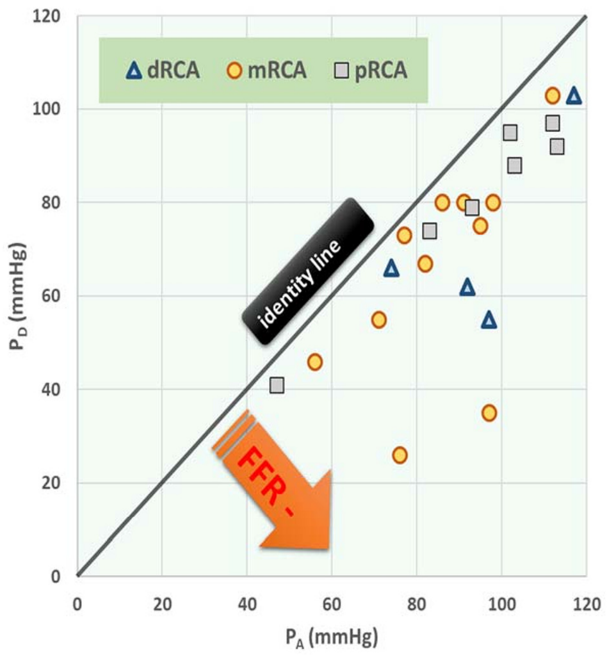

**FIGURE 5 |** Post-stenotic pressure ($P_D$) vs. mean aortic pressure ($P_A$) during hyperemia with stenosis at different anatomical locations. Data points refer to 22 patients with right coronary artery (RCA) stenosis. The three symbols specify the anatomical location of each stenosis, being distal (d), medial (m), or proximal (p). The black (identity) line corresponds with a fractional flow reserve (*FFR*) of 1.00 (i.e., no stenosis). Regression line: $P_D = 0.873\ P_A - 6.836$, R = 0.728, $P < 0.001$, $N = 22$. In the section Discussion, this graph is compared with **Figure 4** which shows results from the *in silico* study.

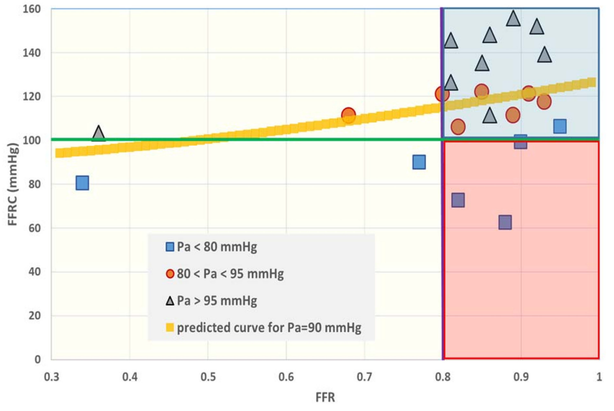

**FIGURE 6 |** Fractional flow reserve (*FFR*) and the intrinsic companion (*FFR$_C$*). The interpretation of *FFR* is not unique, as a large spread of the co-metric *FFR$_C$* can be discerned. In the past the region between 0.75 and 0.80 was termed the "gray zone." Data points having FFR > 0.80 (purple line) are often considered to refer to patients who do not require revascularization. However, the situation becomes different if the *FFR* companion (*FFR$_C$*) is accepted as a second criterion. When, for example, the green line is taken as an additive cut-off level, then the data located in the red shaded area do not simultaneously fulfill both criteria. Obviously, establishment of combined cut-off levels requires robust evaluation in large patient groups. The yellow curve is calculated for $P_A$= 90 mmHg on the basis of Equation (7), i.e., $FFR_C = P_A\sqrt{1+FFR^2}$.

2. The upper-right panel shows a somewhat similar non-linear S-shaped dependence of $FFR_C$ upon α (Equations 7 and 17), for four different setting of the parameters: $R_0/R_C = 0.04$ or 0.1 with $P_V/P_A = 0$ or 0.1 (see legend in upper-left panel) with $P_A = 100$ mmHg is all four cases. Comparison of $FFR_C$ with *FFR* shows a marked shape difference for the smaller valued α's, and a completely different $FFR_C$ scale, running from 100 to 140 mmHg, i.e., ranging between $P_A$ and almost $P_A\sqrt{2}$ (see Equation 7). In summary, the dependence of $FFR_C$ upon α is somewhat similar to the dependence of *FFR* upon α.
3. The lower-left panel shows that the dependence of $P_D$ upon α (Equations 7 and 17) is a scaled version of *FFR* for the four different setting of the parameters: $R_0/R_C = 0.04$ or 0.1 with $P_V/P_A = 0$ or 0.1 (see legend in upper-left panel) with $P_A = 100$ mmHg is all four cases. The only difference with *FFR* is the fact that the scale runs from 0 to 100 mmHg while the curves start ($\alpha = 0$) at $P_V$ and end ($\alpha = 1$) at approximately $(1+R_0/R_C)^{-1}\ P_A$ (see Equation 14). In summary, the dependence of $P_D$ upon α is a scaled version of the dependence of *FFR* upon α.
4. The lower-right panel shows the dependence of *FFR* upon $P_D$ (Equations 7 and 17), which is exactly a straight line through the origin for the four different settings of the parameters: $R_0/R_C = 0.04$ or 0.1 with $P_V/P_A = 0$ or 0.1 with $P_A = 100$ mmHg in all cases. This single straight line is easily explained by rewriting the previous result $P_D = P_A\ FFR$ (Equation 7) as $FFR = P_A{}^{-1}\ P_D$. Now it becomes evident that in a graph this relation is a straight line through the origin with a slope $P_A{}^{-1}$. In summary, the dependence of *FFR* upon $P_D$ is reflected by a straight line.

**Figure 4** shows the dependence of $P_D$ on $P_A$ for a particular degree of stenosis α (each dot represents a particular case of values of α, $P_D$ and $P_A$. Note that the distance between the points is increasing or, equivalently, the density is decreasing, for a decreasing α.

## Patient Study

The distribution of $P_A$ and $P_D$ data pairs is presented in **Figure 5**. The spread of $FFR_C$ for the recorded *FFR* values is shown in **Figure 6**, while **Figure 7** illustrates that *FFR* sharply declines in a non-linear manner when the diameter reduction decreases beyond 60%. Note that in this study 2 out of 3 data pairs indicate that *FFR* can still be above the 0.80 cut-off level, while the associated diameter reduction is as large as 70%. Also is shown that the cross sectional area based stenosis metric α (running in opposite direction along the abscissa) follows a sigmoid pattern, as theoretically predicted (Equation 17). **Figure 8** presents *FFR* against mean pressure as measured distal from the coronary stenosis, using adenosine induced hyperemia. The blue curve refers to the best fitting regression (yielding $R^2 = 0.581$), calculated on the basis of the theoretically derived formula $FFR = P_D/(c_1+c_2^* P_D)$ described elsewhere (11). This approach ensures that the theoretical point where the value for *FFR*

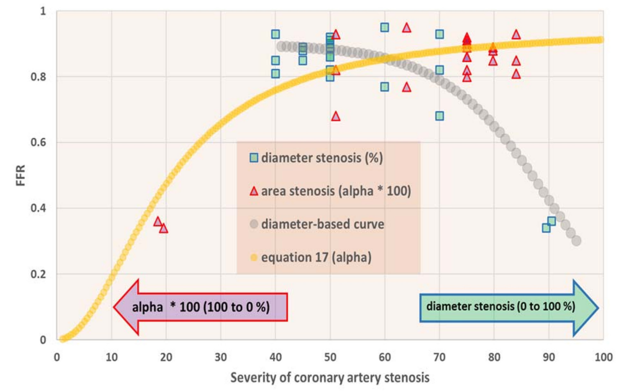

**FIGURE 7 |** Fractional flow reserve (*FFR*) in dependence of degree of coronary artery stenosis. For the patients studied ($N = 22$), the *FFR* is shown vs. percentage diameter stenosis (squares) as well as vs. the metric $\alpha$ as defined in Equation (8) (triangles). On the abscissa the scales for these metrics run in opposite directions, and therefore all data points are shown twice. Note that *FFR* sharply drops if the stenosis exceeds 70% diameter reduction. The curve for $\alpha$ (Equation 17) shows a sigmoid pattern. In the section Discussion, this graph is compared with results from the *in silico* study (**Figure 3**, upper-left).

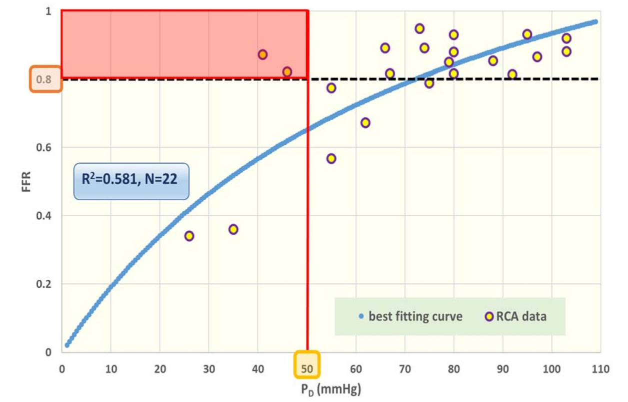

**FIGURE 8 |** Fractional flow reserve (*FFR*) against post-stenotic mean pressure ($P_D$). Data points for cardiac patients ($N = 22$) with right coronary artery (RCA) stenosis. The blue curve refers to the best fitting regression ($R^2 = 0.581$), predicted on the basis of the theoretically derived formula $FFR = P_D/(c_1{+}c_2P_D)$. The black broken line indicates the traditional cut-off level at 0.80 for *FFR*. The various data points near this line can be further characterized by specifying the prevailing $P_D$ value. The red line reflects a tentative complementary cut-off for the co-variable $P_D$, assuming that a driving $P_D$ below 50 mmHg is inadequate for appropriate perfusion. Acceptance of this criterion implies that the patients within the red rectangular area are in jeopardy. Clearly, any suggested combination of cut-off levels requires future robust evaluation in large patient groups. In the section Discussion, this graph is compared with results obtained from the *in silico* study (**Figure 3,** lower-right).

vanishes occurs at $P_D = 0$ mmHg, while *FFR* also asymptotically approaches the upper limit of 1.0 as $P_D$ increases to its physiological maximum. $FFR_C$ vs $P_D$ yields $R = 0.91$.

## Evaluation of FFR Data Presented in the Literature

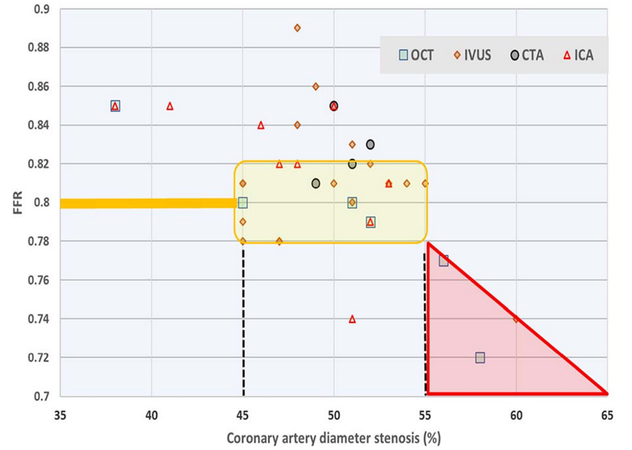

**FIGURE 9 |** Survey of relationship between FFR and diameter stenosis. Average values reported in 38 studies on the basis of four measurement techniques: optical coherence tomography (OCT), intravascular ultrasound (IVUS), computed tomography angiography (CTA), and intracoronary angiography (ICA). Most authors employ linear regression or fit a second order polynomial for their study participants. The yellow shaded area refers to values of $0.78 \leq FFR \leq 0.82$ around the common cut-off point, which narrow range corresponds with (averaged) diameter reduction anywhere between 45 and 55%. Data from Chu et al. (17).

As the relationship between FFR and the degree of stenosis is the main subject of this study, we also collected a variety of data from the literature. In a computational fluid dynamics (CFD) modeling study (12) it was shown that uncertainty in minimum lumen diameter had the largest impact on hemodynamic simulations, followed by boundary resistance, viscosity and lesion length. Also, uncertainties were not additive, and only slightly higher than the highest level found for a single parameter. Also based on CFD and using angiographic images it was demonstrated (13) that sensitivity analysis for physiological lesion significance was influenced less by coronary or lesion anatomy (33%) than by microvascular physiology (59%). Using a reduced-order model for the estimation of *FFR* (rather than 3D) based on blood flow simulations that incorporated clinical imaging and patient-specific characteristics, others found that model errors were small, and that uncertainty related to the factor by which peripheral resistance is reduced from baseline to hyperemic conditions proved to be the most influential parameter for *FFR* predictions, whereas uncertainty in stenosis geometry had greater effect in cases with low *FFR* (14). Similarly, 296 lesions were studied (15) and the authors compared (by linear regression) various clinically relevant measures, including diameter stenosis ($R = 0.565$), lesion length ($R = 0.306$), reference vessel cross sectional area ($R = 0.195$), and the myocardial supply area subtended by the coronary vessel under study ($R = 0.504$). In an attempt to further simplify calculations a 1D model was compared with a 3D model, and found to yield nearly similar findings for *FFR* (16). Findings reported in 38 studies (17) are summarized in **Figure 9** which further illustrates the discrepancy between *FFR* and diameter-based indicators of coronary luminal obstruction.

## Clinical Implications

For coronary arteries we analyzed the relationship between local diameter stenosis and the associated pressure gradient using a simple mathematical model. In clinical practice the pre- and post-stenotic pressures are obtained during induced hyperemia, and the key metric *FFR*, calculated for medical decision making, considers the minimum value of the ratio of these two pressures. We derived that the resulting dimensionless ratio requires consideration of an associated companion $FFR_C$, which is the Pythagorean mean of the two pressures involved. Similar considerations apply to the separate category of coronary flow reserve metrics, as well as to recently introduced alternative metrics such as adenosine-free $P_D/P_A$ and wave-free approaches. As on theoretical grounds any companion (as defined in our study by the pertinent hypotenuse) may not be neglected just for simplicity or convenience reasons, it is necessary to evaluate the precise clinical impact of $FFR_C$ in large scale patient studies.

# DISCUSSION

Limitations of myocardial perfusion, due to coronary arterial stenosis, are best described by pressure-flow relationships. In clinical practice, such investigations are limited to the estimation of either coronary artery diameter, pressure, or flow. Historically diameter reductions were calculated from coronary angiograms with emphasis on anatomy. Subsequent analysis referred to physiology and was based on (surrogates of) flow measurements aimed at determination of the reserve capacity, i.e., the maximum flow increase during hyperemia. One of the most popular approaches does not directly measure flow, but rather the ratio of two pressures measured proximally and distally from the stenosis during hyperemia, and is referred to as *FFR* (the primary measure evaluated in this study). Next simplified versions were explored, including ratios obtained during the (wave-free) diastolic phase (18), and even ratios without induction of hyperemia. Agreements and differences among resting coronary physiological indices led to the query: *Are all things equal?* (19). Recently, prudent thoughts were formulated regarding comparisons of various techniques, while pointing to the question what is precisely compared with what, and that question was formulated against the background and role of the acclaimed "gold standard" (20). Therefore, the aim of our study was a model-based evaluation of the *FFR*, because the model provides a complete knowledge and a full control ("gold standard") of the conditions. Moreover, the model enables the detailed evaluation of the characteristics of the *FFR*, although *in silico*. Then, the *in silico* study outcomes have been compared with patient data regarding coronary diameter (reduction), pressures proximal and distal to the stenosis during baseline and adenosine. So, the *in silico* study is used to generate predictions that are subsequently verified using available clinical data.

The outline of the discussion is as follows: first, the answers to our four research questions (see section Introduction) are discussed point-by-point; secondly, the *in silico* study outcomes are compared with clinical data; thirdly, the results of our study are put into the perspective of other model studies; finally, the limitations of our study are discussed.

The *FFR* was evaluated as a measure of arterial coronary stenosis by using a simple mathematical model of the coronary system. The coronary circulation was modeled with two Poiseuillian hemodynamic resistances, one for the arterial part and one for the capillary and venous part and an aortic and venous pressure (see **Figure 1**), all in close correspondence with the original approach (7). The arterial stenosis was described by reduction of cross-sectional surface in Poiseuilles law (Equations 8–11). This simple model allowed the calculation of explicit formulae (with graphs) for the flow *F* (Equation 12), the distal-to-stenosis pressure $P_D$ (Equation 14), the *FFR* (Equation 17), all as a function of the degree of stenosis α. This model and these formulae and associated graphs, allow the evaluation of the *FFR* as a measure of arterial stenosis. First, our main objectives in this study (see section Introduction) are discussed point-by-point:

- Firstly, the *FFR's definition and its theoretical consequences*. The *FFR* is defined as the ratio of the maximum myocardial blood flow in presence of a stenosis and the theoretical maximum myocardial blood flow an absence of the stenosis. Pijls and De Bruyne argued that the intended *FFR* can be approximated by the ratio of the mean distal-to-stenosis pressure and the mean aortic pressure, both measured during a drug-induced hyperemia. Our analysis confirmed, not surprisingly, the Pijls and De Bruyne results but also clearly showed that: (1) the *FFR* is not a simple linear measure of the degree of stenosis (**Figure 3** upper-left panel); and (2) the FFR measured at baseline conditions and during hyperemia are related similarly to the degree of stenosis and, as expected, the *FFR* is larger at baseline than in hyperemia *FFR* (see Equation 6).
- Secondly, the *relation between the FFR and the degree of coronary arterial stenosis* was identified. This relation was found to be an S-shaped curve, possibly significantly influenced by both the size of the capillary resistance relative to the stenotic resistance and the size of the venous pressure relative to the aortic pressure. The S-shaped curve implicates that the sensitivity of the *FFR*, as a measure of stenotic narrowing, is strongly dependent upon the degree of stenotic narrowing itself. Technically speaking, this makes *FFR* a measure of α on an ordinal scale (i.e., equal changes in α yield same-direction but unequal changes in *FFR*) implying that common statistics like means and standard deviations and, parametric statistical tests, like Student's *t*-test, are strictly speaking inappropriate. The influence of the venous pressure may lead to an overestimation of the actual value of the *FFR*. Technically speaking, the *FFR* is a biased measure of α. The influence of the capillary resistance on the steepness the *FFR*-curve changes the sensitivity of the *FFR,* resulting in quite different values of *FFR*. In particular, the *FFR* values measured during baseline and hyperemia are expected to differ significantly, with the baseline *FFR* larger than the hyperemic *FFR* (see Equation 6). All these influences make the *FFR* a biased measure of α and these uncontrolled biases will present themselves as random variations in intra- and inter-individual clinical results.
- In addition, one needs to consider the following trade-off in answering the question whether to determine the *FFR* under hyperemic or baseline conditions: In the upper-left

panel of **Figure 3**, the two upper and two lower curves can be interpreted as the *FFR* at baseline and at hyperemic conditions, respectively (using the following rationale: the $R_0/R_C$ value for the lower lines are larger than for the upper lines. Thus, by the inverse proportionality of $R_C$, the $R_C$ values of the upper lines are larger than for the lower lines, and therefore the upper and lower lines refer to the baseline and hyperemic conditions, respectively). The disadvantage of the "baseline lines" (i.e., the upper lines) over the "hyperemic lines" (i.e., the lower lines) is that these "baseline lines" are far more curved than the "hyperemic lines." So, the sensitivity of the *FFR* for changes for α is expected to be more uniform in the "hyperemic lines." However, the disadvantage of the "hyperemic lines" (lower lines) is that the biasing influence of the venous pressure ($P_V$) is more pronounced compared to the "baseline lines" (upper lines); notice that the distance between the lower "hyperemic lines" is larger compared to the distance between the higher "baseline lines." The relevance of these findings—a more curved hyperemic line vs. a more pronounced influence of venous pressure—is in need of a clinical evaluation study, in particular for the region around the reference value *FFR* = 0.80. In addition, the difference between the baseline and hyperemic lines in the graph indicates that the reference value for *FFR* needs to be chosen significantly different for the hyperemic and baseline conditions.
- Thirdly, the *FFR* is *a summary* of two pressures, $P_D$ and $P_A$, in one ratio, $P_D/P_A$. Our analysis (**Figure 2**) showed an ambiguous interpretation of the *FFR*. That is, a decrease (increase) of the *FFR* not necessarily results from an increase (decrease) of the degree of stenosis. In fact, an unambiguous interpretation of the *FFR* is only possible under the extra condition of a constant arterial pressure $P_A$. This is a somewhat surprising finding because intuitively one expects the *FFR* to be controlled for variation in $P_A$ by the fact that the *FFR* normalizes $P_D$ to $P_A$. In conclusion, in the present clinical experience with *FFR* the decrease in $P_D$ may be larger than in $P_A$ and, hence, the *FFR* will decrease with a worsening of the stenosis and the disturbing and ambiguous influence of varying $P_A$ is interpreted as random variations (noise). As a suggestion for further clinical research, the relative contribution of $P_D$ and $P_A$ on *FFR* can be easily assessed in clinical data by taking the logarithm of the *FFR*, i.e., $\ln(FFR) = \ln(P_D) - \ln(P_A)$ and, then performing a linear regression analysis to the line $\ln(FFR) = A^*\ln(P_D) - B^*\ln(P_A) + C$; the size and significance of parameters *A* and *B* indicate the relative importance of $P_D$ and $P_A$ to *FFR*.
- Fourthly, given the complex dependence of the *FFR* on the degree of stenosis and the additional biasing influences of the venous pressure and capillary resistance, one might wonder whether the *FFR* as pressure ratio can be improved. *To hint for an alternative*: clearly the stenotic pressure drop, i.e., $P_A - P_D$ in the model (**Figure 1**) is of key importance, but needs to be compared with the pressure drop over the capillary and venous part of the circulation, i.e., $P_D - P_V$. Hence, an obvious choice seems to define the alternative *FFR* as $(P_A - P_D)/(P_D - P_V)$, which equals $(F\,R_0(\alpha))/(F\,R_C) = R_0/R_C\ 1/\alpha^2$ (by Equation 11) or, reversely, by rewriting to get α at the left side, the measure of the degree of stenosis is $\alpha = \sqrt{\{R_0/R_C\ (P_D - P_V)/(P_A - P_D)\}}$. Although this alternative provides explicitly the degree of stenosis and is free of a biasing influence of the venous pressure, this alternative still suffers from the influence of the intra- and inter-individually varying baseline stenotic and capillary resistances. Probably this is a drawback of all attempts to characterize stenotic resistances by a measure based on pressure measurements alone. Fundamentally, limitations of myocardial perfusion due to arterial coronary stenosis are best described by pressure-flow relationships but, in clinical practice, such investigations are often limited to the estimation of coronary artery diameter, pressure, or flow. So, the best practice needs to be found by a mathematical-physical approach, further guided by a subsequent clinical evaluation of stenotic measures.

This completes the discussion of our main objectives regarding the *in silico* study.

The comparison of the outcomes of the *in silico* study with the clinical patient data regarding coronary diameter (reduction) yields the following results:

- The *in silico* model predicts a relation of $FFR_C = P_A\sqrt{\left(1 + FFR^2\right)}$ (see Equation 7). Indeed, the clinical data in **Figure 6** reveals such a quadratic relation, but with a large amount of scatter due to inter-individual variation of $P_A$.
- The *in silico* model predicts a S-shaped dependence of *FFR* on α (**Figure 3**, upper-left panel). Indeed, the clinical data in **Figure 7** shows the upper part of the S-shaped form, while the lower part of the S-shape (severe stenosis) is not visible in **Figure 7** simply because these severe cases of stenosis are not present in our clinical data set. So, the clinical data is in accordance with the *in silico* model prediction. Note that different measures of stenosis are used. **Figure 7** shows both the stenotic diameter reduction and α, while in **Figure 3** the free lumen area based metric α is used.
- The *in silico* model predicts, for an increasing degree of stenosis, a decreasing density of cases in the plot of $P_D$ vs. $P_A$ (see **Figure 4**) and, indeed, this is observed in the clinical data of **Figure 5**.
- The *in silico* model predicts a linear relation between *FFR* and $P_D$ with a slope ${P_A}^{-1}$, for the case of a constant $P_A$ (that is a straight line from the lower-left corner to the upper-right corner). In **Figure 8** the clinical data indeed shows this relation in presence of a large amount of scatter due to inter-individual variation of $P_A$. Based on the calculation of $c_1$ and $c_2$ (derived from **Figure 5**) a best fitting curve (blue) was constructed. If a tentative second criterion ($P_D$ cut-off e.g., at 50 mmHg) is applied, then the data points in the red shaded rectangular are do not meet both requirements. This choice implies that two patients are judged to have a functional coronary stenosis despite the fact that their $FFR > 0.80$. Obviously, this approach assumes that the cut-offs for *FFR* and $P_D$ are independent. Therefore, it is very well-conceivable that the criterion for *FFR* may vary with the prevailing $P_D$ level. Based on machine learning methods we have already

demonstrated the applicability of a non-linear divider when analyzing ejection fraction in heart failure patients (21).

- For *FFR*, a "gray zone" has been discussed in the literature with values between 0.80 and 0.75 (1). Although this range covers only 5% of the complete theoretical range, the more important issue is the fact that a substantial portion of patients is located within this range of uncertainty. This completes the confirmation of the *in silico* study predictions by our clinical data.

To put our study in perspective: Various modeling approaches have been employed to evaluate the severity of coronary stenosis (22). Some investigators (23) applied numerical modeling of the flow in a stenosed coronary artery in relation to main hemodynamic parameters. Using a resistive model of an epicardial stenosis (0–80% diameter reduction) in series with the coronary microcirculation at maximal vasodilation, *FFR* was evaluated for changes in coronary microvascular resistance (0.1–0.6 mmHg.min/ml), aortic pressure (between 70 and 130 mmHg), and coronary outflow pressure (0–15 mmHg), and it was found that the sensitivity of *FFR* to these hemodynamic changes was highest for stenoses of intermediate severity (23). Recent studies employ either a patient-specific lumped-parameter model of the coronary circulation (9) or applied the SimVascular Cardiovascular Modeling Package (24). Meta-analysis of *FFR* vs. quantitative coronary angiography and non-invasive imaging for evaluations of myocardial ischemia resulted in relatively poor concordance among outcomes (22). Furthermore, a visual-functional mismatch has been reported between coronary angiography and *FFR* (25). Pellicano et al. documented that angiography derived expressions for *FFR* matched those using traditional pressure ratios, thus claiming to integrate anatomy and physiology (26).

In contrast, our investigation concerns *in silico* studies, combined with actual patient data for the RCA; the characteristics (i.e., the scale property and the bias) of the *FFR* are described as a man-made measure (technical term estimator) of arterial coronary stenosis in a simple resistive model of the coronary circulation similar to the original model used by Pijls and De Bruyne. The higher *FFR* sensitivity for stenoses of intermediate severity was confirmed (23). Moreover, the profound influence of venous pressure was emphasized but the main difference with earlier approaches is the introduction of $FFR_C$ as a co-measure of *FFR*. Our graphical-mathematical analysis (with use of Cartesian and polar coordinates) indicates clearly that summarizing two pressures ($P_D$ and $P_A$) in one ratio (*FFR*) only partly captures the information actually collected, and that the complementary information contained in the companion $FFR_C$ appears to be clinically relevant. As a provocative example: Consider the case of an $FFR = 0.80$ calculated form $P_D = 40$ mmHg, and a worrisome low $P_A = 50$ mmHg. This situation implies that the patient is both hypotensive (27) and that the perfusion pressure is low. Yet, the *FFR* is not abnormal. One would object, of course, that the $P_D$ and $P_A$ pressures themselves are clear warning signs. But that is precisely the point we emphasize, as their ratio (the *FFR*) is an inadequate summary of two separately already relevant pressures. One must take into account both pressures, or the combination of *FFR* and the $FFR_C$ to acquire the full picture. Only under the very restrictive condition that the $FFR_C$ is constant, the *FFR* is an unambiguous measure of the degree of stenosis. In summary, our investigation evaluates the characteristics of the *FFR* as measure of the degree of stenosis; our main conclusion is that the *FFR* is insufficient a measure of stenosis because: (1) the *FFR* (without $FFR_C$) cannot be interpreted unambiguously; (2) the *FFR* is on ordinal scale (unit differences in *FFR* are not proportional to unit changes in stenosis with as result that standard statistics, like means, standard deviations, Student's *t*-test) do not apply and non-parametric methods must be applied; (3) the uncontrolled influences of venous and aortic pressure and the capillary resistance on the *FFR* present themselves in the final results as random variations (noise) while, factually, these variations originate from imperfections of the *FFR* as metric.

Pressure loss across a stenosis is a function of resistance, whose components include morphologic factors (including stenosis entrance angle, orifice configuration, length of stenosis, exit angles) as well as physiologic factors such as flow and associated myocardial supply area (28). Recently, the incremental value of also considering the subtended myocardial mass for identifying *FFR*-verified ischemia was confirmed using quantitative CT angiography (29). Furthermore, as explicitly formulated in an editorial, the question arises "*which of the two instruments for gauging stenosis, FFR or angiography, is at fault*" (30). Given the rather constant diameter (among comparable individuals) of the unaffected vessel (which variable is the rather constant number in the denominator for % diameter reduction), it would seem that changes for the pertinent hypotenuse, here associated with diameter reductions due to occlusion, are less pronounced compared to the hypotenuse variation associated with *FFR* determinations, as $P_A$ (which is the denominator in *FFR*) is subjected to a wide range of variations.

This completes the discussion of our analysis against the background of studies which employ *FFR* as a gold standard to evaluate functional limitations associated with epicardial coronary artery stenosis.

## LIMITATIONS

Our model-based evaluation of the *FFR* as measure of the degree of stenosis was based on the simple model of the coronary circulation originally used (7). As a result, our study is limited because of (1) the use of Poiseullian resistances in a model that neglects the influences of a non-Poiseuillian pressure-flow relation in the coronary arteries, (2) the neglect of neural and hormonal factors and the autoregulation in the microvascular bed (prearterioles), (3) the neglect of the geometry of the coronary tree, (4) sex-specific differences, extensively reported in the literature (2, 31), were not investigated. Preliminary analysis showed that our approach is still feasible to arrive at similar results for the more complicated cases with non-Poiseuillian and autoregulatory effects on resistance. Moreover, the present model's focus is on hemodynamic resistances only while neglecting the Windkessel dynamics of the coronary system, but a preliminary analysis shows that similar results are found by using a model including the Windkessel properties, yet the manuscript's margin is too small to provide details.

Also, it must be noted that all studies relating *FFR* to relative stenosis severity, including our own investigation, compare two dimensionless ratio-based metrics (32). Such comparisons neglect the corresponding companion metrics. While both constituents of $FFR_C$ may assume a wide range of values (see e.g., **Figure 5**), it can be stated that the denominator term in the α or S% metrics have a rather fixed value for each vessel, given any particular patient while taking into account body mass and sex (31). The rather fixed reference level in case of diameters or areas clearly renders a more insightful interpretation to this sub-group of ratios.

The *FFR* approach is limited from a technical point of view, as it only considers hyperemic data. Inclusion of baseline values recorded for $P_A$ and $P_D$ may assist in developing a more comprehensive characterization of myocardial perfusion abnormalities.

## CONCLUSIONS

The dependence of the *FFR* on the degree of stenosis shows an S-shaped form. Consequently, *FFR* is a measure of the ordinal scale. Moreover, the marked disturbing influences of the aortic and venous pressures and the capillary resistance on the *FFR* will be significantly manifested as random variations (noise) in intra- and inter-individual clinical results. These problems are partly caused by the neglect of the *FFR*'s companion, namely the $FFR_C$ (32). Taken together, the combined use of *FFR* and $FFR_C$, or alternatively $P_D$ and $P_A$ when considered in unison, provide more complete information on a flow limiting coronary stenosis. When analyzing ratios, it may also be useful to consider a logarithmic transformation.

## ETHICS STATEMENT

This retrospective study in patients from Cardiovascular Center, Aalst, was exempt from permission, as stated by the local ethics committee. All patients provided permission to use their data for investigational purposes.

## AUTHOR CONTRIBUTIONS

TF designed the study, developed the software for the simulation studies, and wrote the initial version. RM developed the first versions of the software for the simulation studies and contributed to the text. GH collected patient data and implemented clinical background. PK designed the study, illustrated clinically relevant aspects, and complemented the text.

## REFERENCES

1. Heyndrickx GR, Tóth GG. The FAME trials: impact on clinical decision making. *Interv Cardiol.* (2016) 11:116–9. doi: 10.15420/icr.2016:14:3
2. Taqueti VR. Sex differences in the coronary system. In: Kerkhof PLM, Miller VM, editors. *Sex-Specific Analysis of Cardiovascular Function*. Cham: Springer (2018). p. 257–78. doi: 10.1007/978-3-319-77932-4_17
3. Kang SJ, Ahn JM, Han S, Lee JY, Kim WJ, Park DW, et al. Sex differences in the visual-functional mismatch between coronary angiography or intravascular ultrasound versus fractional flow reserve. *JACC Cardiovasc Interv.* (2013) 6:562–8. doi: 10.1016/j.jcin.2013.02.016
4. Kim CH, Koo BK, Lee JM, Shin ES, Park J, Choi KH, et al. Influence of sex on relationship between total anatomical and physiologic disease burdens and their prognostic implications in patients with coronary artery disease. *J Am Heart Assoc.* (2019) 8:e011002. doi: 10.1161/JAHA.118.011002
5. Kerkhof PLM, Osto E, Tona F, Heyndrickx GR, Handly N. Sex-specific interpretation of coronary flow reserve and fractional flow reserve metrics, including their companions. *Conf Proc IEEE Eng Med Biol Soc*. (2019) 2019:7006–9. doi: 10.1109/EMBC.2019.8857589
6. Topol EJ, Nissen SE. Our preoccupation with coronary luminology. The dissociation between clinical and angiographic findings in ischemic heart disease. *Circulation.* (1995) 92:2333–42. doi: 10.1161/01.CIR.92.8.2333
7. Pijls NHJ, De Bruyne B. Coronary pressure measurement and fractional flow reserve. *Heart.* (1998) 80:539–42. doi: 10.1136/hrt.80.6.539
8. Kerkhof PLM, Mérillon JP, Yoo BW, Peace RA, Parry G, Heyndrickx GR, et al. The Pythagorean theorem reveals the inherent companion of cardiac ejection fraction. *Int J Cardiol.* (2018) 270:237–43. doi: 10.1016/j.ijcard.2018.06.074
9. Duanmu Z, Yin M, Fan X, Yang X, Luo X. A patient-specific lumped-parameter model of coronary circulation. *Nat Sci Rep.* (2018) 8:874. doi: 10.1038/s41598-018-19164-w
10. Westerhof N, Stergiopulos N, Noble M. *Snapshots of Hemodynamics: An Aid for Clinical Research and Graduate Education*. New York, NY: Springer (2010).
11. Kerkhof PLM, van de Ven PM, Yoo BW, Peace RA, Heyndrickx GR, Handly N. Ejection fraction as related to basic components in the left and right ventricular volume domains. *Int J Cardiol.* (2018) 255:105–10. doi: 10.1016/j.ijcard.2017.09.019
12. Sankaran S, Kim HJ, Choi G, Taylor CA. Uncertainty quantification in coronary blood flow simulations: impact of geometry, boundary conditions and blood viscosity. *J Biomech.* (2016) 49:2540–7. doi: 10.1016/j.jbiomech.2016.01.002
13. Morris PD, Silva Soto DA, Feher JFA, Rafiroiu D, Lungu A, Varma S, et al. Fast virtual fractional flow reserve based upon steady-state computational fluid dynamics analysis: results from the VIRTU-Fast study. *JACC Basic Transl Sci.* (2017) 2:434–46. doi: 10.1016/j.jacbts.2017.04.003
14. Fossan FE, Sturdy J, Müller LO, Strand A, Bråten AT, Jørgensen A, et al. Uncertainty quantification and sensitivity analysis for computational FFR estimation in stable coronary artery disease. *Cardiovasc Eng Technol.* (2018) 9:597–622. doi: 10.1007/s13239-018-00388-w
15. Shiono Y, Kubo T, Tanaka A, Kitabata H, Ino Y, Tanimoto T, et al. Impact of myocardial supply area on the transstenotic hemodynamics as determined by fractional flow reserve. *Catheter Cardiovasc Interv.* (2014) 84:406–13. doi: 10.1002/ccd.25300
16. Blanco PJ, Bulant CA, Müller LO, Talou GDM, Bezerra CG, Lemos PA, et al. Comparison of 1D and 3D models for the estimation of fractional flow reserve. *Sci Rep.* (2018) 8:17275. doi: 10.1038/s41598-018-35344-0
17. Chu M, Dai N, Yang J, Westra J, Tu S. A systematic review of imaging anatomy in predicting functional significance of coronary stenoses determined by fractional flow reserve. *Int J Cardiovasc Imaging.* (2017) 33:975–90. doi: 10.1007/s10554-017-1085-3
18. Kern MJ, Seto AH. Is instantaneous wave-free ratio a new standard of care for physiologic assessment of coronary lesions? More questions than answers. *Circulation.* (2017) 136:2295–7. doi: 10.1161/CIRCULATIONAHA.117.029567
19. Kern MJ, Seto AH. Agreement and differences among resting coronary physiological indices – Are all things equal? *J Am Coll Cardiol.* (2017) 17:2124–7. doi: 10.1016/j.jacc.2017.08.069
20. Tóth GG, Wijns W. Circulus vitiosus of validation. *Eur Heart J.* (2018) 39:4082–5. doi: 10.1093/eurheartj/ehy724

21. Alonso-Betanzos A, Bolón-Canedo V, Heyndrickx GR, Kerkhof PL. Exploring guidelines for classification of major heart failure subtypes by using machine learning. *Clin Med Insights Cardiol.* (2015) 9(Suppl. 1):57–71. doi: 10.4137/CMC.S18746
22. Christou MAC, Siontis CM, Katritsis DG, Ioannidis JPD. Meta-analysis of fractional flow reserve versus quantitative coronary angiographys and noninvasive imaging for evaluations of myocardial ischemia. *Am J Cardiol.* (2007) 99:450–6. doi: 10.1016/j.amjcard.2006.09.092
23. Shalman E, Rosenfeld M, Dgany E, Einav S. Numerical modeling of the flow in stenosed coronary artery. The relationship between main hemodynamic parameters. *Comput Biol Med.* (2002) 32:329–44. doi: 10.1016/S0010-4825(01)00033-6
24. Lan H, Updegrove A, Wilson NM, Maher GD, Shadden SC, Marsden AL. A Re-engineered software interface and workflow for the open-source SimVascular Cardiovascular Modeling Package. *J Biomech Eng.* (2018) 140:024501-1–11. doi: 10.1115/1.4038751
25. Park SJ, Kang SJ, Ahn JM, Shim EB, Kim YT, Yun SC, et al. Visual-functional mismatch between coronary angiography and fractional flow reserve. *JACC Cardiovasc Interv.* (2012) 5:1029–36. doi: 10.1016/j.jcin.2012.07.007
26. Pellicano M, Lavi I, De Bruyne B, Vaknin-Assa H, Assali A, Valtzer O, et al. Validation study of image-based fractional flow reserve during coronary angiography. *Circ Cardiovasc Interv.* (2017) 10:e005259. doi: 10.1161/CIRCINTERVENTIONS.116.005259
27. Verdier-Watts F, Rioufol G, Mewton N, Sanchez I, Green L, Bonnefoy-Cudraz E, et al. Influence of arterial hypotension on fractional flow reserve measurements. *EuroIntervention.* (2015) 1:416–20. doi: 10.4244/EIJV11I4A82
28. Kern MJ. Seeing and not believing: understanding the visual-functional mismatch between angiography and FFR. *Catheter Cardiovasc Interv.* (2014) 84:414–5. doi: 10.1002/ccd.25616
29. Yang DH, Kang SJ, Koo HJ, Kweon J, Kang JW, Lim TH, et al. Incremental value of subtended myocardial mass for identifying FFR-verified ischemia using quantitative CT angiography: comparison with quantitative coronary angiography and CT-FFR. *JACC Cardiovasc Imaging.* (2019) 12:707–17. doi: 10.1016/j.jcmg.2017.10.027
30. Seiler C. Deconstructing the idol of fractional flow reserve using the IDEAL report. *Eur Heart J.* (2016) 37:2081–3. doi: 10.1093/eurheartj/ehv688
31. Kerkhof PLM, Peace RA, Macfarlane PW. Sex- and age-related reference values in cardiology, with annotations and guidelines for interpretation. *Adv Exp Med Biol.* (2018) 1065:677–706. doi: 10.1007/978-3-319-77932-4_41
32. Kerkhof PLM, Peace RA, Handly N. Ratiology and a complementary class of metrics for cardiovascular investigations. *Physiology.* (2019) 34:250–63. doi: 10.1152/physiol.00056.2018

**Conflict of Interest:** The authors declare that the research was conducted in the absence of any commercial or financial relationships that could be construed as a potential conflict of interest.